



**HAL**  
open science

# Rock mass mechanical behavior in deep mines: in situ monitoring and numerical modelling for improving seismic hazard assessment

Francesca de Santis

## ► To cite this version:

Francesca de Santis. Rock mass mechanical behavior in deep mines: in situ monitoring and numerical modelling for improving seismic hazard assessment. Earth Sciences. Université de Lorraine, 2019. English. NNT: 2019LORR0020 . tel-02130780

**HAL Id: tel-02130780**

**<https://hal.univ-lorraine.fr/tel-02130780v1>**

Submitted on 16 May 2019

**HAL** is a multi-disciplinary open access archive for the deposit and dissemination of scientific research documents, whether they are published or not. The documents may come from teaching and research institutions in France or abroad, or from public or private research centers.

L'archive ouverte pluridisciplinaire **HAL**, est destinée au dépôt et à la diffusion de documents scientifiques de niveau recherche, publiés ou non, émanant des établissements d'enseignement et de recherche français ou étrangers, des laboratoires publics ou privés.



## AVERTISSEMENT

Ce document est le fruit d'un long travail approuvé par le jury de soutenance et mis à disposition de l'ensemble de la communauté universitaire élargie.

Il est soumis à la propriété intellectuelle de l'auteur. Ceci implique une obligation de citation et de référencement lors de l'utilisation de ce document.

D'autre part, toute contrefaçon, plagiat, reproduction illicite encourt une poursuite pénale.

Contact : [ddoc-theses-contact@univ-lorraine.fr](mailto:ddoc-theses-contact@univ-lorraine.fr)

## LIENS

Code de la Propriété Intellectuelle. articles L 122. 4

Code de la Propriété Intellectuelle. articles L 335.2- L 335.10

[http://www.cfcopies.com/V2/leg/leg\\_droi.php](http://www.cfcopies.com/V2/leg/leg_droi.php)

<http://www.culture.gouv.fr/culture/infos-pratiques/droits/protection.htm>



Université de Lorraine  
Ecole Nationale Supérieure des Mines de Nancy  
Laboratoire GeoRessources  
École doctorale SIRENa

## Thèse

Présentée pour l'obtention du titre de

Docteur de l'Université de Lorraine

En Géosciences

Par

Francesca DE SANTIS

# Rock mass mechanical behavior in deep mines: in situ monitoring and numerical modelling for improving seismic hazard assessment

Soutenue publiquement le 5 février 2019

Devant le jury composé de :

<b>Beata ORLECKA-SIKORA (Ass. Pr.)</b>	Institute of Geophysics, Polish Academy of Sciences	Rapporteur
<b>Martin GRENON (Pr.)</b>	Université Laval, Québec, Canada	Rapporteur
<b>Evelyne FOERSTER (PhD)</b>	Commissariat à l'énergie atomique et aux énergies alternatives, France	Examinatrice
<b>Katshidikaya TSHIBANGU (Pr.)</b>	Université de Mons, Belgique	Examineur
<b>Yann GUNZBURGER (Mcf.)</b>	GeoRessources, Université de Lorraine, France	Directeur de thèse
<b>Pascal BERNARD (Pr.)</b>	Institut de Physique du Globe de Paris, France	Co-directeur de thèse
<b>Isabelle CONTRUCCI (PhD)</b>	Institut National de l'Environnement Industriel et des Risques, France	Encadrante
<b>Savka DINEVA (PhD)</b>	Luleå University of Technology, Suède	Invitée
<b>Anders NYSTRÖM (Ing.)</b>	Boliden, Suède	Invité



# Acknowledgments

At the end of this very enriching experience, I would like to express my special appreciation and thanks to the people who have contributed to this work.

Je tiens à remercier fortement mon directeur de thèse Yann Gunzburger, mon co-directeur Pascal Bernard et mes encadrants Isabelle Contrucci et Vincent Renaud. C'est grâce à votre soutien, vos conseils et votre disponibilité que j'ai pu mener cette thèse à son terme. Merci Yann pour ton intérêt, ta disponibilité, tes idées et pour m'avoir toujours poussé à faire de mon mieux. Merci beaucoup aussi pour m'avoir rappelé à plusieurs reprises qu'une thèse n'est jamais terminée ! Ça m'a permis de ne pas me perdre et de garder à l'esprit mon objectif. Pascal, tu m'as montré la magie de la sismologie et tout ce qu'on peut apprendre et découvrir en analysant un signal microsismique. Je t'en remercie beaucoup ! Isabelle, merci de m'avoir accueilli à l'Ineris au tout début de mon arrivée, lorsque je ne parlais pas encore en français et que j'avais très peu de connaissances sur la sismicité induite. Tu as été toujours disponible et pleine de conseils à me donner tout au long de ce projet de thèse. Nous avons aussi partagé l'expérience bizarre et marrante de se perdre dans la forêt suédoise sous la neige. Vincent, tu m'as fait découvrir le monde de la modélisation numérique. C'est uniquement grâce à ton investissement, ton intérêt et tes enseignements que j'ai pu énormément apprendre sur la modélisation en très peu de temps. Merci d'avoir été patient et disponible à chaque fois que je t'ai appelé pour te dire : FLAC à planté !

Special thanks go to Shahram Mozaffari for having been my mentor and my guide underground the mine. My gratitude goes also to Anders Nyström for all the interesting discussions and the support he gave me. Johan Olsson, Lena Lilja and Michaela Åberg Seliö helped me tremendously in interpreting and understanding the complex geology of Garpenberg mine. Thank you for this and also for the very nice time spent in their office in Garpenberg. A special thank is also for Savka Dineva who was present at numerous PhD meetings with very interesting advices.

I also would like to thank Beata Orlecka-Sikora, Martin Grenon, Evelyne Foerster and Katshidikaya Tshibangu for having participated to the thesis jury and for their interest and their brilliant suggestions on this work.

Je tiens à remercier aussi particulièrement Jannes Kinscher et Armand Lizeur pour toutes nos discussions et pour l'aide précieuse qu'ils m'ont donnée tout au long de ce parcours. Mes remerciements vont également à Alice Tonnellier, Roxane Muller, Nicolas Spitzensteder et Régis Toussaint. Chacun de vous a énormément contribué à la réalisation de cette thèse. C'était un grand plaisir de travailler avec vous ! Un grand merci aussi pour Emmanuelle Klein et Pascal Bigarré pour m'avoir soutenue énormément et pour leur confiance en mes capacités. Je remercie également toute l'équipe de l'Ineris et de GeoRessources et très particulièrement tous les doctorants avec qui j'ai partagé le statut de thésard avec toutes les joies et les difficultés qui y sont associées.

Un ringraziamento speciale anche alla mia famiglia e ai miei cari amici in Italia. Siete il mio punto fisso nella mia vita qua e là in Europa.

Last but not the least, I would like to express all my gratitude to the miners who work every day deep inside the earth.

# Résumé élargi

Afin d'améliorer notre compréhension des phénomènes mécaniques qui induisent la sismicité dans les mines profondes, cette thèse propose d'étudier la réponse des massifs rocheux à l'exploitation minière à travers une approche multi-paramètres. Pour ce faire, les données géophysiques et géotechniques enregistrées *in situ* ont été comparées et interprétées à l'aide d'un modèle géomécanique 3D, en considérant les caractéristiques de la méthode d'exploitation et de la géologie locale. La méthodologie proposée a été appliquée au gisement de Lappberget dans la mine de Garpenberg (Suède), où le minerai polymétallique est extrait par la méthode « Sublevel stoping » jusqu'à des profondeurs de 1300 m. Cette méthode d'exploitation consiste à extraire le gisement à l'aide de tirs (explosifs) effectués entre deux niveaux consécutifs de la mine, en créant des cavités de 25 m de hauteur, dites « Stopes ».

L'étude s'est déroulée sur une période de deux ans, entre février 2015 et décembre 2016, au cours de laquelle la sismicité induite par l'exploitation minière a été surveillée par un réseau sismique, tandis que les variations de contrainte et de déplacement ont été mesurées par deux cellules de mesure de contrainte et un extensomètre, tous installés près des zones excavées. Au cours de la période d'étude, 52 stopes ont été extraits, dont le Stope 13 qui a été complètement exploité sur toute la hauteur de la zone étudiée. Cela a constitué une occasion unique de suivre la réponse du massif rocheux au fur et à mesure de la progression des excavations.

Les données sismiques enregistrées au cours de la période d'étude ont été analysées en tenant compte de leurs caractéristiques spatio-temporelles par rapport à la production minière. Ensuite, la réponse du massif rocheux a été interprétée en fonction des paramètres sismiques à la source ainsi que d'autres caractéristiques des événements microsismiques. Puis les données sismiques ont été comparées et interprétées avec les mesures géotechniques. Par la suite, un modèle numérique 3D statique, élastoplastique, de grandes dimensions (cube de 1,5 km d'arête), à maillage dense a été construit. Celui-ci intègre la géométrie précise des 4 unités lithologiques observées et le calage avec les mesures de contrainte a permis de retrouver l'état de contrainte vierge. Le modèle simule l'excavation des 52 stopes exploités dans le gisement de Lappberget pendant la période étudiée, ce qui permet d'analyser la réponse du massif rocheux en termes de contraintes et de déformations induites dans toute la zone d'intérêt, ainsi que d'autres paramètres mécaniques. Enfin, les résultats du modèle ont été comparés à l'analyse des données sismiques afin de mieux déterminer tous les mécanismes en jeu.

Le premier résultat a été obtenu par l'étude du catalogue microsismique : on montre que les tirs de production jouent un rôle primordial dans la génération de la sismicité induite, même si l'activité microsismique est plus dépendante de la séquence minière, que du volume exploité. En particulier, le Stope 13, qui a été complètement excavé pendant la période étudiée, a fortement influencé le taux de sismicité. On observe une première période (jusqu'en mai 2016) caractérisée par une faible réponse du massif rocheux à l'exploitation minière, suivie d'une augmentation globale de l'activité sismique pendant une deuxième période de forte réponse à l'exploitation. L'analyse spatiale des événements a mis en évidence deux zones principales d'activité sismique : le cluster central, autour du Stope 13 et près de la zone de production, et le cluster de droite dans la partie Est de la mine, en coïncidence avec une région caractérisée par la présence de certaines zones géologiques faibles (talc-schistes). Le cluster central est sismiquement actif au long de toute la période étudiée, tandis que le

cluster de droite ne devient une source intense de sismicité que dans la seconde moitié de 2016, pendant la période de forte réponse du massif rocheux à l'exploitation minière. En général, la sismicité induite dans le gisement de Lappberget présente des magnitudes plutôt faibles si on la compare à d'autres mines à des profondeurs similaires (p. ex. Fritschen, 2010 ; Kgarume et al., 2010 ; Kubacki et al., 2014 ; Vallejos et McKinnon, 2011). En effet, la magnitude du moment ( $M_w$ ) pour l'ensemble des données analysées varie entre  $-2 \div 0,8$ . Les événements caractérisés par  $M_w \geq 0$  ne représentent qu'une petite partie de l'ensemble des données et se rencontrent principalement dans le cluster central.

La sismicité semble résulter principalement de la réaction directe du massif rocheux aux changements de contraintes induits par les tirs de production, où des augmentations soudaines du taux sismique sont observées immédiatement après les explosions. Cinq des six séquences sismiques analysées sont liées à la production dans le Stope 13. Ceci est valable à la fois pour le cluster central et le cluster droit, de sorte que les événements du cluster droit sont spatialement éloignés des zones excavées, mais temporellement en coïncidence avec les explosions. La sismicité déclenchée dans le cluster droit a été interprétée en tenant compte de divers facteurs concomitants tels que :

- (i) des conditions de surcontrainte de la zone du cluster central dans les dernières phases d'exploitation du Stope 13 ;
- (ii) la dissipation d'une grande quantité d'énergie coïncidant avec les deux derniers tirs de production dans le Stope 13, et
- (iii) la distribution hétérogène du champ de contrainte dans la zone du cluster droit en raison des hétérogénéités lithologiques locales.

En effet, à mesure que l'excavation progresse dans le cluster central, les roches voisines subissent une augmentation de l'état de contrainte et le taux de sismicité augmente rapidement. Lorsque de nouveaux tirs sont réalisés, les contraintes élevées à l'intérieur du volume de roche dynamitée doivent être redistribuées dans le massif rocheux environnant, ce qui influence le champ de contrainte locale dans la zone du cluster droit. Ici, en raison d'une lithologie peu homogène, le champ de contrainte local est réparti de manière hétérogène, avec de fortes contraintes dans les roches rigides entourées de lentilles de faible raideur. En raison de cette configuration particulière, même de faibles changements de contrainte induits par des explosions lointaines (dans le Stope 13) peuvent déclencher une sismicité dans le cluster droit.

En plus du dynamitage, les hétérogénéités géologiques jouent un rôle primordial dans la redistribution du champ de contrainte et, par conséquent, dans la nucléation et la propagation des fractures au sein du cluster droit. Il a été postulé que les fractures dans le cluster droit sont très probablement nucléées à l'intérieur de roches dures et que leur développement est stoppé, en raison de la présence de lentilles faibles au contact direct avec les roches rigides. Par conséquent, les événements du cluster droit présentent des magnitudes et des rayons à la source plus faibles par rapport à la population du cluster central. De plus, en raison de l'hétérogénéité du champ de contrainte locale, les événements du cluster droit sont en moyenne plus énergétiques et se caractérisent par des contraintes apparentes et des chutes de contraintes plus élevées par rapport à la sismicité du cluster central.

En plus du dynamitage et de l'influence de la géologie locale, un deuxième mécanisme, caractérisé par une réponse plus lente et persistante après les tirs, semble être à l'origine de la sismicité à la fois

dans le cluster central et dans celui de droite. Cette dernière composante de la sismicité a été considérée comme responsable des réactivations différées du taux de sismicité observé dans la plupart des séquences sismiques analysées, ainsi que de la seule séquence sismique non liée aux tirs de production sur les six séquences observées pendant la période d'étude. Ce second type de sismicité a été associé à des phénomènes de fluage induits par le dynamitage. En effet, de nombreuses observations portent à exclure un mécanisme type « cascade d'événement », lorsque les événements plus forts dans une séquence sismique déclenchent une nouvelle activité sismique par transfert de contraintes. Premièrement, le taux de sismicité n'est pas lié à la taille des événements, de sorte que les réactivations retardées observées dans de nombreuses séquences sismiques analysées ne sont pas induites par des événements microsismiques plus importants. De plus, les réactivations ne se produisent pas nécessairement au même endroit que l'activité sismique précédente, ce qui indique l'occurrence d'un mécanisme agissant à plus grande échelle. Enfin, les réactivations différées de la sismicité sont principalement observées après des périodes d'activité sismique régulière ou après des périodes où aucun événement ne s'est produit. Toutes ces observations impliquent qu'il ne s'agit pas d'une simple cascade d'événements microsismiques qui déclenche des événements supplémentaires, c'est pourquoi un modèle basé sur le fluage a été proposé. Plus précisément, la thèse montre que l'exploitation minière induit des déformations asismiques à travers des phénomènes de fluage dans les roches de faibles caractéristiques mécaniques, qui chargent lentement les aspérités sismiques environnantes jusqu'à leur rupture en provoquant la sismicité.

Ce dernier modèle proposé est en partie confirmé par les mesures de déformation effectuées près du Stope 13 pendant la période étudiée. En effet, leur analyse met en évidence, d'une part, que la plupart des stopes ont été excavés sans induire de phénomènes sismiques, mais plutôt des déformations asismiques. D'autre part, les déformations mesurées montrent des évolutions temporelles, ce qui implique l'occurrence de phénomènes de fluage. Par ailleurs, on observe une bonne proportionnalité entre le taux de sismicité et l'évolution des déformations mesurées dans le temps. Cela implique que l'activité sismique décroît proportionnellement au taux de décroissance des déformations asismiques induites. Cette dernière observation est conforme aux modèles proposés dans la littérature (Bourouis et Bernard, 2007 ; Naoi et al., 2015) où les aspérités sismiques sont chargées et forcées à la rupture à cause du fluage agissant autour de celles-ci.

Dans la deuxième partie de cette thèse, un modèle géomécanique élastoplastique 3D a été réalisé à partir d'une reconstruction précise de la géologie, du calage de l'état de contrainte vierge et du phasage d'excavation minier. Le modèle numérique simule 70 étapes d'excavation. L'objectif du modèle numérique développé dans cette thèse consistait, d'une part, à caractériser plus en profondeur la réponse du massif rocheux à l'exploitation minière dans toute la zone d'étude et, d'autre part, à analyser les corrélations entre les résultats du modèle et la sismicité induite.

En premier lieu, le modèle numérique proposé met en évidence l'influence des zones géologiques faibles sur la distribution des contraintes, des déformations et de la plasticité. En effet, ces zones, caractérisées par des propriétés mécaniques significativement plus faibles par rapport au gisement, ne sont pas en mesure de supporter un chargement important. Par conséquent, les contraintes sont transférées aux roches rigides environnantes, ce qui a pour effet d'élargir l'extension des zones de fortes contraintes, en particulier aux limites des zones faibles. En conséquence, le champ de



contrainte est hétérogène autour des excavations et de grandes déformations sont observées à l'intérieur des lentilles de talc-schiste.

De plus, la modélisation numérique souligne la forte influence du phasage minier sur la (re)distribution des contraintes. En particulier, il a été démontré qu'en raison du phasage couplé ascendant et descendant choisi pour le Stope 13, le dernier bloc central de ce stope a subi de fortes contraintes qui se sont intensifiées avec la progression des excavations. Cette observation est tout à fait en accord avec les mesures géotechniques effectuées, ainsi qu'avec la sismicité observée, qui s'est intensifiée en coïncidence avec les dernières étapes d'exploitation du Stope 13.

Même si la plupart des résultats de la modélisation numérique semblent être en accord avec les observations sur le terrain, il y a certains aspects de la sismicité induite que le modèle ne peut expliquer entièrement. Premièrement, il est difficile de corrélérer les résultats du modèle avec la sismicité du cluster de droite. Cela est évident lorsqu'on cherche des corrélations entre l'extension spatiale des zones soumises à de fortes contraintes et les zones plastiques dans le modèle avec les localisations des événements microsismiques. Le cluster de droite se caractérise par des volumes plastiques plutôt faibles et les zones où la plasticité est observée dans le modèle ne coïncident pas avec les zones sismiques actives. De même, les contraintes induites et les changements de contraintes ne semblent pas assez forts pour justifier des niveaux aussi élevés de sismicité induite dans la zone du cluster droit, qui reste très éloignée des excavations (à environne 80 m de distance). D'autre part, en analysant les résultats du modèle numérique à plus petite échelle, c'est-à-dire dans des sphères centrées sur les hypocentres des événements microsismiques, on observe une influence de la production du Stope 13 sur les changements de contraintes dans la zone du cluster droit. Cela démontre que le modèle peut expliquer les changements de contraintes induits dans le cluster droit par des tirs de production effectués à distance, bien que les variations de contraintes soient d'intensité similaire d'une étape à l'autre, de sorte qu'aucune distinction claire ne peut être faite entre les changements de contraintes qui entraînent une sismicité et ceux qui n'ont donné lieu à aucun événement sismique.

Les principales raisons de l'écart observé entre les résultats du modèle et la sismicité du cluster droit doivent être recherchées dans les mécanismes qui peuvent entraîner une sismicité à distance, mais qui ne sont pas inclus dans le modèle. D'après l'analyse des données sismiques, on suppose que la sismicité du cluster droit est fortement influencée par des hétérogénéités géologiques, ce qui donne lieu à des régions où les contraintes sont " accumulées " et où la sismicité induite par des tirs distants est de préférence nucléée. Les hétérogénéités géologiques dans la région du cluster droit ont été attribuées aux grands volumes de matériaux faibles qui sont plus abondants dans cette région de la mine que dans la région centrale et sur le côté Ouest. Cependant, dans le modèle numérique, la seule présence de matériaux faibles ne semble pas suffisante pour induire des contraintes plus élevées et, par conséquent, une activité sismique importante dans le cluster droit. Cela donne à penser qu'un phénomène n'est pas pris en compte dans le modèle. Une première cause peut être liée aux propriétés mécaniques choisies pour les zones de faiblesse, qui n'ont pas été caractérisées par des essais en laboratoire. De plus, le gisement a été considéré comme un matériau homogène caractérisé par les mêmes propriétés dans l'ensemble du modèle. Toutefois, le minerai du secteur se distingue par la présence de sulfures massifs interstratifiés dans du calcaire. Au contraire, à mesure que nous nous déplaçons vers l'Ouest, la géologie devient plus homogène, où la minéralisation se produit dans des réseaux de veines imbriquées dans une unité de micaquartzite. L'hétérogénéité des

minerais devrait probablement être prise en compte dans le modèle pour pouvoir reproduire des contextes géologiques plus réalistes et, par conséquent, des conditions plus propices à la sismicité à distance.

Comme expliqué précédemment, la sismicité du cluster droit semble également être influencée par des mécanismes de fluage. Par conséquent, des améliorations au modèle numérique pourraient probablement être obtenues en considérant un modèle de comportement qui prend en compte le fluage des zones faibles, ce qui induirait probablement des transferts de contraintes sur de plus grandes distances. Cependant, des recherches plus approfondies devraient être faites au préalable pour déterminer le modèle de comportement le plus approprié à appliquer et pour choisir une ou plusieurs lithologies auxquelles il serait attribué.

De meilleurs résultats ont été obtenus en comparant les résultats du modèle numérique avec la sismicité du cluster central. C'est particulièrement vrai pour l'analyse des changements de contrainte, de déformation et de plasticité dans le temps, dont la moyenne est calculée dans le modèle à l'intérieur de sphères centrées sur les hypocentres des événements sismiques. Cette analyse met en évidence l'occurrence d'une période où les contraintes calculées au sein du cluster central ne fluctuent que légèrement autour de leur valeur la plus élevée, alors que les déformations et la plasticité continuent à augmenter. On observe une chute de contrainte significative coïncidant avec les deux derniers tirs d'exploitation dans le Stope 13, ce qui a également entraîné le déclenchement des séquences sismiques les plus significatives, dans le cluster central et dans celui de droite. Cette dernière période a été interprétée comme la réponse fragile du massif rocheux au sein du cluster central. La tendance observée pour les contraintes du modèle au cours de cette dernière période est cohérente avec l'idée que la sismicité à distance au sein du cluster droit est déclenchée lorsque le cluster central n'est plus en mesure de supporter des charges supplémentaires.

Enfin, une bonne proportionnalité a été trouvée entre la tendance temporelle du moment sismique cumulatif des événements du cluster central et la variation temporelle de certaines sorties du modèle (notamment l'énergie plastique, le volume plastique et la déformation déviatorique), cumulées dans les sphères. Toutefois, la proportionnalité ne peut être atteinte que lorsque la sismicité est principalement due à des changements de contraintes directement induits par le dynamitage. Dès que d'autres mécanismes non pris en compte dans le modèle (comme le fluage) interviennent dans le déclenchement de la sismicité, les paramètres sismiques et les paramètres du modèle n'ont plus la même tendance temporelle. Malgré cette limitation inhérente aux hypothèses retenues pour la modélisation numérique, ce résultat semble prometteur pour d'éventuelles corrélations quantitatives entre le modèle et les variables sismiques et souligne l'importance de considérer dans le modèle tous les mécanismes qui contribuent à déclencher la sismicité. D'autre part, à ce stade, les corrélations temporelles entre variables sismiques (mesure) et mécaniques (modèle) pourrait servir d'indicateur pour des mécanismes supplémentaires entraînant la sismicité (en plus de ceux s'ajoutant à l'effet immédiat de changement de contrainte induit par le dynamitage).

Les résultats de cette thèse démontrent qu'une approche combinée qui associe les données sismiques et géotechniques à la modélisation numérique peut améliorer considérablement la compréhension de la réponse des massifs rocheux à l'exploitation minière. La combinaison de ces méthodologies dans une approche intégrée peut réduire considérablement leurs limites explicites

qui sont évidentes lorsque ces instruments sont considérés séparément. Cela est particulièrement vrai si on veut analyser non seulement le comportement sismique, mais aussi les processus asismiques induits par les excavations souterraines.

# List of contents

Chapter 1 – Introduction .....	1
1.1 Mining-induced seismicity mechanisms.....	2
1.2 Monitoring of mining-induced seismicity and hazard assessment .....	5
1.3 Motivation, strategy and structure of this thesis.....	7
Chapter 2 – Study area: Garpenberg mine and Lappberget orebody.....	10
2.1 An introduction to Garpenberg mine.....	10
2.2 Geological setting and initial stress state.....	12
2.2.1 Lappberget orebody and weakness zones .....	14
2.2.2 Initial stress state and elastic rock mass properties.....	15
2.3 Mining method and sequencing.....	20
2.4 Geophysical and geotechnical monitoring in Lappberget.....	23
2.4.1 Extensometer data .....	24
2.4.2 Strain measurements .....	25
2.4.3 Microseismic data.....	28
2.5 Seismic activity and observed damage.....	29
Chapter 3 – Seismic data processing.....	33
3.1 Routines of seismic data acquisition and processing.....	33
3.1.1 Type of recorded seismic signals .....	36
3.1.2 Challenges and common errors in daily data processing.....	38
3.2 Picking consistency evaluation - The Wadati analysis.....	39
3.3 Evaluation of microseismic network performances.....	42
3.3.1 EMAP algorithm methodology .....	43
3.3.2 EMAP application to Lappberget microseismic network .....	44
3.4 Considerations about the extension of the analyzed area .....	51
3.5 Seismic source parameters estimation .....	53
3.5.1 Considerations on source parameters uncertainties .....	57
Chapter 4 – Rock mass response to mining .....	59
4.1 Spatiotemporal behavior of microseismic activity and mine blasts .....	59
4.1.1 Seismic sequences and clusters.....	64
4.2 Analysis of seismic source parameters.....	71
4.2.1 Temporal variation in b-value .....	77
4.3 What drives seismicity?.....	78
4.4 Analysis of geotechnical observations .....	82
4.5 Summary and discussion .....	91
Chapter 5 – Numerical modelling.....	96

5.1	Numerical modelling techniques.....	96
5.2	Model choice and strategy .....	99
5.3	Description of the model.....	100
5.3.1	Model geometry and boundaries.....	100
5.3.2	Model meshing.....	103
5.3.3	Initial and boundary conditions.....	104
5.3.4	Modelled elements and mechanical effect of paste fill .....	106
5.3.5	Constitutive laws and mechanical properties .....	108
5.3.6	Simulated mining sequence .....	112
5.4	Comparison with in situ geotechnical measurements .....	115
5.5	Model results and interpretations .....	117
5.5.1	Analysis of stress distribution.....	118
5.5.2	Analysis of strain distribution.....	124
5.5.3	Analysis of plastic zones and influence of weak geological materials .....	126
5.5.4	Temporal evolution of model parameters .....	128
5.6	Discussion and conclusion.....	129
Chapter 6 – Combined analysis of seismicity and numerical modelling.....		133
6.1	Relating induced seismicity with geomechanical modelling.....	133
6.2	Strategy of comparison in our work.....	136
6.3	Qualitative comparison at large-scale.....	137
6.3.1	Plastic zone and seismic activity.....	137
6.3.2	Instability criteria and seismic activity .....	139
6.4	Quantitative comparison at small-scale.....	144
6.4.1	Model and seismic parameters at punctual locations .....	145
6.4.2	Model and seismic parameters at spheres location .....	149
6.5	Summary and conclusion .....	156
Chapter 7 – Summary, conclusions and perspectives.....		159
7.1	Microseismic and geotechnical data analysis and interpretation.....	160
7.2	Numerical modelling and mining-induced seismicity .....	162
7.3	General perspectives.....	164
Bibliography .....		166
Annex A: Supplementary figures and tables .....		175
Annex B: Galleries and stopes geometry reconstruction .....		182
Annex C: Weakness zones geometry reconstruction .....		185
Annex D: Model meshing .....		187

# List of figures

Fig. 1.1 - Mechanisms of anthropogenic seismicity and industrial activities. ....	1
Fig. 1.2 - Models of fractures mechanisms in mines and the associated P-wave radiation field.. ....	3
Fig. 1.3 - Radiated seismic energy and volume of extracted rock mass.....	7
Fig. 2.1 - Geographical location of Garpenberg mine and its orebodies.....	11
Fig. 2.2 - Garpenberg mine production .....	12
Fig. 2.3 - Geological map of Garpenberg area and geological cross section of Lappberget orebody....	13
Fig. 2.4 - Orebody, weak and very weak geological zones in block 1250.....	14
Fig. 2.5 - Location of stress measurements and representation of the overcoring method .....	16
Fig. 2.6 - Stereographic representation of stress state retrieved by Ineris.....	18
Fig. 2.7 - Stereographic representation of stress state retrieved by SINTEF .....	18
Fig. 2.8 - Plan view of one mine level in block 1250.....	20
Fig. 2.9 - Excavation geometry in block 1250.....	21
Fig. 2.10 - Mining sequence in Lappberget block 1250.....	22
Fig. 2.11 - Geophysical and geotechnical monitoring network.....	23
Fig. 2.12 - Extensometer data .....	24
Fig. 2.13 - Permanent strain measurements.....	26
Fig. 2.14 - Spatiotemporal trend of microseismic activity.....	29
Fig. 2.15 - Boliden database on microseismic activity.....	30
Fig. 2.16 - Observed damage in Lappberget orebody .....	31
Fig. 2.17 - Rock falls due to weak zones .....	31
Fig. 2.18 - Recent failures in 1250 block of Lappberget .....	32
Fig. 3.1 - Lappberget microseismic network .....	34
Fig. 3.2 - Seismograms and spectrograms of some MSE.....	37
Fig. 3.3 - Seismograms and spectrograms of mine blasts, boulder blasts and noise related to mining operations. ....	37
Fig. 3.4 - Modified Wadati diagrams for Lappberget microseismic dataset .....	40
Fig. 3.5 - Example of erroneous picking on a signal related to working activities .....	41
Fig. 3.6 - Root mean square error between theoretical and calculated origin times .....	41
Fig. 3.7 - Schematic illustration of location simulation procedure .....	44
Fig. 3.8 - PGV of S-waves for some located MSE.....	45
Fig. 3.9 - Local magnitudes distribution of Lappberget microseismic events .....	47
Fig. 3.10 - Horizontal profile of minimum detected and located magnitude.....	47
Fig. 3.11 - Vertical profile of minimum detected and located magnitude .....	48
Fig. 3.12 - Distribution of predicted location errors.....	50
Fig. 3.13 - Events located within the Ineris monitored area .....	52
Fig. 3.14 - Events located outside and within the Ineris monitored area .....	53
Fig. 3.15 - Examples of corner frequency and moment magnitude estimation.....	54
Fig. 3.16 - Example of seismic data processing before computing spectral ratio.....	56
Fig. 3.17 - Spectral ratio for Q-factor determination .....	56
Fig. 4.1 - Number of microseismic events and mine blasts per hour.....	60
Fig. 4.2 - Temporal distribution of microseismic activity and mine blasts.....	61
Fig. 4.3 - Characteristics of some PB .....	62

Fig. 4.4 - Seismic energy and extracted rock mass volume .....	62
Fig. 4.5 - Space distribution of MSE.....	63
Fig. 4.6 - Comparison between microseismic events number and extracted stope volumes .....	64
Fig. 4.7 - Magnitude-time history chart .....	65
Fig. 4.8 – Space and time distribution of seismic sequences .....	67
Fig. 4.9 - Space and time distribution of Sequence 4.....	68
Fig. 4.10 - Space distribution of Sequence 5 and Sequence 6.....	69
Fig. 4.11 - Temporal distribution of Sequence 5 and Sequence 6.....	71
Fig. 4.12 - Frequency-magnitude relationship for the events within CC and RC .....	72
Fig. 4.13 - Cumulative distribution of source radius for the events within the two clusters.....	73
Fig. 4.14 - Cumulative distribution of seismic energy and S-wave to P-wave energy ratio .....	74
Fig. 4.15 - Histogram of apparent stress and stress drop .....	76
Fig. 4.16 - Energy-moment and moment-corner frequency relationships .....	76
Fig. 4.17 - Temporal b-value variation.....	78
Fig. 4.18 - Probability density function of normalized interevent times.....	79
Fig. 4.19 - Histogram of interevent times $\tau$ and interevent time over time.....	80
Fig. 4.20 - Seismicity rate and p-value estimation .....	82
Fig. 4.21 - Comparison between excavation advancement in Stope 13, strain measured by PD and PH cells, extensometer data and seismic activity.....	83
Fig. 4.22 - Strain measurements at PH cell during Shift 1 and Shift 2.....	85
Fig. 4.23 - Strain measurements at PD and PH cells during Shift 3. ....	86
Fig. 4.24 - Strain measurements at PH cell during Shift 4 and Shift 5.....	87
Fig. 4.25 - Strain measurements at PD and PH cells during Shift 6 .....	87
Fig. 4.26 - Strain measurements at PD and PH cells during Shift 9 .....	88
Fig. 4.27 - Strain measurements at PD and PH cells during Shift 10. ....	89
Fig. 4.28 - Comparison between strain measurements and cumulative number of MSE .....	90
Fig. 4.29 - Comparison between geotechnical measurements and cumulative number of MSE during Sequence 6 .....	91
Fig. 5.1 - Numerical model geometry.....	101
Fig. 5.2 - Galleries and stopes reconstruction in block 1250.....	102
Fig. 5.3 - Weakness zones reconstruction in block 1250.....	102
Fig. 5.4 - Final volumetric mesh of the whole numerical model.....	103
Fig. 5.5 - Upper levels, block 1250 and orebody below -1260 m .....	104
Fig. 5.6 - Geometry and mesh of the elementary model for paste fill influence evaluation .....	107
Fig. 5.7 - Hoek and Brown failure criterion for Lappberget modelled materials .....	111
Fig. 5.8 - Illustration of post-failure behaviors for different rock mass qualities.....	111
Fig. 5.9 - Step-by-step galleries and stopes excavation in the numerical modelling .....	113
Fig. 5.10 - Comparison between Plastic Model #2 and #3 .....	114
Fig. 5.11 - Comparison between model and CSIRO cells data.....	115
Fig. 5.12 - Comparison between model and extensometer data.....	117
Fig. 5.13 - Mining sequence at model step 0.13 and 52 .....	118
Fig. 5.14 - Contour plot of XX-stress.....	119
Fig. 5.15 - Principal stress tensor orientation at Step 52 .....	119
Fig. 5.16 - Contours of deviatoric stress along a vertical section .....	120
Fig. 5.17 - Contour of deviatoric stress along the horizontal plane .....	121

Fig. 5.18 - Difference in computed deviatoric stress between subsequent excavation steps.....	123
Fig. 5.19 - Contours of deviatoric strains along a vertical section.....	124
Fig. 5.20 - Contours of deviatoric strains along horizontal planes.....	125
Fig. 5.21 - Distribution of predicted plastic zones along a vertical section.....	126
Fig. 5.22 - Effect of weak zones on plasticity, stress and strain distribution. ....	127
Fig. 5.23 - Variation in plastic zone extension during time.....	128
Fig. 5.24 - Temporal evolution of model parameters.....	129
Fig. 5.25 - Comparison between elastic and elastoplastic models.....	131
Fig. 6.1 - Comparison between plastic zones and microseismic events.....	138
Fig. 6.2 - Predicted “unstable regions” based on <i>BSR</i> criterion.....	141
Fig. 6.3 - Predicted “unstable regions” based on maximum shear stress variation criterion.....	143
Fig. 6.4 - Predicted “unstable regions” based on tensile criterion.....	144
Fig. 6.5 - Point sources locations and spheres.....	145
Fig. 6.6 - Schematization of temporal criterion chosen to associate each MSE to a singular modelled excavation step.....	146
Fig. 6.7 - PCA results for the first selected group of parameters.....	147
Fig. 6.8 - Contour maps of mean deviatoric stress and mean apparent stress.....	148
Fig. 6.9 - Mean deviatoric strain and plastic volume within spheres.....	150
Fig. 6.10 - Mean deviatoric stress within spheres and temporal evolution of seismic activity.....	151
Fig. 6.11 - Five regions of the strain-softening response for a moderately jointed rock mass.....	152
Fig. 6.12 - Average deviatoric strains versus average deviatoric stresses.....	153
Fig. 6.13 - Temporal variation of seismic moment and some model parameters.....	155
Fig. 6.14 - Principal strains and stresses at Step 34.....	156



# List of tables

Tab. 2.1 - Rock mass properties .....	17
Tab. 2.2 - Magnitudes of measured principal stresses.....	17
Tab. 2.3 - Computed initial stress state.....	20
Tab. 2.4 - Characteristics of production blasts and extensometer shifts.....	25
Tab. 2.5 - Characteristics of stress-strain shifts and of related PB.....	27
Tab. 3.1 - Mean values of background noise and PGV of P and S-waves.....	45
Tab. 3.2 - Calibration blast specifications.....	51
Tab. 4.1 - Details of production blasts and microseismic sequences.....	65
Tab. 4.2 - Characteristics of major strain shifts detected by CSIRO cells, displacement shifts measured by downward extensometer (ED) and seismic sequences observed between 2015 and 2016.....	84
Tab. 4.3 - Summary of major differences observed between CC and RC seismicity.....	92
Tab. 5.1 - Numerical modelling techniques and constitutive models.....	97
Tab. 5.2 - Back-computed virgin state of stress .....	105
Tab. 5.3 - Elastic properties and density of paste fill and orebody.....	106
Tab. 5.4 - Summary of modelled mining sequence.....	107
Tab. 5.5 - Summary of model results .....	108
Tab. 5.6 - Variability in material properties as retrieved from Boliden analysis.....	109
Tab. 5.7 - Retained mechanical parameters for numerical modelling.....	109
Tab. 5.8 - Chosen values of $m_i$ and $GSI$ for modelled materials.....	110
Tab. 5.9 - Additional parameters needed for the constitutive law applied to Lappberget ore.....	112
Tab. 5.10 - Differences between performed plastic models.....	114
Tab. 5.11 - Selected model steps and mined-out stopes .....	118
Tab. 6.1 - Selected model steps and mined-out stopes for qualitative comparison .....	137
Tab. 6.2 - Model and seismic parameters considered for comparison.....	146
Tab. 6.3 - Selected groups of model and seismic parameters and variables transformations.....	147
Tab. 6.4 - Seismic sequences and model steps .....	149
Tab. 7.1 - Non-exhaustive list of major advantages and disadvantages of geophysical monitoring, geotechnical measurements and numerical modelling.....	164

# Glossary

## Abbreviations

Abbreviation	Description
1C	1 component seismic probe
3C	3 components seismic probe
AU	Acquisition unit
BB	Boulder blast
CC	Central cluster
CC <sub>M</sub>	Central cluster in numerical model space
COV	Coefficient of variation
DB	Development blast
ED	Downward Extensometer
EDZ	Excavation damaged zone
EMAP	Numerical approach for Evaluating Microseismic Array Performances
fft	Fast Fourier transform
IMS	Institute of Mine Seismology
Ineris	French National Institute for Industrial Environment and Risks
IPGP	Institute de Physique du Globe
J1,2,3,4,5,6,7,8,9,10,11,12	Gauges of CSIRO cells
MSA	Microseismic activity
MSE	Microseismic events
N	Seismic noise
PB	Production blast
PCA	Principal component analysis
PD	Permanent descending strain cell
pdf	Probability density function
PH	Permanent horizontal strain cell
R	Receiver
RC	Right cluster
RC <sub>M</sub>	Right cluster in numerical model space
S <sub>1,2,3,4,5,6</sub>	Seismic sequences numbered from 1 to 6
SNR	Signal-to-noise ratio
UTC	Coordinated universal time
VS	Virtual seismic sources

# Symbols

Symbol	Unit	Description	Symbol	Unit	Description
A		Amplitude	s(f)	-	Receiver amplification site effect
A <sub>0</sub>		Amplitude at the source	t <sub>0</sub>	s	Origin time
BSR	-	Brittle shear ratio	t <sub>p</sub>	s	P-wave time arrival
CFS	MPa	Coulomb failure stress	t <sub>s</sub>	s	S-wave time arrival
ΔCFS	MPa	Coulomb failure stress changes	u(f)	-	Displacement spectra
E	J	Radiated seismic source energy	u <sup>M<sub>w</sub></sup>	-	Moment magnitude spectra
E <sub>Y</sub>	Pa	Young's modulus	UCS	MPa	Uniaxial compressive strength
E <sub>s</sub> /E <sub>p</sub>	-	S-wave to P-wave energy ratio	V <sub>p</sub>	m/s	P-wave velocity
ERR	MJ/m <sup>2</sup>	Energy release rate	V <sub>s</sub>	m/s	S-wave velocity
ESS	MPa	Excess shear stress	V <sub>p</sub> /V <sub>s</sub>	-	P-wave velocity to S-wave velocity ratio
f <sub>c</sub>	Hz	Corner frequency	Δσ	MPa	Stress drop
GSI	-	Geological strength index	ε	mm/m	Strain
I	-	Instrumental response	ε <sub>q</sub>	mm/m	Von Mises equivalent strain or deviatoric strain
J <sub>1,2,3</sub>	-	Stress tensor invariants	ε <sub>1</sub>	MPa	Major principal strain
M <sub>0</sub>	N·m	Seismic moment	ε <sub>2</sub>	MPa	Intermediate principal strain
M <sub>C</sub>	-	Magnitude of completeness	ε <sub>3</sub>	MPa	Minor principal strain
M <sub>L</sub>	-	Local magnitude	μ	N/m <sup>2</sup>	Shear modulus
M <sub>min</sub>	-	Minimum detectable magnitude	ν	-	Poisson's coefficient
M <sub>w</sub>	-	Moment magnitude	ρ	kg/m <sup>3</sup>	Density
n	-	Geometrical spreading	σ̄	-	Stress tensor
p	MPa	Mean stress	σ <sub>a</sub>	MPa	Apparent stress
PGV	m/s	Peak ground velocity	σ <sub>c</sub>	MPa	Compressive strength
Q	-	Quality factor	σ <sub>1</sub>	MPa	Major principal stress
q	MPa	Von Mises equivalent stress or deviatoric stress	σ <sub>2</sub>	MPa	Intermediate principal stress
r	m	Distance	σ <sub>3</sub>	MPa	Minor principal stress
r <sub>0</sub>	m	Source radius	τ	s	Interevent time
R	-	Radiation pattern	Ω	-	Low frequency plateau of u(f)

## Nomenclature

Name	Description
Backfill or paste fill	Material pumped into stope voids for being reclosed after exploitation
Boulder blasts	Blasts performed on isolated blocks of rock to reduce their size
Development blasts	Blasts performed in horizontal drill holes to excavate galleries
Drift	General term for referring to mine galleries
Footwall	Area of bedrock in contact with the orebody at gallery entrance
Footwall drift	Gallery within the footwall which gives access to the stopes
Hanging wall	Area of bedrock in contact with the orebody at the end of galleries
Host rock and bedrock	The rock surrounding the ore deposit
Ore or orebody	Rock containing precious minerals which need to be extracted
Production blasts	Blasts performed in vertical drill holes to extract the ore
Shotcrete	Slurry of concrete sprayed onto walls and roofs of mine galleries
Stope	Name given to mined-out areas for orebody extraction
	Name given to each column of a mine block
Stope back	Part of the gallery at the back of an open stope
Waste rock	Rock which does not contain commercially valuable minerals

# Chapter 1

## Introduction

Underground human activities (e.g. mining, petroleum production, fluid injection) produce alterations of the hydro-mechanic rock mass conditions, which can generate rupture phenomena and lead to seismicity when the rock mass strength is exceeded. This man-made seismic activity, generally referred to as anthropogenic seismicity, can cause damage to underground facilities as well as to surrounding urbanized areas, leading to serious socio-economic impacts. In this framework and due to the increasing need for strategic raw materials, anthropogenic seismicity is nowadays an important topic which concern both the scientific and the nonscientific communities. Understand the causes which lead to human-related seismicity is thus a fundamental purpose with the aim of mitigating and prevent the associated risks.

Generally, changes in the stress state or in the pore pressure of rock masses surrounding industrial operations are the major mechanisms which can bring to anthropogenic seismicity. According to McGarr et al. (2002), a partial separation of the dominant mechanism can be done considering the type of industrial activity (Fig. 1.1). Therefore, fluid injection operations (e.g. hydrocarbons extraction, geothermal energy production) are mainly associated with seismicity driven by pore pressure increase, while changes in normal and/or shear stress are the mechanisms mostly involved with operations resulting in mass or volume changes (e.g. open pits, underground mines, dams). Finally, a combination of these mechanisms can also be possible, for example in the case of dams and reservoirs, as well as for hydrocarbons extraction. However, this classification is a clear simplification of real mechanisms that are often more complex, such that anthropogenic seismicity remains difficult to forecast and control (Grigoli et al., 2017).

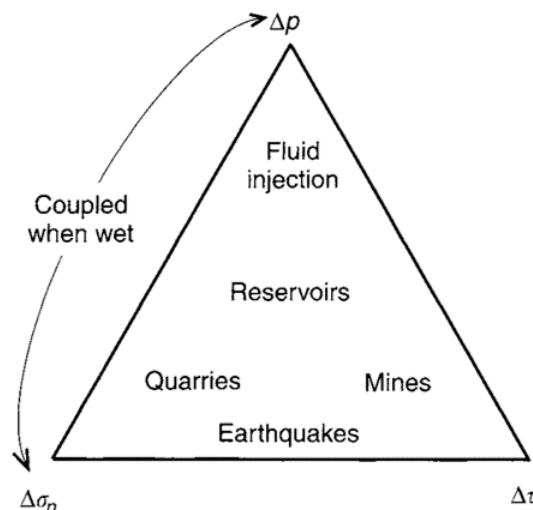


Fig. 1.1 - Mechanisms of anthropogenic seismicity and industrial activities (modified after McGarr et al., 2002). The three corners of the triangle indicate changes in pore pressure ( $\Delta p$ ), shear stress ( $\Delta \tau$ ) and normal stress ( $\Delta \sigma_n$ ).

A review of world-wide case studies on anthropogenic seismicity can be found in McGarr et al. (2002), while for a focus on European cases the reader is referred to Grigoli et al. (2017). A recent

report, published by Ineris (the French National Institute for Industrial Environment and Risks), provides a rich documentation of seismic events caused by disparate underground operations, together with a review of the measures employed to prevent and mitigate associated risks (Contrucci and Klein, 2018). It is worth mentioning that a large and interactive database of human induced earthquakes has been recently published online. Details about this project, together with an extensive review of some of the case studies can be found in Wilson et al. (2017) and Foulger et al. (2018), respectively.

Anthropogenic seismicity related to underground mining excavations, also referred to as mining-induced seismicity, is probably one of the most documented types of seismicity caused by human activities. It is also the most dangerous in terms of injuries and fatalities that directly concern underground mine workers. The first earthquake associated with underground mining activities occurred in South Africa in the last decade of the 19<sup>th</sup> century. About ten years later, this earthquake was recognized to be caused by mining operations in the Witwatersrand gold mine (McGarr et al., 2002). Since then, and thanks to the installation of underground seismic networks for monitoring mining-induced seismicity, earthquakes related to mining excavations have been observed worldwide. Due to significant depths of exploitation, which can reach up to 4 km, and high extraction rates, mining-induced seismicity is still largely experienced in South Africa, where characteristics of this man-made seismicity have been largely studied by researches (e.g. Boettcher et al., 2015; Durrheim et al., 2006; Durrheim, 2010; Julià et al., 2009; Naoi et al., 2011). Even if fatalities have been reduced, the number is still high with several tens of deaths per year (Foulger et al., 2018). Other countries that experience significant rates of mining-induced seismicity, even with the occurrence of large events, are: Australia (e.g. Hudyma et al., 2008a, 2008b; Hudyma and Potvin, 2004), Canada (e.g. Hudyma, 2009; Milne and Berry, 1976; Potvin and Hudyma, 2001; Urbancic and Trifu, 2000), China (e.g. Li et al., 2007 and the references therein) and USA (e.g. Kubacki et al., 2014; Wang and Ge, 2008). While in Europe, seismicity related to underground mines is mostly experienced in Poland (e.g. Lasocki, 2005; Leśniak and Isakow, 2009; Lizurek et al., 2015; Orlecka-Sikora et al., 2012; Stec, 2007), Germany (e.g. Bischoff et al., 2010; Fritschen, 2010) and Sweden (e.g. Dineva and Boskovic, 2017; Holmgren, 2015; Larsson, 2004; Nuannin et al., 2005; Olivier et al., 2015).

Thanks to decades of researches, many improvements have been achieved in the understanding of mining-induced seismicity and significant efforts have been made to mitigate the associated risks. However, this problem is far from being solved and still represents a major concern for underground stability and mine worker safety. In this framework, this thesis contributes to a deeper understanding of the rock mass response to mining, that is how the rock mass behaves to stress changes induced by excavations. In the following section, major characteristics of mining-induced seismicity are reviewed. Then, motivations, strategies and structure of this thesis are presented.

## 1.1 Mining-induced seismicity mechanisms

When rock mass volumes are extracted due to underground mine excavations the virgin state of stress is disturbed. This results in the reorganization of the local stress field which can lead to seismic and aseismic strains in surrounding rocks. The seismic component of the rock mass response is linked with rupture phenomena which emits seismic signals transmitted through the rock as elastic waves (Wang and Ge, 2008). Mining-induced seismicity is, thus, the result of fractures propagation inside

the rock mass. This seismicity, referred to as microseismic activity, is characterized by small moment magnitudes, generally lower than 0, which do not result in visible damage. However, long-term microseismic activity creates fracture networks within rock masses and thus have an influence on their stability (Wuestefeld et al., 2011). When larger energies are involved in the rupture process, rock failures can occur and these are generally referred to as rockfalls or rockbursts (Cook, 1976). Rockfalls are relatively nonviolent falls of rock under the influence of gravity, whereas rockbursts are associated with a sudden release of strain energy resulting in a violent ejection of rocks (Ortlepp and Stacey, 1994). Rockbursts are the major cause of fatalities in mines (Gibowicz and Kijko, 1994) and their occurrence become progressively more important as the average depth and the extent of mining operations increase (Cook, 1976; Hudyma et al., 2008a; Hudyma and Potvin, 2010). The general term rockburst is commonly employed for describing damaging events with significant different mechanisms. For a classification of rockbursts types the reader is referred to Ortlepp (1997).

Hasegawa et al. (1989) propose six conceptual models of expected source mechanisms in mines (Fig. 1.2). These mechanisms originally described for phenomena observed in Canadian mines have been adopted by many authors in other mining contexts (e.g. Teyssoneyre et al., 2002, Hudyma, 2008, Sileny and Milev, 2008). Unlike natural earthquakes, mine earthquakes may have source mechanisms that are not double-coupled or non-double-coupled (Hasegawa et al., 1989, Sileny and Milev, 2008). The first three mechanisms presented by Hasegawa et al. (1989) belong to this category (Fig. 1.2a, b, and c). These concern the collapse of the roof of the cavity (rockfall) as well as rockbursts, pillar burst and tensile fractures. The other three proposed mechanisms correspond to double-couple mechanisms (Fig. 1.2d, e and f). These are due to stress readjustment either on pre-existing faults or with the creation of new fractures at the excavation face.

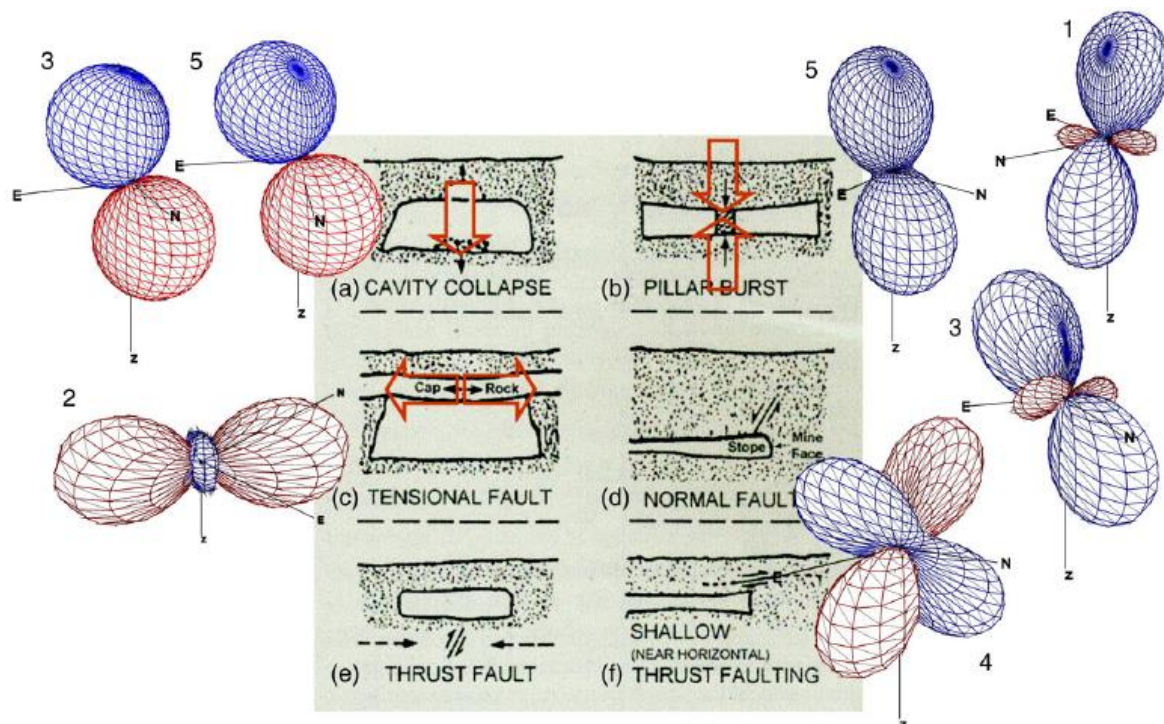


Fig. 1.2 - Models of fractures mechanisms in mines and the associated P-wave radiation field. In red compression, in blue dilation (Hasegawa et al., 1989, Sileny and Milev, 2008).

The first mechanism (Fig. 1.2a), namely the block fall of the cavity roof, takes place in two phases. The first is the detachment of rock from the roof, and the second is the fall of this rock on the ground. This phenomenon can be modeled by a simple force directed downwards. Rockburst can be modelled by the same mechanism even if these latter failures release a much greater energy. The pillar burst (Fig. 1.2b) is due to converging vertical forces acting on the pillars. This phenomenon is modeled by a vertical dipole, the associated radiation field is that of an implosion. The third type of failure process (Fig. 1.2c) is related to tensile failures which can occur in the middle of wide rooms or excavations. The forces involved in this mechanism are horizontal and of opposite directions, modelled by a horizontal dipole. Besides non-double-coupled mechanisms, the most common type of fracturing is normal faulting at the mine face (Fig. 1.2d), generally due to stress concentration caused by blasting. Thrust faults (Fig. 1.2e) can occur when the major principal stress is horizontal and mining activities have decreased the vertical stress enough to initiate slip in the intact bedrock or along pre-existing faults. Finally, nearly horizontal reverse faults can also occur over a cavity (Fig. 1.2f). These failures correspond to horizontal layers sliding on each other in response to the cavity roof subsidence. Both normal and inverse faults present a radiation field corresponding to a double-coupled mechanism.

Mining-induced seismicity is usually classified in two distinct categories (e.g. Gibowicz and Kijko, 1994; Hudyma, 2009; Richardson and Jordan, 2002; Stec, 2007): the first, referred as induced seismicity, is the seismicity directly connected with stress changes caused by mining operations, whereas the second, called triggered seismicity, is associated with movements along major geological structures, such as faults and discontinuities. In the first case, the entire rupture process, including its size, and not only its nucleation, is driven by mining-induced stresses. Therefore, these events would not have been occurred without any mining (Dahm et al., 2013). Induced seismicity presents lower magnitudes ( $M < 1$ ), with events occurring shortly after mine blasts (Richardson and Jordan, 2002). Source mechanisms of induced events can be different from shear, showing explosive type sources (Stec, 2007). On the contrary, in triggered seismicity tectonic stress plays a primary role, and mining activities only contribute for a small fraction of the stress change (Grigoli et al., 2017). Triggered events occur along geological discontinuities prone to failure, such that even small stress perturbation caused by mining can be sufficient for triggering seismicity (Dahm et al., 2013; Stec, 2007). This means that mining nucleates the failure, i.e. have the potential to accelerate a rupture which would have occurred naturally, while the rupture process is totally controlled by tectonic stresses (Dahm et al., 2013). These events are normally more energetic, they can occur at some distance from mine workings and can be characterized by an erratic time distribution (Gibowicz and Kijko, 1994), as driven by stress changes at larger temporal and spatial scales.

Apart from the influence of tectonic stress and mining-induced stress, the interaction between subsequent seismic events through static stress transfer has been as well recognized as a mechanism influencing mining seismicity. This was firstly observed in natural seismology (Stein, 1999) and interpreted as a self-triggering between consecutive events, where stress changes induced by larger events strongly affect location and timing of subsequent seismic activity. Marsan et al. (1999) studied spatiotemporal characteristics of seismicity recorded in the Creighton Mine (Canada), observing stress diffusion mechanisms between events and their influence on stronger events occurrence. Within the same mine, Ma et al. (2016) conducted a passive seismic tomography to investigate changes in the stress field before and after the occurrence of major events. They observed significant



changes in seismic velocity associated with large magnitude events, indicating increasing stress levels around the locations of major events before and after their occurrence. However, it was not demonstrated whether large magnitude events are the cause of increasing stresses or if these are still an effect of mine production. Orlecka-Sikora et al. (2012) studied two large seismic events (local magnitude higher than 3), occurred in the Rudna copper mine (Poland), to investigate whether their static stress changes could influence subsequent seismicity. Authors found that stress variations induced by major events, evaluated in terms of Coulomb stress change, strongly influenced rate and location of subsequent seismicity in the following two months. In addition, they also pointed out the primary role played by regions characterized by negative Coulomb stress changes. In these areas, the inhibiting effect of stress variation induced by major events appears to prevail over new stress changes imposed by mining front advancement. Authors concluded that stress variation due to larger events should be integrated in routine mine seismic hazard assessment.

More recently, Naoi et al. (2015) discovered small ( $-5.1 \leq M_w \leq -3.6$ ) repeating earthquakes occurring along a fault in a deep South African gold mine. These events are characterized by same location and very similar waveforms, such that, based on cross-correlation analysis, they can be separated into distinct groups according to similarities in their waveforms. Such repeating earthquakes, or simply repeaters, are observed in many tectonic regions (e.g. Nadeau and Johnson, 1998) and are interpreted as the repeating rupture of the same asperity loaded by aseismic creep around it (e.g. Linde et al., 1996; Perfettini and Avouac, 2004). Bourouis and Bernard (2007) observed similar repeaters during water injection in a geothermal field in France. The authors demonstrated that creep is a consequence of pore pressure increase due to water injection within the aseismic part of the fault; then, repeaters are triggered on locked seismic asperities brought to rupture by aseismic slip around them. Similarly, Naoi et al. (2015) interpreted repeaters recorded in the South African mine as ruptures on same asperities repeatedly loaded by surrounding long-term creep. Unfortunately, the authors do not provide information about possible interaction between mining activity and creep phenomenon.

## 1.2 Monitoring of mining-induced seismicity and hazard assessment

Before major events occur, it is important to analyze the behavior of the induced microseismic activity in an effort of preventing seismic hazardous areas. In this framework, a worldwide recognized tool for studying mining-induced seismicity is the microseismic monitoring technique (e.g. Ge, 2005; Hudyma and Potvin, 2010; Srinivasan et al., 1997), which is nowadays a routine technology for seismic hazard assessment in underground mines. This tool allows quantifying and tracking spatiotemporal and energetic characteristics of the induced seismicity, where microseismic events are fully described by their source location, origin time and at least two other independent source parameters (Mendecki et al., 1999), such as magnitude and radiated energy. One of the advantages of this technology is that mining-induced seismicity presents similar characteristic as natural earthquakes, such that data processing techniques, as well as interpretation approaches, can be directly adopted from natural seismology.

Thanks to this favorable characteristic and with the aim of preventing seismic risk, some authors propose to define re-entry protocols after blasting or major seismic events, based on common seismological parameters (Malek and Leslie, 2006; Tierney and Morkel, 2017; Vallejos and Estay,

2018; Vallejos and McKinnon, 2011, 2010). Re-entry protocols in mines are fundamental to ensure no personnel exposure to seismic hazardous areas, defining restrictions in some regions for a sufficient period of time. In these studies, guidelines for re-entry protocols are, thus, determined defining statistical properties of mining-induced aftershock sequences, based on scaling relations developed in the field of natural seismology, such as the modified Omori law (Utsu et al., 1995), the Gutenberg-Richter law (Gutenberg and Richter, 1944) and the Bath law (Bath, 1965).

Microseismic events analysis is also used in the attempt of assessing rockbursts hazard and for identifying possible precursors. Many authors observe decrease in b-value of the Gutenberg-Richter law prior to the occurrence of major failures (Kubacki et al., 2014; Liu et al., 2013; Nuannin et al., 2005; Pechmann et al., 2008). Similarly, rise in apparent stress (Wyss and Brune, 1968) can be used for identifying regions of the mine with increasing stress levels (Brown and Hudyma, 2017; Hudyma, 2009), where high magnitude events can occur. Alcott et al. (1998) proposed a rockburst hazard assessment criteria based on seismic source parameters, which was applied to back-analyze seven failures in a Canadian mine. Based on seismic energy, seismic moment and apparent stress criteria, the authors were able to delineate regions of increasing hazard, as well as determine precursory and decay trends. Liu et al. (2013) studied temporal variations of some seismic source parameters for a deep copper mine in China, identifying changes in their behavior before large-scale fractures occurred. The authors interpreted signatures in temporal variations of b-value, apparent volume (Mendecki et al., 1999) and energy index (Van Aswegen and Butler, 1993) as precursory indicators for increasing hazard, which allow identifying warning periods before major events.

All these studies demonstrate the considerable efforts made for rockburst hazard assessment and mitigation, nevertheless prediction, especially at short-term, is far from being achieved.

One major aspect which differentiate mining-induced events from natural earthquakes is their inherent dependence on a complex interaction between natural and anthropogenic factors (e.g. Hudyma, 2009; Milev and Spottiswoode, 2002), such as: geological structures and rock mechanical properties, virgin state of stress and mining-induced stress environment, but also mining method, excavated volumes and void geometries. This makes the analysis and the comprehension of induced seismicity more complex, not only because seismic response will be unique at each mine, but also because it requires multiparameter approaches.

Various techniques have been suggested for characterizing the influence of geology and mining practice on the induced seismicity and thus to understand its behavior. Hudyma and Potvin (2010) proposed two sample graphical techniques, the magnitude-time history analysis and the diurnal chart, to understand relations between seismicity and mine production. Milev and Spottiswoode (2002) evaluated seismic activity using the ratio between the cumulative seismic moment and the volume of convergence of mined-out areas, founding that local geology and rock types have an influence on this ratio. Other approaches are based on the correlation between radiated energy or seismic moment with the volume of extracted rock mass (Glowacka and Kijko, 1989; Kijko, 1986; McGarr, 1976). All these techniques aim essentially at determining whether seismicity is a direct response of stress changes induced by blasting or if other factors contribute to increase seismicity rate and define its spatial extent. One example of such seismic hazard assessment is provided by Fritschen (2010), who compared induced seismicity from distinct coal mining districts in Germany. Contrary to the general trend, some coalfields showed different behaviors in the correlation between released seismic energy and volume of extracted coal, as well as in their Gutenberg-Richter distribution. As shown in Fig. 1.3, the correlation between extracted coal and radiated seismic energy

is clearly evident for the Ruhr area (Fig. 1.3a), which implies that seismicity is mostly driven by coal production. On the other hand, no correlation can be found for Dilsburg Ost field (Fig. 1.3b). The authors concluded that seismicity of this latter area is not solely driven by coal extraction and that tectonic loads (i.e. triggered seismicity) may have contributed to further increase seismic energy. They, thus, proposed to avoid mining in these highly stressed regions, to prevent the occurrence of large seismic events.

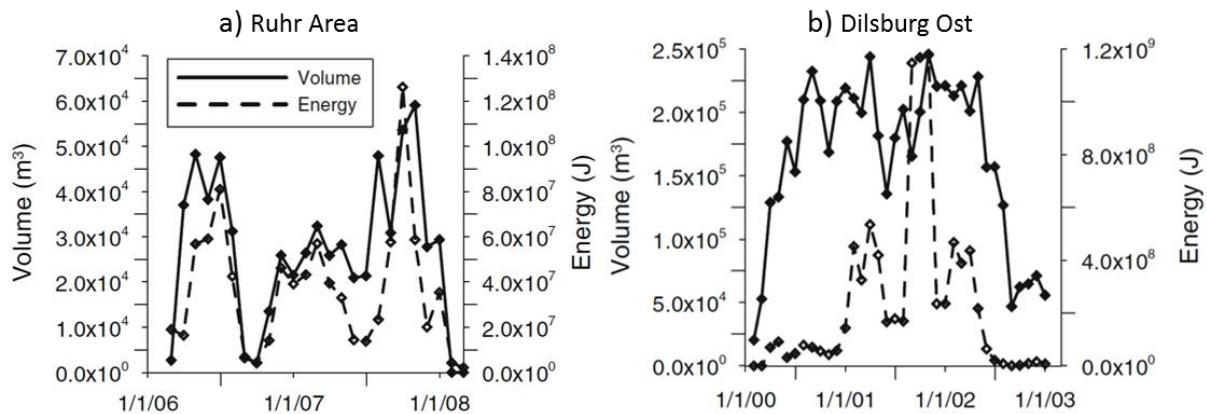


Fig. 1.3 - Radiated seismic energy and volume of extracted rock mass (modified after Fritschen, 2010). Volumes and energies are computed on a monthly basis.

According to Gibowicz (2009), a partial separation between induced and triggered seismicity can be obtained selecting threshold values of magnitude. Indeed, many authors (e.g. Finnie, 1999; Gibowicz & Kijko, 1994; Richardson & Jordan, 2002) have found a bi-modal distribution in the Gutenberg-Richter relation for seismic activity related to mining, which is interpreted as a superposition of induced and triggered events. The former is responsible for the low energy component of the distribution (high b-values), while the latter characterizes the high energy component (low b-values). Recognize these two types of mining seismicity within a dataset can be a valuable tool for drawing consistent statistical seismic hazard analyses and for identifying hazardous geological structures (Gibowicz, 2009). On the other hand, it is widely recognized in the literature that seismic activity in mines is mostly induced. That is, most of the seismic activity recorded by underground monitoring networks is directly related with mining. As a result, its spatiotemporal characteristics can be extremely variable, as mining activities are variable in space and time. In this context, hazard related to seismicity directly induced by mining is generally the major concern (Orlecka-Sikora et al., 2012). Understanding relations between mining operations and seismicity is, thus, crucial to develop valuable seismic management strategies.

A deeper discussion on the analyses and the interpretations of mining-induced seismic events will be provided in Chapter 4 of this thesis, together with applications to a real microseismic dataset.

### 1.3 Motivation, strategy and structure of this thesis

As evinced from the previous section, mining-induced seismicity is a complex phenomenon that depends on many different factors. Its analysis and comprehension are fundamental to characterize and understand the seismic rock mass response to mining. However, to be able to fully describe rock mass behaviors, aseismic processes should as well be taken into account. Indeed, depending on the

mechanism involved (i.e. seismic or aseismic), mining-induced stresses can result in fractures (i.e. seismicity) and/or in aseismic strains, which both may pose significant efforts in terms of rock mass stability and mining strategies, as well as threaten mine workers safety. If mining-seismicity can be monitored by means of seismic networks, aseismic effects induced by mining can be evaluated by means of geotechnical instruments, such as extensometers or strain measurement cells. Seismic monitoring can provide information on large-scale rock mass response when a good coverage of seismic instruments is ensured. While geotechnical monitoring often provides only local measurements, not sufficient for describing the rock mass response at large-scale. To overcome this problem, geo-mechanical numerical modelling can be a powerful tool for estimating stress and strain changes due to large-scale mining.

In this context, this thesis proposes to analyze the rock mass response to mining based on a comprehensive approach, which considers geotechnical and geophysical data, along with 3D numerical modelling, and accounting for mining practices and geological setting. The combined analysis among all these data aims at:

1. Better characterize interactions between stress state modification and the generation of the induced seismicity;
2. Identify and understand seismic and aseismic rock mass behaviors;
3. Understand at which extent mining method, excavated volumes, voids geometries, as well as geological conditions and rock mass properties, influence both seismic and aseismic rock mass behaviors;
4. Evaluate the contribution of numerical modelling tool to seismic hazard assessment in underground mines;
5. Investigate correlations between field data and geo-mechanical numerical modelling to highlight strengths and limitations of the proposed approach.

With the aim of working in a real mine environment, the proposed methodology is applied to the underground hard rock mine of Garpenberg (Sweden), owned by the Boliden mining company. In the framework of the European project I<sup>2</sup>Mine, the French National Institute for Industrial Environment and Risks (Ineris) instrumented a deep area of Garpenberg mine with a monitoring network installed in the end of 2014 at more than 1 km below ground surface. The network consists of both seismic probes and geotechnical cells, for semi real-time monitoring of mining-induced seismicity and quasi-static strain changes in response to excavations. At the same time, Boliden provides information about mine production and blasting practices, which are integrated together with geophysical and geotechnical data to the Ineris web platform e-cenaris. The operational monitoring at Garpenberg mine, together with the research work of this thesis are part of the numerous projects carried out by Ineris in the framework of risk assessment and prevention for underground industrial activities. In agreement with the objectives and the historical know-how of the Ineris on this topic, the rich data flow in constant update collected at Garpenberg mine constitutes a unique opportunity for studying the rock mass behavior at the study site, with the more global purpose of improving seismic hazard assessment in deep mining operations. This thesis focuses on data collected within two years, from 2015, when monitoring network was completely installed, until the end of 2016.

A detailed description of Garpenberg mine is provided in Chapter 2, where mining method and sequencing, together with geological characteristics and rock mass properties are presented.

Considerations about the stress state in the studied area are discussed with the description of some stress measurement carried out into the mine. Finally, the monitoring network is presented and some first considerations about rock mass response to mining are discussed, giving a global overview of recorded data and considering rock mass damage observed underground.

Routine seismic data processing, carried out in the framework of the operational monitoring at Garpenberg mine, is described in Chapter 3, from the acquisition to the classification and the localization of seismic signals. Moreover, methodologies applied in the framework of this thesis for improving microseismic events identification and localization are discussed, together with a numerical approach developed for evaluating seismic network performances. All these analyses aimed, on one hand, at improving the operational monitoring and, on the other hand, at preparing a clean database of microseismic events for further analysis. Finally, the methodology applied to the selected microseismic catalogue for seismic source parameter estimation is described, together with considerations on their uncertainties.

The comprehensive analysis of recorded field data is the subject of Chapter 4, where geophysical and geotechnical data are analyzed separately and then compared among them and considering mining operations. Spatiotemporal and energetic characteristics of recorded microseismic events are investigated and compared with mining method and blasting practices. Some major seismic sequences occurred within the investigated period are identified and related spatial clusters are analyzed in detail. Source parameters are carefully inspected for characterizing microseismic events in terms of energy content and source size, as well as for identifying source regions defined by different events dynamics. Geotechnical measurements, introduced in Chapter 2, are studied focusing on the major strain changes recorded, which are interpreted considering mining method and sequencing. Finally, a comparative analysis between geotechnical and geophysical data is performed, considering reciprocal trends in the temporal behavior of seismic sequences and measured strains. These analyses allow characterizing the rock mass response to mining in the studied area during the investigated period.

Stress and strain changes due to mining excavations are then analyzed by means of a 3D elasto-plastic numerical model, which is presented in Chapter 5. The model simulates the real mine sequencing carried out in the studied area during the two-year period analyzed. Based on a literature review of numerical modelling techniques applied to the case of underground mines, objectives and strategies of the proposed numerical model are discussed. Particular attention is paid to the initialization of boundary and initial conditions, as well as to the chosen rock mass mechanical properties and to the applied constitutive laws. First results of numerical modelling are presented in the end of Chapter 5, where the influence of mining sequence and geological setting on predicted strains, stress field and damaged zone extensions is discussed.

The combined analysis of seismic data and numerical modelling results is presented in Chapter 6. A review of methodologies taken from the literature is provided, based on which a strategy of comparison is proposed for the current work. Finally, seismic and model outputs are compared to investigate whether qualitative and/or quantitative correlations exist.

In the last section (Chapter 7), the most important achievements of this thesis are summarized and discussed. Outlooks for further studies aimed at improving the methodologies proposed in this work are as well suggested.

## Chapter 2

# Study area: Garpenberg mine and Lappberget orebody

To understand the interaction between stress modification due to mining and induced seismicity, a good knowledge of the specific geological setting and mining practice is essential. For this reason, this chapter intends to give a global overview of Garpenberg mine and more particularly of the deepest area of Lappberget orebody, which represents the study area of this thesis. Most of the information collected in this chapter were obtained thanks to a one-month technical stay at Garpenberg mine. The technical visit was focused on the analysis of the specific mining method applied, as well as on the local geological context. This was achieved through daily visits into the mine in direct contact with mine geologists and rock mechanics engineers. But also collecting and analyzing previous studies on ground failures that occurred at Garpenberg mine.

Geological aspects such as rock types and properties, presence of fractures and discontinuities, as well as the characteristics of the mined orebody, can have a strong influence on stress state redistribution and on microseismic activity pattern. In the same way, knowledge of mining method and sequencing is fundamental to understand how rock mass responds to mining. These considerations will be addressed in the current chapter that is organized as follow: first, the history of Garpenberg mine will be briefly presented, together with some information about production and mining process, from the extraction to mineral separation (Section 2.1). Then, geological characteristics of the study area are described and presented together with some stress measurement carried out for retrieving the initial state of stress (Section 2.2). Section 2.3 focuses on mining method and mine sequencing of the study area. While, in Section 2.4, the geophysical and geotechnical monitoring network is presented, and a first overview of recorded data is given. The chapter ends with the discussion of the most typical damage observed underground (Section 2.5).

### 2.1 An introduction to Garpenberg mine

Garpenberg is located in central Sweden (Fig. 2.1) and is one of the oldest non-ferrous metal mines still in operation in the country. First documented extractions in the area date back to the 13<sup>th</sup> century, but it is only during the 17<sup>th</sup> century that Garpenberg mine became the second largest copper producer in Sweden, with 60 tonnes of extracted raw copper per year (van Koppen, 2008). Boliden company acquired the mine in 1957 starting a massive exploration campaign and moving the production area from the South to the North (Fig. 2.1). Since then, four new orebodies have been discovered, including the Lappberget orebody which is the largest in the mine, together with Dammsjön. A schematic vertical profile with indication of main orebodies and mine facilities is shown in Fig. 2.1.

The two mining areas, North and South, were connected by a 3 km drift in 2003, while mining in Lappberget has begun in 2004. Nowadays, Lappberget orebody is divided into four blocks in its vertical extension from 554 m to 1257 m below ground surface. These blocks represent the areas

currently under exploitation within the orebody. The deepest block, called block 1250, ranges from -1108 m to -1257 m and represents the study area of this thesis. Its approximate location within the orebody is depicted in Fig. 2.1 and it will be presented in detail in the next Section. At the time of writing, new galleries are under development below block 1250 for the future exploitation of a deeper area, more than 1300 m below ground surface.

Until today several mining methods have been applied in Lappberget for ore extraction. Initially, the cut-and-fill method has been used at different blocks of the orebody, but from 2012 this method has been fully replaced by transversal open stoping, also called sublevel stoping. This latter is the only mining method still applied in Lappberget (Ghasemi, 2012) and it will be described in detail in Section 2.3.

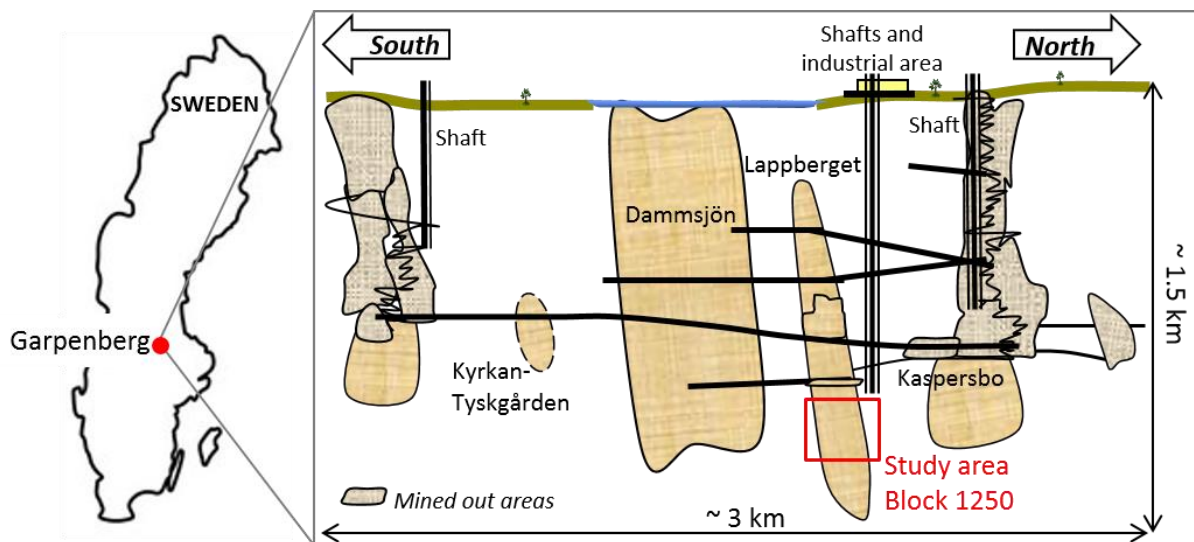


Fig. 2.1 - Geographical location of Garpenberg mine and its orebodies. Red rectangle indicates the study area of the thesis.

Nowadays, the headquarter of the mine is in the area of Garpenberg North where are found, as well, the personnel and the ore hoists, the concentrator and the paste fill plant. The access to the mine is ensured by two shafts in addition to a ramp which allows vehicles traffic. Once blasted, the ore is transported by trucks to one of the two underground crushers, and then hoisted to the concentrator at surface. Here the ore undergoes a process of grinding, flotation and dewatering to produce zinc, lead and copper mineral concentrates, which are then sent to the smelters. Part of the waste rock separated in the concentrator is sent to the paste-fill plant where it is mixed with a binder (blast furnace slag and cement) and pumped back into the mine for backfilling.

Production at Garpenberg mine increased considerably in the last four years, from 1.5 Mt in 2013 to 2.6 Mt of extracted ore in 2017 (Fig. 2.2a), the ore being mainly constituted by zinc and silver together with copper, lead and gold (Fig. 2.2b) as by-products (Boliden 2017 annual report).

According to 2017 data, Garpenberg ore reserves have been estimated at 78 Mt, with an increase of about 95% with respect to 2015 prediction. The mining company has, thus, decided to increase production at 3 Mt per year. With this production rate Garpenberg's lifespan is now estimated at 25 years (Boliden 2017 annual report).

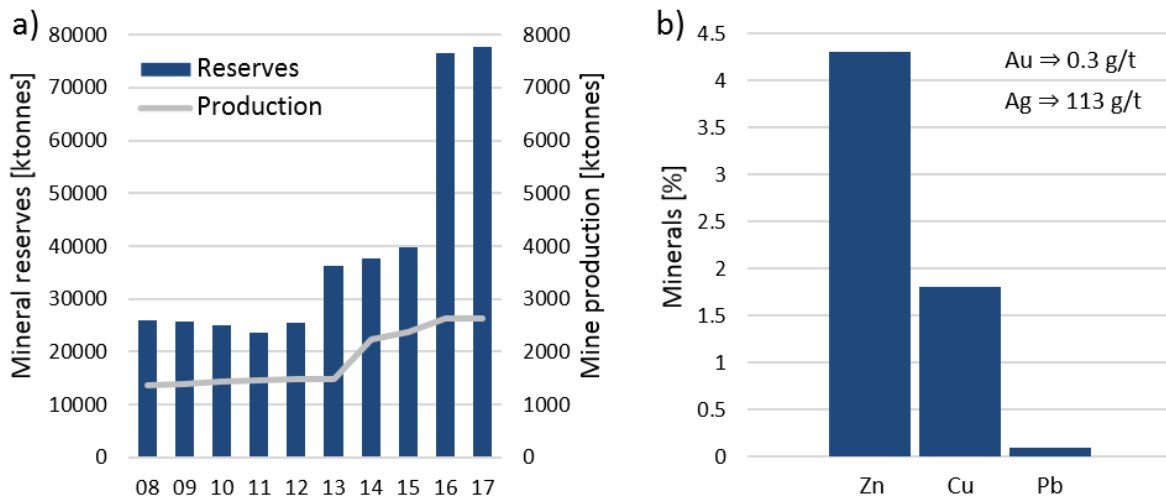


Fig. 2.2 - Garpenberg mine production. (a) Mineral reserves and mine production from 2008 until 2017. (b) Mineral content of the ore extracted in 2017. Mineral abbreviations are as follows: Zn - zinc, Cu - copper, Pb - lead, Au - gold, Ag - silver. (data: Boliden 2017 annual report)

As production increases, minerals will be extracted from larger depths. It is well known from the literature (Foulger et al., 2018; Kijko, 1986; McGarr, 1976) that mining-induced seismicity, and related hazard, increases with depth, as well as with the exploitation rate. A good comprehension of seismic (and aseismic) mechanisms induced by mining is fundamental for a reliable hazard assessment and for improving mine infrastructures and mine worker safety. This is important even in a modern mine as Garpenberg, where robot technology and remote systems have replaced numerous manual activities.

## 2.2 Geological setting and initial stress state

Garpenberg ore is a volcanogenic hydrothermal deposit formed mainly by stratabound replacement below the seafloor, within the caldera vent of a large shallow marine rhyolite-dacite volcano (Allen et al., 2003). The volcanogenic hydrothermal process can be explained by seepage of cold seawater through fractures into a shallow submarine volcano. Here the fluid undergoes a high-temperature reaction due to the presence of hot rocks and it thermally expands, becomes lighter and flows up again towards the ocean. The mineralization process starts during seawater rise, when metals present in volcanic rocks are dissolved and concentrated as polymetallic sulphides deposits. For a complete description of the volcanogenic hydrothermal process and the consequent formation of massive sulphide deposits, the reader is referred to Tornos et al. (2015).

At Garpenberg, an extensive limestone reef was present just below the seafloor, and it formed both a barrier and a chemically reactive trap that focused precipitation of metals along the base of the limestone (Allen et al., 2003). Moreover, just after, or immediately prior to the mineralization, Garpenberg volcano formed a caldera, with the emptying of the magma chamber and the subsequent collapse of the volcano edifice. This complex process leads to the formation of the Garpenberg limestone-skarn hosted deposit, that is the largest known concentration of polymetallic sulphide orebodies in the region, containing mainly galena (lead - Pb), sphalerite (zinc - Zn), chalcopyrite (copper - Cu), together with silver (Ag) and gold (Au) (Jansson, 2011). After the



formation, the ore deposit has been significantly modified by subsequent tectonic deformations and metamorphism (Allen et al., 2003).

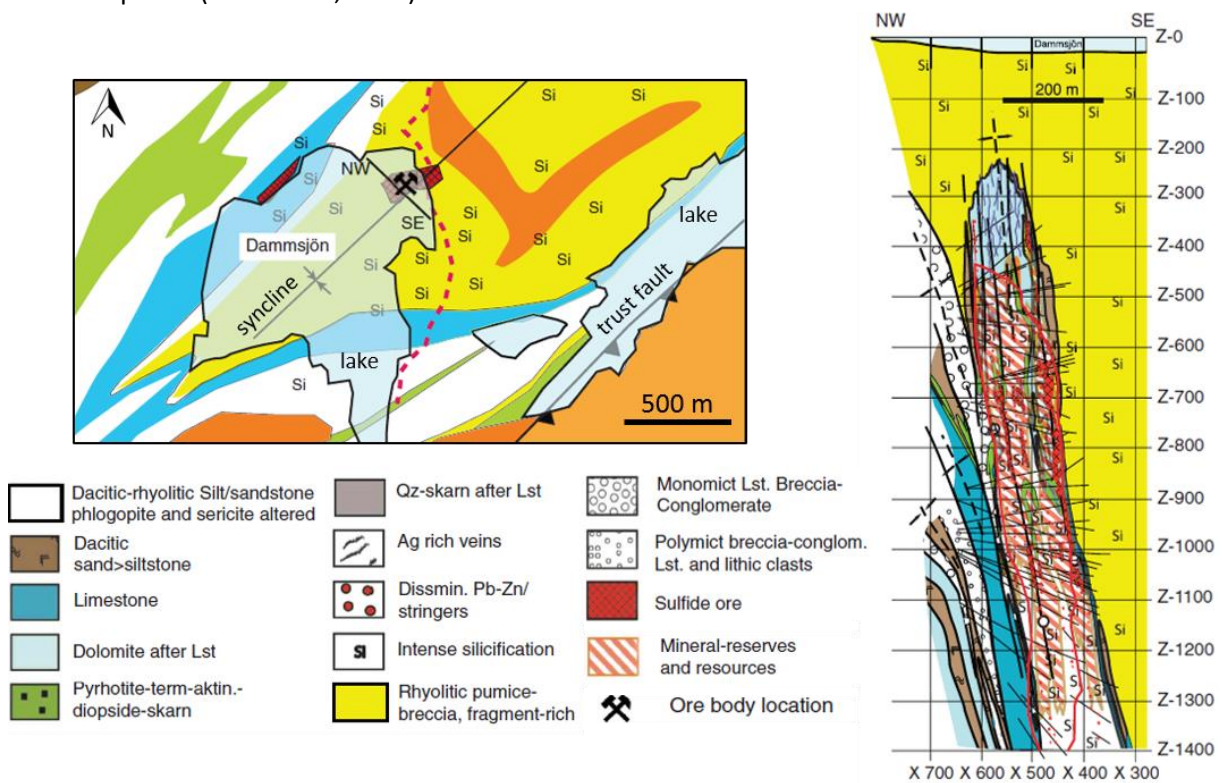


Fig. 2.3 - Geological map of Garpenberg area (on the left) and geological cross section of Lappberget orebody (on the right) (after Ahmadi et al., 2013). The cross section is taken along the NW-SE profile shown in the geological map (on the left). In the cross section, depths and lengths are given in meters and in the mine coordinate system. Note that X and Y directions are inverted between mine coordinate system and Ineris one, such that the X reported in the figure corresponds to the Y in Ineris coordinates.

Lappberget is one of the biggest orebodies of the entire deposit, presenting a steeply inclined, almost vertical structure (Fig. 2.3 on the right). It is situated in a syncline and hosted in a limestone unit, which is the only non-volcanic rock of the formation, below a superficial stratum of volcanic and sedimentary rocks (in yellow in Fig. 2.3). The limestone presents different grades of metamorphism, showing gradual alteration into dolomite and skarn as the mineralization is approached, and with zones of transformation of the dolomite into talc that are very common at the contact with the ore. The orebody itself, which will be described in more details in the next section, is mainly constituted by sulphides in the form of massive volumes as well as in small veins. The lowest unit of the formation, characterized by different layers of metamorphic volcanogenic rocks, is mainly constituted by quartzite and schist (van Koppen, 2008). No faults are observed in the proximity of Garpenberg mine area. A trust fault is encountered at more than 1 km distance, toward the south-east direction (Fig. 2.3 on the left).

The here described geology is extremely simplified as each unit presents many different rock types. Indeed, mine geologists have classified more than 190 rocks which can be encountered underground in the mine. The exhaustive list of rock types is presented in Tab. A.1. For the scopes of this thesis, such a detailed geological description is not needed, thus, rock types will be significantly simplified, as it will be discussed in Chapter 5.

### 2.2.1 Lappberget orebody and weakness zones

Lappberget orebody presents a whole vertical extension ranging between -435 m and -1600 m, as modelled by mine geologists. Focusing on the study area of this thesis (the block 1250), between -1108 m and -1257 m, the orebody (light red in Fig. 2.4) has a maximum length of about 300 m (along the X direction), while its width can be extremely variable, being thinner in the eastern area and wider toward the west. The maximum width, which is encountered in the central area of 1250 block is of about 140 m.

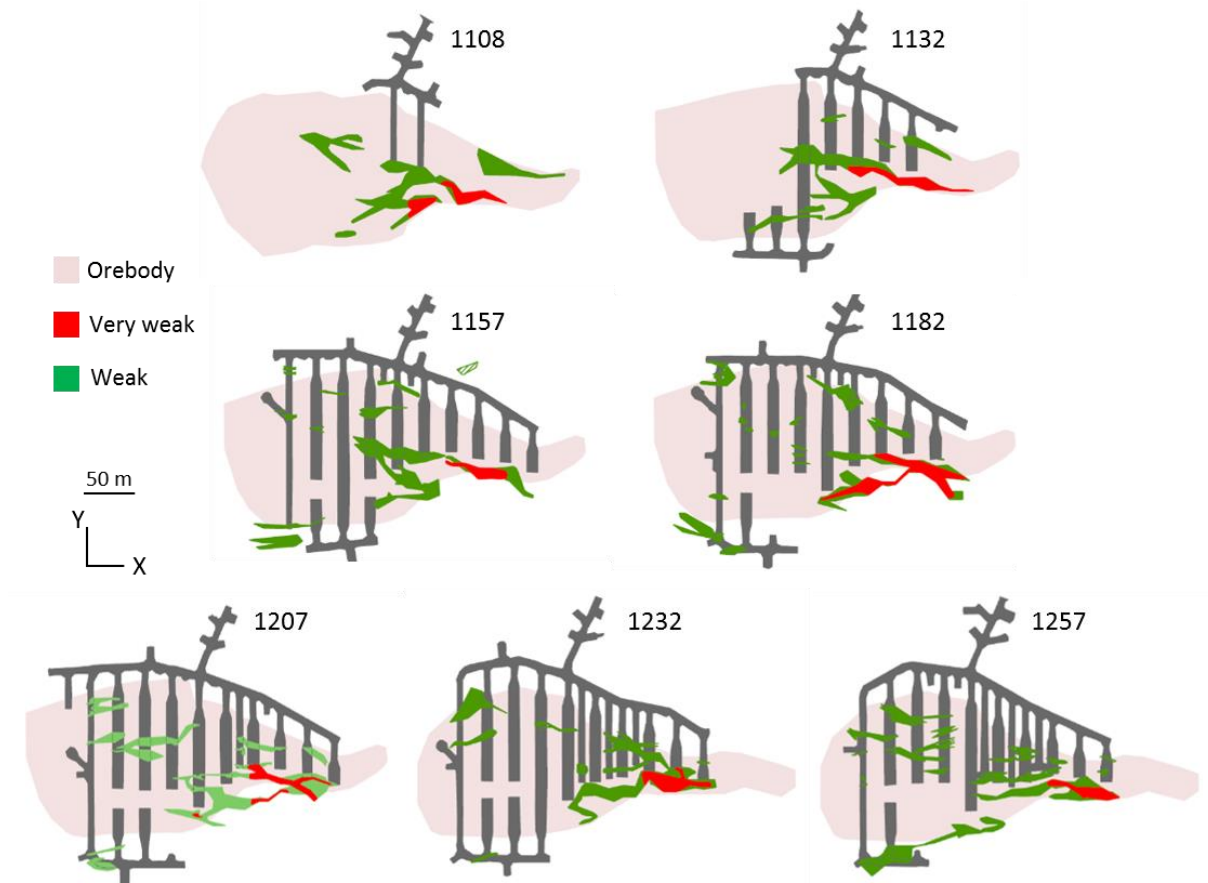


Fig. 2.4 - Orebody, weak and very weak geological zones in block 1250. Weak and very weak zones configuration is updated at October 2017. Gray profiles indicate mine galleries.

The ore appears to be heterogeneous: its eastern area (type A ore) is characterized by massive sulphide deposits mainly hosted in the limestone/dolomite unit, while, moving toward the west, the ore presents an irregular and heterogeneous mineralization (type C ore) within a host rock of mica-quartzite (Olsson 2018, personal communication, 2 May). Normally, this latter type of mineralization is referred to as “stringer” or “impregnated”, as the minerals occur in veins networks inside the host rock. The veins can be very diffuse as well as very dispersed (Olsson 2016, personal communication). Aside from the stringer mineralization, C ore presents as well massive sulphide bands of a few centimeters in thickness. These bands are called “remobilized ore” and they follow the tectonic structures in the rock mass, containing bigger amount of silver and lead compared to zinc (van Koppen, 2008).

All along the orebody the presence of mechanically weak zones is observed (in green Fig. 2.4). These areas occur as intrusions of large to small size, with a complex geometry inside the orebody and its

host rock. The geological definition of these weak zones is quite complex and cannot be based only on one lithology type or one specific mineral type. Weak zones of the studied area are composed by lenses of schists in the metal deposit, as well as by rock blocks containing massive amounts of soft minerals, like talc and chlorite. Moreover, zones of contacts between different rock types are also regarded as weak zones, especially when rock types of highly varying stiffness are mixed together (Olsson 2017, personal communication, 1 September). In addition to weak zones, mine geologists identified also the so-called very weak zones (in red in Fig. 2.4). These areas are characterized by the massive presence of schists extremely rich in talc. As visible in Fig. 2.4, weak and very weak zones are more intensely deployed along the eastern side of the mine, in coincidence with the A ore zone. Their intensity is gradually reduced toward the C ore zone in the western side of the mine, where very weak zones are not encountered.

Weak and very weak zones raise significant questions in term of mine sequencing and induced seismicity, as it will be later discussed. However, it is difficult to get a complete picture of weakness zones profiles. Indeed, their geometry is known only on the horizontal plane, per each level of the mine. This means that, their vertical extension between two consecutive levels (around 25 meters) is not precisely known, neither modelled by mine geologists. Moreover, the level-by-level geometry of weakness zones is in constant update as a new drift is excavated and geological surveys are made possible. In this thesis, we will always refer to the geometry update of October 2017 which is shown in Fig. 2.4, further changes to this configuration will not be considered.

The described setting, in terms of orebody and weak zone features, results in a marked variability of geological characteristics moving from the east toward the west side of the mine, i.e. from the A to the C ore. Firstly, the orebody cannot be considered as a homogeneous rock mass with constant properties. Indeed, the mineralization and the bedrocks change significantly. Similarly, weak zones distribution differs in the horizontal direction. Based on these evidences, the eastern side of the mine can be considered extremely heterogeneous. The limestone/dolomite is abundantly replaced by massive volumes of sulfides and skarn, which are cut by large weak zones of schist. This means that very stiff rock masses are interbedded with extremely soft materials, making the peculiarity of this area. Indeed, schist can also be found in the central and the western area and the mica quartzite can be schistose in itself, but schist within the eastern side stands out due to the fairly difference to the dolomite and the massive sulfides (Olsson 2018, personal communication, 3 May). On the contrary, the central and the western area of the mine can be considered more homogeneous, with the mica quartzite interrupted by smaller sulphide volumes and the presence of less diffuse weak zones.

Small fractures due to geology or induced by mining are both observed in Lappberget, even if no major fractures are reported. However, geological surveys routinely done by mine geologist do not include the analysis of fractures or joints. Therefore, their location, intensity and orientation are not known, which constitutes an important lack of information for the scope of this thesis.

### 2.2.2 Initial stress state and elastic rock mass properties

In underground mines, the stress state can be split in two components: (i) the virgin or initial state of stress prior to any underground excavation and (ii) the induced stress, i.e. the stress variation due to mine openings. Initial stresses are dependent on many parameters such as depth, rock mass properties and geological (tectonic) settings, which define the local stress state within rock masses. When openings are excavated, local stresses need to be redistributed in surrounding rocks, resulting

in the alteration of the initial stress pattern. This change in stress intensity and/or orientation due to mine excavations is referred to as mine-induced stress. Knowledge about stress state before and after excavations is extremely important as it strongly influences the local rock mass response to mining, both in terms of seismic and aseismic strains.

Stress measurements in Garpenberg were firstly performed in 2004 by SINTEF company with the overcoring method, at levels 883 and 967 below ground surface, in close proximity to Lappberget orebody (precise coordinates are not available). Later, in December 2014, new stress measurements were carried out by Ineris within block 1250. These latter measurements were performed by the overcoring method with CSIRO Hi strain cells, in two boreholes drilled from Stope 15 toward Stope 13 at 1155 m depth (Fig. 2.5a and b). During the measurement campaign, permanent CSIRO Hi cells were as well installed (PD and PH in Fig. 2.5b) for monitoring quasi-static stress changes during mining.

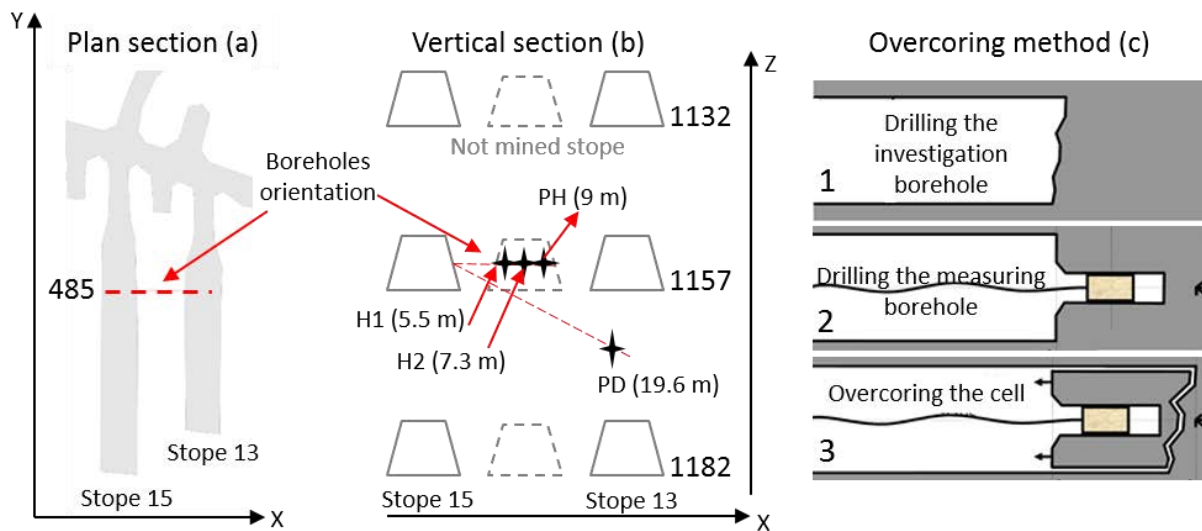


Fig. 2.5 - Location of stress measurements (a, b) and schematic representation of the overcoring method (c). (b) H1, H2, PH and PD are the cell's names, with PD and PH used for long-term stress monitoring (these have not been overcored). Numbers near cell's names indicate the location of the cells inside boreholes. Levels elevation is reported in meters on the right side of the figure. (c) Description of overcoring method. Refer to the text for description of steps 1, 2 and 3. (after Bouffier et al., 2015)

The overcoring method can be summarized in 3 main steps (Fig. 2.5c): an investigation borehole is drilled to the area where measures are needed (1 in Fig. 2.5c); a measuring borehole with smaller diameter is drilled at the end of the previous hole and the three dimensional strain measurement cell with known orientation is glued inside (2 in Fig. 2.5c); finally, the area with the instrument is overcored with a larger diameter and strains in overcored rock are measured while the stresses are progressively released (3 in Fig. 2.5c).

Under the assumption of an elastic behavior of the rock mass, the stress tensor is retrieved from the measured strains by applying the Hooke's law and knowing the elastic properties of the rock. For this purpose, biaxial tests were performed on overcored H1 and H2 samples, both taken within the orebody. Results are presented in Tab. 2.1. The variation of Young modulus between the two samples can be explained by the strong heterogeneity of the ore (Bouffier et al., 2015). Similarly, biaxial tests were performed on core samples obtained during the SINTEF campaign (Tab. 2.1). In this

case, samples were retrieved within limestone. Due to lithological variations within the Ineris and SINTEF samples, the obtained parameters are significantly different between the two campaigns. In terms of comparison, Tab. 2.1 reports as well the mechanical parameters retrieved by biaxial test on the ore, during another measurement campaign which took place in two boreholes at level 852 (van Koppen, 2008). Results of estimated mechanical properties are highly different between each other, indicating a strong heterogeneity of the rock, where local parameters can be strongly different from one point to another, both within the limestone and in the orebody. This agrees with observations made in the previous section, where geological heterogeneities have been already pointed out.

Tab. 2.1 - Rock mass properties. Measured elastic parameters, rock mass density and uniaxial compressive strength (UCS) during Ineris (Bouffier et al., 2015) and SINTEF (van Koppen, 2008) campaigns. For comparison, measured parameters during a third campaign are as well reported.

Measurements	Sample	Depth [m]	Lithology	Young modulus [GPa]	Poisson's ratio	Density [kg/m <sup>3</sup> ]	UCS [MPa]
Ineris (2014)	H1	1155	Ore	44.9	0.23	3030*	150
	H2			64.1	0.23		
SINTEF (2004)	level 883	883	Limestone	55	0.17	2714	73
	level 967	967		60	0.12	2722	100
-	Hole 1	852	Ore	84.7	0.15	3331	196
	Hole 2			90.7	0.15	3270	146

\*Density reported for Ineris measurements is the average value resulting from three laboratory tests.

Based on the parameters reported in Tab. 2.1 for Ineris and SINTEF campaigns, stresses were determined by means of inversion from the measured strains. Inversion results are summarized in Tab. 2.2 in terms of principal stresses magnitudes, while the corresponding orientations are reported in Fig. 2.6 and Fig. 2.7 for Ineris and SINTEF measurements, respectively.

Tab. 2.2 - Magnitudes of measured principal stresses during Ineris (Bouffier et al., 2015) and SINTEF (van Koppen, 2008) campaigns.

Measurements	Depth [m]	Sample	$\sigma_1$ [MPa]	$\sigma_2$ [MPa]	$\sigma_3$ [MPa]
Ineris (2014)	1155	H1	57	46	26
		H2	56	40	28
SINTEF (2004)	883	level 883	45	24	20
	967	level 967	26	18	11

On one hand, considering Ineris results, measured stresses at H1 and H2 look quite similar in terms of magnitude, and both show a strong anisotropy, with a sub-vertical minor principal stress ( $\sigma_3$ ) and significantly higher horizontal stresses, with major ( $\sigma_1$ ) and intermediate ( $\sigma_2$ ) stresses oriented parallel (along Y direction) and perpendicular (along X direction) to mine's drifts, respectively. This is particularly true for measurements at H2 (Fig. 2.6 on the right), while at H1 horizontal stresses appear rotated of 40° and 310° with respect to drift direction for the major and the intermediate stress, respectively (Fig. 2.6 on the left). The minor vertical principal stress forms an angle of 212° and 207° with respect to the vertical direction for H1 and H2 measurements, respectively.

On the other hand, results obtained by SINTEF appear significantly different in terms of magnitude between each other (Tab. 2.2), while they look similar in terms of orientations. However, the horizontal stresses are not represented by the same principal stress component in the two measurements: the intermediate stress is oriented horizontally for measurements at 967 m and vertically in the case of 883 elevation (Fig. 2.7). The significant differences observed for stress measurements at levels 883 and 967 has been interpreted as due to different geological settings (Nyström 2018, personal communication, 21 December). In addition, nearby excavations may have influenced stress intensity and orientation. Indeed, the measuring point at 883 elevation is in close proximity ( $\approx 25$  m) to a large electric workshop which was under construction at the time of measurements (van Koppen, 2008).

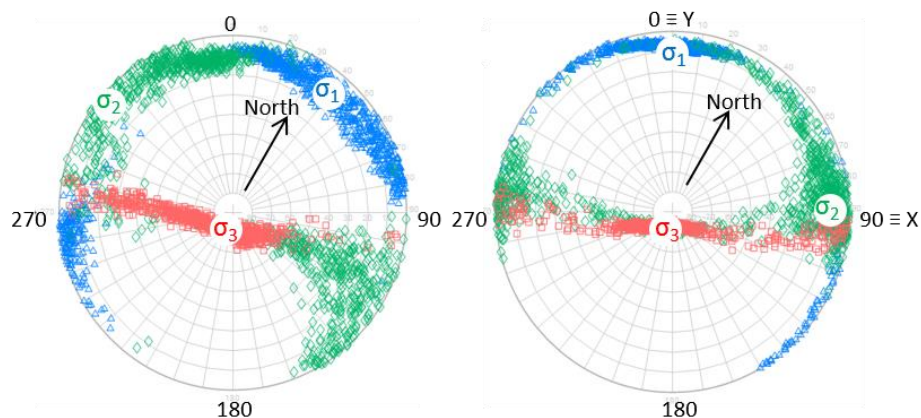


Fig. 2.6 - Stereographic representation of stress state retrieved by Ineris. H1 measurements are reported on the left, while results for H2 are on the right. Stress orientations are reported with respect to drifts direction ( $0^\circ \equiv Y$  direction of the mine). Approximative direction of true North is shown on the figure.

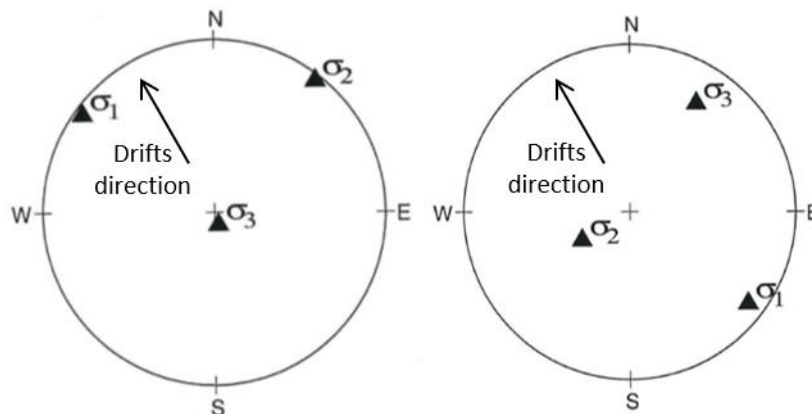


Fig. 2.7 - Stereographic representation of stress state retrieved by SINTEF. Measurement at level 967 are reported on the left, while the figure on the right refers to measurements performed at level 883. Orientations are given with respect to true North. Approximative drifts orientation is reported on the figure.

The strong anisotropy observed in Ineris measurements between horizontal and vertical stresses is in accordance with the Scandinavian stress field. This is characterized by a major principal stress in the sub-horizontal direction (van Koppen, 2008), generally close in magnitude to the intermediate horizontal principal stress (Larsson, 2004). Müller et al. (1992) report about large scatter of stress orientations in Northern Europe, independently from the method applied for the measurements. According to the authors, this scatter is observed in overcoring and hydraulic fracturing data, as well

as in fault plane solutions. Nevertheless, they report a mean orientation of the major horizontal principal stress in Scandinavia equals to  $N120^{\circ}E \pm 45^{\circ}$ . For depths greater than 300 m, and according to Stephansson (1988), mean major horizontal stress tends to align with NW-SW orientation.

Beside the significant differences observed between Ineris and SINTEF measurements, neither of the measured stresses can be assumed to be equal to the virgin stress state. Indeed, at the time of measurements, excavations had already been performed in Lappberget orebody, which may have influenced the stress state at the measuring point locations. In 2014, when Ineris campaign was carried out, production within the shallower mining areas above block 1250 was already at advanced stages and a large amount of paste fill was replacing the preexistent rock mass. In addition, H1 and H2 measurements were performed at about 10 m from the closest gallery, whose diameter is in the order of 10 m. This configuration can thus have an influence on local stress state at the measuring points. The excavation advancement within Lappberget orebody at the time of the SINTEF measurement is not precisely known, but, as already discussed, the measuring point at level 883 was taken at about 25 m from an electric workshop whose dimensions are 6x40x50 m (van Koppen, 2008).

To retrieve the virgin stress state (prior to any excavation) an inverse problem approach was adopted as reported by Souley et al. (2018) and Tonnellier et al. (2016). These authors back-computed the initial stress state of Lappberget orebody by means of elasto-plastic numerical modelling, and considering stress measured during Ineris campaign at H1 and H2 cells. Assuming test values for initial principal stresses, the model reproduced all previous excavations (in the upper levels and in block 1250) obtaining modelled stress values at H1 and H2 locations. Repeating this procedure several times and changing initial imposed stresses, the virgin stress state was determined as the one that minimizes the difference between measured and computed stresses. Inverse problem approaches, as the one described above, are largely applied in rock engineering, especially to retrieve the initial stress state as well as unknown mechanical and hydraulic rock mass properties (Jing, 2003). As pointed out by Zhao et al. (2012), numerical model inversion is frequently the sole methodology capable of deriving reasonable stress states at large scale, when measurements performed in specific areas only reflect the local stress field.

The final virgin stress state retrieved through the described methodology is reported in Tab. 2.3. It was obtained by imposing that the vertical principal stress at depth 1155 m equals to the overburden weight:  $\sigma_{zz} = 3030 \left[ \frac{kg}{m^3} \right] * g \left[ \frac{m}{s^2} \right] * 1155 [m] = 34.3 MPa$ , where  $g$  is the gravity. Orientation of the stress state assumes that the major principal stress is parallel to mine drifts (along the Y direction of the mine) and that the intermediate principal stress is oriented along the X direction of the mine. This is consistent with principal stresses orientation measured at H2 (Fig. 2.6 on the right). The back-computed virgin stress state shows a strong difference between horizontals and vertical stress magnitudes, while a lower stress anisotropy is observed on the horizontal plane. The stress gradient obtained from the computed virgin stress is as well reported in Tab. 2.3. Based on this gradient the stress state at levels 883 and 967, where SINTEF measurements were carried out, should be:  $\sigma_y = 36 MPa$ ,  $\sigma_x = 33.6 MPa$ ,  $\sigma_z = 26.5 MPa$  for the shallower depth (883 m) and  $\sigma_y = 39.6 MPa$ ,  $\sigma_x = 36.7 MPa$ ,  $\sigma_z = 29 MPa$  for the deepest level (967 m). These values are significantly higher than that measured during the campaign (Tab. 2.2), highlighting the strong influence of mining excavations on stress field redistribution, as it was already pointed out looking at the differences among SINTEF measurements between mining levels. In addition, uncertainties in the measurements can also be responsible for the observed differences. Compared with Ineris measured stresses, one can observe a significant

reduction (of about a factor 1.2) in vertical stresses with respect to the retrieved virgin vertical stress. This is most probably linked to the large quantity of extracted rock mass above level 1250, which have significantly reduced the stress state in the vertical direction as measured in December 2014.

Tab. 2.3 - Computed initial stress state (before any mining) at level -1155 m as reported by Souley et al. (2018) and stress gradient as a function of mine depth.

Initial stress state at level 1155 [MPa]		Stress gradient [MPa/m]	
$\sigma_1 (\sigma_y)$	47.3	$g_{H/y}$	0.041
$\sigma_2 (\sigma_x)$	44.4	$g_{h/x}$	0.038
$\sigma_3 (\sigma_z)$	34.3	$g_{v/z}$	0.030

The complete picture given by stress measurements and retrieved rock mass properties highlights strong geological heterogeneities, even within similar lithologies, as well as an anisotropic and heterogeneous stress field which appears highly influenced by surrounding excavations. Understanding how and why mining influences the local stress state and the induced seismicity is one of the objectives of this thesis, together with the investigation of the mechanical role played by a such a heterogeneous geological setting.

## 2.3 Mining method and sequencing

Sublevel stoping is the mining method employed in the deepest area of Lappberget orebody (1250 block). This is a mass-mining method which ensure a recovery of the orebody close to 100 %.

At each level of the mine, a gallery called “footwall drift” is excavated parallel to the ore, which is then accessed by means of crosscut drifts perpendicular to the footwall (Fig. 2.8). Drifts length is largely based on orebody profile, geological structures and geotechnical issues; thus, it is very variable across the ore. The geometry described above is maintained along the whole height of the orebody, creating separated levels along the mine (Fig. 2.9a) with a vertical distance of 25 m between each other. Each level can be accessed by a helicoidal ramp located near the footwall drift and connected to the personnel shaft. Drifts excavation is performed by blasting on horizontal drillholes (development blasts – DB), with an explosive load ranging between 100 kg and 970 kg per round, for a volume of extracted rock mass of about 300 m<sup>3</sup>.

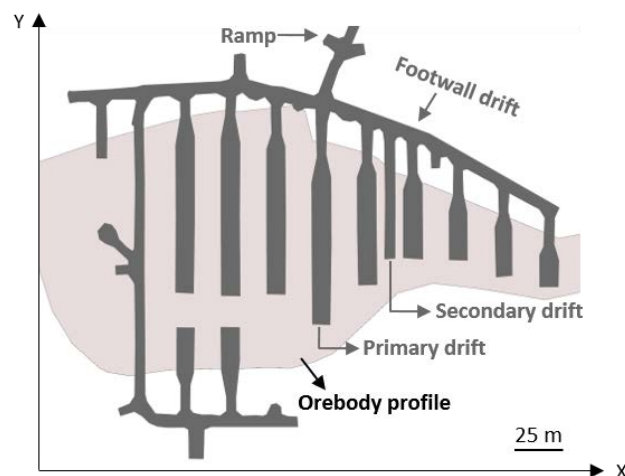


Fig. 2.8 - Plan view of one mine level in block 1250. The picture depicts mine galleries and the orebody profile.



Ore production is, then, ensured by stope excavation. Stopes are vertical columns of rock mass lying between consecutive drifts along the entire height of the mine (Fig. 2.9a). Their production is performed by blasting in vertical drillholes (production blasts – PB), which allows to mine out and, then, collect the orebody between two consecutive levels (Fig. 2.9b). Indeed, the entire stope is excavated level-by-level, drilling and then blasting the rock mass from the upper level to the bottom one, where the blasted material falls by gravity. It is important to make a clarification about mine terminology. Indeed, the rock mass volume extracted per each PB is also referred as to stope, like the entire column to which it belongs. To be identified, each stope is numbered from 5 to 21, with numbers growing from the eastern toward the western side of the mine (Fig. 2.9a). When a PB is performed, the excavated stope will be identified by the column number and by the lower level from which the ore was drawn. As an example, the stope excavated from column 7 between levels 1207 and 1232 will be referred as to “Stope 7 1232 #1”. The final number (#1) indicates the position of the stope along the length of the drift, as illustrated in Fig. 2.9b. Indeed, more than one blast round is needed to excavate a stope along the entire length of a drift (Fig. 2.9b) and the number of rounds can vary from 2 to 6, depending on the drift lengths. Normally, the first blast (Blast #1 in Fig. 2.9b) is the smallest as, at the beginning, there is not enough free surface for the rock to break properly. Once the first part of the stope is emptied, it ensures the space for the following bigger blasts (Blast #2 and Blast #3 in Fig. 2.9b). The time taken for blasting a stope along the entire length of a drift can be variable from 2 months to one year for longer drifts.

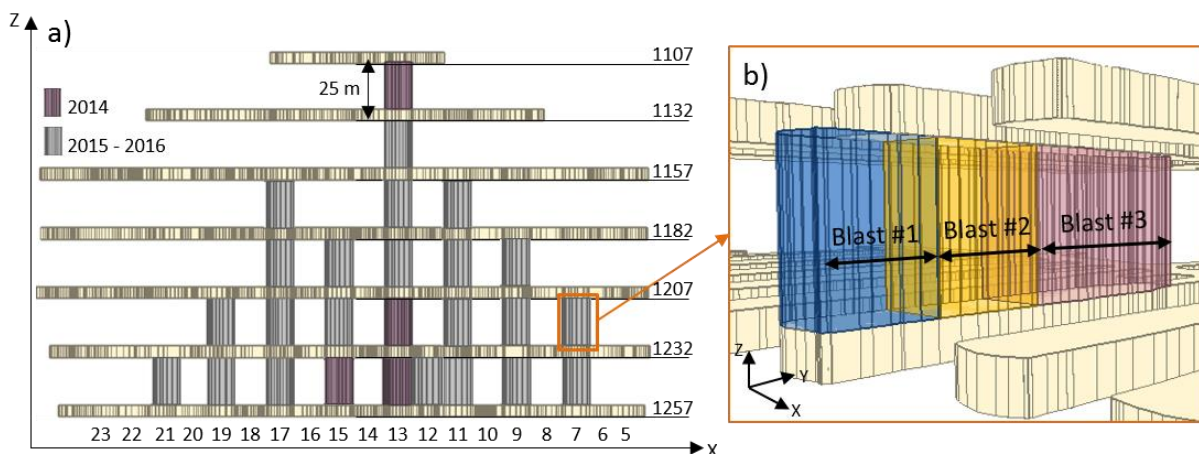


Fig. 2.9 - Excavation geometry in block 1250. (a) Vertical section showing all the stopes (gray and violet rectangles) excavated between 2014 and 2016. Mine depths are indicated in meters on the right side of the figure, while numbers on the bottom refer to stope's (column's) names. (b) 3D view between two consecutive levels, showing the blast design along the length of a drift.

Due to the large quantity of extracted rock mass, PB are bigger than DB, with an explosive load ranging between 1000 kg and 9500 kg. This results in a volume of extracted rock mass varying between 1000 m<sup>3</sup> and more than 6000 m<sup>3</sup> per round.

The mining method is based on a sequence of alternated primary and secondary stopes. In block 1250 primary stopes are named by odd numbers, while even numbers indicate secondary stopes (Fig. 2.9a). As the name suggests, primary stopes are the first to be blasted, while secondary stopes, located in between, are excavated only when the adjacent primaries have been mined and backfilled. One advantage of such primary-secondary sequence is that, during the excavation of primary stopes, secondary stopes act as pillars, giving support and stability to the structure. In the same way, during

the exploitation of secondary stopes, the support action is in part ensured by primary ones that are already backfilled. Therefore, primary stopes require a backfill made with high-strength paste composed by a mixture of waste rocks and a binder, which is directly pumped into the mine from the paste fill plant. On the other hand, the binder is not needed in the backfill of secondary stopes, which are then refilled only with waste rock.

Another important issue that governs mine planning and design is the mine sequencing that defines the way in which mining progresses throughout the orebody. The main concern in stope sequencing in deep orebodies is the high-stress condition encountered because of the depth. Stope sequencing needs to be thought such that overstressing of pillars is avoided. In such conditions, it is very common to advance in a bottom-up direction, following a pyramid shape with a sawtooth pattern (Ghasemi, 2012). This ensures stress transfer toward the lateral abutments and into secondary stopes, together with the production of a large number of stopes.

In 1250 block, sequencing follows a particular scheme, as illustrated in Fig. 2.9a and Fig. 2.10a and b. Namely, the first stope (column) to be extracted is the central one (Stope 13) that is mined over its entire height advancing both top-down and bottom-up. One block of Stope 13, between levels 1157 and 1182, was left as pillar and exploited last. Contemporarily, many primary stopes were taken from the sides following a pyramid shape that is driven from the middle to the abutments. The coupled bottom-up and top-down advancement of Stope 13 is justified by the need of avoiding large stresses in the upper level of the block, to avoid large magnitude events and to be sure to achieve a pyramid shape (Nyström 2018, personal communication, 20 June). Indeed, a 20 meters sill pillar separates the upper level of the study area (at -1108 m) from the bottom (at -1080 m) of the previous mining zone. High stress states within the sill pillar may be expected as stresses induced by blasting within the upper and lower mining areas are concentrated there. As will be later discussed, the chosen mining sequence in block 1250 strongly influenced stress redistribution and the induced seismicity pattern. In this thesis, we will focus on production performed between 2015 and 2016, thus, later excavations will not be considered.

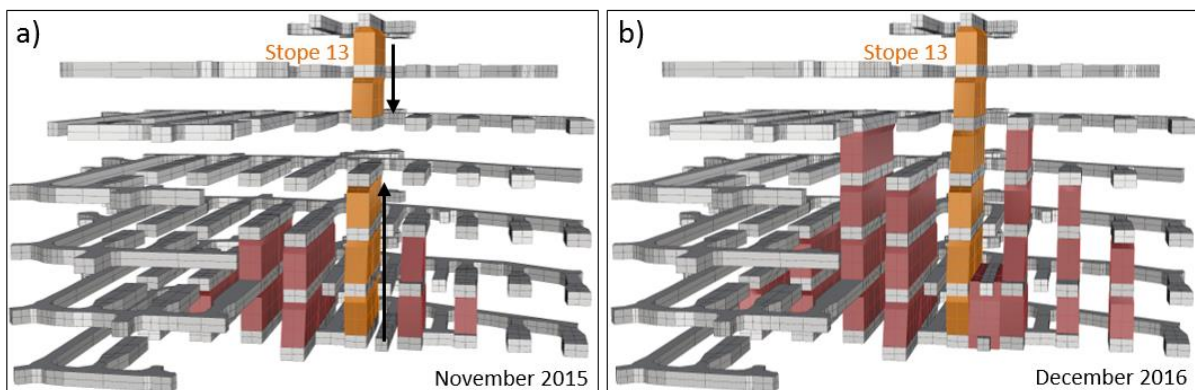


Fig. 2.10 - Mining sequence in Lappberget block 1250. The figure shows extravagation advancement from November 2015 (a) to December 2016 (b). The two arrows near Stope 13 illustrate the top-down (down arrow) and the bottom-up (up arrow) sequencing. One can observe the pillar left in the middle of Stope 13 (a), which was extracted last between February and August 2016.

## 2.4 Geophysical and geotechnical monitoring in Lappberget

As already mentioned in Chapter 1, block 1250 of Lappberget has been instrumented with a monitoring network in the end of 2014. The network, installed by Ineris, consists of, both, strain cells and seismic sensors for monitoring quasi-static strain changes and microseismic activity as excavations progress.

Permanent CSIRO strain cells, PD and PH, have been installed close to Stope 13 at level 1157. More precisely, PH cell has been set up in a horizontal borehole within the secondary Stope 14, while, PD cell has been set up in a downward borehole in Stope 13 (Fig. 2.5 and Fig. 2.11). With this configuration, strain monitoring aims at determining strain, and in turn stress variations in Stope 13 between levels 1157 and 1182, which constitutes the rock volume planned to be mined last in the entire column 13. At the same time, PH cell ensures the comparison of stress state between primary and secondary stopes until the end of the exploitation in Stope 13 (Tonnelier et al., 2016). Strain cells perform one measurement per hour of 12 strains in different directions, with accuracy about  $\pm 5 \mu\text{m/m}$ . This allows determining stress changes by inversion, assuming an elastic behavior of the rock.



Fig. 2.11 - Geophysical and geotechnical monitoring network. Black numbers on the right refer to mine levels' depth.

Seismic monitoring network is equipped with six 1-component (1C) and five 3-component (3C) 14 Hz geophones installed in such a way that microseismic activity can be recorded within the whole block 1250 (Fig. 2.11). The acquisition system is operating in triggering mode with an imposed threshold on amplitudes and with a sampling frequency of 8 kHz. A detailed description of the seismic network will be provided in the next Chapter, together with the discussion of signals analysis and processing.

In addition to the Ineris monitoring network, Boliden has installed an extensometer (ED) in Stope 15 at level 1182, which is set in a downward borehole inside Stope 14 and toward Stope 13 (Fig. 2.11). The extensometer is 17 m long with 6 anchor points at a distance of about 3 m from each other. The extensometer's head have six independent sensors which measure displacements of each anchor

relative to the head, with a 10  $\mu\text{m}$  resolution. Extensometer's readings were initially recorded three times per day, but since March 2016 records are performed every 2 hours.

In the following sections, data recorded between 2015 and 2016 by Lappberget monitoring network are briefly presented. These will, then, be analyzed in detail in the following chapters of this thesis.

### 2.4.1 Extensometer data

Fig. 2.12a depicts downward extensometer readings from April 2015 to December 2016. During this time, the instrument was frequently out of order because of mining works, thus, continuous measurements are not available along the whole analyzed period. Nevertheless, we can observe three important displacement shifts which are all related to production in the adjacent Stope 13 at levels 1182 and 1207 (Fig. 2.12b). Characteristics of PB and extensometer shifts are reported in Tab. 2.4.

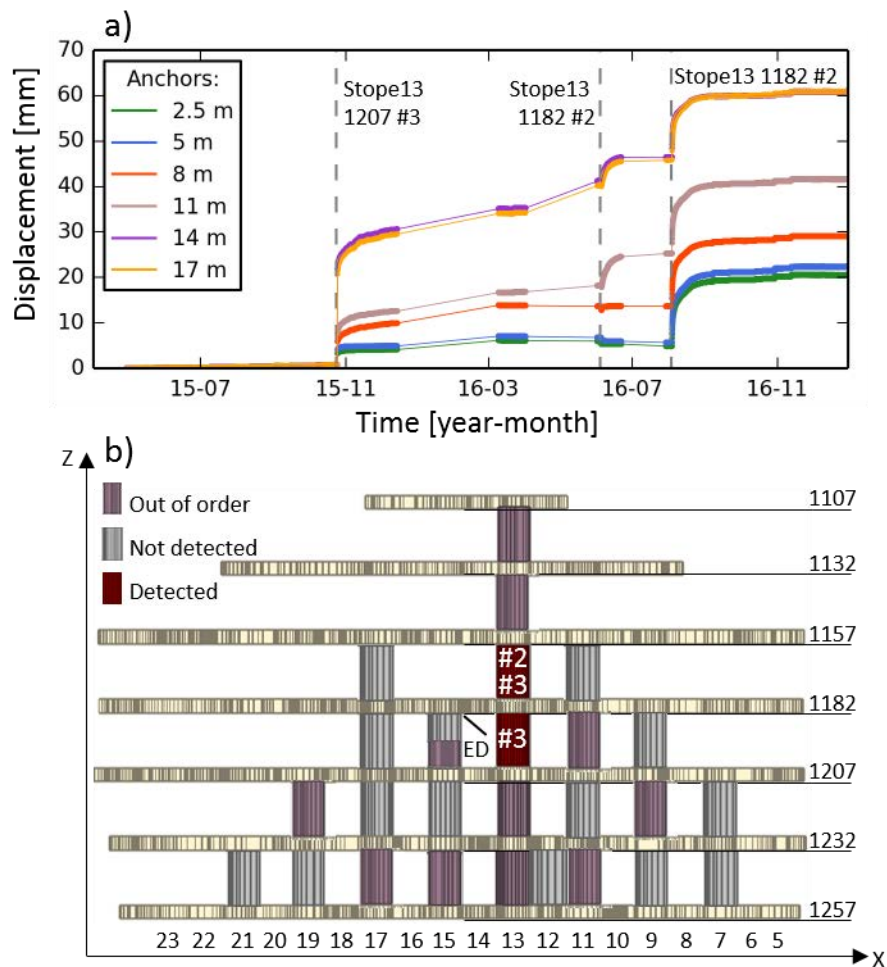


Fig. 2.12 - Extensometer data. (a) Extensometers readings. Each curve refers to a different anchor, as reported in the legend. Dots are the available measures, while continuous lines indicate out of order periods. The absence of dots within the first shift (2015-10-24) is due to the frequency of data recording, which was fixed at three times per day in that period. Dashed gray lines indicate the time of occurrence of PB which induced the displacement shifts. (b) Stopes produced from 2014 until December 2016. Violet rectangles indicate stopes produced before available extensometer data or when instruments were out of order. Gray rectangles refer to stopes non-detected by the extensometer, while red rectangles are the detected stopes. With the numbers indicate PB numbers, as reported in (a).

The first shift occurred on the 24<sup>th</sup> of November 2015, resulting in sudden displacements of 2.5 mm up to 21 mm for anchors at 2.5 m and 14 m, respectively. These displacements were related to the third-round blast of Stope 13 at level 1207, which was performed the same day at about 17 m distance from the extensometer (Fig. 2.12b and Tab. 2.4). Apart from the first two anchors, displacements kept growing in the following weeks, at least until the beginning of November 2015 when a new PB was performed.

The second shift was observed on the 4<sup>th</sup> of June 2016 in coincidence with the second-round blast in Stope 13 level 1182 (Fig. 2.12). In this case displacements are smaller and almost not visible on the first three anchors, while anchors at 11 m, 14 m and 17 m show a gradual displacement increase, ranging from 4 mm to 5 mm 10 days after the blast.

The last recorded shift occurred on the 3<sup>rd</sup> of August 2016 and it is linked to the third-round blast in Stope 13 level 1182 (Fig. 2.12). After this blast, Stope 13 was completely mined-out. We observe a sudden displacement of around 7 mm at all anchors, which kept rising until the end of the month, reaching more than 10 mm on the 18<sup>th</sup> of August.

Tab. 2.4 - Characteristics of production blasts and extensometer shifts. Information about explosive load are given by Boliden, while the volume of extracted rock mass is determined after 3D reconstruction of the stopes based on 3D laser scan of mine voids. Note that the maximum extensometer displacement is computed for  $t = 24$  h after the blast, while distances are computed from the middle of the extensometer to the centroid of the blasted volume.

Time	Stope	Explosive [kg]	Extracted rock volume [m <sup>3</sup> ]	Max. displacement [mm]	Average distance [m]
2015-10-24	13_1207 #3	5473	6702	21	17
2016-06-04	13_1182 #2	6597	3978	1.3	27
2016-08-03	13_1182 #3	4527	4346	7	22

As reported in Tab. 2.4, the magnitude of the observed displacements seems to be in accordance with the distance to the excavated stopes and to the volume of extracted rock mass. This trend may be confirmed by blasts #1 and #2 at level 1207 of Stope 13, performed respectively at 43 m and 32 m from the extensometer, which resulted in smaller volumes of extracted rock (3275 m<sup>3</sup> and 2784 m<sup>3</sup> for blast #1 and blast #2, respectively). Indeed, no displacement shifts were recorded by the extensometer after these blasts. Similar observations can be made for the first-round blast at level 1207 of Stope 15. Another interesting aspect highlighted by extensometer data is the persistence of displacements during time. Indeed, after the sudden displacement shift immediately following the blasts, rock masses are subjected to slow but gradually increasing displacements over time. This feature may indicate that stress field redistribution is not instantaneous, but a long-lasting process which may need several weeks to stabilize. These preliminary observations on the mechanical behavior of rock masses in response to mining will be deeper analyzed in Chapter 4, where time-dependent effects will be discussed.

## 2.4.2 Strain measurements

Permanent strain measurement cells started to be operational in January 2015. The temporal trend of strain measurements at PD and PH cells is reported in Fig. 2.13a and b. Within the analyzed period, we observe 15 and 19 strain shifts at PD and PH, respectively. Most of the shifts are recorded immediately after some PB performed in Stopes 11, 13, 15 and 17, as reported in Fig. 2.13c and Tab.

2.5. Beside strain shifts directly triggered by PB, two additional shifts not related to production occurred when Stope 13 was almost completely excavated. The first shift (n° 10 in Tab. 2.5) was induced by the development of a drift in Stope 13, while the second (n° 18) is not related to any mining operation. Considering all recorded shifts, the average distance between cells and detected stopes ranges between 56 and 59 m for PD and PH, respectively, with a maximum distance of more than 90 m, indicating a greater sensitivity of these instruments compared to the extensometer.

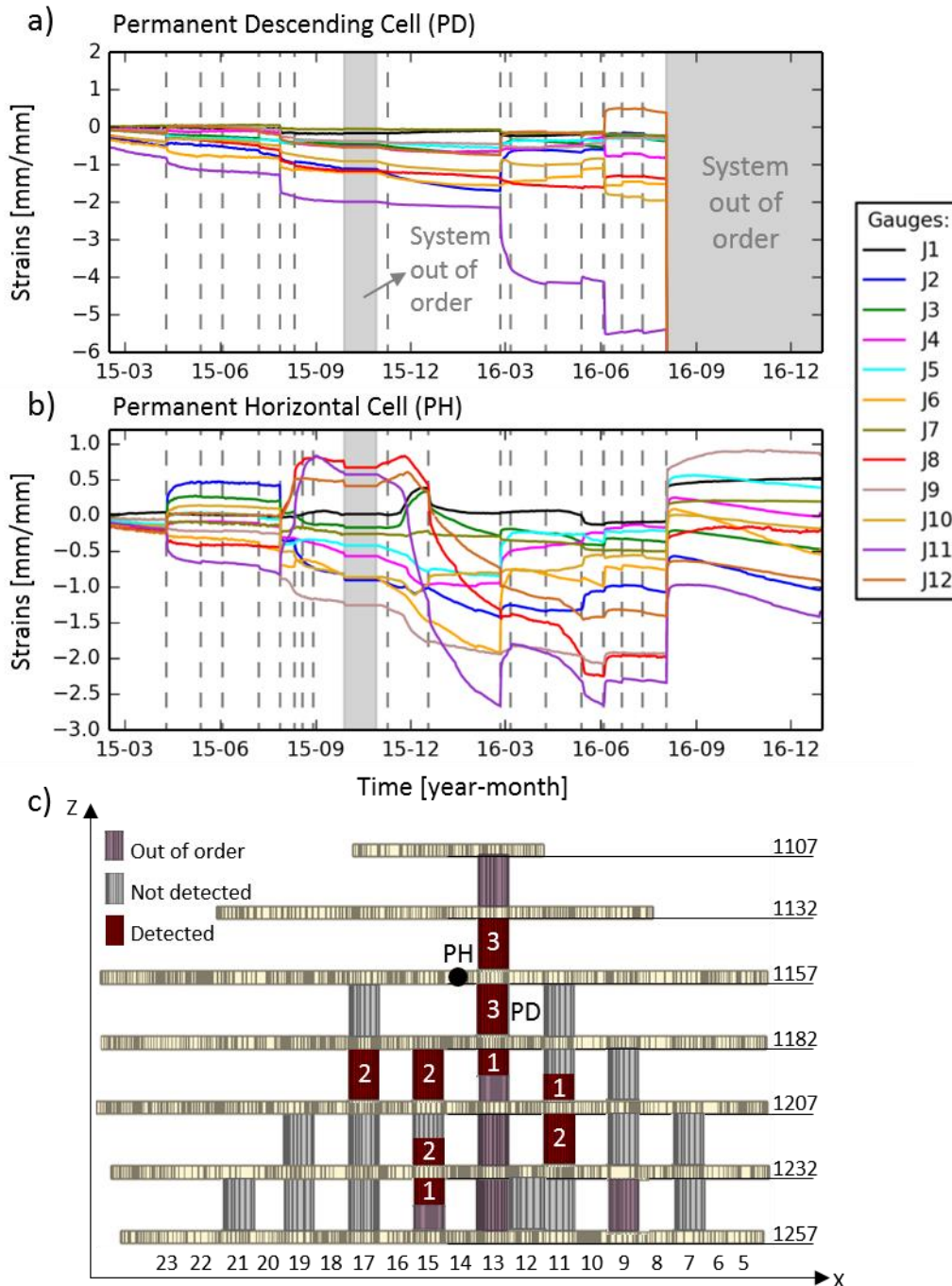


Fig. 2.13 - Permanent strain measurements. (a) Readings of strain cells at PD in the two-years period analyzed. (b) Same as in (a) but for PH cell. (c) Location of stopes produced in the study period. (a, b) Each curve refers to a different gauge within the cells, as reported in the legend. Dashed gray lines indicate the time of occurrence of detected strain shifts. Gray bands show the period in which cells were out of order. (c) Color code for stopes is the same as in Fig. 2.12b, while with the numbers indicate the number of detected PB by strain cells at each

level and stope. Note that PD cell is located in the middle of Stope 13 level 1182, thus it is covered by the stope and not visible in the image.

Based on the measured strain shifts and assuming an elastic behavior of the rock mass, Ineris computed the stress tensor by means of inversion (Amadei and Stephansson, 1997), using the Ineris software SYTGEOstress (developed with Mathematica). The in situ stress tensor  $[X]$  is related to the matrix of strain measurements  $[B]$  by an influence matrix  $[M]$  which depends on rock mass properties and CSIRO cells orientation:

$$[B] = [M][X] \quad (2.1)$$

The stress tensor is thus retrieved by inversion of the linear system in equation 2.1, where the number of equations is higher than the number of unknowns (12 equations given by the 12 strain gauges to determine the 6 components of the stress tensor). In SYTGEOstress the system is solved by least square method that is equivalent to the pseudo-inverse of matrix  $[M]$ :  $[X] = [M]^+[B]$  with  $[M]^+ = [M]^T([M][M]^T)^{-1}$ . Values of retrieved stresses are reported in Tab. 2.5. Maximum stress shifts can be variable from 0.15 MPa up to more than 50 MPa.

Tab. 2.5 - Characteristics of stress-strain shifts and of related PB. Explosive load, rock mass volume and distance between excavations and strain cells are determined as in Tab. 2.4. Maximum stress shift is assessed based on principal stresses and considering the stress state immediately prior and immediately following the blast. Positive number indicate unloading. Bold font indicates stronger shifts.

Shift n°	Time	Stope	Explosive [kg]   volume [m <sup>3</sup> ]	Distance PD PH [m]	Max. strain PD PH [ $\mu\text{m}/\text{m}$ ]	Max. stress shift PD PH [MPa]
<b>1</b>	<b>2015-04-10</b>	<b>13_1157 #1</b>	<b>3553   2239</b>	<b>40   37</b>	<b>100   411</b>	<b>1.5   5.6</b>
2	2015-05-13	15_1232 #1	4302   3970	92   97	20   30	0.33   0.45
3	2015-06-03	15_1232 #2	6444   3724	78   71	15   -12	-0.16   -0.55
<b>4</b>	<b>2015-07-08</b>	<b>13_1157 #2</b>	<b>4212   2910</b>	<b>31   27</b>	<b>-74   -53</b>	<b>-1.3   -0.9</b>
<b>5</b>	<b>2015-07-28</b>	<b>13_1157 #3</b>	<b>6669   5330</b>	<b>22   15</b>	<b>-449   -654</b>	<b>-7.9   -13.9</b>
<b>6</b>	<b>2015-08-11</b>	<b>13_1207 #1</b>	<b>4172   3275</b>	<b>57   64</b>	<b>50   325</b>	<b>0.8   3.2</b>
7	2015-08-19	11_1232 #1	4152   2807	-   73	-   38	-   0.5
8	2015-08-29	11_1232 #2	4781   3534	-   65	-   34	-   0.4
9	2015-11-09	15_1257 #2	4177   4563	91   82	-18   -14	-0.37   -0.21
<b>10</b>	<b>2015-12-18</b>	<b>13_1157</b>	<b>105   -</b>	<b>-   10</b>	<b>-   -320</b>	<b>-   -9.7</b>
<b>11</b>	<b>2016-02-25</b>	<b>13_1182 #1</b>	<b>2963   2758</b>	<b>39   43</b>	<b>600   635</b>	<b>8.1   9.5</b>
<b>12</b>	<b>2016-03-06</b>	<b>11_1207 #2</b>	<b>4827   5503</b>	<b>45   57</b>	<b>33   62</b>	<b>0.8   1.1</b>
<b>13</b>	<b>2016-04-09</b>	<b>17_1207 #1</b>	<b>3440   2527</b>	<b>80   81</b>	<b>68   23</b>	<b>1.2   0.6</b>
<b>14</b>	<b>2016-05-13</b>	<b>17_1207 #2</b>	<b>-   6497</b>	<b>66   67</b>	<b>142   40</b>	<b>2.3   0.6</b>
15	2016-06-03	15_1207 #2	5544   4345	82   79	42   29	0.65   0.45
<b>16</b>	<b>2016-06-04</b>	<b>13_1182 #2</b>	<b>6597   3978</b>	<b>27   32</b>	<b>-1181   142</b>	<b>-9.1   3.0</b>
<b>17</b>	<b>2016-06-21</b>	<b>15_1207 #2</b>	<b>6766   7078</b>	<b>55   59</b>	<b>98   53</b>	<b>1.5   0.9</b>
<b>18</b>	<b>2016-07-11</b>	-	-	-	<b>34   77</b>	<b>-0.71   -0.32</b>
<b>19</b>	<b>2016-08-03</b>	<b>13_1182 #3</b>	<b>4527   4346</b>	<b>-   18</b>	<b>-   2561</b>	<b>-   52</b>

Of the total 19 shifts, 13 (in bold in Tab. 2.5) are the most significant in terms of intensity and are mainly related to production in Stope 13. The first three major shifts resulted from PB in Stope 13 at level 1157. As already observed by Tonnellier et al. (2016), the strain shift recorded after the first-round blast (n° 1) is unexpectedly important when compared with shift n° 4, which is related to the

second-round blast performed at the same level. Indeed, despite the larger volume of extracted rock mass and the smaller distance to the cells, shift n° 4 resulted in lower strain and stress changes with respect to Shift n°1 (Tab. 2.5). Similar considerations can be made for the first-round blast of Stope 13 level 1207 (shift n° 6), which shows considerable magnitudes despite the small excavated volume, with much higher strains at PH. Unfortunately, the other two blasts performed at this level were missed by the cells due to a problem in the acquisition system. Production of Stope 13 at level 1182 presents analogous features. Indeed, strains are much lower at PH for shift n° 11 than for shift n° 16, even if the cell is further from the excavation and the mined volume is lower.

Based on these preliminary observations, recorded strain shifts do not appear proportional to the volume of extracted rock mass, neither to the distance from the excavations. This anomalous trend may indicate that further mechanisms contribute to stress field redistribution, in addition to the immediate perturbation induced by blasting. Shift n° 18, which was not directly triggered by mining operations, may be another indication for additional mechanism influencing the local stress state. To be able to comprehend how rock mass responds to mining, the identification and the understanding of all influencing factors is fundamental and will be deeper addressed in this thesis.

### 2.4.3 Microseismic data

During the two-years period analyzed the seismic monitoring network recorded more than 800 events within the studied area. After back-analysis of 2015 data and localization improvements, as it will be described in the next Chapter, retained events are more than 760. Indeed, events localized in the upper levels of the mine, outside block 1250, were discarded from further analysis. This choice is motivated by monitoring strategy, but also because of a lack of information about production data outside block 1250, which are fundamental for the objectives of this thesis.

If compared with other deep hard rock mines, 1250 block of Lappberget orebody is not particularly seismically active. Indeed, microseismic activity rate is on average in the order of 2 events per day, which is a low value compared with other deep underground mines (e.g. Fritschen, 2010; Kgarume et al., 2010; Kubacki et al., 2014; Vallejos and McKinnon, 2011).

Fig. 2.14 reports spatiotemporal characteristics of mine blasts and microseismic events localized around mine galleries. We observe a temporal correlation between microseismic activity and PB (Fig. 2.14c). Indeed, the cumulative curve of MSE shows a stepwise trend with important increases of seismicity rate immediately after some PB. This tendency, which appears intensified in the second half of 2016, highlights that seismic activity is not homogeneous during time but punctually enhanced by the occurrence of PB. However, seismic rock mass response appears to be very variable from a blast to another, as, in some cases, seismicity rate remains almost constant despite the considerable number of performed blasts.

Spatial distribution of MSE (Fig. 2.14a and b) points out two main seismically active zones deployed in the central area and in the eastern side of the mine. The correlation between seismic activity and PB positions is not straightforward. Indeed, the intense production of the western side did not result in an intense seismic activity, while most of the events are observed in the eastern side where few PB were performed.

These preliminary observations on the reciprocal spatiotemporal distribution of MSE and mine blasts, highlight some correlations between mining and seismic activity, even if the nature of this correlation



is not clear and needs deeper investigations. It is the aim of this thesis to understand if mining-induced stresses are solely responsible for seismic activity in Lappberget orebody, or if other factors, such as for example the geological setting and the mining sequence, may play a significant role.

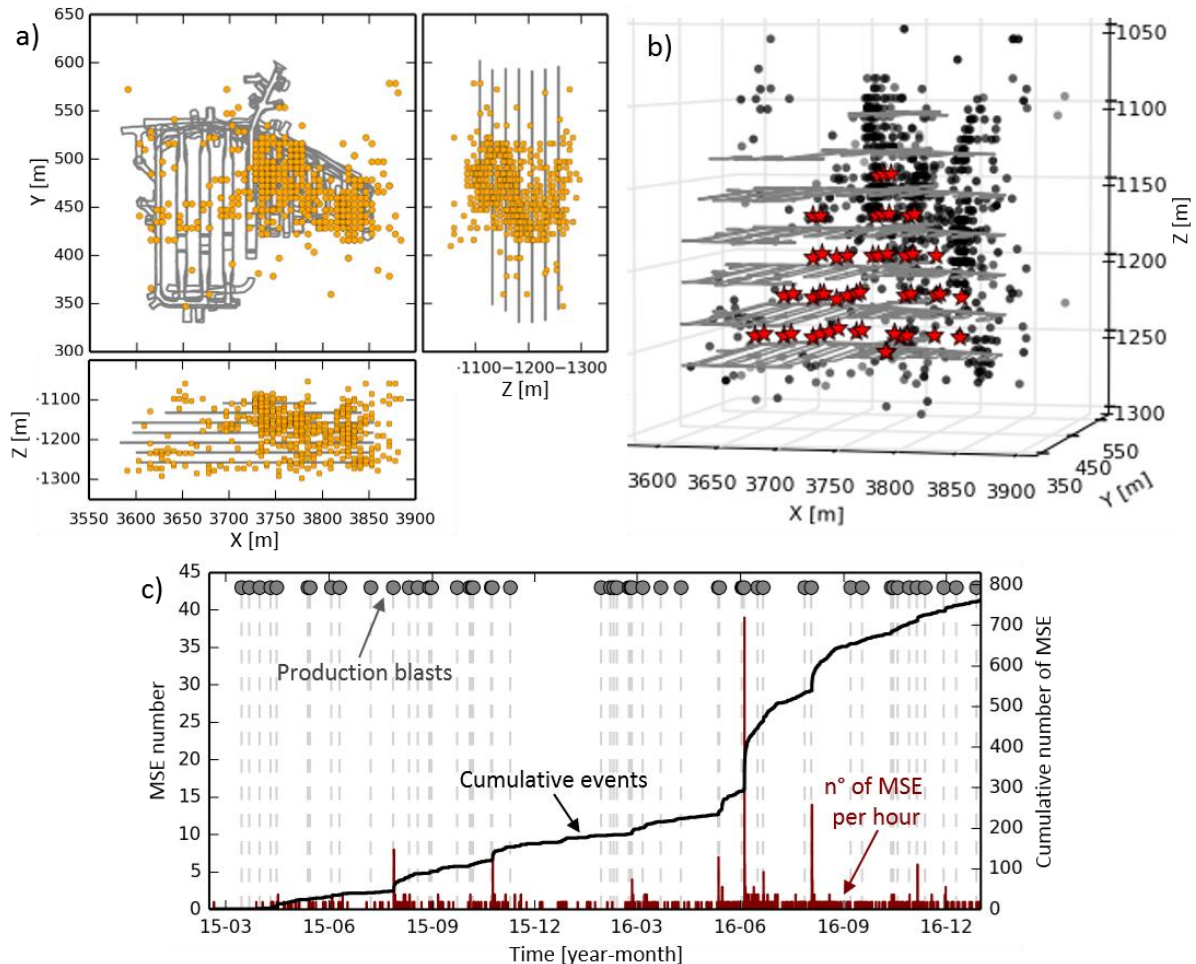


Fig. 2.14 - Spatiotemporal trend of microseismic activity. (a) 2D plots of microseismic events localization within the study area between February 2015 and December 2016. (b) 3D plot of same events (black dots) presented in (a), with the addition of PB positions (red stars). (c) Events per hour (dark red) and cumulative number of events (black) related to PB occurrence (gray dots and dashed lines).

## 2.5 Seismic activity and observed damage

Up to now, no rockbursts neither other major failures have been observed in the studied area of Lappberget orebody. Most of visible damage occur within stope openings or in galleries at the opening back (where the opening back refers to the gallery of an open stope). Other types of damage can be stress-related or linked to weakness zones.

Boliden has produced an internal database of the main microseismic events recorded in Garpenberg mine from 2009 until 2016, associating the events to the damage observed on site. Seismic data were recorded by a monitoring network installed by the Institute of Mine Seismology (IMS) in a shallower zone of Lappberget. If interested in the description of this network, the reader is referred to Olivier et al. (2015). According to the database, Lappberget experienced 59 significant seismic events from

August 2012 until January 2016, which were located in the upper part of the orebody, between levels 464 and 993. Even if these events are outside the study area of this thesis, their analysis can give valuable information about the rock mass response to mining in Lappberget orebody.

Among the total dataset, we observe 52 major events with local magnitude ( $M_L$ ) ranging between 0 and 1.5, while the remaining are smaller events ( $-1.8 < M_L < 0$ ) which lead to damage. As reported in Fig. 2.15, most of major events have  $M_L \leq 0.6$  and they are mostly located within 10 meters from the excavated front. Smaller events have similar distances from excavations, except one event which is located 40 m away.

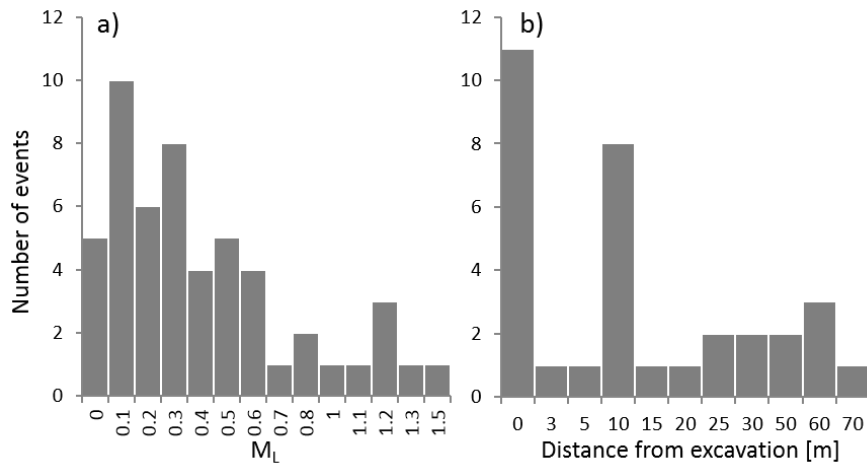


Fig. 2.15 - Boliden database on microseismic activity. (a) Major seismic events reported in function of their local magnitude. (b) Major events reported in function of the distance from excavations.

As suggest by the substantial number of events at a distance from the excavation equal to 0 (Fig. 2.15b), damage mostly occurred within stope openings. An example of this type of failures is given by the event that occurred on 2015-07-22 in stope 5 at level 602. The event, with  $M_L = 0.3$ , was felt at the surface and it resulted in the widening of the excavated stope (Fig. 2.16a). This failure was most probably due to high stresses and because of the presence of a weak zone near the excavated area (Mozaffari 2016, personal communication, 15 February).

Beside stope openings, most of the failures can be observed within drifts at the opening back or in adjacent galleries. This mainly results in the occurrence of fractures and/or falls of rock and shotcrete (Fig. 2.16b), broken bolts and water leakage. In the end of 2011 a strain burst occurred at level 896 of Lappberget, causing important damage as, for example, rock falls, cracks on the floor and heaving of new and existent fractures. Boliden classified the damage as level 4 on 5 for, both, rock and support structures, based on the rock and support damage scales proposed by Kaiser et al. (1992). Four years after the event, this area of the mine presents deterioration of pillars in the footwall drift, floor heave, and water leakage, which indicates the presence of fractures (Fig. 2.16c and d). No other seismic events related to this area were reported in the Boliden database, but it is obvious that stress related deformations are occurring in the zone. Such deformations can be observed in many levels of Lappberget, in particular on footwall pillars. The explanation of these phenomena is that stresses are gradually distributed through the pillars due to adjacent stopes extraction, inducing irreversible strains, or plasticity, when the elastic capacity of the rock is exceeded (van Koppen, 2008).

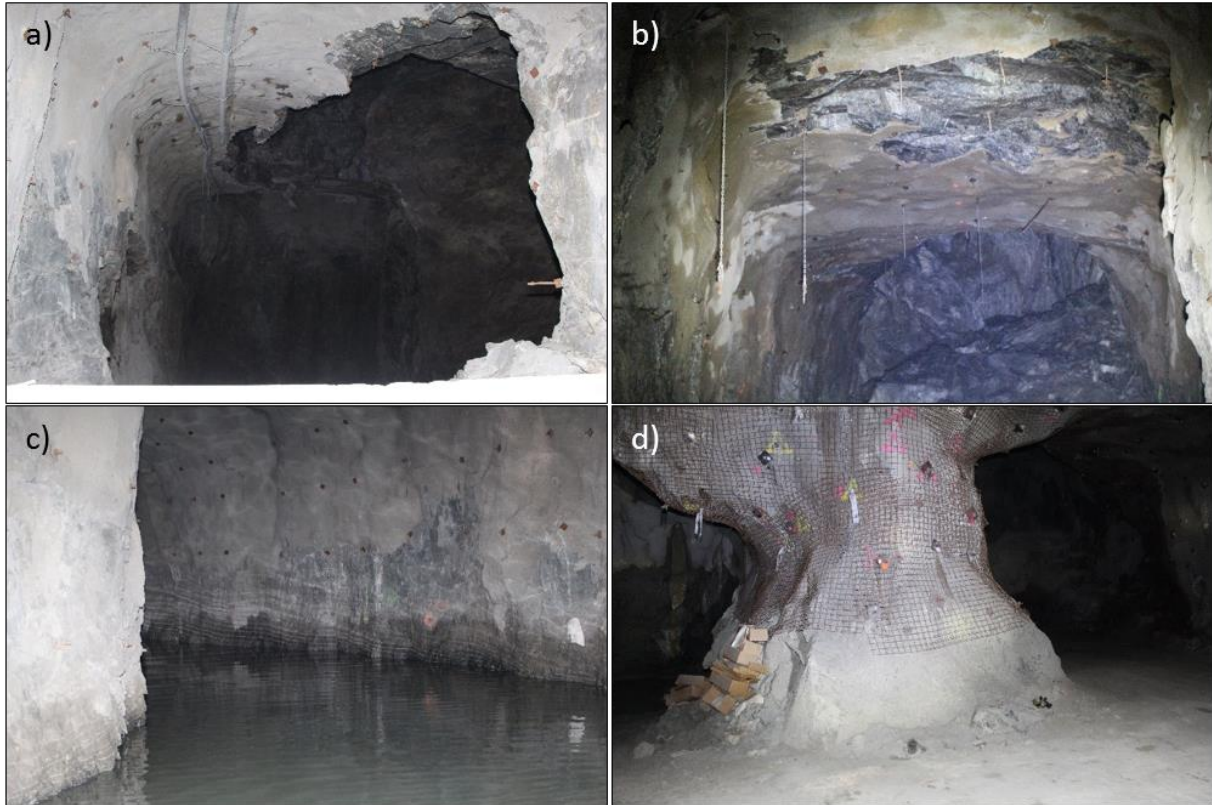


Fig. 2.16 - Observed damage in Lappberget orebody. (a) Failure at the stope opening in Stope 5 level 602. (b) Shotcrete and rock damage in Stope 15 level 926. (c) Flooding in a drift due to water leakage through fractures. (d) Pillar deformation in the footwall drift of level 896. (photos: Mozaffari, 2016)

Rock falls are the most observed damage caused by the presence of weak zones. This especially occurs when a crosscut drift hits a weak zone, resulting in a sudden collapse of drift's face. Failures of this type are often observed in block 1250, as shown in Fig. 2.17. Sometimes, failures can also happen at drift's walls, when drifts are excavated across the weak zone. Finally, these weak areas are also linked with leakage and/or flooding, since production water filtrates throughout fractured layers.

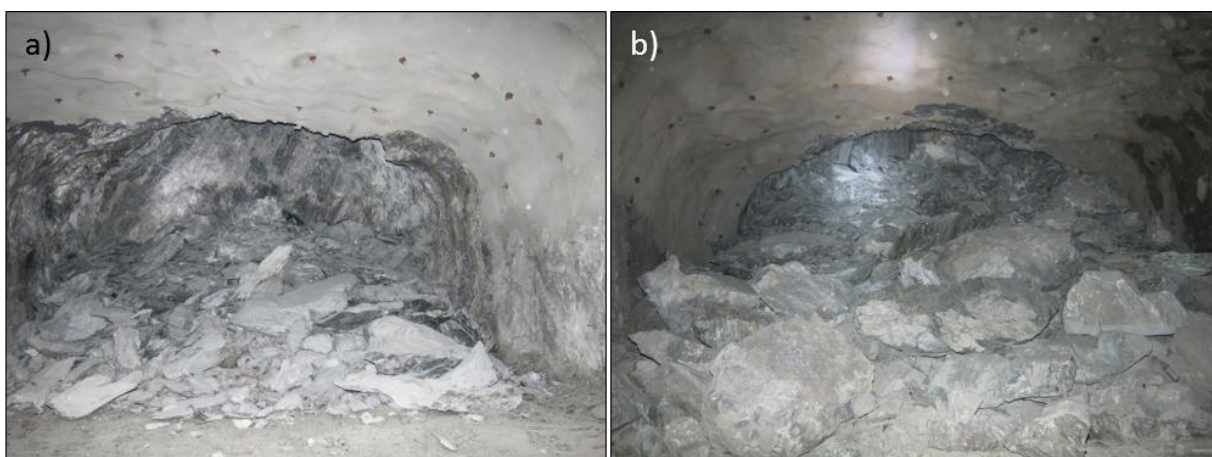


Fig. 2.17 - Rock falls due to weak zones. (a) Stope 9 level 1232. (b) Stope 15 level 1132. (photos: Olsson, 2016)

Main failures observed in block 1250 between 2015 and 2016 are similar to the damage so far presented and appear to be closely related to the last stages of production in Stope 13. In February

2016, the first-round blast performed at level 1182 of Stope 13, which is the last part of this stope to be extracted, resulted in the spalling of the opening back at level 1157. Later, in March 2016, damage were observed in the adjacent Stope 15 level 1157, where floor heave and floor cracks occurred. It must be mentioned that instabilities in this area, in the form of bolt failures and wall damages, started prior to production in Stope 13 at level 1182, and were, then, intensified once the blast occurred. Around the second half of May 2016 cracks and, then, roof failure took place in Stope 13 level 1157 (Fig. 2.18a), where spalling and opening back deterioration were already observed in February of the same year. Finally, the most recent failure was noticed in August 2016, when a rock fall occurred in Stope 15 level 1108 (Fig. 2.18b), destroying one probe of the seismic monitoring network. This happened few weeks after the complete exploitation of Stope 13. In addition, starting from February 2016, major deformations were noticed as well in stopes 7 and 9 at levels 1157 and 1182. These preliminary field observations highlight a strong influence of Stope 13 excavation on surrounding rock masses, inducing both immediate and long-lasting effects. In this thesis, attention will be given to understand the mechanisms induced by Stope 13 excavation on neighboring rocks.

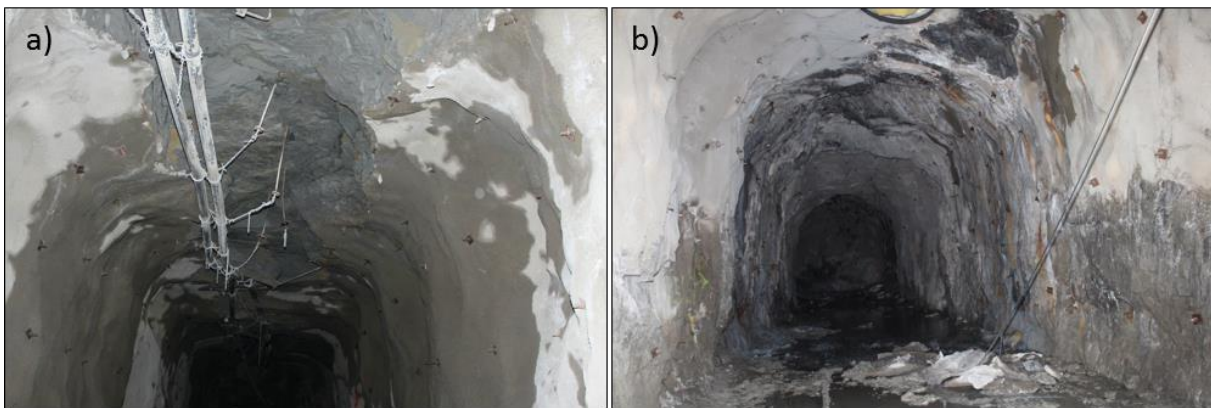


Fig. 2.18 - Recent failures in 1250 block of Lappberget. (a) Roof failure in Stope 13 level 1157 in May 2016. (b) Rock fall in Stope 15 level 1108 in August 2016. (photos: Mozaffari, 2016)

It is important to underline that, beside visible failures, there are many smaller damage which cannot be directly observed on site. This is the case of fractures occurring within the rock mass not at direct contact with drift's walls. Moreover, as drifts are shotcreted very soon after excavation, if displacement on fractures is not large enough to damage the shotcrete layer, fractures will not be visible. Similarly, many strain processes may not be directly observable. For these reasons, seismic and strain monitoring are two valuable tools which can give a more complete picture of what is happening within the rock mass.

# Chapter 3

## Seismic data processing

Seismic data analyzed in this thesis are the result of microseismic monitoring carried out by Ineris in the block 1250 of Lappberget orebody, which started in February 2015 and is still ongoing at the time of writing. An essential step of this thesis is, thus, represented by the routine seismic data treatment in semi real-time, which is aimed at classifying the recorded signals and locate their sources with the best possible accuracy.

This chapter intends to describe the routine seismic data processing, from the acquisition to the localization of recorded signals, carried out in the framework of the operational monitoring (Section 3.1). The attention will be particularly focused on the most important errors which can be made during routine data processing and on the solutions which were put in place to avoid and correct these errors (Section 3.2). This was done, on one hand, for improving operational monitoring and, on the other hand, for constructing a clean database of seismic signals to be further analyze in the framework of this thesis. One of the challenges of seismic monitoring in active mines is the ability to recognize microseismic events in a very seismic noisy environment. This operation is not straightforward as recorded seismic catalogues are often complex and characterized by a large amount of “non-event” signals due to mining operations. For this reason, a good knowledge of seismic data characteristics, in terms of amplitude, energy, duration and frequency content, is essential in order to be able to distinguish microseismic events, related to rock mass fractures, from seismic noises caused by blasting or other type of mining activities. Once identified, microseismic events are localized based on manual picking of P- and S-waves arrival times. Manual picking is often hard to perform, and the identified time series may be affected by random or systematic errors which are then reflected on events location accuracy.

In addition, Lappberget seismic network performances are evaluated in this chapter through a numerical approach, which is presented in Section 3.3 together with the results of its application to Lappberget microseismic network. The methodology allows determining the minimum magnitude that can be detected and located in the source region and the distribution of predicted location errors. Based on these results, and according to available data about mine production and local geology, Section 3.4 presents the selected seismic dataset which will be further analyzed in Chapter 4. Finally, the methodology applied for estimating seismic source parameters of selected data is presented in Section 3.5, while the analysis of the results will be the subject of the next chapter.

### 3.1 Routines of seismic data acquisition and processing

As already introduced in Chapter 2, a permanent microseismic monitoring network was installed in block 1250 of Lappberget orebody, between December 2014 and February 2015. The network consists of 6 1C and 5 3C 14 Hz geophones, installed in 5-to-20-meter-deep, vertically-oriented or inclined boreholes, covering a monitored area with a volume of about  $64 \times 10^6 \text{ m}^3$  between -950 m and -1350 m of depth (Fig. 3.1). Geophones are deployed over three mine levels (1108, 1182 and

1257) referred as A, B and C, where also acquisition units (AU) for data transfer are installed (see Tab. A.2 for exact probe positions and orientations). Timestamping is ensured with a GPS installed at the surface and linked by Ethernet connection to each AU, with a resolution of 1 ms.

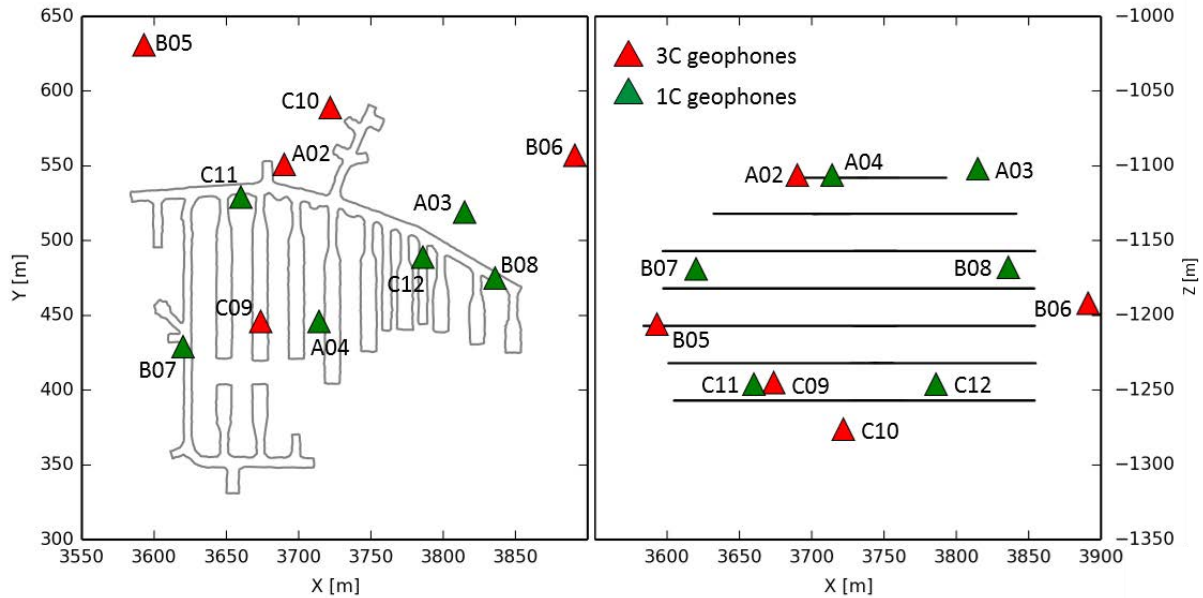


Fig. 3.1 - Lappberget microseismic network. Plan view (on the left) and vertical profile (on the right). Red triangles refer to 3C seismic probes, while green triangles indicate 1C probes. Mine levels profiles are also shown in the figure.

The acquisition system is operating in triggering mode with 8 kHz sampling frequency, while the triggering threshold, based on amplitudes, is fixed at 200 digits ( $\approx 5.35 \times 10^{-6}$  m/s). Moreover, it has been imposed that an event should be retained only if it triggers at least 2 probes per each AU on at least two levels. This results in increasing at 4 the minimum number of probes for a seismic signal to be retained. If less probes are triggered, the signal is considered as isolated and discarded for further analysis. This choice is motivated by monitoring needs. Indeed, as Lappberget is a production area, which is active 7 days a week and 365 days per year, many seismic signals are due to mine works (e.g. drilling, bolting, mucking, trucks or other vehicles). Therefore, limiting the minimum number of triggering probes should reduce the number of working-noise signals. However, this additional condition on the acquisition system has straightforward limitations for research needs, reducing significantly the number of detectable microseismic events (MSE), especially the smallest ones. Finally, a 1 kHz analog low-pass Butterworth filter is applied to the data at the moment of their acquisition.

Once detected, seismic signals are sent to the Ineris monitoring center where they are processed in semi real-time with the Ineris software suite SYTMIS, and searchable online via the interface [e.cenaris](http://e.cenaris). MSE localization is based on P an S-waves arrival times as well as on P polarization angles (dip and azimuth), which improves events localization when few seismic probes are available (Contrucci et al., 2010). However, polarization angles are only considered for 3C probes. A probabilistic approach is used to solve the inverse problem (Tarantola and Valette, 1982) and determine the hypocenter with the maximum likelihood. This consists in maximizing the probability density function (pdf) of the hypocenter by minimizing the misfit between observed and theoretical parameters, i.e. between observed and theoretical arrival times and polarization angles, using the L2-

norm. The hypocenter is determined by the Oct-Tree nonlinear method (Lomax et al., 2000), which is a grid search technique based on a successive division of the space into cubes, depending on the pdf value per each cube. To apply this method, a homogeneous velocity model is assumed with  $V_P = 6535$  m/s and  $V_S = 3703$  m/s for P and S-waves respectively ( $V_P/V_S = 1.765$ ), which was determined by calibration blasts and which agrees with the local geological context (Tonnellier et al., 2016). The searching space of the Oct-Tree algorithm is limited to a volume of 2000 m side along X, Y and Z directions, while successive cube dimension is ranging from 7 to 50 m. For taking into account velocity model uncertainties, an error of 0.002 m/s is fixed on travel times, while arrival times picking errors are set to 0.002 m/s and 0.003 m/s for P and S-wave respectively, which correspond to a location error of around 13 m considering P-wave velocity. Finally, polarization angles errors are set at  $10^\circ$  for azimuth and  $15^\circ$  for dip.

P and S-wave arrival times are determined by manual picking. In the case of 3C probes the S-wave picking is made simpler by means of waveform rotation (Abdul-Wahed et al., 2001; Cichowicz, 1993). Indeed, knowing probes orientation and assuming a straight ray path between source and receiver, the waveform can be rotated following the polarization direction of the signal. This means that the seismogram will be reoriented along three axes (LQT) which correspond to the P polarization direction (L-axis) and the two polarization directions of S-wave (Q and T axes). As a result, S-wave picking is facilitated on Q and/or T axes where P phase should appear significantly reduced (Fig. A.1). At the same time, P polarization angles are retrieved.

Besides events localizations, local magnitude ( $M_L$ ) and radiated seismic energy ( $E$ ) are routinely determined as a standard procedure of daily data processing. Seismic source energy is estimated with a time-domain methodology, as the integral of the squared velocity seismogram and considering both P and S-waves. Only 3C probes are used for  $E$  estimation, whose final value is given by the arithmetic mean on all considered probes:

$$E = \frac{4\pi\rho}{N} \sum_{n=1}^N R_n^2 \left( V_P \int_{t_{Pn}}^{t_{Sn}} v_n(t)^2 dt + V_S \int_{t_{Sn}}^{t_{En}} v_n(t)^2 dt \right) \quad (3.1)$$

where  $\rho = 3000$  kg/m<sup>3</sup> is the rock mass density determined by laboratory measurements on dry samples (Tonnellier et al., 2016),  $N$  the total number of 3C probes,  $R_n$  the hypocentral distance at probe  $n$ ,  $V_P$  and  $V_S$  the P and S-wave velocity,  $t_{Pn}$  and  $t_{Sn}$  the P and S-wave arrival time at probe  $n$ ,  $t_{En}$  the end time of the signal (95% of the emitted  $E_s$  reached) and  $v_n$  the ground velocity detected by the geophone.

Local magnitude of MSE is based on the computed radiated seismic energy. It was calibrated in order to be consistent with the  $M_L$  estimated by another seismic monitoring network installed by the Institute of Mine Seismology (IMS) in the upper levels of Lappberget orebody, outside of the Ineris monitored area. This latter magnitude is estimated based on an empirical relationship derived from Vaal River and West Wits mines in South Africa, which takes the following form for Garpenberg mine:

$$\log_{10} PGV = 0.58M_L - 1.85 \log_{10} r + 1.05 \quad (3.2)$$

where, PGV is the peak ground velocity (m/s) of the signal and  $r$  is the source-receiver distance (m). Calibration between these two magnitude scales was performed considering around 30 MSE located by both networks, IMS and Ineris. Event's energies estimated by Ineris network were then compared

with  $M_L$  estimated by IMS for the same events, obtaining the following relationship between  $M_L$  and  $E$ :

$$M_L = 0.8 \log_{10} E - 3.35 \quad (3.3)$$

This equation is thus used in the routine processing of MSE for the estimation of their local magnitude. The choice of calibrating these magnitude scales is motivated by monitoring needs, in order to obtain comparable magnitudes between the two seismic networks installed in Lappberget orebody. However, even if the obtained  $M_L$  is related to measured radiated seismic energy, its value is not comparable to the true size of the events. Moreover, the attenuation law used by IMS for  $M_L$  estimation (equation 3.2) is empirical and derived from other mines, thus, it does not take into account the real attenuation effects on wave propagation in Lappberget environment. For these reasons, as it will be described in Section 3.5, a moment magnitude scale was estimated and used to further characterize Lappberget microseismic activity.

### 3.1.1 Type of recorded seismic signals

MSE recorded in Lappberget orebody between 2015 and 2016 present generally emergent onsets and a predominance of the S-phase (Fig. 3.2a, c, e, g). Signals are characterized by short durations, ranging from about 0.03 s to 0.7 s, and low amplitudes, generally smaller than 0.1 mm/s. For events characterized by high Signal-to-Noise-Ratios (SNR), P and S phases are generally distinguishable in the seismograms, even if the beginning of the S phase can be covered by the coda of P-wave, due to short travel distances. Three main classes of MSE can be distinguished according to their frequency content: (i) low frequency events with frequencies smaller than 500 Hz (Fig. 3.2a, b), (ii) large frequency band events, whose frequency intervals vary between 20 and more than 1000 Hz (Fig. 3.2c, d, e, f) and (iii) high frequency events with most of the energy distributed in frequencies which may be higher than 3000 Hz (Fig. 3.2g, h). A well-defined dominant frequency is not observed for any of the mentioned MSE classes, with intensities almost homogeneously distributed along frequency intervals. Due to the wide range of frequency bands, events reprocessed for the scope of this theses were corrected to remove the effect of the 1 kHz low-pass filter automatically applied to the data. The correction, required for source parameter estimation (Section 3.5), was applied within the band 200 ÷ 3000 Hz to avoid excessive distortion of original signals.

MSE characterization based on their frequency content highlights that rock mass extraction in Lappberget orebody may induce different event characterized by distinct dynamics. This first insight is interesting and will be later discussed in this thesis with the analysis of seismic source parameters which will give valuable information about the rock mass behavior in response to mining.

Besides MSE, a large number of signals recorded by the monitoring network are related to mine blasts and other types of mining operations. Indeed, as written at the beginning of this chapter, Lappberget orebody is currently under production, thus, it is characterized by intense blasting and working activities. Blast signals, related to PB and DB, are characterized by long duration, lasting in some cases more than 4 seconds, and by variable amplitude and frequency contents, depending on their distance from the seismic monitoring system. Indeed, blasts performed outside of the Ineris monitored area present lower frequencies (Fig. 3.3a, b), ranging between around 20 and 1000 Hz, than blasts performed within the monitored volume (Fig. 3.3c, d), which can show frequencies higher than 1000 Hz. Seismograms of these latter blasts are frequently saturated, showing a swarm-like shape due to a micro-delay between blasting of each explosive charge within separated drill holes (Fig. 3.3c).



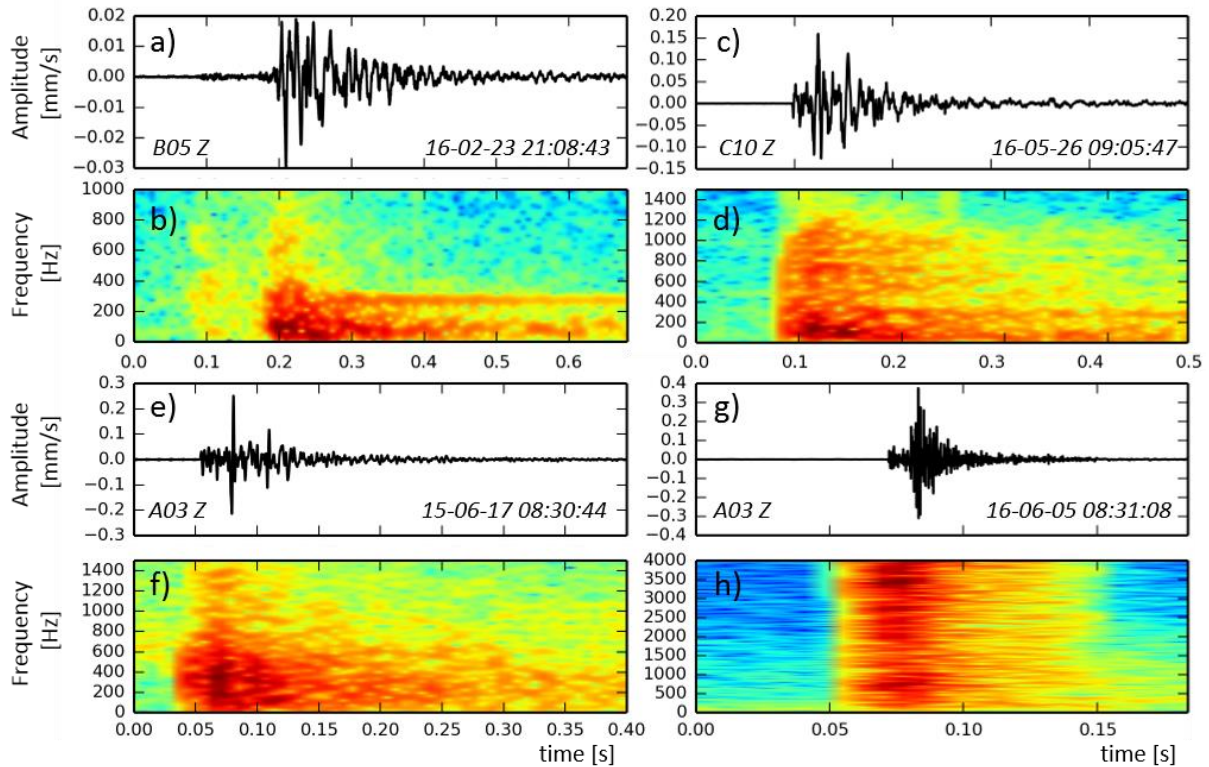


Fig. 3.2 - Seismograms (a, c, e, g) and spectrograms (b, d, f, h) of some MSE. Spectrograms are computed using a 0.032 s window length with 90% overlap, while intensities represent the power spectral density. Note that time and frequency scales can be variable from an event to another. All the events shown in this figure have been corrected by removing the effect of the 1 kHz low-pass filter. Times reported at the bottom right side of seismograms are given in UTC, while seismic probes and channels are indicated at the bottom left side.

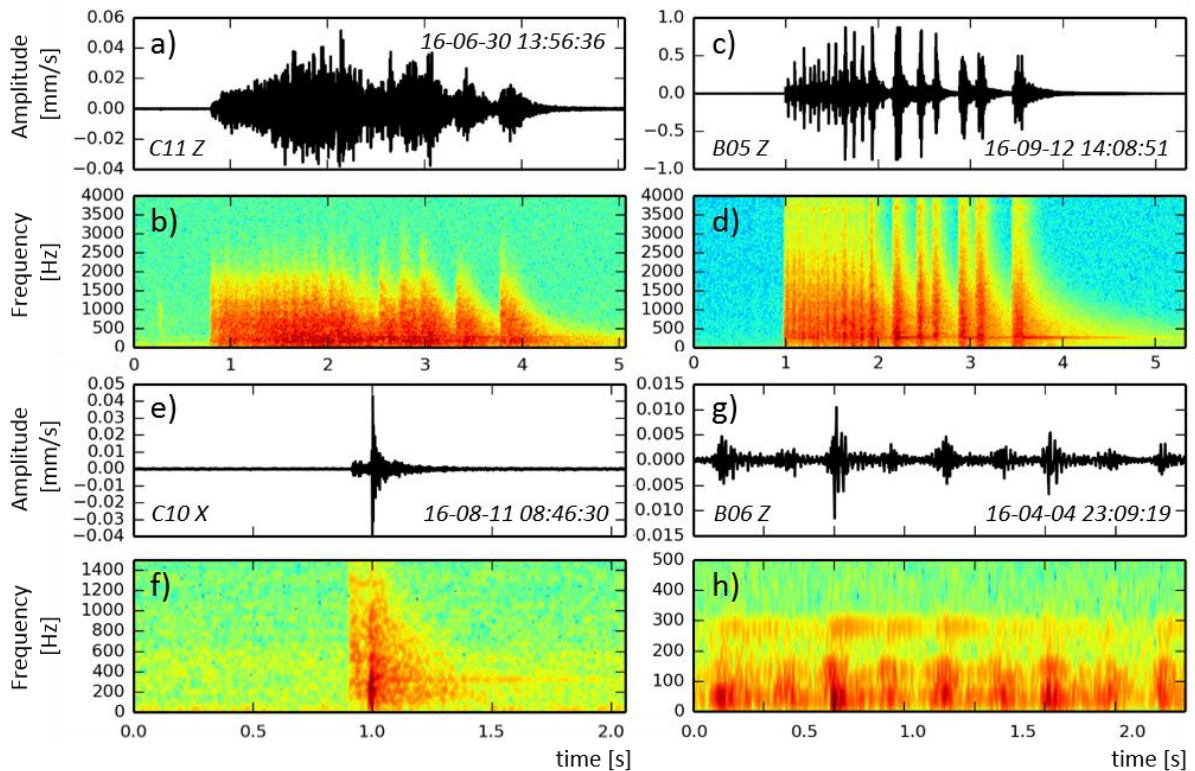


Fig. 3.3 - Seismograms and spectrograms of mine blasts (a, b, c, d), boulder blasts (e, f) and noise related to mining operations (g, h). Spectrograms have been computed as in Fig. 3.2. Times are given in UTC.

Besides PB and DB, boulder blasts (BB) also produce microseismic signals which can be recorded by the network. These blasts are performed on isolated blocks of rock resulting from PB, whose size need to be further reduced. Blasting procedure is carried out in the same way as for PB and DB, by charging and blasting separated drill holes. However, the amount of explosive is significantly smaller than that used during production and development. The related seismic signal (Fig. 3.3e) appears strongly similar to that of MSE, in terms of waveform shape and signal duration, while the frequency content (Fig. 3.3f) is rather smaller, with dominant frequencies in the range  $20 \div 150$  Hz.

Finally, machine related signals, due to mining operations other than blasts, are also largely recorded by the network. An example of this type of signals is presented in Fig. 3.3g, together with its spectrogram (Fig. 3.3h). The frequency content is generally lower than 500 Hz with a predominant mono-frequential behavior which can sometimes present spikes in correspondence with the electrical harmonic frequencies. In some cases, as in the example presented in Fig. 3.3g, these noise signals appear repeated in time with a regular timing between each pick. However, machine related signals can be very variable as they are dependent from the type of activity. As a result, some of these records can be confused with MSE when classification is only based on waveforms.

### 3.1.2 Challenges and common errors in daily data processing

As highlighted in the previous section, signals recorded by the network are complex and related to various sources. An important task of the daily data treatment is the ability to recognize MSE and distinguish them from mine blasts and noises due to mine works, by visual inspection of seismic records. PB and DB are normally easy to identify, due to their unambiguous seismogram (Fig. 3.3a, c) and thanks to the regularity in blasting procedure (occurring at around 04:00 and 16:00 in local time). On the contrary, BB are much more difficult to distinguish from MSE as they can be performed at any time and only in few cases it is possible to be informed about their occurrence. In addition, their signals (Fig. 3.3e), in terms of waveform and duration, can be confused with that of MSE. Another difficulty comes from some signals related to mine works. Indeed, when these are not regularly repeated in time, as in the example of Fig. 3.3g, their waveform can look similar to that of MSE.

Beside waveforms classification, another challenge in the daily data treatment is due to picking of phase arrivals on triggered signals. Indeed, manual picking is often hard to perform, especially for MSE that present a low SNR. Moreover, when events are close to seismic probes, it can be difficult to distinguish between P and S arrivals, with S waves often covered by the coda of P ones. Time series picking can then be affected by different errors in arrival times identification and these errors are reflected on events location accuracy. These errors can be even more important if we consider that manual picking is performed by different operators.

With the aim of understanding the rock mass response to mining and identifying seismic hazardous areas for large damage prevention, a correct identification of real MSE related to induced rock mass fracturing and their accurate localization are two aspects that significantly influence the analysis of mining-induced seismicity. Indeed, the presence of blast and/or noise-related signals within MSE catalogues leads to erroneous interpretation of rock mass processes. At the same time, the wrong classification of MSE within noise and/or blast categories results in a loss of information which can be sometimes important. Once catalogues have been filtered from outliers due to “non-event” signals, the accurate localization of the real MSE is another basic concern. As reported by Mendecki et al. (1999), precise events localization is not only necessary for identifying rockbursts potential areas, but

also because all subsequent interpretation and seismological processing, such as for example source parameters estimation, depend on location.

Based on these considerations and taking into account the complexity of Lappberget signals and the difficulties in manual picking, a back-analysis of seismic signals recorded from February 2015 to June 2016 was carried out. The aim of this work was, on one hand, the evaluation and correction of P and S phase picking and, on the other hand, a better signal classification to remove from the database all the recordings erroneously classified as MSE. Methodology and results of this analysis are discussed in the next section.

## 3.2 Picking consistency evaluation - The Wadati analysis

A suitable methodology for picking consistency evaluation is the Wadati diagram analysis (Wadati, 1933) which was already applied to earthquake data (Romano et al., 2013), as well as to mining-induced seismicity (Julià et al., 2009). Wadati diagram was originally introduced to estimate the origin time ( $t_0$ ) of seismic events, plotting on a diagram the phase arrival times difference ( $T_S - T_P$ ) as a function of P arrival times ( $T_P$ ) for a single event recorded at different stations. To avoid working on single events, the modified Wadati diagram (Chatelain, 1978) was preferred as it allows grouping all the events in a single diagram, comparing time difference of P and S phases on station pairs.

Considering  $x_i$  and  $x_j$  as the hypocentral distances of a seismic event at two stations  $i$  and  $j$ , one can write:

$$\Delta T_P = t_{Pi} - t_{Pj} = (x_i - x_j)/V_P \quad (3.4)$$

$$\Delta T_S = t_{Si} - t_{Sj} = (x_i - x_j)/V_S \quad (3.5)$$

where  $t_P$  and  $t_S$  are P and S waves' arrival times, respectively, while  $V_P$  and  $V_S$  are waves' velocities. Combining equations (3.4) and (3.5) we obtain:

$$\Delta T_S = \left(\frac{V_P}{V_S}\right) \Delta T_P \quad (3.6)$$

which represents the equation of a line with slope equal to  $V_P/V_S$ . Equation (3.6) is valid only assuming a propagating medium of constant velocity and, thus, a straight ray-paths joining sources and receivers. This assumption, even not true in a real geologic medium, is often employed in seismic analysis, introducing inevitable uncertainties which are although reduced when short source-receiver distances are considered (Julià et al., 2009), as in the case of Lappberget monitored area.

For applying the modified Wadati analysis to Lappberget microseismic dataset, we considered all the MSE recorded between February 2015 to June 2016, for a total of 1225 signals. For some of the events, only 3C probes were considered. This was a forced choice as S-phase picking was not performed on 1C probes during 2015. Moreover, data coming from probe C09 are available only until June 2015 when the probe was destroyed. At the same time, due to a problem of timestamping on probes B05 and B06, we had to discard data of these two stations between the 16<sup>th</sup> December 2015 and the 3<sup>rd</sup> of January 2016. For all the other data, time arrival differences of P and S waves were computed on all the available station pairs, resulting in a total dataset of 4968 points. Fig. 3.4a shows the modified Wadati diagram for the initial dataset. The best fit line is determined by both ordinary least-square (in blue) and orthogonal (in red) regression. The latter fitting is particularly suitable

when data are affected by errors on both variables. Indeed, if it is reasonable to suppose bigger inaccuracy on S-phase pickings, errors on P-phase pickings cannot be neither excluded. Standard deviation lines for the orthogonal regression are then used for outlier identification, which resulted in 217 phases.

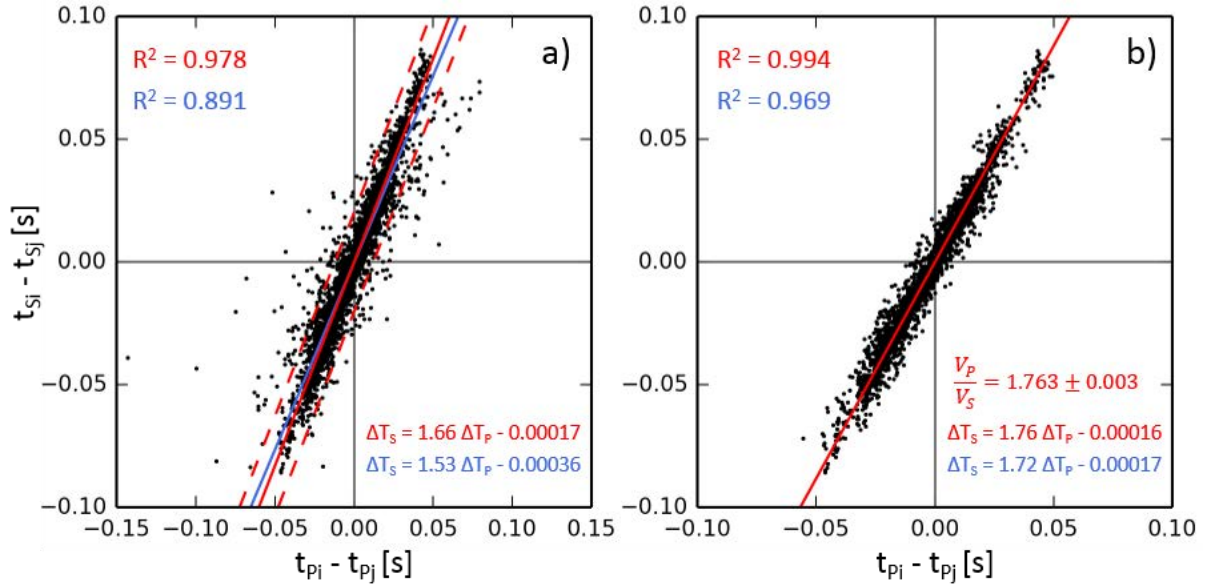


Fig. 3.4 - Modified Wadati diagrams for Lappberget microseismic dataset. (a) Original dataset. Red and blue lines represent orthogonal and ordinary least-square regressions, respectively. Dashed red lines report the standard deviation of the orthogonal regression. Regressions coefficients are color coded as the lines. (b) Final dataset after outlier correction and removal. For better visualization, the ordinary least-square regression line is not reported in the diagram, while its coefficient is indicated in blue. The estimated value of  $V_p/V_s$ , determined on the orthogonal regression, is reported together with its standard deviation.

Identified outliers were carefully inspected and, when possible, phase picking has been refined. Most common errors are due to erroneous interpretation of the S phase arrival. However, as expected, inaccuracies on P phase pickings were also observed, especially for low SNR events. Frequently, picking errors result in discrepancies of the S-P travel time at different stations, which can be due to erroneous picking on both P and S phases, or due to S phase picking even if any S phase occurs. This latter case is particularly observed on machine noise-related signals or isolated blast signals which were erroneously classified as MSE. An example of such case is presented in Fig. 3.5. The P-wave appears correctly picked at each sensor, but the S-P travel time is inconsistent with the first arrival. Indeed, as P and S-wave velocities are constant, the faster the P phase arrival, the smaller the S-P travel time. S phase pickings in Fig. 3.5 show the inverse situation, with decreasing S-P travel times for increasing P arrivals, which is unrealistic. A better inspection of this signal reveals a mono-frequential behavior which suggests a working noise source, rather than a real process of rock mass fracturing. This means that the modified Wadati analysis, and the inspection of the detected outliers, also helped in identifying errors in data classification. Indeed, of the whole outlier dataset, around 60 signals erroneously classified as MSE have been identified thanks to the described procedure. For this reason, the entire original MSE dataset has been re-checked for noise and blast signals removal. After this operation, more than 100 recordings were eliminated from the original catalogue.

Modified Wadati diagram of the final dataset after outlier removal and picking correction is presented in Fig. 3.4b. One can observe the significant increase in the R-squared value for both

orthogonal and least-square regression, with the former that shows a better correlation. Catalogue correction results also in the increase of the estimated  $V_P/V_S$  ratio, which raised from 1.66 to 1.76 considering orthogonal regression results. The final estimated  $V_P/V_S$  value is strongly consistent with the assumed velocity model ( $V_P = 6535$  m/s,  $V_S = 3703$  m/s,  $V_P/V_S = 1.765$ ), validating its accuracy and highlighting its stability during time. This latter result suggests that mine excavations and paste filling may induce only local changes of propagating medium properties, which remained almost unaltered if the whole investigated region is considered.

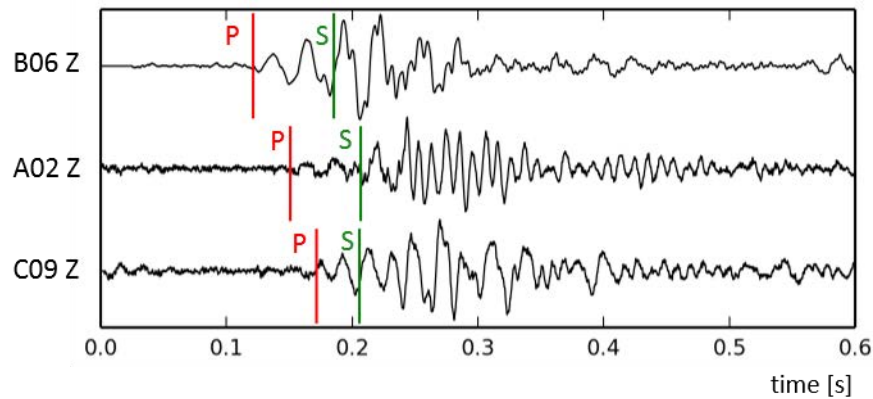


Fig. 3.5 - Example of erroneous picking on a signal related to working activities (15-04-18 06:52:12). Recordings from three stations (B06, A02 and C09) have been sorted by P-wave arrival. Red and green lines indicate the P and S phase arrivals, respectively, as retrieved by manual picking performed during routine data treatment.

Considering the events from July to December 2016 in addition to the back analyzed catalogue for the period February 2015 – June 2016, the whole Lappberget microseismic dataset is constituted by around 1200 MSE. Of these, more than 800 are located inside the Ineris monitored area, while the remaining are distributed outside of this volume and particularly at shallower depths in coincidence with other productive areas of the mine. Fig. 3.6 shows the distribution of root mean squared error (RMS) between travel times residuals observed at different stations for all the events located within the Ineris monitored area during almost two years of recording (from February 2015 until the end of December 2016).

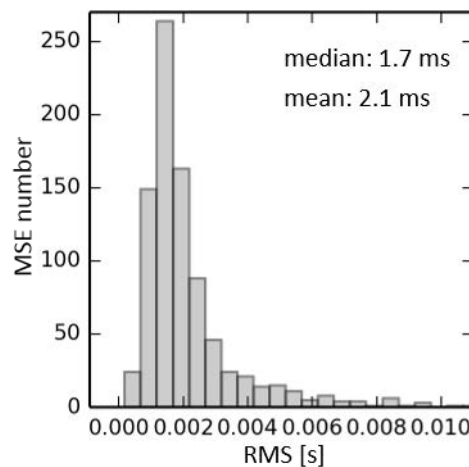


Fig. 3.6 - Root mean square error between theoretical and calculated origin times. Only MSE located within the Ineris monitored area are considered for the analysis.

More than 80% of these events are characterized by RMS lower than 3 ms and a mean RMS of around 2.1 ms. This corresponds to location errors smaller than 20 m and a mean location error of 13.7 m, considering P-wave velocities. Further consideration about location accuracy are addressed in the next section, where a numerical method for array performances evaluation is presented and applied to Lappberget microseismic monitoring network.

Results presented in the current section show that the modified Wadati approach is particularly suitable for Lappberget dataset, helping in efficiently identifying picking errors. Even if not developed within the current work, the methodology could be implemented in an automatic way on the real-time data processing for a regular evaluation of picking consistency. Moreover, this could also allow verifying changes within the  $V_p/V_s$  ratio, which would indicate variations of propagating medium properties due to excavations.

### 3.3 Evaluation of microseismic network performances

As already discussed in the previous section, detection and location accuracy of MSE is a critical issue that significantly affects mining-induced seismicity analysis. Besides picking uncertainties, events location is also related to seismic network configuration, i.e. the number and the position of recording seismic probes. This is even more important in the context of active mines where network geometry can change over time due to production needs. Generally, seismic array performances, in terms of detection and location capabilities and expected location errors, has a strong impact on the identification of seismic hazardous areas. More precisely, detection-location performances mean the ability of a network to detect and locate seismic events of different magnitudes in a given source region as a function of the ambient noise. On the other hand, the prediction of location errors denotes the reliability of the spatial seismic source estimation, as a function of event's magnitude.

Commonly, detection performances are evaluated by the magnitude of completeness  $M_c$  (e.g. Nanjo et al., 2010; Stabile et al., 2012), which is defined as the minimum magnitude above which all the events within a certain region can be recorded reliably and completely (Schorlemmer and Woessner, 2008). Events with magnitude smaller than  $M_c$  can be recorded by the network, until the minimum detectable magnitude ( $M_{min}$ ), but some of them will be missing in the catalogue.

Methodologies for  $M_c$  estimation are based on the b-value computation and on the analysis of possible deviations from the Gutenberg-Richter power law (Amorese, 2007; Woessner and Wiemer, 2005). As these approaches use only information from earthquake catalogs, other authors (e.g. Schorlemmer and Woessner, 2008) prefer estimating  $M_c$  based on empirical data, such as amplitude threshold studies and phase arrival analysis.

In this thesis, Lappberget array performances have been evaluated by numerical simulations with the aim of determining: (i) the minimum magnitude that can be detected and located in the source region and (ii) the distribution of predicted location errors for a specific magnitude value. For this purpose, we further developed an algorithm (Matrullo and Lizeur, 2015) for the evaluation of microseismic array performances (EMAP), based on the methodology proposed by Stabile et al. (2012). This development was included in the SYTMISauto software. Methodology and application of the proposed algorithm to Lappberget microseismic network are presented in the next sections. This approach was published in the proceeding of the 9<sup>th</sup> International Symposium on Rockbursts and Seismicity in Mines (De Santis et al., 2017).

### 3.3.1 EMAP algorithm methodology

The network performances evaluation begins dividing the monitored volume in a regular grid of virtual seismic sources (VS) and by defining a background noise (N) at each seismic station. Knowing the velocity model and the network geometry, theoretical values of P and S-waves arrival times ( $t_p$  and  $t_s$ ), together with theoretical values of polarization angles, are determined per each couple virtual source-receiver (VS-R). Based on the velocity model, maximum theoretical amplitudes ( $A_{max}$ ) are computed at each receiver per each VS and for different values of local magnitude ( $M_L$ ), in a given magnitude range [ $M_L^{min} \div M_L^{max}$ ]. Theoretical amplitudes are, then, compared with the background noise at each probe, for computing theoretical signal-to-noise ratios ( $A_{max}/N$ ). In order to determine the minimum magnitude which can be detected and located by the network at each virtual source location, the theoretical SNR are compared with thresholds values imposed for detection and location, respectively. Moreover, an additional constraint is imposed on the minimum number of observations, among P, S-waves and polarization angles, which is required for detection and location purposes. Selection criteria on the number of observations and on threshold values have been set as follows:

- (i) Definition of SNR thresholds for considering observations:
  - (a) P-waves threshold:  $S_P/N \geq (S_P/N)_{min} \Rightarrow$  minimum SNR for a P-wave to be detected;
  - (b) S-waves thresholds:  $S_S/N \geq (S_S/N)_{min}$  and  $\Delta(t_S-t_P) \geq \Delta(t_S-t_P)_{min} \Rightarrow$  minimum SNR and minimum time arrival difference between P and S-waves for an S-wave to be detected;
  - (c) Polarization angles:  $S_A/N \geq (S_A/N)_{min} \Rightarrow$  minimum P-wave SNR needed for retrieving polarization angles.
- (ii) Definition of the minimum number of observations:
  - (a) Detection evaluation:  $n_{Detect} \geq n_{Detect_{min}} \Rightarrow$  minimum number of P-waves ( $n_P$ ) which satisfy condition (i-a) for an event to be detected;
  - (b) Location evaluation:  $n_{Loc} \geq n_{Loc_{min}} \Rightarrow$  minimum number of observations, among P, S-waves and polarization angles ( $n_{P,S,A}$ ), which satisfy conditions (i) for an event to be located.

Theoretical SNR ( $A_{max}/N$ ) are compared with the thresholds described above and a count is made on the observations reliably identified by the network, per each VS-R couple and considering all the  $M_L$  values in the range [ $M_L^{min} \div M_L^{max}$ ]. Per each grid point, the minimum detectable and localizable magnitude is determined as the minimum magnitude that satisfies conditions (i) and (ii), as summarized below:

- (iii) Detection: if  $n_P \geq n_{Detect_{min}}$  with  $A_{max}/N \geq S_P/N_{min}$ ;
- (iv) Location: if  $n_{P,S,A} \geq n_{Loc_{min}}$  with  $A_{max}/N \geq S_P/N_{min}$ ,  $S_S/N_{min}$ ,  $S_A/N_{min}$  and  $\Delta(t_S-t_P) \geq \Delta(t_S-t_P)_{min}$

The additional criteria (i-b) imposed on wave arrival times difference for the reliable detection of S-waves, is motivated by the possible coverage of S phase arrival by the coda of P-wave, when events are localized close to receivers.

Expected location errors within the monitored volume are determined considering uncertainties on input observations. Indeed, locating a seismic event means estimating its X, Y and Z positions, as well as its origin time ( $t_0$ ), in a given monitored volume. As all estimations, seismic location is affected by

errors and uncertainties, whose values determine the reliability of the calculated event position or, in other words, the location accuracy of a given seismic network geometry.

EMAP algorithm determines the distribution of expected location errors by location simulations as reported in the example of Fig. 3.7. Indeed, EMAP relocates several times the VS, perturbing the previously computed theoretical values of P and S-waves arrival times and polarization angles, with errors that follow a Gaussian distribution. The expected location error at each source point is, then, given by the average distance between simulated positions (red dots in Fig. 3.7) after data alteration and the real location (blue star in Fig. 3.7).

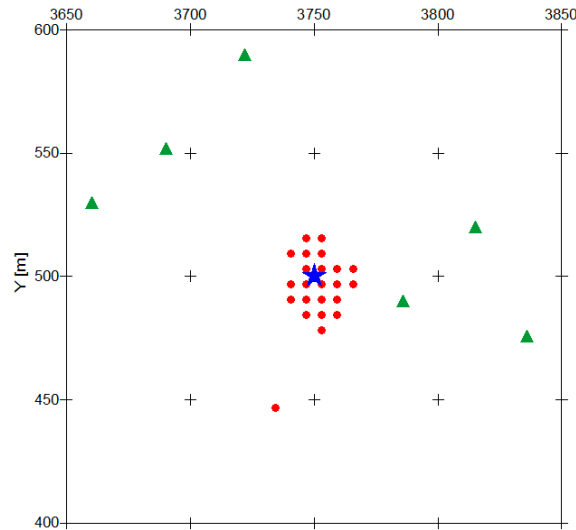


Fig. 3.7 - Schematic illustration of location simulation procedure. The star indicates the real position of a virtual seismic source, while red dots display its relocated positions after input data alteration. Green triangles show seismic probe positions, while black crosses represent other virtual seismic sources.

### 3.3.2 EMAP application to Lappberget microseismic network

To be able to calculate synthetic amplitudes and arrival times, it is essential to know the velocity model and the attenuation relationship in the monitored area, and to previously determine the background noise at each seismic probe.

The attenuation law used for Lappberget network is the empirical relationship described by equation 3.2 discussed in Section 3.1, while, the velocity model is the homogeneous model with  $V_P = 6535$  m/s and  $V_S = 3703$  m/s. In order to determine the optimum threshold values for EMAP algorithm, analyses were performed on real data to estimate the average noise at each probe and for determining amplitude characteristics of real records. Noise levels (Tab. 3.1) have been estimated at each probe as the mean value of the maximum noise amplitude, computed on the few second signal preceding the P-wave arrival. The analysis has been performed on real MSE located by the network in 2016. For probes B07 and C09, the average noise of the entire network has been used, as these probes were out-of-order during the analyzed period. Similarly, the mean value of maximal amplitude for P and S-waves has been estimated at each seismic probe (Tab. 3.1). Values have been determined considering the entire signal for S-waves PGV ( $PGV_P$ ), while PGV of P-waves ( $PGV_S$ ) has been retrieved considering the signal between the P and the S-wave arrival times.

However, the use of mean amplitude values for the determination of SNR limits may results in too restrictive threshold values. Indeed, we are interested in the minimum amplitude that can be



detected and located by the network in the presence of noise. Based on this consideration, selected criteria for the minimum number of observation and for threshold values have been set as follows:

- (i) Detection criteria: minimum 4 P-waves with  $S_p/N \geq 6$ ;
- (ii) Location criteria: minimum 8 observations, among P, S-waves and polarization angles, with  $S_p/N \geq 6$ ,  $S_s/N \geq 10$ ,  $\Delta(t_s-t_p) \geq 0.01$  s and  $S_A/N \geq 6$

The minimum number of observations required for an event to be detected (condition i) has been chosen in order to match triggering thresholds discussed in Section 3.1. Note that criteria on polarization angles are taken into account only for 3C seismic probes.

Tab. 3.1 - Mean values of background noise and PGV of P and S-waves.

Probes	Noise max [m/s]	PGV <sub>P</sub> [m/s]	PGV <sub>S</sub> [m/s]
A02	$1.27 \times 10^{-6}$	$3.15 \times 10^{-5}$	$7.26 \times 10^{-5}$
A03	$2.68 \times 10^{-6}$	$6.59 \times 10^{-5}$	$1.52 \times 10^{-4}$
A04	$1.17 \times 10^{-6}$	$2.20 \times 10^{-5}$	$8.00 \times 10^{-5}$
B05	$9.32 \times 10^{-7}$	$1.77 \times 10^{-5}$	$4.44 \times 10^{-5}$
B06	$1.43 \times 10^{-6}$	$4.49 \times 10^{-5}$	$1.39 \times 10^{-4}$
B07	$1.85 \times 10^{-6}$	-	-
B08	$3.50 \times 10^{-6}$	$4.06 \times 10^{-5}$	$1.59 \times 10^{-4}$
C09	$1.85 \times 10^{-6}$	-	-
C10	$1.64 \times 10^{-6}$	$3.62 \times 10^{-5}$	$7.45 \times 10^{-5}$
C11	$2.86 \times 10^{-6}$	$2.78 \times 10^{-5}$	$7.05 \times 10^{-5}$
C12	$1.20 \times 10^{-6}$	$4.32 \times 10^{-5}$	$1.36 \times 10^{-4}$
Average	$1.85 \times 10^{-6}$	-	-

Considering the average noise level of the entire network, the chosen thresholds result in amplitudes of around  $1 \times 10^{-5}$  and  $1.7 \times 10^{-5}$  m/s, for P and S-waves, respectively. These values are in good agreement with minimum amplitudes observed from real data, as reported in Fig. 3.8, which shows that the imposed threshold allows explaining more than 85 % of the events.

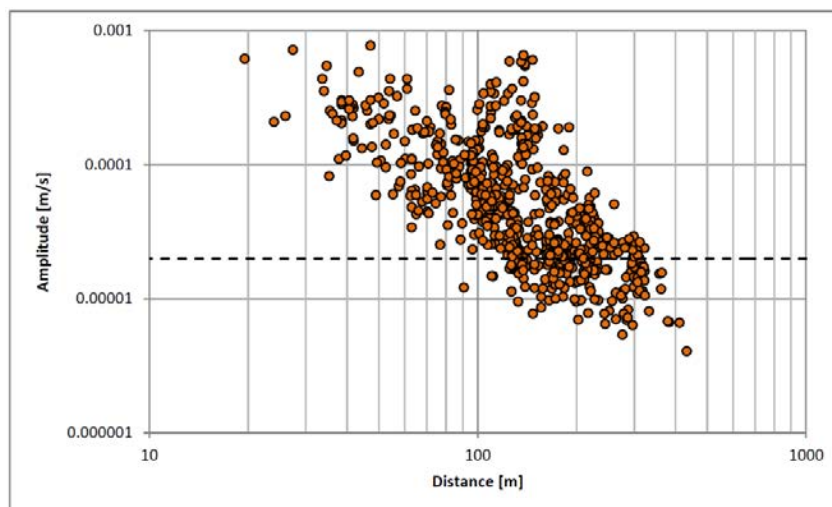


Fig. 3.8 - PGV of S-waves observed at each probe of the network for located MSE with  $-2.1 \leq M_L \leq -1.9$ . The imposed threshold (black-dot line) explains more than the 85% of the events.

Finally, to determine expected location errors, uncertainties on P and S-wave arrival times and on polarization angles have been imposed, with errors that follow a Gaussian distribution. Standard deviations of location parameter errors have been set at 2 ms and 3 ms for P and S waves, respectively, which correspond to a location error of about 13 m considering P-wave velocity. Standard deviations of polarization angle errors have been fixed at  $10^\circ$  for azimuth and at  $15^\circ$  for dip. These values have been chosen in order to be consistent with standard deviations of uncertainties used in the probabilistic model of the localization algorithm (Section 3.1). Input localization parameters are, then, perturbed following the imposed uncertainties and each VS is relocated 100 times.

The area of the mine in which EMAP algorithm was tested is extending on 400 m along the vertical direction (Z), between 950 and 1350 m below ground surface, and on 400 m in the horizontal directions, from 3550 to 3950 m along X axis, and from 300 to 700 m along Y axis, which correspond to the extension of Ineris monitored area. The selected volume has been divided in a regular grid of VS, choosing a grid sampling of 50 m, resulting in a total number of 729 points. This choice has been made to guarantee an optimal compromise between the resolution of detectability and location error maps and the computing time. This is particularly true for location error simulations that require a larger computing time than detection-location analyses, due to the time needed for relocating each virtual source. Moreover, the geometry of Lappberget microseismic network has changed during time, in particular regarding the number of functioning probes. Indeed, due to PB, probes B07 and C09 were destroyed in 2015, reducing the number of probes from 11 to 9. In addition, along 2016, different probes have been disconnected for few weeks up to several months, because of mining works. Therefore, the geometry of the network has periodically changed, ensuring on average a total number of 8 working probes. For this reason and in order to compare network capabilities with different network geometries, EMAP methodology has been tested on two network configurations:

- Configuration 1 (C1) with 11 seismic probes and
- Configuration 2 (C2) which considers 8 probes.

Results are presented in the form of contour maps for detection-location capabilities and predicted location errors, as presented in the next sections.

### 3.3.2.1 Evaluation of detection-location performances

Detection and location performances of Lappberget array were evaluated in the local magnitude range  $-5 \leq M_L \leq 0$ , with an  $M_L$  interval of 0.1, which is in good agreement with magnitudes values of real events (Fig. 3.9). Results are presented in the form of contour maps for a plan view at 1200 m depth (Fig. 3.10), which corresponds approximatively to the central depth of the network, and for a vertical section at  $y = 550$  m (Fig. 3.11). Contour maps were obtained by interpolation of information available at each VS using the Kriging method.

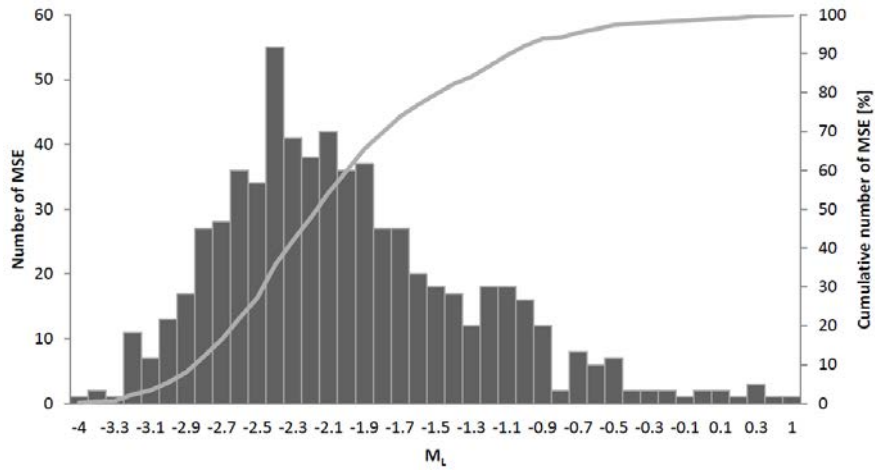


Fig. 3.9 - Local magnitudes distribution of Lappberget microseismic events. Only events located inside the Ineris monitored area and recorded between February 2015 and December 2016 are considered.

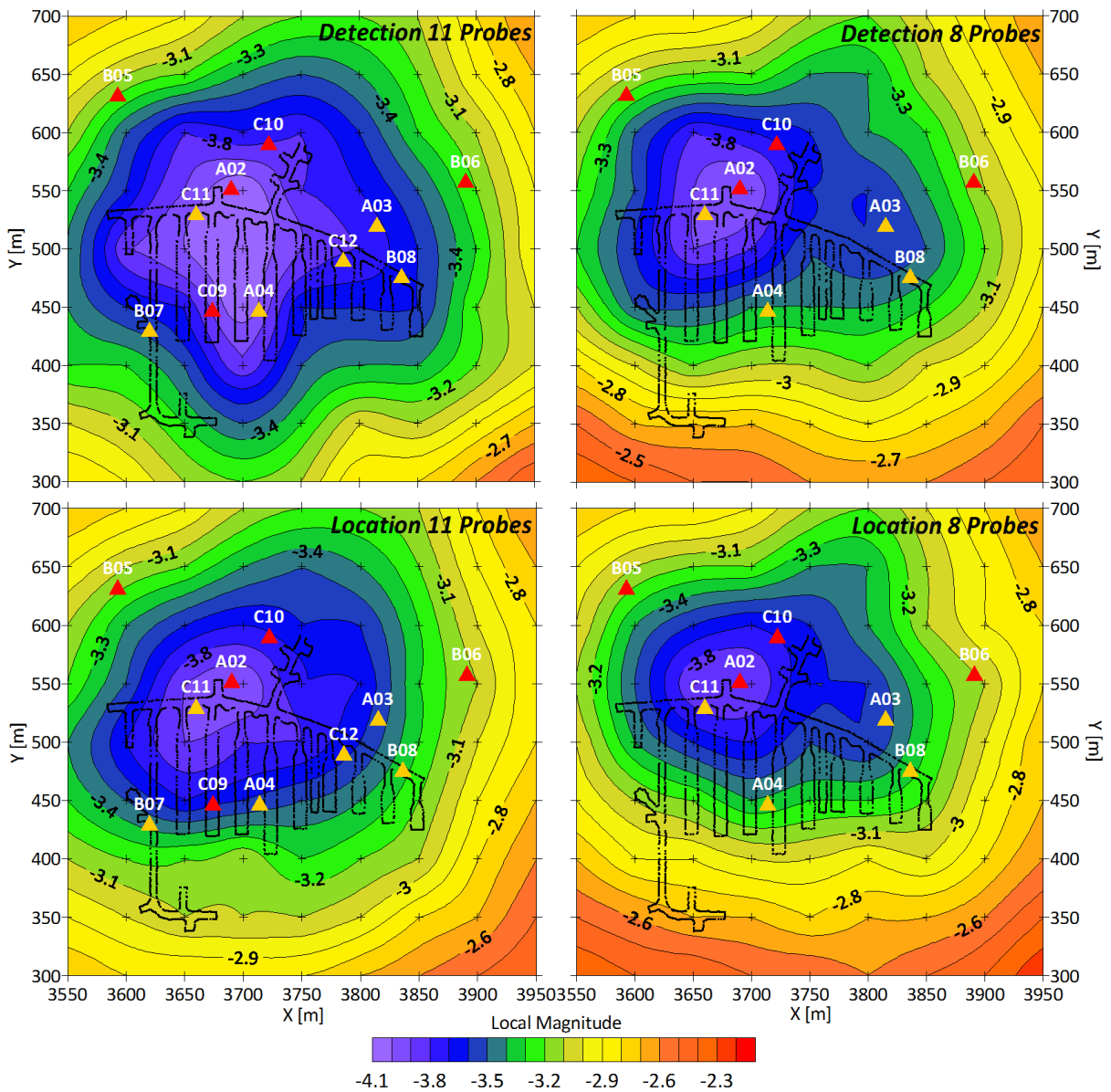


Fig. 3.10 - Horizontal profile of minimum magnitude detected (at the top) and located (at the bottom) for C1 (on the left) and C2 (on the right) configurations, at 1200 m depth. Crosses indicate the position of virtual

seismic sources. Triangles show the projection of 1C (in yellow) and 3C (in red) seismic probes at level -1200. Mine galleries profile of level -1207 is also shown in the figures.

We observe a small variation of the minimum magnitude value between detection and location performances and between C1 and C2 configurations. Indeed, minimum detectable magnitudes are equal to -4.1 and -4, for C1 and C2, respectively, with an increase of only 0.1 when considering location performances for both configurations. Differences between detection and location are particularly visible on the extension and the shape of contour lines, both in the horizontal (Fig. 3.10) and vertical (Fig. 3.11) direction. This trend is even more evident when comparing results of the two network geometries. Indeed, configuration C1 guarantees the detection of MSE with  $M_L$  smaller than -3.3 in the entire area of mine galleries (upper left map in Fig. 3.10), while, for C2 configuration, the detection of these  $M_L$  is achieved in a smaller area (upper right map in Fig. 3.10).

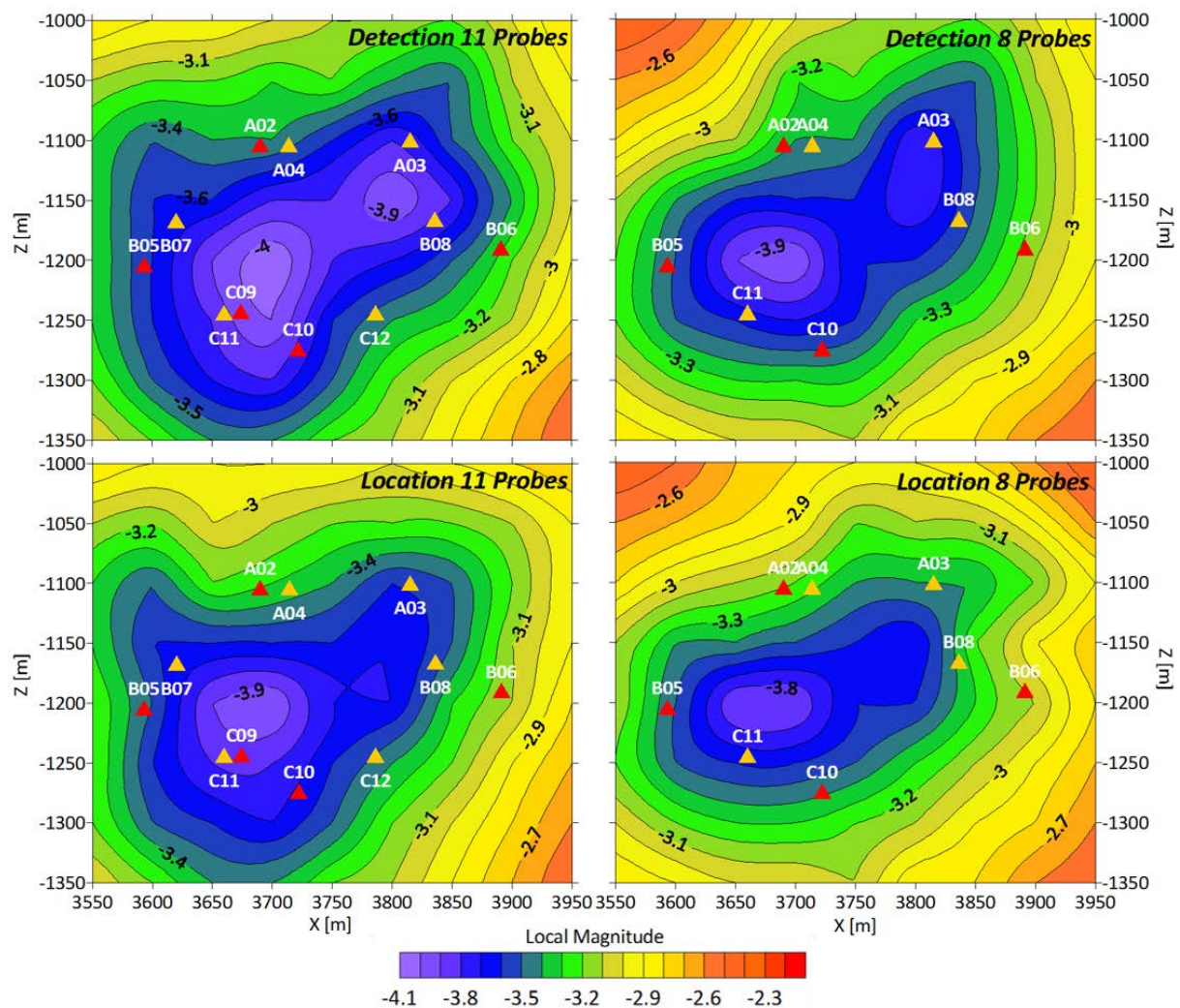


Fig. 3.11 - Vertical profile of minimum magnitude detected (at the top) and located (at the bottom) for C1 (on the left) and C2 (on the right) configurations, for  $y = 550$  m. Color code for seismic station is the same as in Fig. 3.10.

Network capabilities, both in terms of detection and location performances, are strongly asymmetrical. At 1200 m depths, better performances are observed in the NW side of the mine. This is due to the higher density of seismic stations in this area and between -1150 and -1250 m depths (Fig. 3.11), but also to lower noise levels at probe B05, which is located far away from exploited

galleries and mine works. When moving toward the upper levels of the mine, particularly between around -1150 and -1100 m, the observed trend is inverted, with improved detection capabilities in the eastern side of mine galleries, in close proximity to stations A03 and B08 (Fig. 3.11 at the top). This shift of network performances from the west to the east area for increasing elevations is not observed in location capabilities (Fig. 3.11 at the bottom). In this latter case, better performances are achieved at lower levels in the west side of mine galleries and this is due to network geometries and to the lower density of 3C probes in the eastern area.

As expected, better performances are encountered when considering a bigger number of probes, and this is particularly true in the vertical direction where we observe a strong reduction of detection and location capabilities of C2 configuration with respect to C1 configuration. In the horizontal direction both networks present a bed coverage toward the hanging wall of the mine (i.e. toward lower Y values). It appears clearly that the installation of new probes near the hanging wall would have been suitable for improving network capabilities around produced stopes, in particular after the reduction of available probes. Even if some analysis were conducted in order to choose the best position for new probes, the installation was unfortunately not performed. This is a strong constrain of seismic monitoring in active mines, where network geometries can change frequently and unexpectedly and where the design of the arrays needs to take into account not only geophysical needs but also mine production plans and the availability of suitable galleries.

### 3.3.2.2 Evaluation of expected location errors

Prediction analysis of location errors was performed by location simulations, as described in Section 3.3.1. Error values for each VS are determined as the mean distance between its real position and the 100 relocated positions after input data alteration. Fig. 3.12 shows simulation results for C1 and C2 configurations on a plan view and along a vertical profile, for a local magnitude of -2. This value is in agreement with previous results on detection and location capabilities and it represents one of the most common values of  $M_L$  for real MSE located in the monitored area (Fig. 3.9).

C1 configuration presents a circular trend of expected errors in all directions (Fig. 3.12 on the left). The location is more accurate in the central area of the network, between 1100 and 1200 m below ground surface, where mean location errors are smaller than 13 m. The more we depart from the central area of the array, the more location errors become important, reaching values of around 25 m at the edges of the monitored volume. In agreement with detection-location performances results, the footwall of the mine presents more consistent locations than the hanging wall, where mean location errors can be higher than 15 m. This is due to the distribution of Lappberget network that is more deployed in the direction of the footwall, as the hanging wall of the mine was less developed at the time of seismic probes installation (C1 configuration).

C2 configuration shows a significant reduction in location accuracy, with minimum mean errors of around 17 m. Moreover, location errors do not exhibit a circular trend, especially along the Y axes. Indeed, the elimination of 3 probes reduced location accuracy and resulted in a loss of homogeneity in seismic probes distribution that affected the symmetrical trend of location errors. Given these results and considering C2 configuration, it can be concluded that maximum mean location errors in the production area are at least smaller than the distance between two galleries, equals to 20 m, when considering a seismic source of  $M_L = -2$ .

For C1 configuration three additional simulations were computed for  $M_L$  equals to -3, -2.5 and -1, in order to retrieve the distribution of expected location errors for other  $M_L$  values. Results for simulations at  $M_L = -1$  and  $M_L = -2.5$  show a distribution of location errors that not differs significantly from the simulation carried out with events magnitude of -2. Same location errors are observed in the central part of the network, with minimum errors of 10 meters, while at the boundaries the error increases when a local magnitude of -2.5 is considered, reaching values of around 40 meters. This outcome demonstrates that, varying the dimension of microseismic events down to  $M_L = -2.5$ , the accuracy in events location remains similar in the middle of the network, where seismic sources are more constrained; conversely, departing from the central area, smaller events will be located with higher errors than bigger events.

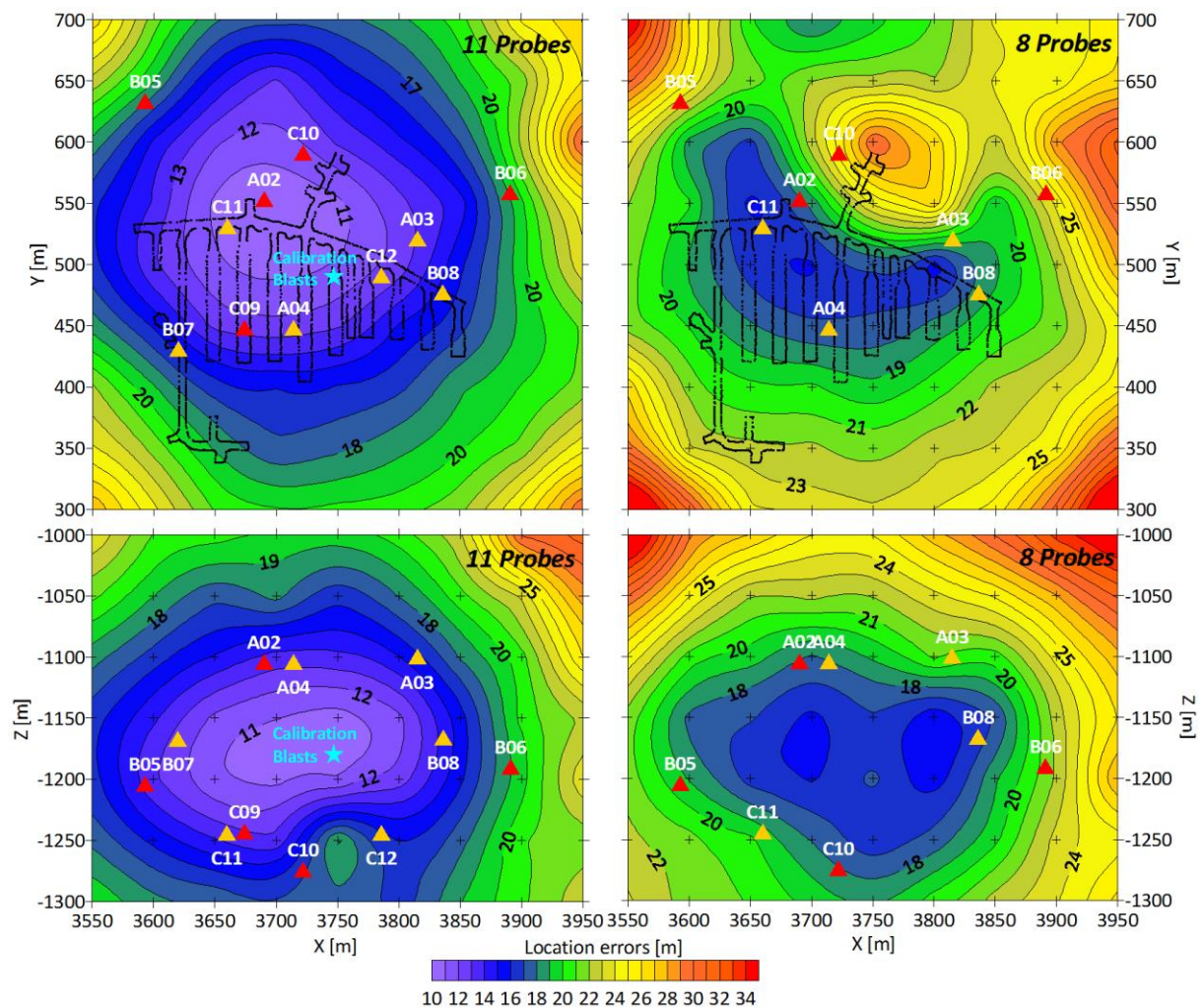


Fig. 3.12 - Distribution of predicted location errors for C1 (on the left) and C2 (on the right) configurations on a plan view at 1200 m depth (at the top) and along the vertical profile for  $y = 500$  m (at the bottom), considering a seismic source of  $M_L = -2$ . Location errors are given in meters. Color code for seismic stations are the same as in Fig. 3.10. The blue star indicates the position of calibration blasts.

When considering simulation at  $M_L = -3$ , location errors increase also in the middle of the array where minimum mean errors are in the order of 15.5 m. At the edges of the monitored area errors can reach values of 100 m. Moreover, with a seismic source of -3 many VS couldn't be relocated due to the reduced number of available observations. This means that, even if the network is capable to locate events down to -3, many of them will be missed in the catalogue, while located ones would be

affected by larger location errors. As reported in Fig. 3.9, real events located by Lappberget network are mainly characterized by local magnitudes ranging between -2.8 and -1.7. According to simulations, in this magnitude range predicted location errors remain smaller of 16 m in the whole exploited area.

For verifying the consistence of location error simulations, three calibration blasts with known locations (Tab. 3.2) were used. Blasts were performed in February 2015 with C1 network configuration. Calibration blast positions have been plotted on the location error maps of C1 configuration (Fig. 3.12 on the left). As reported in Tab. 3.2, calibration blasts have higher estimated magnitudes than that used in the simulation. However, simulations performed for  $M_L = -1$  and  $M_L = -2.5$  demonstrate that in the central area of the network location accuracy remain similar. As a consequence, the projection of calibration blasts on the maps determined for  $M_L = -2$  is representative of their location error since blasts were performed in the central area of the network.

Tab. 3.2 - Calibration blast specifications. Location errors are estimated as the difference between true locations and calculated ones.

Load [kg]	X [m]	Y [m]	Z [m]	Location error [m]	$M_L$
0.5				12	-0.8
1.0	3747	490	-1180	9	-1.1
2.0				12	-1.6

According to simulations, blasts may have location errors between 10 and 11 m, which is in good agreement with real location errors estimated between 9 and 12 m (Tab. 3.2). Calibration blasts have been projected on the horizontal profile at 1200 m depth and on the vertical profile at  $Y = 500$  m, with a difference of around 20 m with respect to their real position. This can explain the small discrepancy between real errors and simulated ones, concluding that location errors estimated by numerical simulations are in good agreement with real location errors.

### 3.4 Considerations about the extension of the analyzed area

Considering results of EMAP methodology on location error estimation, both for C1 and C2 configurations, it seems clear that best performances are achieved in a volume ranging between around -1100 m and -1250 m along Z direction, from 3600 m to 3850 m along X direction and between 400 m and 550 m along Y direction. This approximately correspond to the area around mine galleries in Lappberget orebody, where the majority of MSE are located and mining activities are performed. Analysis of MSA recorded in Lappberget area in the period 2015 ÷ 2016, which will be presented in the next Chapter, will focus on MSE localized in this reduced volume of the monitored area. The exact extension of the analyzed area is as follow:  $3580 \leq X \leq 3900$ ,  $340 \leq Y \leq 580$  and  $-1300 \leq Z \leq -1050$ . This results in a final MSE catalogue of 762 events, against around 800 events if the whole Ineris monitored area is considered for the period February 2015 – December 2016. Fig. 3.13 reports the position of events discarded from further analysis (gray dots in Fig. 3.13) as they are located outside the smaller selected volume of the monitored area. Most of them are encountered at shallower depths, above -1100 m, where production is also ongoing. Few events are as well observed at deeper elevations, below -1260 m, where new galleries started to be developed during 2016. The

choice of focus on events located around mine galleries is motivated by location accuracy, as well as by the interest in correlating the recorded microseismic activity with mine production performed in the area. Large amount of information about mining activities (e.g. mine sequencing, timing of blasts, observed damages) and geology, which are fundamental for a correct interpretation and analysis of the rock mass response to mining, were only available for the block 1250 of Lappberget between levels 1108 and 1257. Moreover, the identification of hazardous areas around mine galleries is one of the basic concerns of rockburst risk assessment, as collapses within mine galleries pose significant risks for mine workers and mine infrastructures.

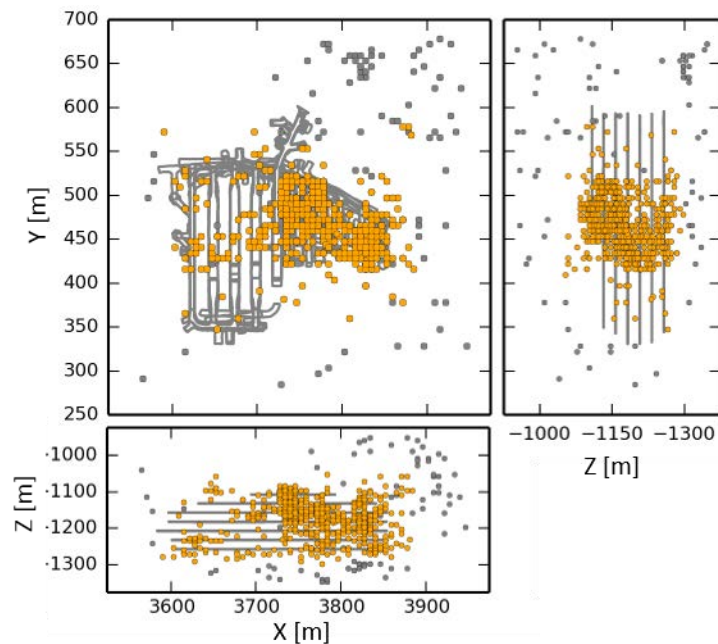


Fig. 3.13 - Events located within the Ineris monitored area (orang and gray dots) and events located within the smaller selected area (orange dots).

Besides MSE occurring within the Ineris monitored area, many events ( $\sim 350$ ) recorded between 2015 and 2016 have been located outside of this area, as reported in Fig. 3.14. Discarding events occurring between around 3500 m and 4000 m along the X axis and from 300 m and 600 m along Y, which are located near zones under exploitation in Lappberget orebody, a strong activity is also observed within the hanging wall and the foot wall of the mine, as well as on its sides. This latter seismicity may be in part due to excavations within other orebodies, Kaspersbo and Dammsjön at the eastern and the western side of Lappberget, respectively (see Fig 2.1 in Chapter 2).

It would be important to study in detail this seismicity observed at larger distances from excavations, in order to characterize events in terms of magnitude and location and to identify eventual spatiotemporal clusters. Indeed, mining-induced stress changes, frequently higher than 1.5 MPa and with peaks which can rise above 40 MPa (see Tab. 2.5 in Chapter 2), are significantly larger than stress changes which naturally trigger earthquakes. Consequently, induced stresses may be capable of reactivating quiescent faults, even at certain distance from excavations, which may result in large seismic events. Even if this analysis is out of the scope of this thesis, it is important to keep in mind this aspect for future researches.



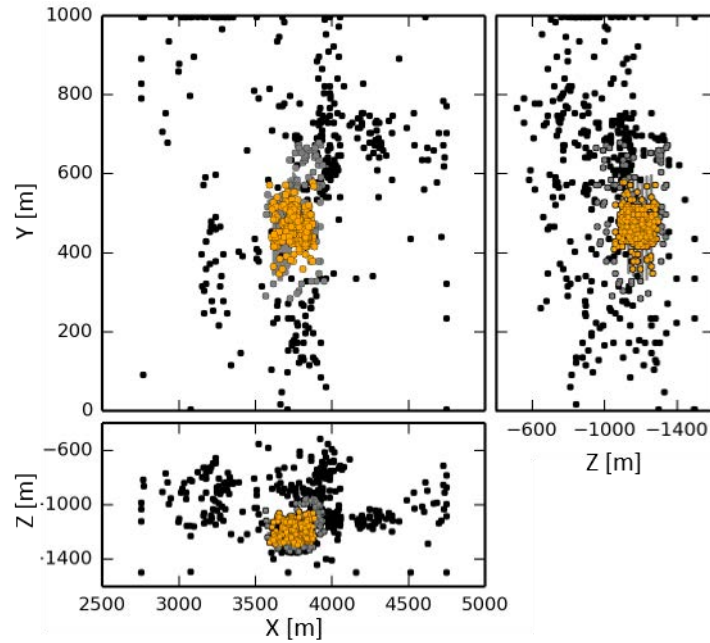


Fig. 3.14 - Events located outside the Ineris monitored area (black dots), events belonging to Ineris monitored area (gray and orange dots) and events within the analyzed area (orange dots). Note that, for a better visualization, X, Y and Z axes are not in the same scale.

### 3.5 Seismic source parameters estimation

As discussed in Section 3.1, the only seismic parameters determined during data treatment of monitoring procedure are the local magnitude and the radiated seismic energy. For better characterize Lappberget microseismic activity, source parameters, such as moment magnitude ( $M_w$ ) corner frequency ( $f_c$ ) and seismic moment ( $M_0$ ) were additionally estimated. Indeed, determining at least two of the aforementioned parameters it is possible to characterize the size of the seismic source with straightforward implications for a better understanding of seismic processes related to mining excavations.

Following the methodology proposed by Kinscher (2015), seismic source parameters have been calculated using a frequency-domain approach, which was implemented in the Ineris software SYTMIS, and considering the S-wave spectra only. Parameters determination consists in minimizing the misfit between observed spectra and Brune's model theoretic spectra (Brune, 1970):

$$u(f) = M_0 \frac{R}{4\pi\rho V_s^3} \frac{1}{1 + (f/f_c)^2} \left[ \exp\left(\frac{-\pi r f}{Q_s V_s}\right) \frac{1}{r} \right] \quad (3.7)$$

where  $u(f)$  is the displacement spectra,  $V_s$  the S-wave velocity,  $f_c$  the corner frequency,  $r$  the source-receiver distance,  $R = 0.6$  the S-wave radiation pattern,  $Q_s$  the quality factor for S-waves and  $M_0$  the seismic moment defined as (Brune, 1970):

$$M_0 = \Omega_s 4\pi\rho r V_s^3 R^{-1} \quad (3.8)$$

with  $\Omega_s$  the low frequency plateau of  $u(f)$ .

To improve the fitting, displacement spectra are converted to moment magnitude spectra (Kinscher, 2015), with observed ( $u_{obs}^{M_w}$ ) and the theoretic ( $u_{synt}^{M_w}$ ) spectra which take the following formulations:

$$u_{obs}^{M_w}(f) = \frac{2}{3} \log \left[ u(f)I(f)^{-1} \frac{4\pi\rho r V_S^3}{R} \right] - 1.6 \quad (3.9)$$

$$u_{synt}^{M_w}(f) = M_w + \frac{2}{3} \left[ \log \left( 1 + \left( \frac{f}{f_c} \right)^2 \right) - \frac{\pi r f}{Q V_S} \log(e) \right] \quad (3.10)$$

where  $I(f)$  is the instrumental response, while  $M_w$  is determined from the seismic moment following Kanamori (1977):

$$M_w = \frac{2}{3} \log_{10} M_0 - 6.1 \quad (3.11)$$

Source parameters ( $f_c$  and  $M_w$ ) are determined by fitting between theoretic and observed spectra. Misfit between spectra is minimized using a grid search technique varying  $M_w$ ,  $f_c$  and the quality factor ( $Q$ ) in a range of predefined values and considering a ponderation function which takes into account the gap between signal and noise spectra. The computation is performed by optimization, considering all recording probes (3C and 1C) simultaneously. Fig. 3.15 reports examples of moment magnitude and corner frequency estimation for four MSE. Finally,  $M_0$  is determined by inversion of equation 3.11.

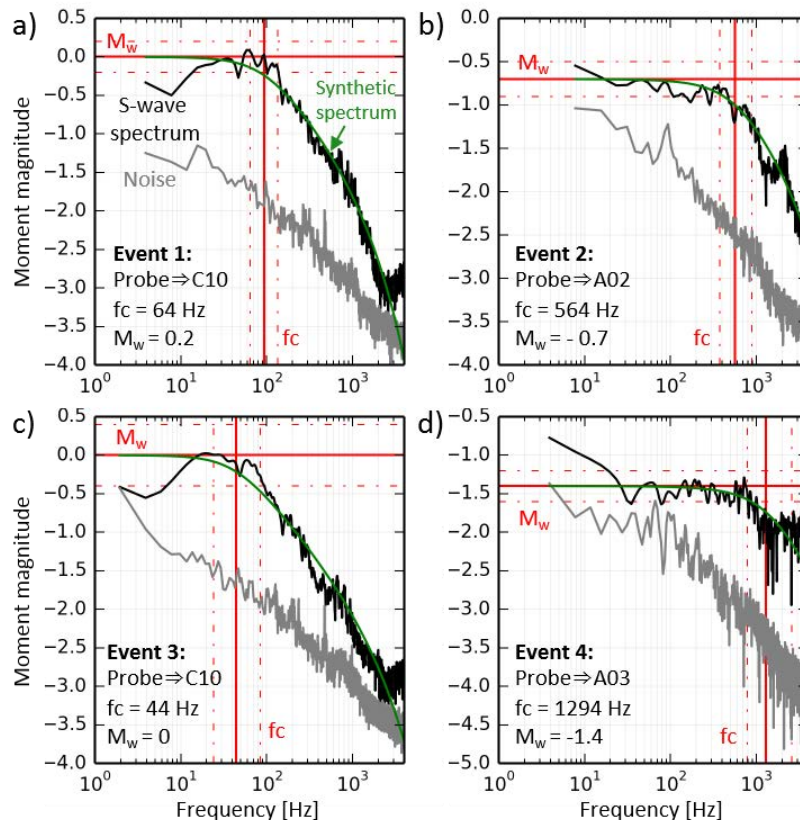


Fig. 3.15 - Examples of corner frequency and moment magnitude estimation. Events considered in this figure are the same shown in Fig. 3.2. Black and gray curves represent the observed moment magnitude spectra for seismic signal and background noise, respectively, while green curve is the fitting of Brune's model synthetic spectra on the data. Red lines indicate moment magnitude and corner frequency estimations, together with their uncertainties (dashed red lines).

Variation ranges of  $M_w$  and  $f_c$ , needed for spectra inversion, have been determined from available recordings, choosing a moment magnitude range between -3 and 1, while the corner frequency range has been set between 14 and 3000 Hz, due to the large frequency content of MSE and considering probes instrumental response. Before spectra calculation, seismic traces have been corrected to remove the effect of the low-pass filter at 1 kHz (see Section 3.1).

In order to constraint the Q-factor, the spectral ratio technique (Feustel, 1998; Pasolini, 2008) was applied to a set of 20 selected events. Q is a measure of the inelastic attenuation, which results in decreasing amplitude and frequency content of seismic signals, and it depends on the attenuation properties of the crossed medium. The higher the Q-factor the lower the wave attenuation (Wilkie and Gibson, 1995). Seismic wave attenuation can be described by the following equation:

$$A(f) = s(f)A_0(f) \frac{1}{r^n} \exp\left(\frac{\pi f r}{Q_{P,S} V_{P,S}}\right) \quad (3.12)$$

where  $s(f)$  is the receiver amplification site effect,  $A_0(f)$  is the signal amplitude at the source,  $n$  is the geometrical spreading,  $r$  the source-receiver distance,  $V_{P,S}$  the seismic wave velocity,  $Q_{P,S}$  the quality factor and  $f$  the frequency. Subscripts P and S refer to P and S-wave, respectively.

To avoid assumption on  $A_0$ , the spectral ratio technique allows formulating equation 3.12 as the ratio between recorded amplitudes at station couples:

$$\log_{10}\left(\frac{A_i(f)}{A_j(f)}\right) = \log_{10}\left(\frac{s_i(f)}{s_j(f)}\right) + n \log_{10}\left(\frac{r_j}{r_i}\right) - \frac{\pi f}{Q_{P,S} V_{P,S}}(r_i - r_j) \quad (3.13)$$

where  $i$  and  $j$  indicate two seismic stations.

Neglecting the site amplification term, the amplitude ratio can be rewritten as the equation of a line in the form:  $\log_{10} A(f) = l + mf$ , where  $l$  and  $m$  are respectively the intercept and the slope of the line, which are expressed as follow:

$$l = n \log_{10}\left(\frac{r_j}{r_i}\right) \quad (3.14)$$

$$m = -\frac{\pi(r_i - r_j)}{Q_{P,S} V_{P,S}} \quad (3.15)$$

Thus, the slope of the line defining the ratio of amplitudes recorded at station couples allows determining the Q-factor:

$$Q_{P,S} = -\frac{\pi(r_i - r_j)}{m V_{P,S}} \quad (3.16)$$

In order to apply the spectral ratio technique and determine an average Q-factor for Lappberget monitored area, a subset of around 20 events has been selected, considering events recorded the 4<sup>th</sup> of June 2016 after a PB. Events were selected in order to have similar characteristics, in particular in terms of magnitude and position (Tab. A.3 and Fig. A.2). As source parameters are computed on S-wave spectra, the spectral ratio technique aimed at determining the Q-factor related to S-wave phase. For this reason, before computing the fast Fourier transform (fft) for amplitude spectra determination, S-wave phase was isolated on seismic traces. For doing so, waveforms have been rotated into the wave propagation direction (L, Q, T), as described in Section 3.1, from which only the S-wave propagation directions (Q and T) were selected. To reduce the effect of coda waves, a

hanning window of 0.075 s length has been applied and centered on the maximum amplitude of the signal (Fig. 3.16a and b). The fft is, then, computed on the traces obtained after hanning window application, separately for Q and T directions. Final spectra are given by the resultant of Q and T spectra, which are smoothed for reducing amplitude fluctuation (Fig. 3.16c).

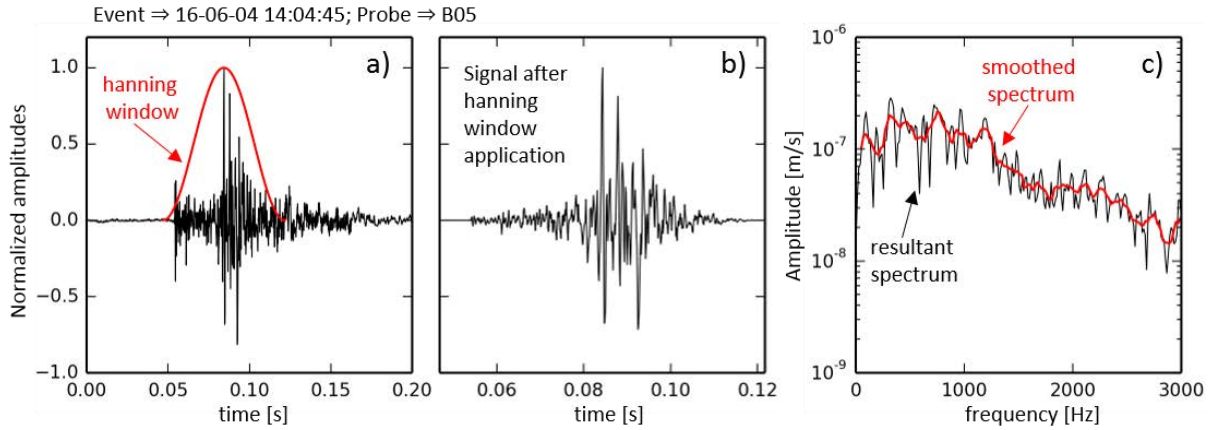


Fig. 3.16 - Example of seismic data processing before computing spectral ratio. (a) Application of the hanning window (in red) on the seismogram. (b) Seismogram obtained after hanning window application. (c) Resultant (black) and smoothed (red) spectrum.

Ratios of amplitude spectra for the selected subset of events were computed considering all the 3C probes which recorded the events. Results are presented in Fig. 3.17. Q-factor is retrieved by regression analysis on the average spectral ratio for all the considered events (in red in Fig. 3.17) and along frequency bands over which the ratio appears stable (area between gray lines in Fig. 3.17).

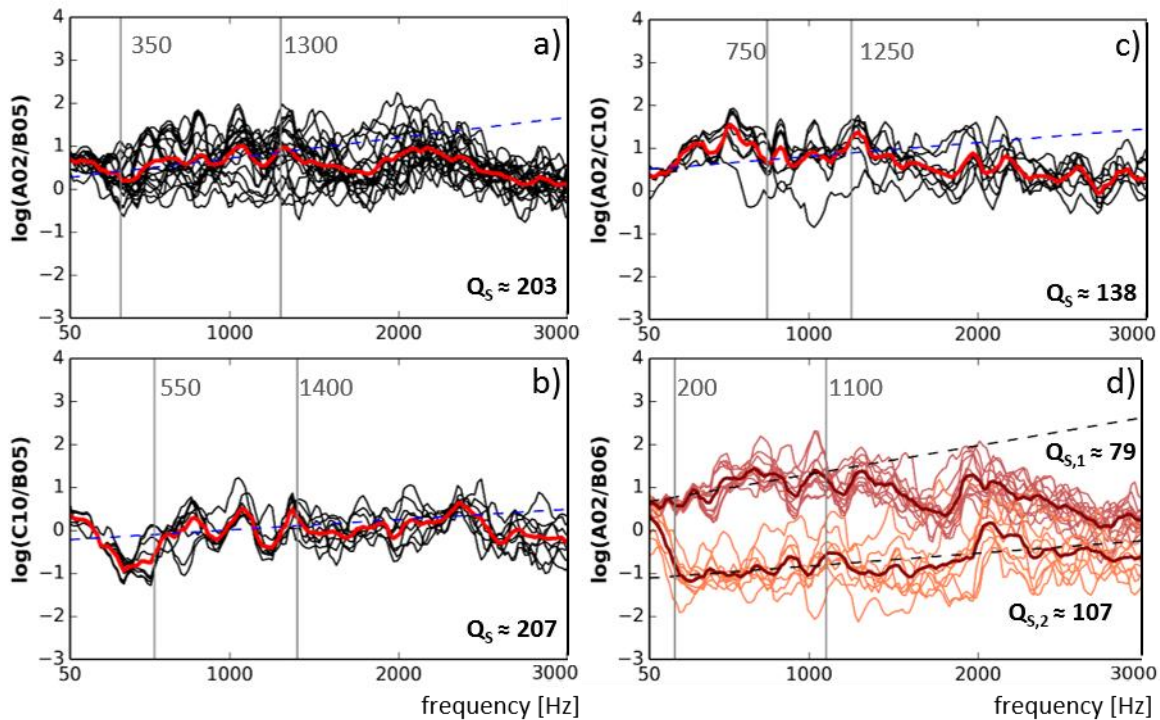


Fig. 3.17 - Spectral ratio for Q-factor determination at different station couples. Thin black and bold red curves represent respectively the spectral ratio per each event and the mean spectral ratio for all the considered events. The same applies to (d) where only colors change. Areas marked by vertical gray lines indicate the

frequency band over which the Q-factor has been determined at each station couple. Q-factors, whose values are reported in the figure, are calculated from the slope of the dashed lines.

As it is visible from Fig. 3.17, spectral ratios are remarkably stable over wide frequency bands, covering more than 750 Hz. The only exception is represented by spectral ratio at probes A02 and C10, where a stable trend can be obtained only for around 500 Hz (Fig. 3.17c). Surprisingly, ratios at probes A02 and B06 (Fig. 3.17d) show diverging trends for groups of events, which do not allow to determine a single average spectrum for the whole considered subset. This result is for itself interesting as it is most probably linked to the presence of a large void along the ray path between sources and receivers. Indeed, selected events were recorded immediately after a PB performed in Stope 13 at level 1182, which resulted in removing almost 4000 m<sup>3</sup> of rock. Events are located around the void and particularly on its eastern and western side (Fig. A.2). Spectral ratios reported in dark red in Fig. 3.17d are all related to the group of events localized on the western side of the excavated stope, with the void interposed between these events and probe B06. Because of this peculiar configuration between events, mine void and recording probes, waveforms experienced a strong attenuation resulting in a low Q-factor, approximately equal to 79. For all the other stations, the estimated Q-factor is never smaller than 100, with a maximum value of 207 at probes C10 and B05. Considerations about voids influence on waveform propagation are important and will need additional analysis in the future. Indeed, this aspect is not further addressed within the work of this thesis. Based on these results, the Q-factor variation range for automatic computation of seismic source parameters was fixed at 50 ÷ 300. This choice is motivated by the observed variation within the estimated Q-factors and for taking into account the probable influence of voids on attenuation characteristics.

Thanks to the described methodology,  $M_w$ ,  $M_0$  and  $f_c$  were determined for the whole catalogue of MSE located within the Ineris monitored area and recorded between February 2015 and December 2016. In addition, the computation of these parameters was implemented within the routine monitoring procedure performed by Ineris at Garpenberg mine, starting from 2017. Results of source parameters will be analyzed and discussed in detail in the next chapter.

### 3.5.1 Considerations on source parameters uncertainties

As discussed in the previous section, the computation of seismic source parameters is dependent on many variables. This can have a strong influence on source parameter uncertainties and, thus, on the estimation accuracy. Stork et al. (2014) provide an exhaustive assessment of source parameters robustness as a function of the methods and the parameters chosen for the computation.

Corner frequency is a quite instable parameter, whose estimation can be problematic and affected by high uncertainties. Indeed,  $f_c$  is strongly influenced by seismic waves attenuation and by the instrumental response of geophones, which plays a primary role in its estimation. Lappberget microseismic dataset is characterized by very broadband frequency signals. As visible in Fig. 3.15a and b, corner frequency and moment magnitude estimations are more accurate for events characterized by corner frequencies between around 100 and 500 Hz. At lower frequencies estimation errors may be higher, as observed for event 3 in Fig. 3.15c, due to limited spectral resolution and instrumental response. In these cases,  $M_w$  may be underestimated, while  $f_c$  is overestimated. At frequencies higher than 1 kHz, signals alteration may be expected due to recording geophones with consequent larger errors in corner frequency estimation. An example of these type of signals is given in Fig. 3.15d.

Seismic moment (equation 3.8) is strongly influenced by errors in events localization and velocity model. As previously discussed, location errors are in the order of 10 m, while errors in the velocity model can be estimated at around 10 m/s. Discarding the influence of rock mass density for which uncertainties are not known, and using a simple propagation error analysis as proposed by Stork et al. (2014), we obtain percentage errors in seismic moment estimates of around 0.6%.

Finally, the number of seismic stations used for parameters estimation is another aspect that influence their accuracy.

Based on this consideration and in order to reduce the number of seismic events affected by high uncertainties, the minimum number of sensors for source parameters determination has been fixed at four, discarding events where less probes were available. Moreover, events whose corner frequency reached the minimum or the maximum value imposed by the grid search technique (14 and 3000 Hz, respectively) have been removed from the catalogue. Even with these precautions, uncertainties on source parameters remain. However, in the following the analysis on seismic source parameters will focus on overall trends, rather than on singular values, which reduces the influence of uncertainties on consequent interpretations.

# Chapter 4

## Rock mass response to mining

Microseismic events (MSE) in underground mines are the result of deformations and fractures induced by excavations, which produce an alteration of the virgin stress field and a consecutive re-adjustment of the local stress state. Seismicity is, thus, a measure of rock deformation and damage caused by human activity. In this context, before the occurrence of major underground damage, it is important to understand the nature of induced MSE with the goal of forecasting seismic active areas.

Aiming at better understand interactions between stress modifications induced by mining and the generation of seismic activity, different factors need to be considered: geological structures and rock properties, initial state of stress and stress modifications, as well as mining method, excavation geometry and blasting practice, are some of the principal aspects affecting seismic activity in mines. This interaction between natural and anthropogenic parameters makes the understanding of mining-induced seismicity more complex, not only because the seismic response to mining will be unique at each mine, but also because it requires multi-parameter approaches.

Based on these considerations, the present chapter analyzes Lappberget microseismic data recorded from the installation of the seismic network, in February 2015, until the end of December 2016, with the aim of understanding how rock masses respond to mining and what are the interactions between stress modifications and local geological properties. During the chosen period, 52 stopes were mined out of which Stope 13 was completely excavated. This gave the unique opportunity of following the rock mass response to the excavation advancement within this stope until its complete production.

The chapter is organized as follow: first, the spatiotemporal and energetic characteristics of the induced seismicity are compared with blast locations and extracted rock mass volumes (Section 4.1). Then, the spatiotemporal behavior of same major seismic sequences and identified spatial cluster are detailed analyzed (Section 4.1.1). Source parameters, determined with the methodology described in the previous chapter, are carefully inspected (Section 4.2) in order to characterize MSE in terms of energy content and source size and for identifying source regions defined by different events dynamics. To investigate the degree of correlations between MSE, the interevent time distribution is analyzed and discussed to understand the mechanisms which drives microseismic activity (Section 4.3). Finally, geotechnical measurements, introduced in Chapter 2, are analyzed together with seismic data and interpreted considering mining method and sequencing (Section 4.4). Obtained results are, then, summarized and discussed in the last section (Section 4.5).

Some of the analysis presented in this chapter are published in: De Santis et al., 2018. Impact of geological heterogeneities on induced-seismicity in a deep sublevel stoping mine. Pure and Applied Geophysics.

### 4.1 Spatiotemporal behavior of microseismic activity and mine blasts

The most important underground operations which can induce microseismic activity (MSA) in Lappberget area are production blasts (PB) and development blasts (DB). It is then interesting to

compare the temporal and spatial occurrence of MSE with blasting activity. At Garpenberg mine blasting procedure is carry out twice per day: during night, around 04:00, and in the afternoon, around 16:00, considering the Swedish local time (UTC+1). As the seismic acquisition system works in coordinated universal time (UTC), blast-related signals are recorded around 02:00 and 14:00 during summer time and at 03:00 and 15:00 during winter time. Fig. 4.1 shows the hourly distribution of MSE and mine blasts for the two-years period analyzed, with the time expressed in UTC. Of the total 52 PB occurred within the analyzed period, only 5 were done at night time (during summer time), while the remaining were performed in the afternoon. During the afternoon blasting period, production is particularly active in summer time, with the occurrence of 35 PB, against 12 PB in winter time, and almost the double of DB.

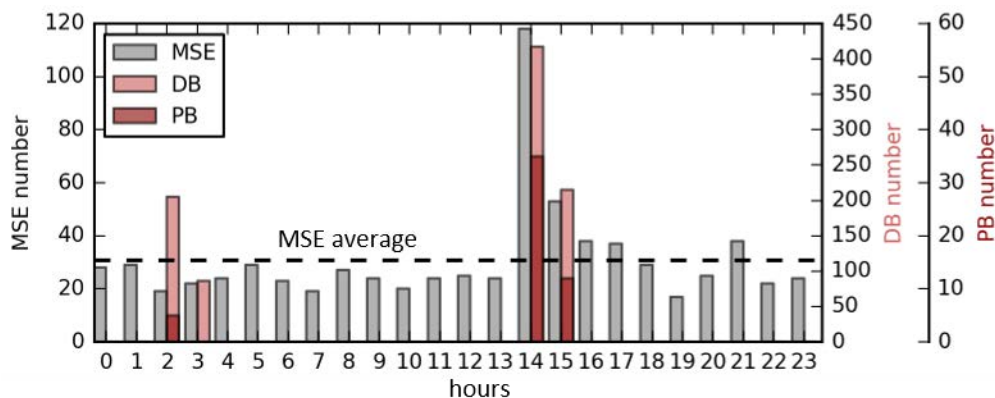


Fig. 4.1 - Number of microseismic events and mine blasts per hour over the period 2015-2016. Dashed line indicates the average number of microseismic events per hour. The hourly occurrence of PB and DB is shown by red and pink bars, respectively, while microseismic events are reported as gray bars. Time is expressed in UTC.

Some interesting features can be observed in the hourly distribution of MSE. The strongest seismic activity occurs in coincidence with the afternoon blasting period and particularly in summer time, when MSE are around three times higher than the hourly average. On the contrary, seismicity rate remains at low levels during night, when less explosions are performed of which only few PB. Outside of the afternoon blasting period, we do not observe important rises of seismic activity, suggesting that mine blasts, and particularly PB, have a key role on seismicity rate, inducing deformations and accelerating cracks propagation in the surrounding rock masses. The hourly chart also suggests that PB have a stronger impact than DB in generating seismic activity. This behavior can be explained considering the amount of extracted rock mass. Indeed, PB, whose explosive load can be 10 times bigger than DB, result in a much larger amount of extracted rock mass per round and, therefore, in higher deformations and stress modifications, which intensify rock mass damages.

The temporal distribution of MSA and mine blasts (Fig. 4.2) confirms that MSE are more related to PB (dots in Fig. 4.2) than to DB (crosses in Fig. 4.2). Indeed, periods of intense development are not followed by rise in seismicity rate, while sudden increases of MSE are observed immediately after some PB. Stress perturbations due to DB appear to be weak or not strong enough to induce significant seismic activity. However, seismicity induced by PB is extremely variable from one blast to another and this seems to be not proportional to the volume of extracted rock mass. This trend is particularly evident when plotting the cumulative number of MSE only with those PB after which important increases of seismicity rate are observed (Fig. 4.3a). Indeed, exploited volumes for the



selected blasts vary in all possible ranges and the intensity of the induced seismicity is not proportional to the relative amount of extracted rock mass. No correlation is found neither when considering PB charge. This suggests that, if PB have a primary role in MSA generation, seismicity rate is not controlled by the volume of excavated stopes. When looking at the position of the selected PB (Fig. 4.3b), it is interesting to observe that these are all related to production in Stope 13 and particularly to the last stages of its exploitation. The induced seismic activity is, thus, more dependent on blast position, i.e. on mine sequence, than on the volume of extracted rock mass.

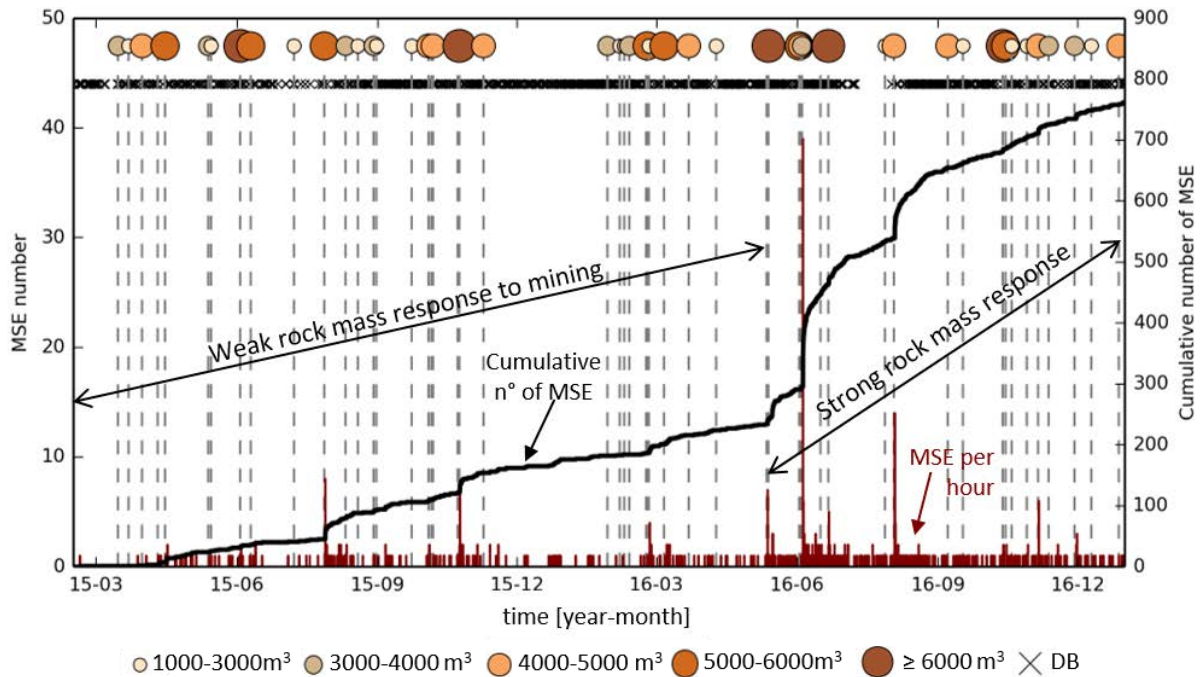


Fig. 4.2 - Temporal distribution of microseismic activity and mine blasts between February 2015 and December 2016. The red line represents the number of MSE per hour, while their cumulative number is reported by the black curve. PB (dots) and DB (crosses) are reported on the top of the chart. PB are colored and sized in function of the amount of extracted rock mass as reported in the legend. The vertical dashed lines indicate the time of occurrence of PB.

The observed poor correlation between MSA and extracted rock mass volumes is confirmed by Fig. 4.4, where the monthly cumulative seismic energy is compared with the monthly cumulative volume of extracted rock mass. The correlation between mining induced seismicity and the volume of extracted rock mass was firstly observed by McGarr (1976), who showed the proportionality between the cumulative seismic moment released at the time of excavation and the induced volume change due to tabular stopes excavation in a deep gold mine in South Africa. Kijko (1986) demonstrated that seismic moment can be replaced by seismic energy which will then be proportional to the volume of extracted rock mass.

No evident correlation can be found when plotting together seismic energy of Lappberget microseismic dataset and excavated stope volumes during the two-years period analyzed (Fig. 4.4). This suggests that stresses induced by mining are not solely responsible for the induced seismicity. A similar trend was observed for seismic activity of a German coal mine by Fritschen (2010), who concluded that seismicity was influenced by geological structures.

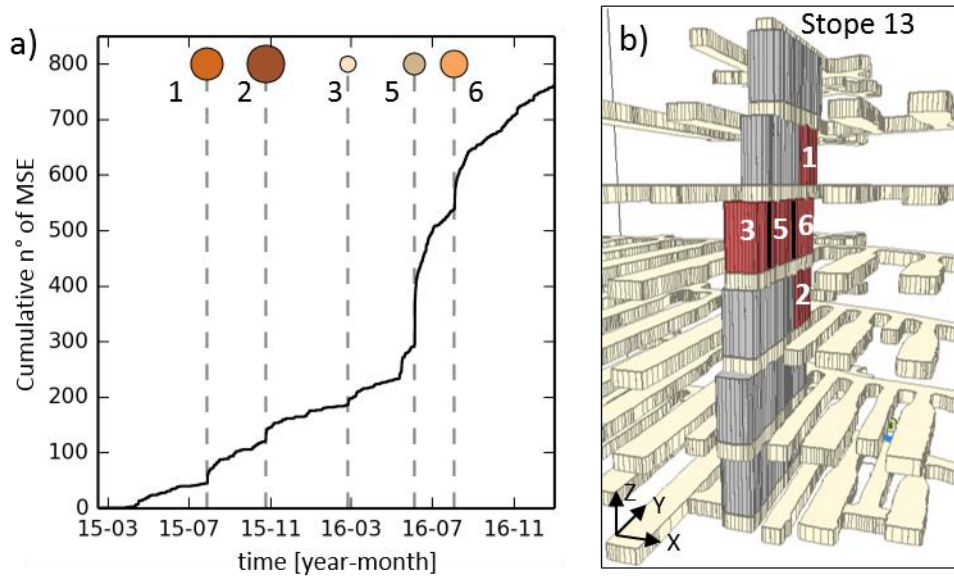


Fig. 4.3 - Characteristics of some PB which induced important increases of MSA. (a) Same chart as in Fig. 4.2 with only significant PB. These latter are reported in function of the volume of extracted rock mass (refer to Fig. 4.2 for the legend). (b) Position of mined volumes in Stope 13 which induced accelerations of seismicity rate. Stopes are numbered as in (a). Gray stopes indicate rock mass volumes already excavated and backfilled with paste.

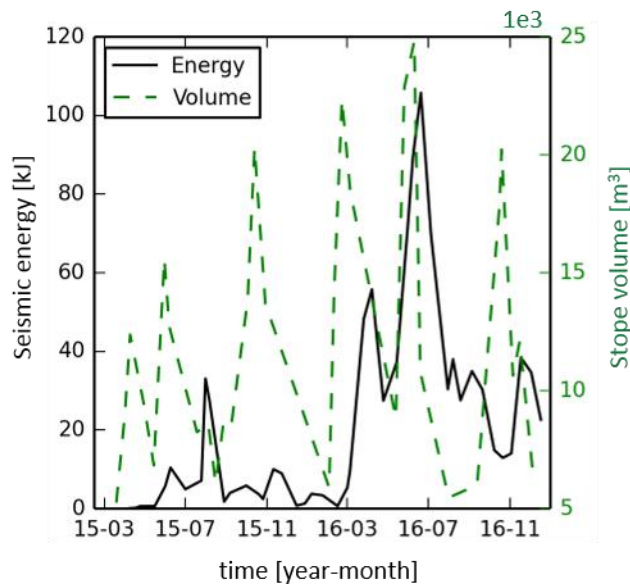


Fig. 4.4 - Seismic energy and extracted rock mass volume. Energy (in black) and extracted stope volume (in green) are reported as cumulative values per month, considering all the events recorded from 2015 to 2016, as well as all the stopes produced in the same period.

The temporal distribution of MSE shown in Fig. 4.2 highlights another interesting feature. Indeed, two distinct behaviors in the rock mass response to mining are visible. During 2015 and until May 2016, we observe a weak response: periods of intense production are not followed by significant increase of MSE and the cumulative curve exhibits, generally, a constant slope. Except for some cases, most of the stopes were excavated without generating seismic activity or inducing small perturbations that resulted in few seismic events. From the 10<sup>th</sup> of November 2015 until the 28<sup>th</sup> of January 2016, production was interrupted and consequently MSE rate rapidly decreased, despite the

high rate of DB. When production restarted, seismic activity was not significantly intensified, remaining at low levels until May 2016. On the other hand, since May, the slope of MSE cumulative curve presents a stepwise trend that demonstrates fast changes in seismicity rate. Consequently, the rock mass response to mining appears here to be stronger, suggesting bigger stress changes that result in the acceleration of crack generation and propagation.

Seismicity rate is strongly influenced by seismic network sensitivity. Indeed, the addition of new recording probes may result in misleading increases of MSE, which are linked with network performances, instead of being related to a real rock mass response change. As already discussed in the previous chapter, Lappberget network configuration has significantly changed during time, with a gradual reduction of seismic probes. Therefore, if the observed variation in seismicity rate is a result of network sensitivity, one would have expected a progressive reduction of seismic events number, rather than a rise. It can, thus, be concluded that the seismicity rate change observed in Fig. 4.2 is not an artifact due to network sensitivity variation but a real change in rock mass response to mining.

Space distribution of MSE in the two-years period analyzed is particularly interesting. Indeed, two clusters are clearly distinguishable (Fig. 4.5a and b). One cluster is observed in the central area of the mine, between stopes 11 and 15, while the second is deployed in the eastern side of the mine, between stopes 5 and 7. These clusters will be referred to as Central Cluster (CC) and Right Cluster (RC), respectively. Events located outside these two clusters represents only around the 21% (159 events) of the whole analyzed dataset. Different trends within CC and RC are observed between periods of weak and strong rock mass response to mining. In the first period (Fig. 4.5a), CC presents high seismicity rate, with events homogeneously distributed along the entire height of the monitored area, while RC is not intensely seismically active, with around 30 events located in this area. On the contrary, during the period of strong rock mass response to mining (Fig. 4.5b), seismic activity within CC is mostly concentrated in the upper levels of the mine and RC presents an intense seismic activity, which covers the entire height of the study area.

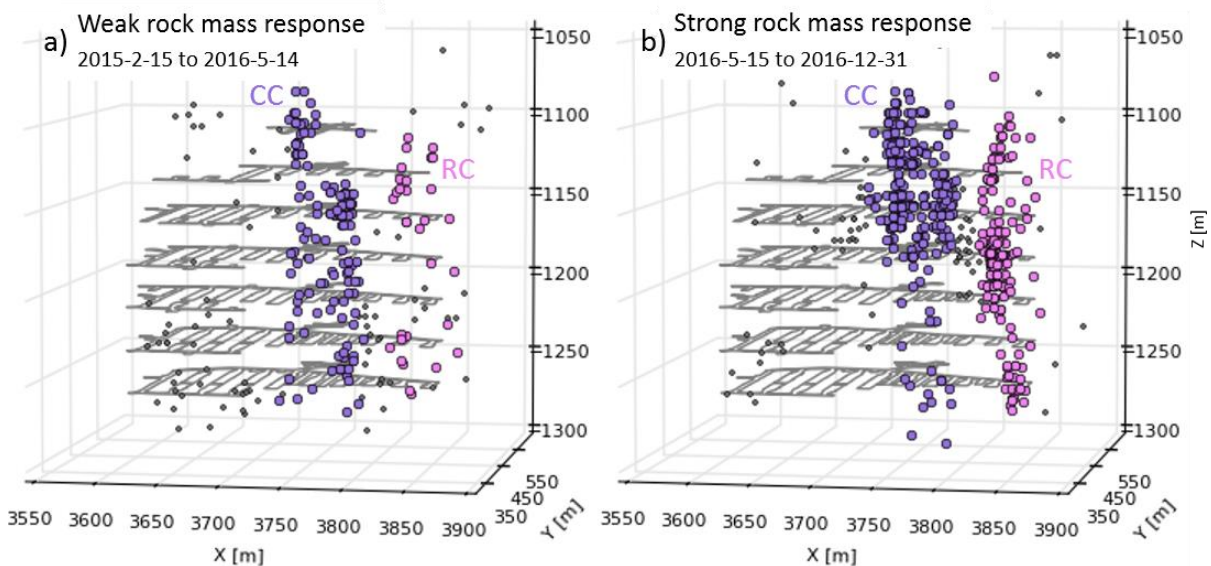


Fig. 4.5 - Space distribution of MSE during the periods of weak (a) and strong (b) rock mass response to mining. Two spatial clusters are observed: Central Cluster (CC, in violet) and Right Cluster (RC, in pink). Gray dots represent events located outside of these two clusters.

In order to analyze possible spatial correlations between MSE and excavated stopes, Fig. 4.6a and b report the number of MSE and the cumulative volume of extracted stopes calculated over sliding windows along X (Fig. 4.6a) and Z (Fig. 4.6b) directions. One can observe a good correlation between events number and exploited volumes in the CC area, while, the strong MSA observed within the RC cannot be explained by the small production performed in the same region. In addition, in the western side of the mine high production rates appears to be not followed by an intense MSA. Along depth (Fig. 4.6b) MSE are mainly concentrated in the upper part of the investigated area, while most of the production is performed at lower levels (below -1180 m). Taking these observations together, it can be concluded that no clear relations are observed between blast positions and MSE localization, except for CC along the horizontal X direction.

These preliminary observations on the spatiotemporal behavior of MSE and mine blasts highlight that seismicity in Lappberget area may be not solely related to the immediate stress change induced by blasting and that additional features may probably influence its patterns.

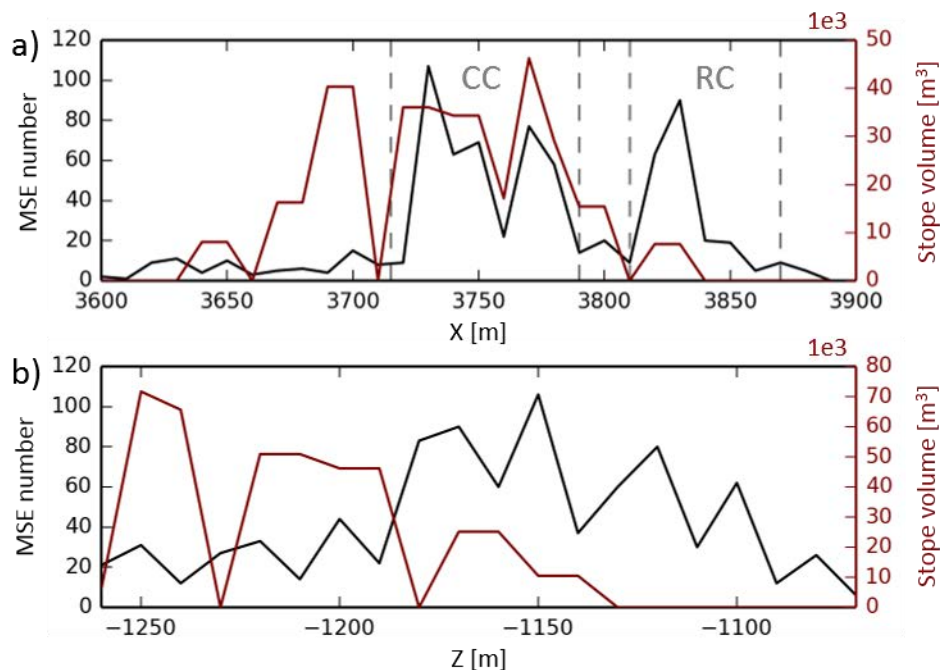


Fig. 4.6 - Comparison between microseismic events number and extracted stope volumes along the horizontal X direction (a) and along depth (b).

#### 4.1.1 Seismic sequences and clusters

During the two-years period analyzed, we observe 6 main seismic sequences characterized by sudden increases in seismicity rate of different intensity (Fig. 4.7). As already underlined in the previous section, these sequences are all linked with production in Stope 13, except the number 4 which is not directly induced by blasting. Characteristics of the sequences together with blasts specifications are reported in Tab. 4.1, while the reader is referred to Fig. 4.3b for stope positions.

Fig. 4.7 shows a magnitude-time history chart (Hudyma and Potvin, 2010), in which events belonging to CC and RC are showed separately. As visible from this chart, the first three microseismic sequences occurred during the period of weak rock mass response to mining (from 2015-02-14 to 2016-05-14), inducing seismic rate increases of different intensity within the CC. In the same period, the

cumulative curve of RC events shows a very slow growth. Starting from May 2016 and, thus, during the period of strong response to mining, MSE within CC sharply increase due to the occurrence of sequences 4, 5 and 6, while the effect in RC appears delayed of few days, as seismic activity begins rising from Sequence 5 on the 4<sup>th</sup> of June 2016. Moreover, it is interesting to underline that the period of strong response to mining starts with a microseismic sequence not directly related to a blast (Sequence 4 in Fig. 4.7).

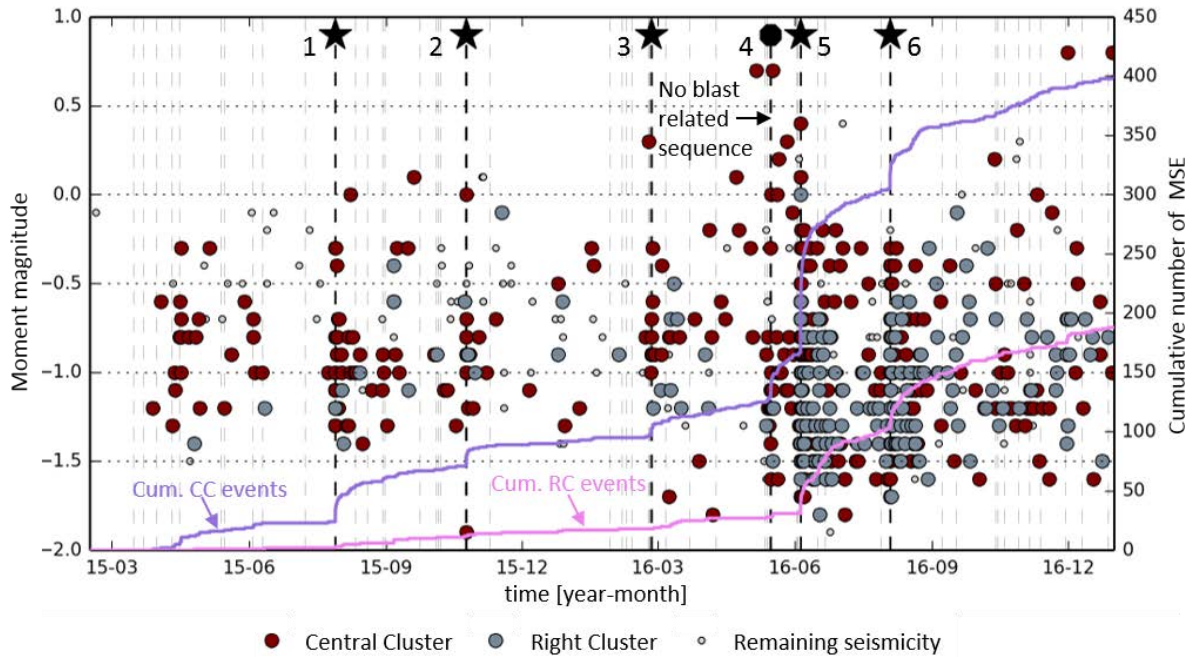


Fig. 4.7 - Magnitude-time history chart. Microseismic events are reported in function of their moment magnitude (on the left y axes) and colored according to their belonging to RC (red), CC (dark gray) or to remaining seismicity (light gray). Stars indicate PB after which blast-related seismic sequences are observed. While, all the other PB are reported by dashed light-gray lines. Black dot marks the beginning of a non-blast related sequence. Sequences are numbered as in Fig. 4.3.

Tab. 4.1 - Details of production blasts and microseismic sequences. Blasts and sequences are numbered as in Fig. 4.7. Depth position of the blasts refers to the lower level of the exploited stope.

Sequence n°	Production blasts					Microseismic sequences	
	Data	Z [m]	Name	Extracted rock volume [m <sup>3</sup> ]	Blast charge [kg]	n° of events	Duration
1	15-07-28	1157	Stope 13 #3	5330	6669	35	13 days
2	15-10-24	1207	Stope 13 #3	6702	5473	16	23 hours
3	16-02-25	1182	Stope 13 #1	2758	2963	10	34 hours
4	16-05-15		-			34	15 days
5	16-06-04	1182	Stope 13 #2	3978	6597	210	2 months
6	16-08-03	1182	Stope 13 #3	4346	4527	121	2 months

Moment magnitude within the analyzed dataset varies in the range -2 and 0.8, with median values of around -1. Events characterized by  $M_w \geq 0$  constitute only a small portion of the whole dataset and are mainly encountered within the CC, except for one event ( $M_w = 0$ ) recorded in the RC during

Sequence 5. Even in the context of mining-induced seismicity, the observed magnitude values are rather small if compared with other deep hard-rock mines. Gibowicz (1995) collected a dataset of more than 1500 mining-induced earthquakes from Canadian, South African, Polish and German underground mines, reporting wide moment magnitude ranges varying from -3.6 up to 4.1. Lizurek et al. (2015) account for a  $M_w = 3.7 (\pm 0.2)$  event occurred in 2013 in the Rudna Copper Mine (Poland), while Nuannin et al. (2005) studied a large dataset of MSE induced by mining in the Zingruvan zinc mine (Sweden), reporting moment magnitudes up to 2.6. These considerations indicate a low potential for large rockbursts occurrence within the study area and this agrees with observations made on site, where only small damages are observed. However, it is important to study and understand the rock mass behavior at this stage, when large MSE are not observed, in order to prevent from the occurrence of strongest events in the future.

Fig. 4.8 reports spatiotemporal characteristics of Sequence 1, 2 and 3 ( $S_1$ ,  $S_2$ ,  $S_3$ ), with time spans variable from 1 day up to 14 days. For the first two sequences, events are mostly clustered close to the excavated stopes, particularly at the openings back and within the secondary stopes on the sides, except for few outliers that depart from this trend.  $S_1$  shows, as well, a small cluster of events mainly located in the upper level of the mine. On the contrary, MSE within  $S_3$  appears more widespread in space, even if two clusters can be observed in the immediate vicinity of the blast and in the upper level of the mine. However, the low MSE number related to this sequence limits spatiotemporal analysis and interpretations.

Spatial migration of MSE during time is not observed for any of the analyzed sequence, indicating that source regions are all triggered immediately after the blast, remaining active for the entire duration of the sequence. During  $S_1$  and  $S_2$  two events with  $M_w = 0$  are recorded, both localized near the exploited areas, where the main MSA is observed (Fig. 4.8a and c). Surprisingly, the biggest event within  $S_1$  occurs several days after the blast, determining a significant increase in the cumulative seismic moment (Fig. 4.8b), while for  $S_2$  it occurs within few minutes following production.

From the temporal point of view, events within  $S_1$  increase fast immediately after the blast for then gradually decrease (Fig. 4.8b), as similar to an Omori decaying law (Utsu et al., 1995). On the contrary,  $S_2$  and  $S_3$  show delayed reactivations of seismicity rate which are not driven by new blasts, neither by higher magnitude events like in a classical main shock-aftershock sequence. Moreover, the temporal variation of the cumulative seismic moment shows interesting features. Indeed, seismic moment for  $S_2$  is almost totally released at the beginning of the sequence, showing a constant rate in the hours immediately following the blast which is only poorly intensified with the delayed reactivation 20 hours later. On the contrary, for  $S_3$ ,  $M_0$  is mostly released during the reactivation of the sequence around 1 day after the occurrence of the blast.

The non-blast related sequence (Sequence 4 -  $S_4$ ), which took place at the beginning of the strong rock mass response period, shows interesting spatiotemporal behaviors. Indeed, events clustered in the upper level and in the central area of the mine, between stopes 13 and 15 at levels 1132-1157 (Fig. 4.9a). The sequence shows delayed reactivation four days after the beginning, with a partial migration of MSE toward the upper level area (Fig. 4.9a and b). Three major events, with moment magnitudes up to 0.7, are related to this sequence, which occur almost randomly in time but clustered in space (Fig. 4.9a and b). In contrast with the previous analyzed sequences, we do not

observe an instantaneous increase of MSE at the beginning of  $S_4$ , with the seismicity rate that grows slowly in time (Fig. 4.9b).

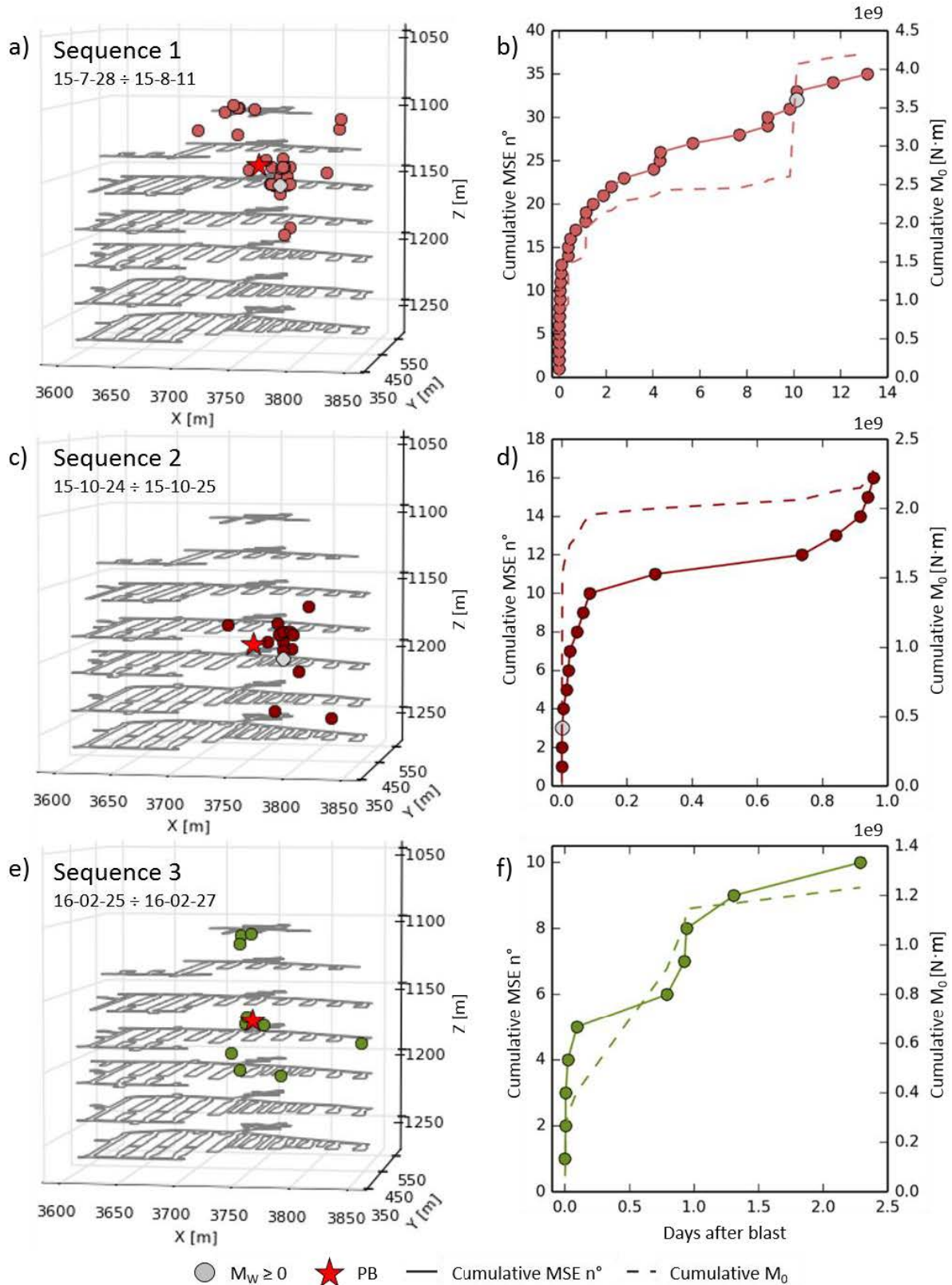


Fig. 4.8 - Space (left panel) and time (right panel) distribution of seismic sequences 1 (a, b), 2 (c, d) and 3 (e, f). Events with  $M_w \geq 0$  are reported as gray dots in time (right panel) and space (left panel), while PB position per each sequence is indicated by red stars. Charts of the right panel reports the cumulative event number (on the

left axis), as well as the cumulative seismic moment (on the right axis), during the temporal duration of each sequence.

When  $S_4$  occurred, no PB were performed, while DB were more deployed in the western area of the mine. Consequently, this microseismic sequence is not directly triggered by a blast but it cannot be neither considered as an aftershock-like sequence, as largest events do not appear first.

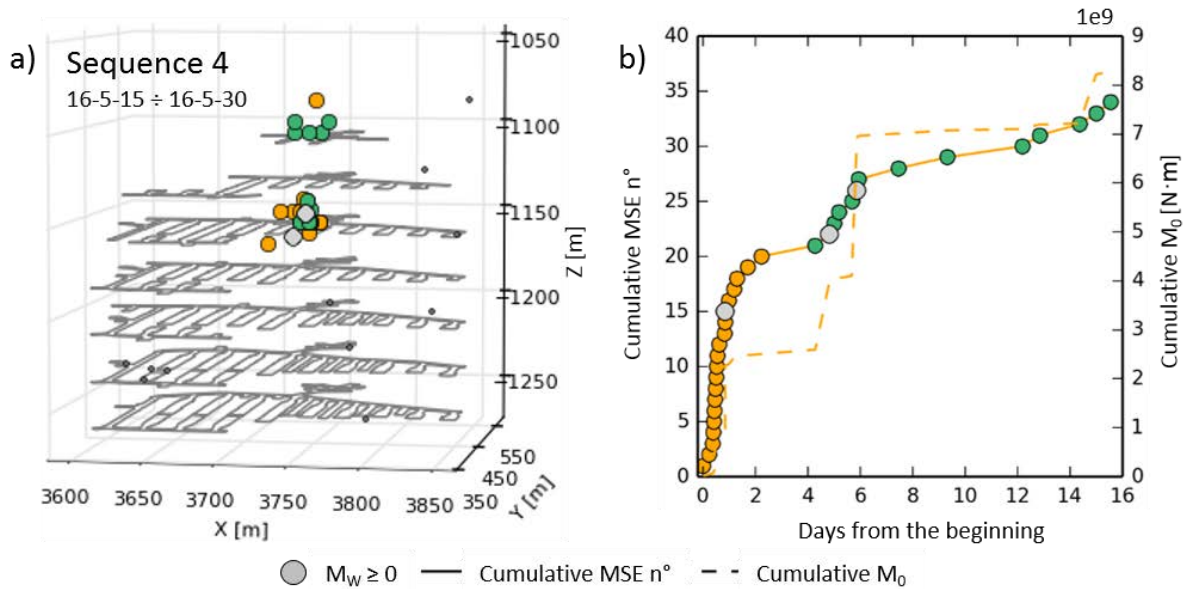


Fig. 4.9 - Space (a) and time (b) distribution of Sequence 4. MSE within the sequence have been divided into two groups according to their time of occurrence. Yellow dots indicate events from the beginning of the sequence until the 17<sup>th</sup> of May, while green dots refer to events occurred during the reactivation of the sequence on the 19<sup>th</sup> of May. Small black dots in (a) represents some events occurred during the time span of  $S_4$  which are although not considered belonging to the sequence.

The last two seismic sequences are the most important in terms of duration and number of events, showing also interesting features in the spatial pattern with a strong delineation of CC and RC areas. Indeed, blast 5 and 6 had the potential to remotely trigger seismicity in the RC, in addition to the induced stress change around the exploited stopes which allowed cracks propagation in the CC (Fig. 4.10a and c). Seismic activity recorded 12 days after the occurrence of Sequence 5 ( $S_5$ ) and before the beginning of Sequence 6 ( $S_6$ ) continued to be observed in the same seismically active areas of CC and RC (Fig. 4.10b). Same trend is encountered for MSE recorded from the 15<sup>th</sup> of August till October 2016 (Fig. 4.10d), when we also observe an intensification of MSA in the lower levels of the RC area. Except for few events, the main activity reported in Fig. 4.10b and d does not seem directly related with the new PB performed in the same time intervals. Therefore, this activity can still be considered belonging to  $S_5$  and  $S_6$ . Fig. 4.10e and f report the spatial distribution of MSE within  $S_5$  and  $S_6$ , respectively, considering the whole temporal duration of these sequences.

Temporal characteristics of MSE within  $S_5$  and  $S_6$  are reported in Fig. 4.11a and b. CC events within  $S_5$  increase extremely fast in the first hours and the seismicity rate remains at important level until two months after the production. Similarly, MSE start to be observed in the RC immediately after the blast, even if they grow slowly and, at the end of the sequence, they are almost two time smaller in number than in the CC. Bigger magnitude events are encountered within few seconds after the blast, both, in CC and RC.



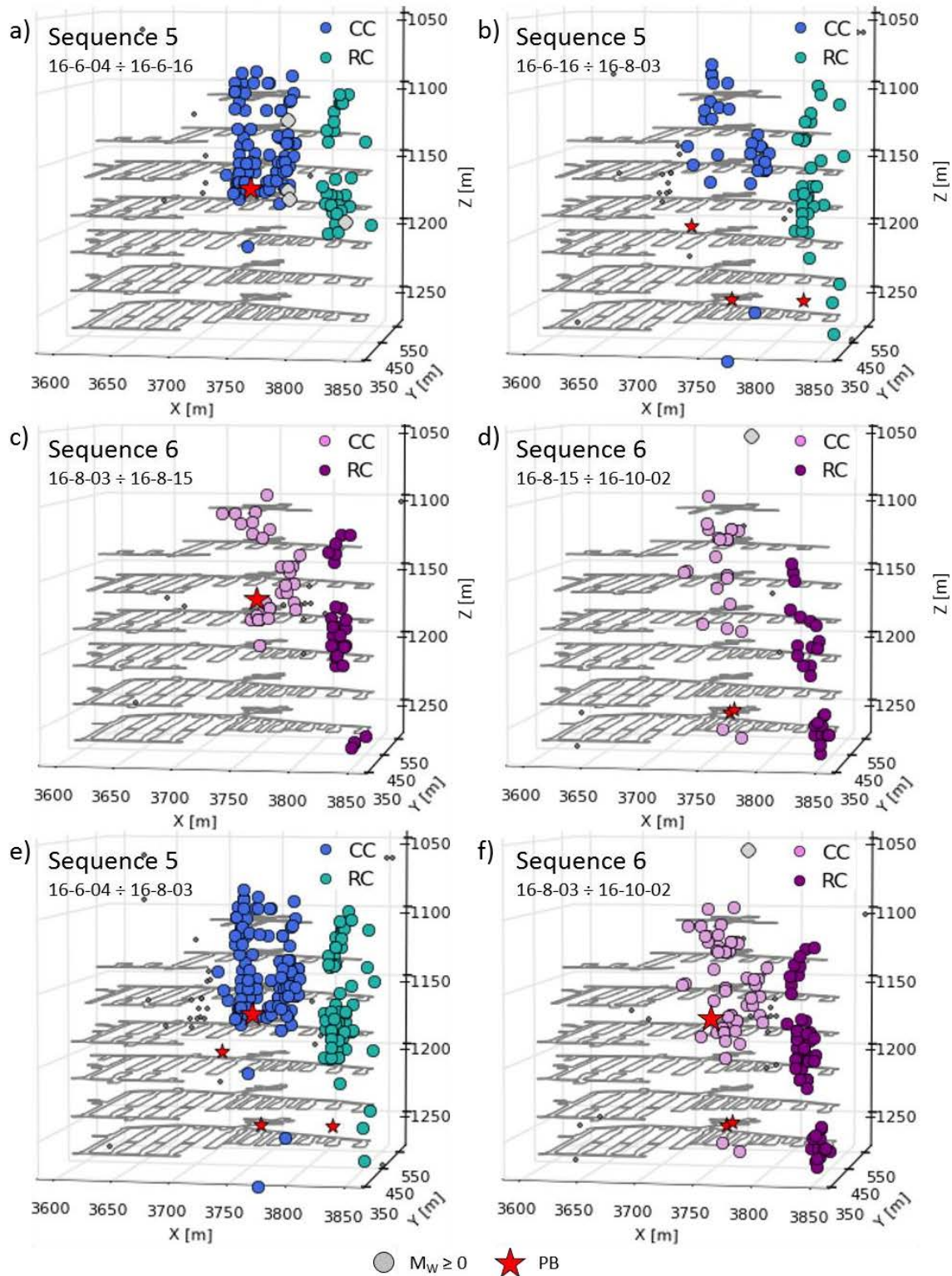


Fig. 4.10 - Space distribution of MSE within Sequence 5 (a, b, e) and Sequence 6 (c, d, f). MSE within the sequences are color coded according to their belonging to CC or RC. Each sequence is shown for two different time periods: during the first 12 days from the blast (a, c) and in the following one and half month (b, d). In addition, the two sequences are also shown for the whole analyzed period of two months (e, f). Large stars indicate the position of PB which induced the sequences, while smaller stars represent the position of other PB performed in the considered periods. Small black dots refer to MSE not belonging to  $S_5$  or  $S_6$ , which occurred during the analyzed intervals of time.

Seismic moment of CC events is almost completely released in the first 10 days of the sequence showing, then, a gradual growth whose trend is strongly similar to that of the cumulative MSE number. On the contrary,  $M_0$  of RC events present an immediate increase after the blast, followed by a steady trend until the end of the sequence. Cumulative seismic moment presents an overall uniform trend for both CC and RC, suggesting that MSE sizes are similar within each cluster. Events within CC are significantly larger than that of RC, as at the end of the sequence the total released moment is about 6 times higher in the CC.

We observe a delayed reactivation of  $S_5$  within RC around 5 days after its beginning (Fig. 4.11a). At the same time, we observe two sub-clusters within the RC in  $S_5$ , one shallower between levels 1107 and 1132 and a deeper one between levels 1157 and 1207 (Fig. 4.10e). However, no specific spatiotemporal patterns which may explain the delayed reactivation of  $S_5$  have been identified. Indeed, MSE are simultaneously nucleated within both sub-clusters, which remain active throughout the whole duration of  $S_5$ . This delayed reactivation is almost not visible when considering the whole seismic activity of  $S_5$ , adding the contributes from RC and CC.

$S_6$  shows a more complex response in CC, with seismicity rate that starts decreasing around 5 days after the blast for then increasing again 14 days later (Fig. 4.11b) without the occurrence of any bigger event. In this case it is probably more correct to speak about delayed acceleration of the sequence instead of delayed reactivation, as it has been done for the previously analyzed cases. Indeed, the observed delayed reactivations occurred just after a period with no seismic activity, while the delayed acceleration of  $S_6$  does not follow a similar trend. After this new acceleration, seismicity rate keeps rising for the following ten days for then dropping dramatically until the end of the sequence. MSE within RC are nucleated simultaneously with CC events, even if they grow slowly at the beginning of the sequence. However, seismicity rate of RC appears more constant during time than in the CC, remaining at important level up to the end of the sequence. Contrary to what has been observed for  $S_5$ , the amount of MSE within CC and RC is around the same in the case of  $S_6$ .

Cumulative seismic moment of CC and RC presents a stepwise trend which indicates the occurrence of events with variable size throughout the sequence, even though any event with  $M_w \geq 0$  is observed. As noticed for  $S_5$ , CC events are bigger in size than in the RC, even if this difference is not as strong as for  $S_5$ .

Temporal characteristics of  $S_5$  and  $S_6$  suggests that MSE are simultaneously nucleated within CC and RC immediately after the blasts, highlighting that seismic activity within RC is remotely triggered by PB occurring in Stope 13. Moreover, spatiotemporal analysis of the 6 seismic sequences enable characterizing the dual behavior observed in seismicity rate during time and with respect to PB. In periods of weak rock mass response to mining ( $S_1$ ,  $S_2$  and  $S_3$ ), seismic activity has a temporally short behavior with MSE mostly clustered in the vicinity of the excavations. Cracks start propagating just after the blast and around the excavated volume, as an immediate response to local stress change induced by blasting. On the other hand, periods of strong rock mass response to mining ( $S_4$ ,  $S_5$  and  $S_6$ ) are characterized by a seismic activity that is long lasting over time and widespread in space. Stress changes induced by blasting have the potential to remotely trigger seismicity in the eastern area of the mine, with a long process of stress field readjustment. As a result, RC, which was almost not seismically active during the first period (February 2015-June 2016), even though few stopes were produced in the immediate vicinity, become a source of seismicity only when events are triggered there (in June 2016) by remote blasts in Stope 13. This means that seismic activity become less

predictable in this second phase of the exploitation, when intense seismic activity starts to be induced at more than 70 m from production area.

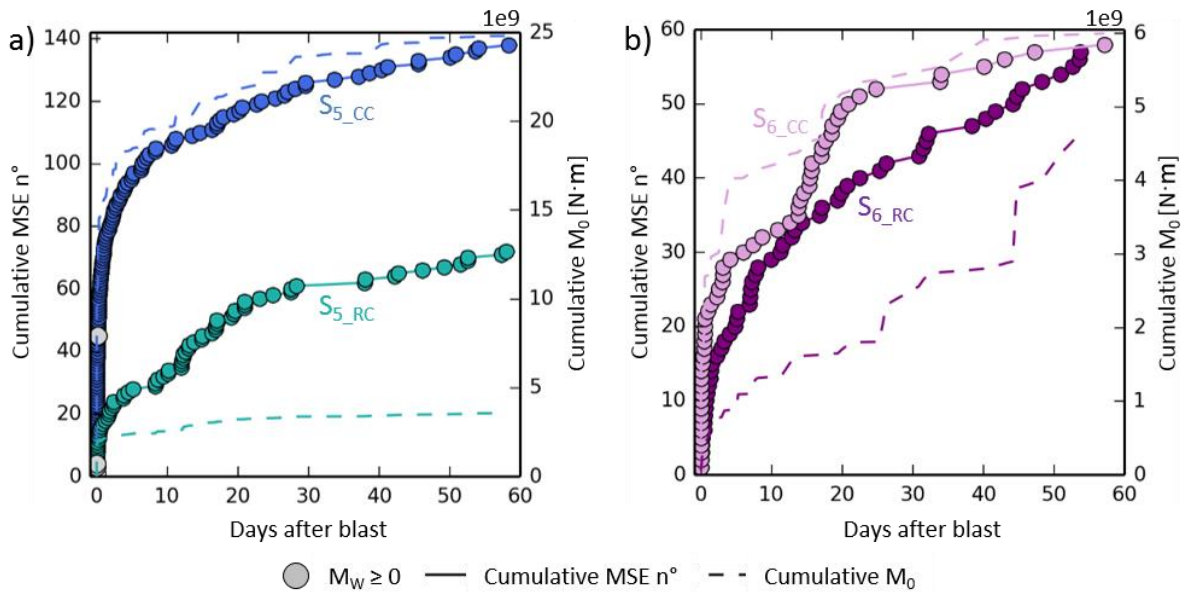


Fig. 4.11 - Temporal distribution of Sequence 5 (a) and Sequence 6 (b). Events are separated in function of their belonging to CC or RC and are color coded as in Fig. 4.10.

If certain levels of seismic activity are expected around exploited stopes, the occurrence of seismic events at a distance from mining excavations needs to be carefully analyzed as they must determine the spatial extension of forbidden areas for mine worker's safety. As reported by Vallejos and McKinnon (2011), re-entry protocols are a common approach for controlling risk after blasts or large seismic events, which are generally applied by restricting access for a sufficient time to specific areas of the mine. For this reason, it is important to understand the mechanisms that lead to this remote seismicity: why it was preferentially triggered in the eastern area of the mine and why this happened in coincidence with the final stages of Stope 13 exploitation.

In addition, delayed reactivations or delayed accelerations of seismicity rate are observed for some of the analyzed sequences, both in period of weak and strong rock mass response to mining. The mechanism of these delayed responses is not straightforward, as MSA is not induced by new blasts, neither by higher magnitude events. However, this trend suggests that other mechanisms contribute to intensify the seismicity rate in addition to the immediate stress change induced by blasting.

## 4.2 Analysis of seismic source parameters

To further characterize Lappberget MSA, seismic source parameters were analyzed, based on the methodology described in Chapter 3, looking for possible distinct behaviors within CC and RC events. As already observed, events with  $M_w \geq 0$  are only encountered in the CC area, except for one event recorded in the RC during S<sub>5</sub>. A common parameter used for determining the frequency-magnitude distribution of seismic populations is the b-value, which is defined by the Gutenberg-Richter law (Gutenberg and Richter, 1944):

$$\log_{10} N(M) = a + bM \quad (4.1)$$

where  $N(M)$  is the number of earthquakes with magnitude greater or equal to  $M$ , while  $a$  and  $b$  are parameters.  $b$  parameter, or b-value, quantifies the proportion between larger and smaller events within a seismic catalogue. It is widely known in the literature (e.g. Mendecki et al., 1999) that differences in b-values between seismic datasets may reflect differences in their dynamics.

When plotting the Gutenberg-Richter frequency-magnitude relation, two distinct behaviors are clearly observed between the two clusters (Fig. 4.12). Indeed, the b-value, which was estimated by least square method (following equation 4.2) with a correlation coefficient of 0.9 and assuming a magnitude of completeness ( $M_c$ ) of -1, is equal to  $1.2 \pm 0.02$  and  $1.8 \pm 0.09$  for CC and RC, respectively. This suggests that the mechanism of small events (i.e. RC) may be different from that of bigger events (i.e. CC) and that CC, characterized by a smaller b-value, presents a larger probability for the occurrence of higher magnitude events. The trend for the complete microseismic catalogue is similar to that of CC events, with  $b = 1.3 \pm 0.03$ .

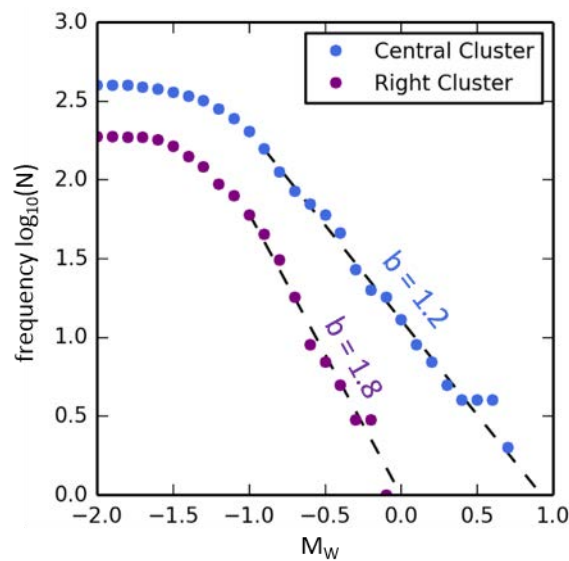


Fig. 4.12 - Frequency-magnitude relationship for the events within CC and RC. The magnitude of completeness appears to be equal to -1 for both datasets.

As reported by Mendecki et al. (1999), b-value is mainly influenced by three characteristics of the rock mass under consideration: (i) the stiffness, (ii) the stress state and (iii) the rock mass heterogeneity. The stiffness is the ability of a rock mass to resist deformation under increasing stresses, thus, the stiffer the system the higher the b-value. Consequently, b-value decreases with increasing stress levels as the stiffness of the rock mass is gradually degraded with growing stresses. In addition, heterogeneous condition of the rock mass lead to higher b-values as ruptures occurring within the stiff rock masses are stopped by the presence of weaker geological areas before growing into a larger MSE. Based on these observations, the higher b-value within the RC is most likely linked to the strong heterogeneity of this area, where stiff rock masses are interbed with weaker geological structures.

This interpretation can be confirmed by the analysis of source radii ( $r_0$ ) for CC and RC events. Source radii were calculated from corner frequency ( $f_c$ ), estimated with the methodology presented in the previous chapter, and considering the circular source model of Madariaga (1976), which assumes constant  $K_c = 0.21$ , for S-waves, and rupture velocity equal to the 90% of the shear-wave velocity ( $V_s$ ):

$$r_0 = K_c \frac{V_S}{f_c} \quad (4.2)$$

Computed source radii for the whole analyzed dataset range between around 0.3 and 32 meters. Ruptures of this size agree with observations made on site, where large fractures are especially encountered in the upper levels of the mine. Median source radius for RC events is equal to 0.9 m, with less than 10% of the events characterized by radii higher than 3 m (Fig. 4.13). On the contrary, more than 60% of the CC events show source dimensions bigger than 3 m, with a median radius of 3.6 m. Therefore, events that nucleates in the RC area have generally smaller source dimensions. Fractures of the RC, which most likely nucleate within the stiff rock mass, cannot propagate along great distances due to the presence of weak plastic lenses at direct contact with the breaking stiff rock mass. This means that local geology of RC has a strong influence on fractures propagation, confirming the previously addressed consideration about b-value and rock mass heterogeneity.

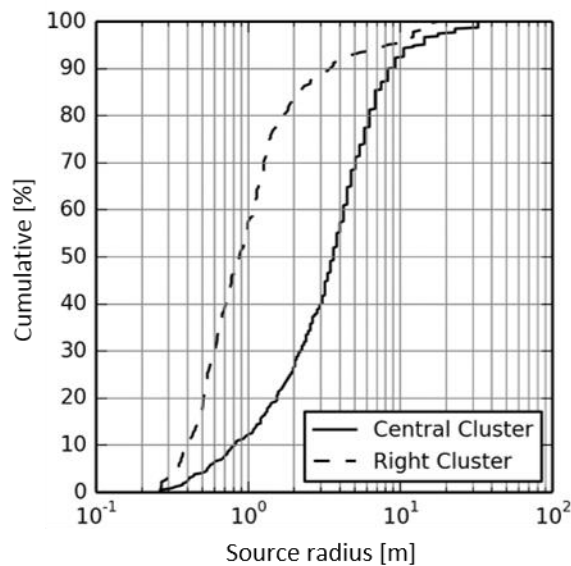


Fig. 4.13 - Cumulative distribution of source radius for the events within the two clusters.

Another evidence for different behaviors in the seismic activity of CC and RC is provided by the analysis of radiated seismic energy. Indeed, the two seismic populations appear characterized by different energy contents (Fig. 4.14a). RC presents a median energy of  $\sim 195$  J, while this value is about a factor of 8 smaller for CC events, whose median energy is  $\sim 25$  J. Following Mendecki et al. (1999), high energy values may indicate elevated stresses within the source region, suggesting that the local stress state differs between the two areas of the mine.

In addition, we observe that there is more S-wave energy in RC events than in the CC population and in the whole microseismic catalogue (Fig. 4.14b). S-wave to P-wave energy ( $E_S/E_P$ ) ratio is considered a good indicator of source mechanism. Indeed, as reported by numerous authors (Gibowicz and Kijko, 1994; Hudyma and Potvin, 2010; Kwiatek et al., 2011), shear failures associated to mining-induced seismicity are characterized by higher  $E_S/E_P$  ratios than tensile fractures. These latter tend to enrich the P radiation, resulting in lower  $E_S/E_P$  values (Kwiatek and Ben-Zion, 2013). Kwiatek and Ben-Zion (2013) report about observational studies on shear dominated earthquakes where the  $E_S/E_P$  ratio has been found ranging between 10 and 30. On the contrary, for tensile source processes this ratio can drop down to 1 (Hudyma and Potvin, 2010). In most of these studies,  $E_S/E_P$  ratio of 10 is considered as a lower bound for shear source mechanism, while events showing smaller values are

interpreted to be related to tensile processes, or to shear failures combined with significant tensile components. Kwiatek and Ben-Zion (2013) assumed an  $E_s/E_p$  ratio of 4.5 as lower bound for pure shear faulting.

For the whole Lappberget microseismic catalogue the  $E_s/E_p$  ratio ranges from 1.4 to 68, which agrees with values found in the literature.  $E_s/E_p$  ratios greater than 10 are observed in both clusters (Fig. 4.14b), even if these values are encountered in more than 40% of the RC events, while they represent only around 10% of the CC population. These results may indicate a probable presence of both shear type and tensile mechanisms, with CC characterized by more tensile fractures than the RC area. This is in agreement with other studies (e.g. Hudyma, 2009) which reports about tensile fractures most likely occurring near the excavation zone. However, these observations have only marginal significance as a moment tensor solution would be necessary to determine the exact focal mechanism of Lappberget induced seismicity.

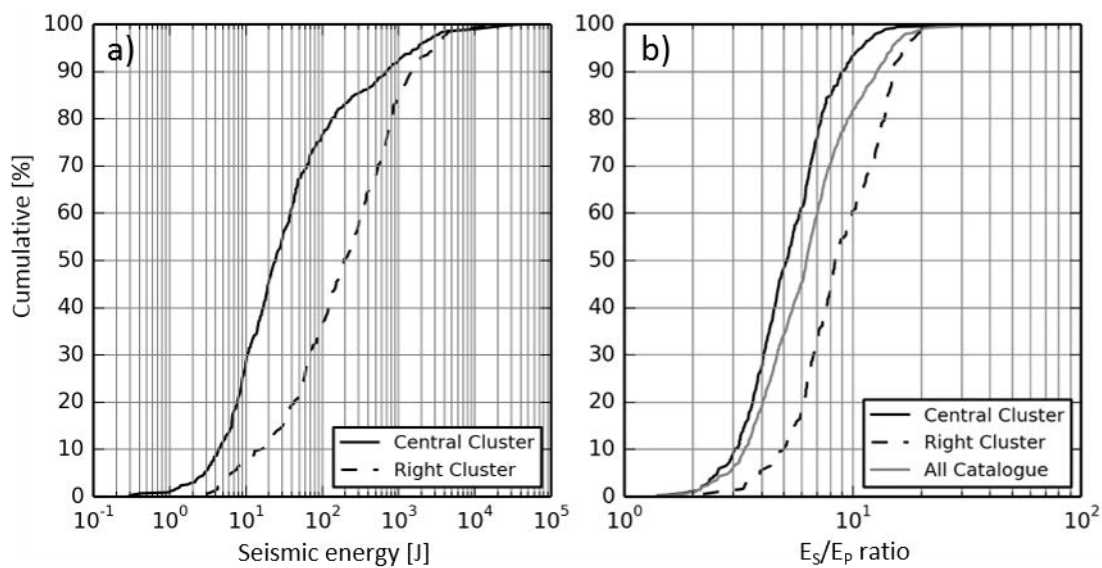


Fig. 4.14 - Cumulative distribution of seismic energy (a) and S-wave to P-wave energy ratio (b).

To better constrain differences so far observed between CC and RC seismicity, apparent stress ( $\sigma_a$ ) and stress drop ( $\Delta\sigma$ ) were analyzed within the two datasets. Indeed, these source parameters can give valuable insights about stress state within the source region at the time of seismic events. Apparent stress can be computed from the following equation proposed by Wyss and Brune (1968):

$$\sigma_a = \mu \frac{E}{M_0} \quad (4.3)$$

where  $E$  [J] is the seismic energy and  $M_0$  [ $N \cdot m$ ] is the seismic moment, which were computed, respectively, from equation 3.1 and 3.11 of the previous chapter.  $\mu$  [ $N/m^2$ ] is the shear modulus of the source material determined from the Young modulus ( $E_Y$ ) and the Poisson coefficient ( $\nu$ ) following the equation:

$$\mu = \frac{E_Y}{2(1 + \nu)} \quad (4.4).$$

Young modulus and Poisson coefficient, which were determined by laboratory test (Tonnelier et al., 2016), are equal to 66 GPa and 0.2, respectively, giving a final value of shear modulus equal to 27.5 GPa.

In addition,  $\Delta\sigma$  is estimated as follow (Eshelby, 1957):

$$\Delta\sigma = \frac{7}{16} \frac{M_0}{r_0^3} \quad (4.5)$$

where  $r_0$  is the source radius estimated by equation 4.2.

Given the dependency of  $\Delta\sigma$  from source radius, stress drop is a model-dependent parameter which assumes a pure shear slip mechanism. On the contrary,  $\sigma_a$  is a model-independent seismic source parameter and can thus be used as estimator of the stress state irrespective of seismic source mechanism (Brown and Hudyma, 2017). Moreover,  $\Delta\sigma$  determination can be less robust than  $\sigma_a$  as it is dependent from  $f_c$  whose estimation can be affected by high uncertainties, as it was described in Chapter 3. Therefore, apparent stress is a more reliable parameter than stress drop.

Results of  $\sigma_a$  and  $\Delta\sigma$  for Lappberget microseismic datasets are reported in Fig. 4.15 and Fig. 4.16. When plotting separately CC and RC events, the distinction between separate population is clearly visible on the diagrams. Indeed, CC events are generally characterized by lower  $\sigma_a$  and  $\Delta\sigma$  than the RC dataset.  $\sigma_a$  for CC varies over more than two orders of magnitudes, between around 0.001 MPa and 0.1 MPa, with only a small portion of events characterized by  $0.1 < \sigma_a < 1$ . On the contrary,  $\sigma_a$  for RC events presents a smaller variation range, between around 0.1 MPa and 1 MPa, tending toward higher apparent stresses with a median value of 0.2 MPa. A small portion of RC events presents apparent stress smaller than 0.1 MPa.

Similar considerations can be addressed for  $\Delta\sigma$ . Indeed, RC events show stress drop ranging between around 10 MPa and 100 MPa, with a median value of  $\sim 17.3$  MPa. On the contrary, for CC the stress drop varies in a larger range, between 0.01 MPa and 10 MPa, with a median value equal to  $\sim 0.6$  MPa. Few events of CC are characterized by  $\Delta\sigma \geq 10$  MPa, overlapping with values mostly observed within RC population. Similarly, a small portion of RC events presents  $\Delta\sigma < 10$  MPa, departing from the general trend observed for this seismic dataset.

Despite these outliers, the general observed trend shows higher apparent stress and stress drop values for RC population compared to CC one. Spatial variations of apparent stress and stress drop are widely observed in mining-induced seismicity (e.g. Kwiatek et al., 2011; Mendecki et al., 1999) and correlated to differences in the rock mass properties and/or to distinct stress states. In agreement with observation made on b-value, seismic energy and fracture dimension, the different trend observed in  $\sigma_a$  and  $\Delta\sigma$  for CC and RC areas can be related to their distinct geological settings, which also contribute for a different stress states within these two areas of the mine. CC, where weak geological zones are less deployed, may have a homogeneous stress field mainly influenced by the massive presence of voids. On the contrary, RC shows strong geological heterogeneities which may have an impact on stress field intensity and orientation. Indeed, weak materials are not able to charge load and consequently stresses need to be redistributed and concentrated in the zones of stiff rocks and minerals surrounding the weak lenses. Due to this heterogeneous distribution of the local stress field, stiff rock masses within weakness zones may present higher stress conditions than the

rocks with similar stiffness but located in more geologically homogeneous areas of the mine (i.e. within the CC and the western area of the mine).

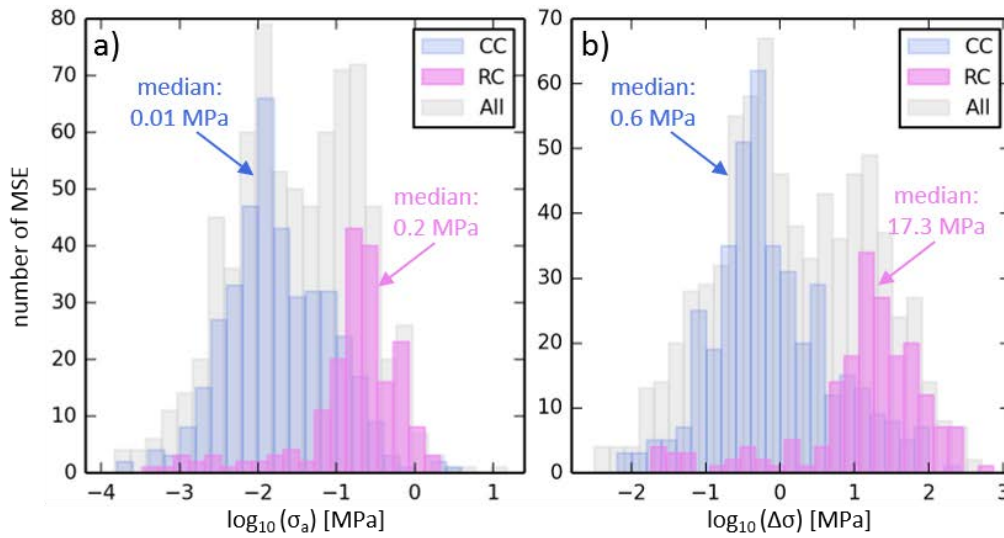


Fig. 4.15 - Histogram of apparent stress (a) and stress drop (b) for the whole microseismic catalogue (gray bars), for CC (blue bars) and RC (violet bars) events. Data are reported in logarithmic scale for a better visualization.

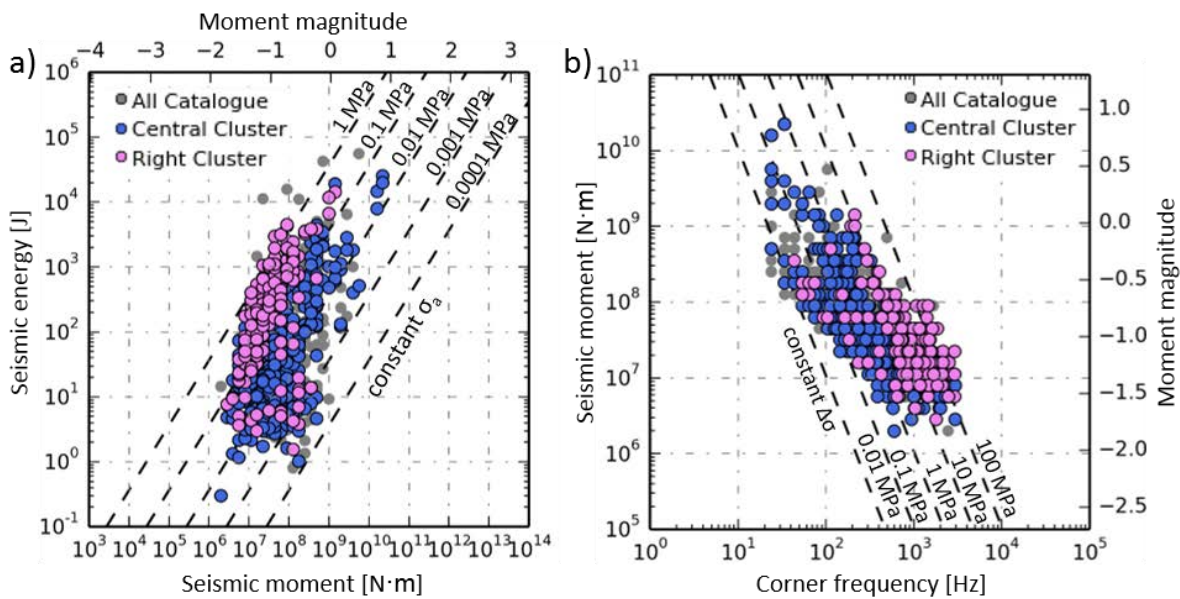


Fig. 4.16 - Energy-moment (a) and moment-corner frequency (b) relationships for the whole seismic catalogue (gray dots), for Right Cluster (violet dots) and Central Cluster (blue dots) events. Lines of constant apparent stress  $\sigma_a$  (a) were calculated following Equation 4.4, while lines of constant stress drop  $\Delta\sigma$  (b) were obtained according to Equation 4.6 and assuming the Madariaga (1976) source model.

In conclusion, seismic source parameters highlight that CC and RC events have significantly different behaviors and that this trend is due to the distinct geological setting observed in these areas of the mine. Geological heterogeneities within RC limit the size of the events here nucleated, resulting in smaller source radii compared to those of the CC area. Moreover, differences in seismic energy, apparent stress and stress drop, suggests that the stress field differs for these two regions of the mine, with RC area characterized by higher stress states. This latter observation explains why MSA



induced by distant blasts was preferentially triggered in the eastern area of the mine rather than, for example, in the western area.

#### 4.2.1 Temporal variation in b-value

Temporal variations of b-value within seismic populations have been widely observed in the literature, both for natural and induced-seismicity. Generally, following the observation made by Scholz (1968) on samples at laboratory scale, b-value decreases (increase) during time are interpreted as an indicator of increasing (decreasing) stresses within the source region, prior to the occurrence of brittle failures (Kubacki et al., 2014). Evidences for this behavior in b-value variation have also been observed on the field. Amitrano et al. (2005) reported a continuous decrease in b-value of seismic data recorded during the period preceding a chalk cliff collapse. Similarly, Hainzl and Fischer (2002) observed a b-value decrease during the three months evolution of an earthquake swarm, interpreting this trend as a successive stress accumulation due to a propagating rupture front. Analogous behaviors have been observed in the b-value of mining-induced seismicity. A 50% decrease in b-value was observed for seismic data recorded before and immediately after a fatal rockburst occurred in 2007 in the Crandall Canyon mine in Utah (Kubacki et al., 2014; Pechmann et al., 2008). Similarly, Nuannin et al. (2005) noticed a good correlation between temporal drops in b-value and subsequent seismicity increase associated with high magnitude events during seven years seismic monitoring in the underground Zingruvan mine (Sweden).

To analyze the temporal variation of b-value for Lappberget microseismic dataset, moving time window with a constant number of events was used. Window length has been set at 50 events with 1 event shift between successive windows. As reported by Nuannin et al. (2005), windows with constant events number avoid artificial fluctuation of the b-value due to samples size variations. Per each window, the b-value has been determined by the maximum-likelihood method (Hainzl and Fischer, 2002):

$$b = \frac{\log_{10} e}{\langle M \rangle - M_c} \quad (4.6)$$

where  $M_c$  is the magnitude of completeness, which was assumed equal to -1, and  $\langle M \rangle$  is the mean magnitude of the analyzed catalogue with  $M \geq M_c$ . Even if network configuration changed over time, the choice of  $M_c = -1$  appears to be consistent over the whole analyzed period (Fig. A.3). Computed b-values show large temporal variations, ranging from  $\sim 0.9$  to  $\sim 1.8$  (Fig. 4.17). Except for a peak observed between  $S_1$  and  $S_2$ , b-value appears rather constant in the first period, fluctuating around a mean value of 1.3, which agrees with the previously determined value by linear regression for the whole analyzed seismic catalogue. A significant reduction in b-value is observed between the occurrence of  $S_3$  and immediately prior the beginning of the self-triggered seismic sequence ( $S_4$ ). b-value, even fluctuating, shows a continuous decrease for two months, until reaching its absolute minimum few days before the occurrence of  $S_4$ . This drop in b-value occurred when the last level (-1182) of Stope 13 started to be excavated with a PB on the 25<sup>th</sup> of February 2016 (grey line number 3 in Fig. 4.17). Even if the blast did not result in a large number of MSE (Fig. 4.8e and Tab. 4.1), the consequent continuous decrease of b-value can be explained by a gradual stress increase which was initiated by this excavation. As in this period seismic activity was mainly localized within the CC (Fig. 4.5a and Fig. 4.7), it is reasonable to think that this stress accumulation was mostly occurring in the CC area. Moreover, the drop in b-value is strongly persistent over time for around two months,

highlighting that additional mechanisms are overlapping to the immediate stress change induced by the blast. Under increasing stresses, the rock is not anymore able to resist deformations and fractures grow fast with the occurrence of the self-triggered seismic sequence, also characterized by a large number of  $M_w \geq 0$  events (Fig. 4.7 and Fig. 4.9). The b-value appears rising again with the beginning of  $S_4$ , reaching the highest peaks during  $S_5$  and  $S_6$ . The increase in b-value within these last sequences can be in part due to a destressing of the CC area, as well as to the intense seismic activity within the RC, where, as observed in the previous section, the b-value is higher (Fig. 4.12) due to strong geological heterogeneities in the area.

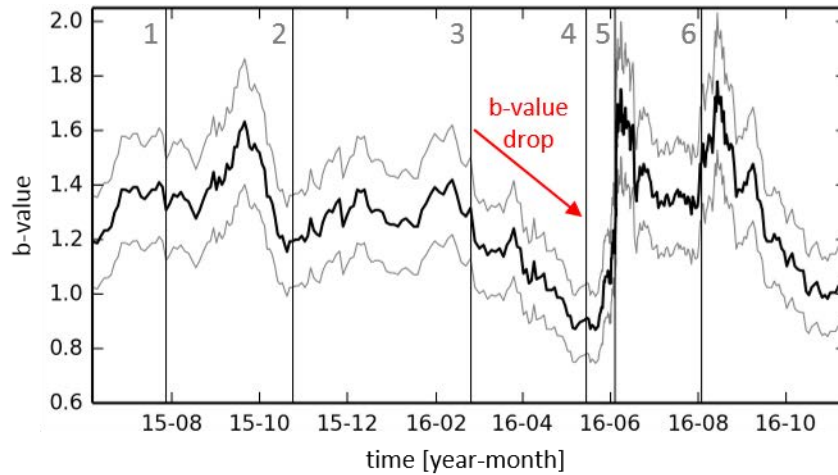


Fig. 4.17 - Temporal b-value variation (black line), together with its standard error (gray lines) for the whole microseismic catalogue. Per each sliding window over which b-values have been calculated (see text), time is considered as the mean time between the first and the last sample of the window. Vertical lines mark the beginning of the six seismic sequences analyzed in Section 4.1.1.

### 4.3 What drives seismicity?

The interevent time ( $\tau$ ) or waiting time distribution provides important insights into earthquake dynamics and the degree of correlation between events. Following Hainzl and Fischer (2002), if events occur randomly in time the probability density of  $\tau$  would be an exponential function of the type  $e^{-\tau}$ , as in a Poisson process. On the contrary, a power law distribution of interevent times indicates causality between consecutive events. Corral (2004) showed that interevent times can be well approximated by a gamma distribution of the form:

$$p(\theta) = \frac{C}{\tilde{\tau}} \frac{1}{\theta^{1-\gamma}} e^{(-\theta/\beta)} \quad (4.7)$$

where  $C$ ,  $\gamma$  and  $\beta$  are parameters, while  $\theta$  is the normalized interevent time  $\theta = \tau/\tilde{\tau}$ , obtained by scaling for the mean interevent time  $\tilde{\tau}$ . Assuming that seismicity is composed by aftershocks obeying the Omori law and Poisson background activity, Molchan (2005) theoretically demonstrated that the decay for large interevent times describes the poissonian part of the process, where the proportion of independent background events is given by the value  $1/\beta$ . For small interevent times, such as  $\theta < 1$ , that is  $\tau < \tilde{\tau}$ , the distribution is driven by the  $\gamma$  parameter, where  $\gamma = 1$  would correspond to a stationary Poisson process, while  $\gamma = 0$  indicates clustering between events, in accordance to an Omori decaying law with exponent 1 (Bourouis and Bernard, 2007; Corral, 2006).

Fig. 4.18a reports the probability density function (pdf) of normalized interevent times for the whole Lappberget microseismic dataset, independently from event magnitudes. In addition, the pdf of interevent times for CC and RC events have been calculated separately and reported in Fig. 4.18b and c, respectively. As proposed by numerous authors (Corral, 2006; Langenbruch et al., 2011; Schoenball et al., 2015), a logarithmic binning of  $\tau$  has been used, where bins are equally sized in logarithmic time and non-uniform in linear space. The pdf is then determined by counting per each bin the number of consecutive events pairs whose  $\tau$  falls into the bin and dividing the count by the length of the bin and the total number of events in the catalogue.

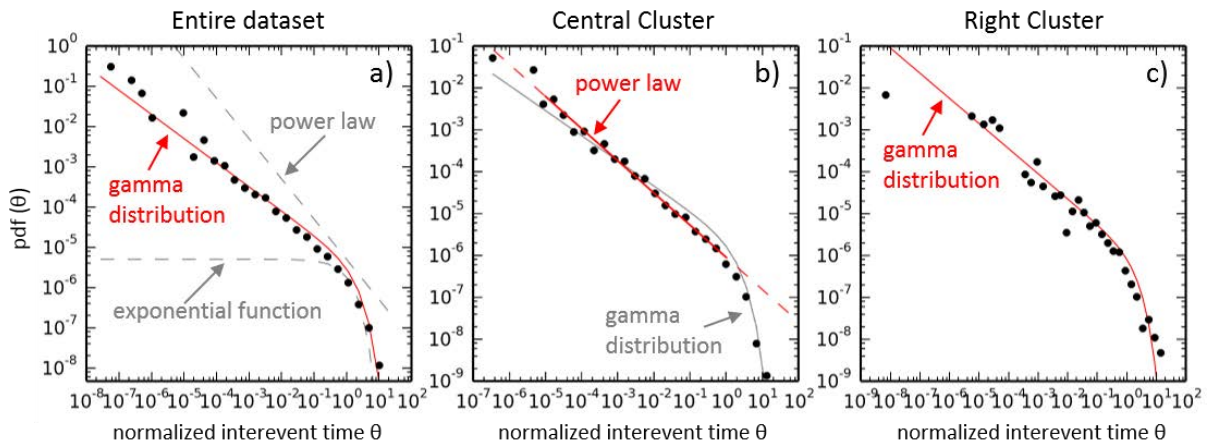


Fig. 4.18 - Probability density function of normalized interevent times. (a) pdf for the entire dataset. Bay way of comparison, an exponential function of the type  $e^{-\theta}$  and a power law  $\theta^{-1}$  are reported by dashed gray curves, while the red curve indicates the gamma distribution that approximates the dataset. (b) pdf of normalized interevent times for CC events. (c) Same as (a) and (b) but for RC population.

The pdf of interevent times for the whole dataset clearly deviates from an exponential function, indicating temporal correlation between events, and it can be quite well approximated by a gamma distribution (Fig. 4.18a) with values  $\gamma = 0.4$  and  $\beta = 1.8$ . Following Molchan (2005), a value of  $1/\beta = 0.56$  corresponds to 56% of independent background events for large interevent times. While, the behavior for small interevent times, characterized by  $\gamma = 0.4$ , indicates temporal clustering between events. This correlation at short time scale may be in part explained by the non-stationarity of seismic activity observed during the two-year period analyzed (Fig. 4.2). Indeed, similar to aftershock sequences, as the seismicity rate increases close to the occurrence of PB, the temporal recurrence of MSE decreases, resulting in smaller waiting times. Seismicity rate gradually decays after the blast, increasing the temporal recurrence of the events, with waiting times which tends to be progressively higher. However, when considering separately the period of weak rock mass response to mining, where seismicity has a more stationary behavior (Fig. 4.2), from the period of strong rock mass response, the probability density function of interevent times does not show significant variations from the distribution shown in Fig. 4.18a.

A direct consequence of blasting may be observed when plotting the probability density function of interevent times only for events belonging to CC area (Fig. 4.18b). Indeed, even if waiting times are not significantly departing from the gamma distribution of the whole dataset (reported in gray in Fig. 4.18b), at short time scales the interevent time seems to be better approximated by a power law (Fig. 4.18b), which is stable over more than 4 orders of magnitude, indicating clustering between events. The proximity to the major production area may have a strong influence on CC seismicity, where events show an aftershock behavior most probably due to sudden stress changes induced by

PB. On the contrary, waiting times distribution for RC events (Fig. 4.18c) clearly shows a dispersion for smaller interevent times, with significantly missing information for normalized waiting times smaller than  $10^{-3}$ , which corresponds to interevent times of around 280 s. For increasing  $\theta$ , RC events present a distribution similar to that observed for the whole microseismic catalogue. If this aspect may be in part due to high triggering thresholds (Chapter 3), which limits the detection of smaller events, it also indicates that most of RC events occur with larger waiting times. This consideration is better visible in the histogram of Fig. 4.19a which, for  $\tau < 10^4$  s, shows a significant reduction of events couples within the RC with respect to CC. This result agrees with observations made in the previous section, where a slower growth of the cumulative curve of RC events was observed during seismic sequences  $S_5$  and  $S_6$ , with respect to the rapid increase of CC cumulative events curve.

When looking at the temporal variation of interevent times (Fig. 4.19b), the role of PB (gray bars) on rupture propagation is clearly evident. Indeed, if  $\tau$  is generally ranging between  $10^4$  and  $10^6$  s, it is in coincidence with PB occurrences that it drops to its smaller values, as expected due to a rise in seismicity rate. Moreover, this effect is more evident within the CC in comparison to the RC, where the temporal recurrence of MSE, even if increased immediately after the blasts, appears lower than in the CC. The effect of blasts in decreasing interevent times is particularly evident for those PB which induced the seismic sequences analyzed in the previous section. Three additional blasts, also reported in Fig. 4.19b, remarkably decreased the interevent time. Moreover, an increase of the temporal recurrence between events is also observed in coincidence with the non-blast related sequence  $S_4$  (numbered as 4 in Fig. 4.19b).

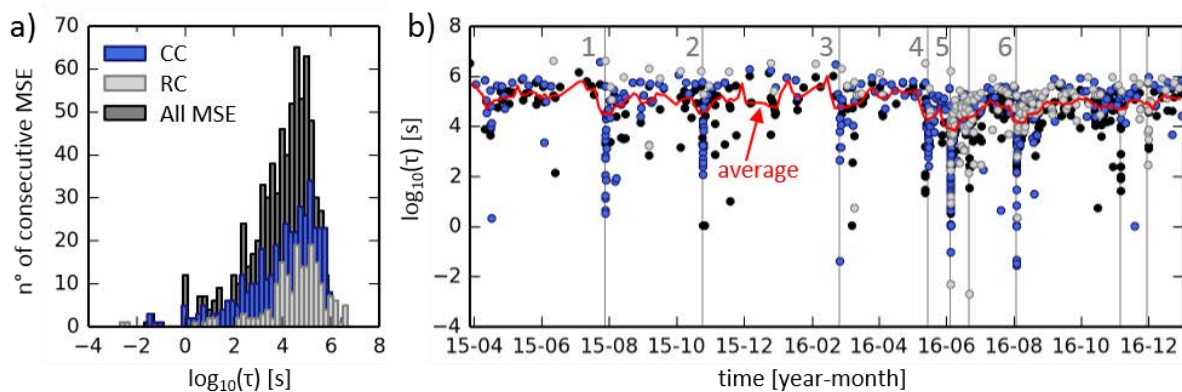


Fig. 4.19 - Histogram of interevent times  $\tau$  and interevent time over time. (a) Number of events associated to a specific value of  $\tau$  for the whole dataset (in gray), for CC (in blue) and for RC (in light gray). (b) Interevent-time distribution over time. The red line represents the average interevent time calculated over seven days moving time window with 50% overlap. Color code for CC, RC and the whole microseismic dataset is the same as in (a). Gray lines indicate the time of occurrence of the seismic sequences analyzed in the previous section, which are numbered as in Fig. 4.7.

Considering results of interevent time distribution, seismicity in Lappberget can be described by two separated components: (i) a mainshock aftershock component where the blast is considered as the mainshock, while the events which rapidly follow are regarded as the aftershocks; and (ii) a more steady and slow component which is persistent after the blasts and which can be the cause of delayed reactivations of seismicity rate observed in most of the previously analyzed seismic sequences. This latter type of seismicity presents features similar to that of seismic bursts or seismic swarms observed in many tectonic settings (Vidale and Shearer, 2006), which are characterized by spatiotemporal clustering of seismic events without the occurrence of any mainshock at the beginning of the sequence. Three possible models have been so far documented in the literature to

interpret seismic swarms: (i) self-triggering between events through stress transfer (Stein, 1999), (ii) fluid pressure fluctuations (Ake et al., 2005) and (iii) creep or aseismic slip of faults with induced ruptures on single asperities (Bourouis and Bernard, 2007). Finally, interaction between pore pressure triggering and aseismic slip have also been observed (Hainzl and Fischer, 2002).

For Lappberget seismicity a model driven by fluid pressure fluctuation can be reasonably excluded, as water does not play a primary role. There are also evidences for excluding the first proposed model. Indeed, temporal distribution of MSE and cumulative moment within the analyzed seismic sequences (Fig. 4.8b, d, f, Fig. 4.9b and Fig. 4.11) clearly deviates from a classical ETAS model or cascade model where the self-triggering mechanism needs to be driven by larger events. Many of the observed reactivations occurred without any increase in the cumulative seismic moment. Moreover, reactivations do not necessary occur at same location of previous activity, as, for example, observed during  $S_4$  (Fig. 4.9), suggesting that a mechanism at more global scales is involved. Finally, except for  $S_6$  within the CC, delayed reactivations happen after a silent period with no seismic activity, which can sometimes last more than 24 hours. These observations demonstrate that Lappberget seismicity is not driven by a simple cascade of earthquakes which triggers additional events, thus, a model driven by aseismic slip seems to be more appropriate. Similar mechanisms have been already observed in deep mines. Naoi et al. (2015) identified repeating earthquakes on the base of waveform similarity in a deep South African mine. They interpreted these events as repeated ruptures on asperities loaded by aseismic slip of surrounding regions. A recent study (Kinscher et al. in preparation), currently ongoing, demonstrates that more than the half of Lappberget events, within the period 2015-2017, can be classified into different multiplet families with highly coherent ( $> 0.9$ ) waveform similarity. Multiplet families appear to be active over weeks up to several months and distributed within the whole investigated area, both in the CC and in the RC. These observations validate the hypothesis of creep mechanisms which act at large scales and that induce fractures along singular asperities.

Most of the analyzed seismic sequences are probably characterized by both types of seismic activities, one directly induced by blasting with an aftershock-like behavior, and another linked with aseismic slip which acts at longer time scales. However,  $S_4$  which was not directly induced by blasting, may be a direct effect of aseismic deformations that slowly load seismic asperities until they break. An evidence for the different behavior of  $S_4$  comes from the analysis of the p-value of the Omori decaying law. Indeed, as reported in Fig. 4.20a, this sequence presents a faster decay which significantly deviates from that of the other analyzed sequences. In addition, when considering separately CC and RC events for  $S_5$  and  $S_6$  (Fig. 4.20b), one can observe that RC seismicity decays slower than CC activity for both sequences. This persistence for a different decaying trend within RC validates the hypothesis of additional mechanisms overlapping to the blast-aftershock effect.

Finally, it can be observed an overall decrease of interevent times (Fig. 4.19b) in coincidence with the non-blast related sequence and, thus, at the beginning of the strong rock mass response period. The average waiting time, even if fluctuating, appears lower than in the preceding period and it seems remaining at lower levels until December 2016. This trend may be interpreted as a period in which the rock mass is under unstable conditions, with the occurrence of a self-triggered sequence, not related to a blast, an overall seismicity rate increase (Fig. 4.7) and a higher recurrence mode of seismicity (Fig. 4.19). It is under these conditions that the RC become an intense source of seismicity,

most probably due to important induced stresses which are then preferentially redistributed within the highly stressed heterogeneous geological area of the RC.

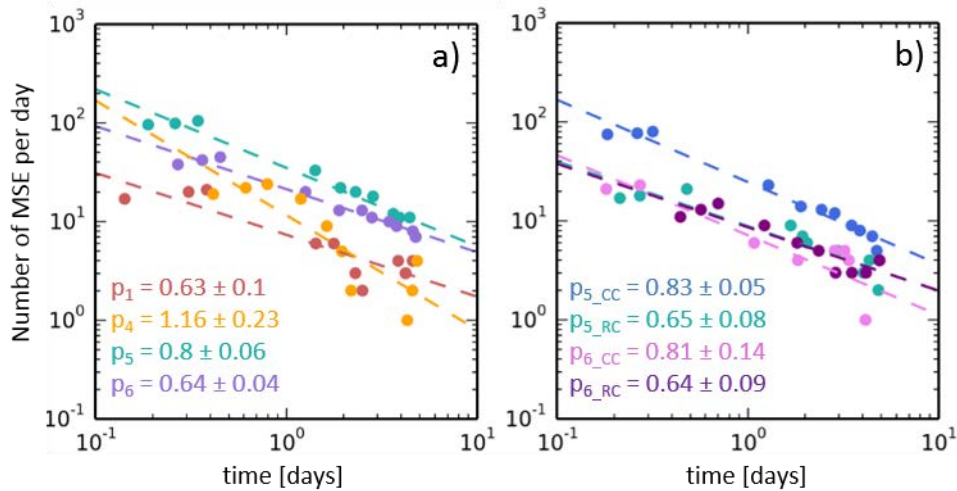


Fig. 4.20 - Seismicity rate and p-value estimation for seismic sequences  $S_1$ ,  $S_4$ ,  $S_5$  and  $S_6$  (a) and for sequences  $S_5$  and  $S_6$  considering separately CC ( $S_{5\_CC}$  and  $S_{6\_CC}$ ) and RC events ( $S_{5\_RC}$  and  $S_{6\_RC}$ ) (b). p-values are determined only considering the first five days of each sequence. Note that  $S_2$  and  $S_3$  have been discarded from the analysis due to their low number of events.

#### 4.4 Analysis of geotechnical observations

As discussed in Chapter 2, strain cells located within (PD cell) and near (PH cell) Stope 13 enabled recording 20 strain shifts between 2015 and 2016, most of which occurred immediately following PB. Of the total detected shifts, 13 are the most significant in terms of intensity (Tab. 4.2), with maximum strains ranging between around 20  $\mu\text{m}/\text{m}$  and more than 2000  $\mu\text{m}/\text{m}$ . The extensometer, which have a lower resolution than CSIRO cells and which experienced frequent malfunctioning, only recorded three shifts (Tab. 4.2) all linked with PB in Stope 13 which also resulted in seismic sequences  $S_2$ ,  $S_5$  and  $S_6$ . In Chapter 2, it was shown that strain shifts are not proportional to the extracted rock mass volume, neither to the distance from the excavation. If we now compare strain measurements with MSA, we also observe that strain shift intensity is not correlated with the corresponding seismicity rate. By mean of example, maximum strain shift recorded by PD cell in coincidence with  $S_1$  was equal to -449  $\mu\text{m}/\text{m}$ , while at the time of  $S_3$  the same cell recorded a much higher strain shift equal to 600  $\mu\text{m}/\text{m}$  (Tab. 4.2). However, seismicity rate was significantly higher during  $S_1$  rather than for  $S_3$ . Similar considerations can be done for extensometer measurements, whose intensity is not proportional to the corresponding seismicity rate. At the same time, in the current chapter, it has been shown that seismic activity is not proportional to the volume of extracted rock mass. These considerations suggest that additional mechanisms overlap with the immediate stress change induced by blasting. In particular, as it will be later shown in this section, it is conceivable to think that the production of most of the stopes mainly resulted in aseismic deformations within the surrounding rock masses, which in turn influence stress field redistribution. Another interesting aspect highlighted by CSIRO cells is that, during the exploitation of Stope 13, first-round blast appears inducing higher strains compared to second-round blast performed at the same level, and this is in contradiction with MSA. It must be reminded that first-round blast is generally the smallest of the level, as it serves as an opening for the following bigger blasts. This

trend is observed at both cells for production at level 1157 (CSIRO shifts 1 and 2), while this is only valid for PH cell at level 1182 (CSIRO shifts 6 and 10) (Tab. 4.2). Similarly, first-round blast at level 1207 (CSIRO shift 4) induced considerable strains despite the small excavated volume, without any intensification of seismicity rate. On the contrary, blast-related seismic sequences analyzed in the present chapter are mostly induced by round #2 or #3. Only  $S_3$ , which is the smallest seismic sequence in terms of number of events, occurred after a first-round blast. The observed unexpected trend in strain shifts compared to seismic activity may be explained considering geological features. Indeed, the hanging wall of Stope 13 is in contact with a massive weak geological zone extending along the entire height of block 1250 (see Fig. 2.4). First-round blasts are performed at the hanging wall, thus very close or in contact to the weak zone. This may result in aseismic slip (i.e. creep) of these talc rich areas, which also influences the local stress state within the interbedded stiff rock masses. As a result, the global stress field is intensified as, on one hand, it is influenced by readjustments needed to compensate the formation of a new void and, on the other hand, it is altered by creep of weak zones which probably acts at longer time scales and on larger areas.

To confirm these preliminary observations and, in order to better constrain the rock mass response to mining, the whole two-years period analyzed has been divided into four main stages characterized by different behaviors in both seismic activity and geotechnical measurements. Identified stages are reported in Fig. 4.21, where they are compared with the progression in the excavation of Stope 13.

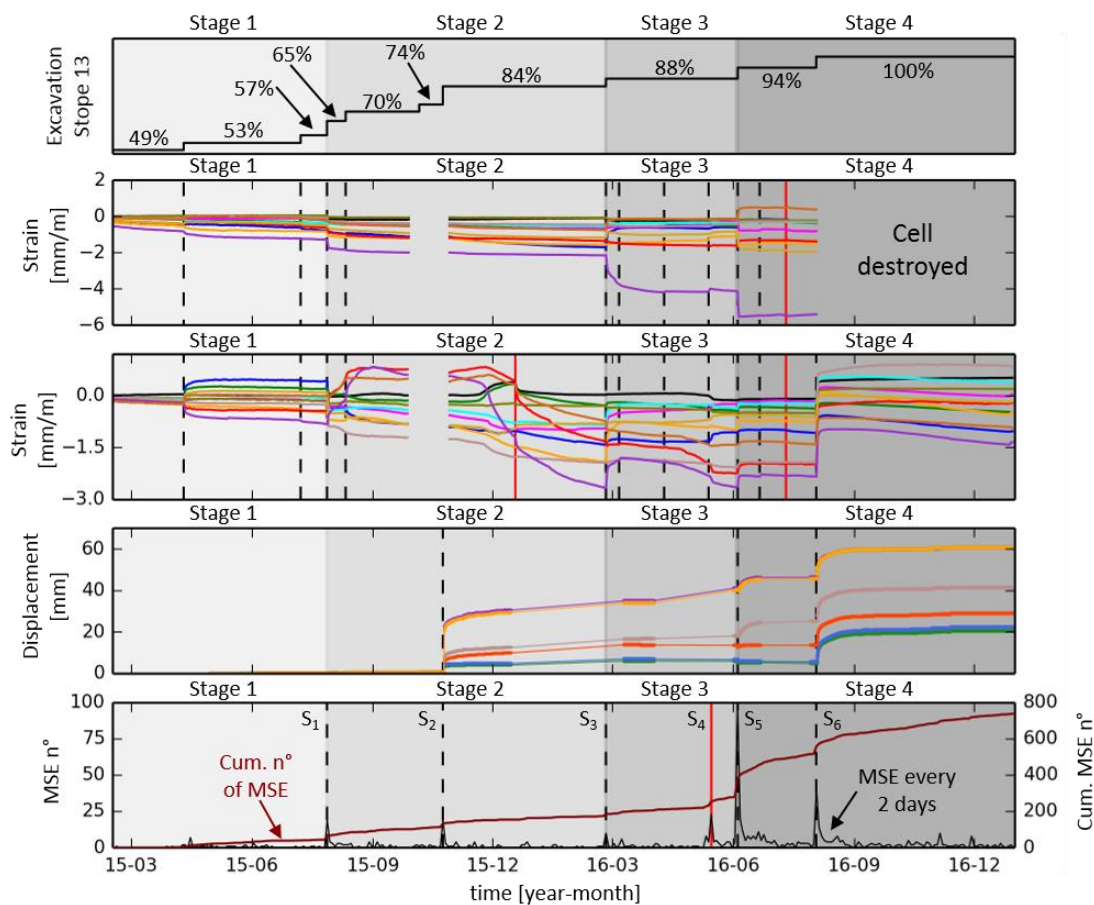


Fig. 4.21 - Comparison between excavation advancement in Stope 13 (first panel), strain measured by PD (second panel) and PH cell (third panel), extensometer data (fourth panel) and seismic activity (last panel). Dashed black lines indicate increase in geotechnical measurements or in seismicity rate. Vertical red lines refer to shifts, or seismic sequences not induced by PB.

Tab. 4.2 - Characteristics of major strain shifts detected by CSIRO cells, displacement shifts measured by downward extensometer (ED) and seismic sequences observed between 2015 and 2016. Note that the maximum extensometer displacement is computed for  $t = 24$  h after the blast, while distances are computed from the middle of the extensometer to the centroid of the blasted volume. Maximum strain shifts recorded by CSIRO cells are determined as the difference between strains immediately prior and immediately following the blasts. Lines with gray background refer to strain shifts not followed by seismicity and not recorded by ED. Salmon background line highlights a displacement shift, which was followed by a seismic sequence, only recorded by ED and missed by CSIRO due to a malfunctioning of the system. Blue background lines refer to strain shifts followed by MSA and missed by ED. Finally, green background lines indicate shifts detected by both CRISO and ED and followed by microseismic sequences. The first column refers to temporal stages identified in Fig. 4.21.

Stage	CSIRO Shift	ED Shift	Seismic sequence	Date	Type of activity	Stope	Explosive [kg]   Volume [m <sup>3</sup> ]	Distance PD PH [m]	Distance ED [m]	Max. strain PD PH [ $\mu\text{m}/\text{m}$ ]	Max. displacement ED [mm]	n° of MSE
1	1			2015-04-10	PB	13_1157 #1	3553   2239	40   37		100   411		
	2			2015-07-08	PB	13_1157 #2	4212   2910	31   27		-74   -53		
2	3		S <sub>1</sub>	2015-07-28	PB	13_1157 #3	6669   5330	22   15		-449   -654		35
	4			2015-08-11	PB	13_1207 #1	4172   3275	57   64		50   325		
		1	S <sub>2</sub>	2015-10-24	PB	13_1207 #3	5473   6702	-	17	-	21	16
	5			2015-12-18	DB	13_1157 #13	105   -	-   35		-   -320		
3	6		S <sub>3</sub>	2016-02-25	PB	13_1182 #1	2963   2758	39   43		600   635		10
	7			2016-03-06	PB	11_1207 #2	4827   5503	45   57		33   62		
	8			2016-04-09	PB	17_1207 #1	3440   2527	80   81		68   23		
	9			2016-05-13	PB	17_1207 #2	-   6497	66   67		142   40		
4	10	2	S <sub>5</sub>	2016-06-04	PB	13_1182 #2	6597   3978	27   32	27	-1181   142	1.3	210
	11			2016-06-21	PB	15_1207 #2	6766   7078	55   59		98   53		
	12			2016-07-11	-	-	-	-		-34   -77		
	13	3	S <sub>6</sub>	2016-08-03	PB	13_1182 #3	4527   4346	-   18	22	-   2561	7	121



The first stage is characterized by very low levels of seismic activity and by the occurrence of two major strain shifts (Fig. 4.21) related to the first and the second-round blasts performed at level 1157 of Stope 13. As already discussed, first shift resulted in much higher strains with respect to the second one, despite a lower volume of extracted rock mass and a farther position to the cells (Tab. 4.2). In addition, strains related to the first shift are evolving during time (Fig. 4.22 on the left), while the second shift is characterized by fast strain changes, which then return quickly to a steady state (Fig. 4.22 on the right). Within 10 days after the blasts, strains had a variation of 247  $\mu\text{m}/\text{m}$  (J2 of PH cell, in blue in Fig. 4.22) for the first shift, while only 40  $\mu\text{m}/\text{m}$  (J6 of PH cell, in orange in Fig. 4.22) were observed for the second shift. This implies that mechanisms of differed strains or creep occurred after the first-round blast performed in Stope 13 level 1157, validating the hypothesis made at the beginning of this section about creep induced by blasting. As a result, stress field redistribution and consequent deformations are not immediate but a long-lasting process during time.

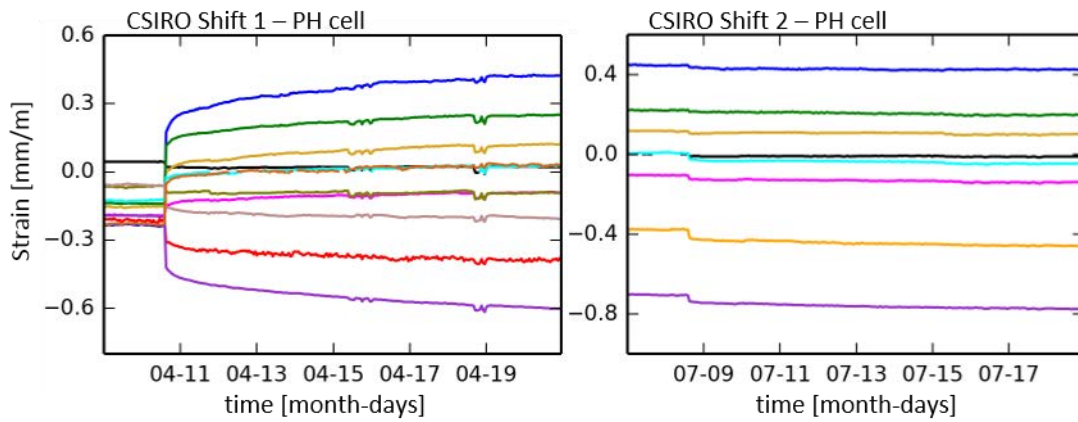


Fig. 4.22 - Strain measurements at PH cell during Shift 1 (on the left) and Shift 2 (on the right). Each line refers to a different gauge.

When the last blast at level 1157 of Stope 13 was taken out at the beginning of the second stage, important strain shifts were observed both at PD and PH cells (Shift 3) and the first microseismic sequence ( $S_1$ ) was detected (Fig. 4.21). Moreover, this second stage is characterized by the occurrence of plastic deformations at PH cell, while PD shows quite stable strains during time after the immediate drop (Fig. 4.23). Plasticity is visible in the temporal trend of some gauges at PH cell (Fig. 4.23b), as well as by the analysis of the coefficient of variation ( $COV$ ), which is defined as follow:

$$COV = \sqrt{\frac{\sum_i (\varepsilon_i - \varepsilon_i^*)^2}{\sum_i (\varepsilon_i^*)^2}} \quad (4.8)$$

where  $\varepsilon_i$  is the measured strain at gauge  $i$ , while  $\varepsilon_i^*$  is the estimated strain. The  $COV$  is then an indicator of the coherence between theoretical and measured data. As we are under the assumption of an elastic behavior of the rock mass, strong discrepancies between theoretical and observed data mean a departing from the elastic assumption and, thus, a probable plastic behavior of the rock mass. The larger the  $COV$  the higher the plasticity at the cell.

The  $COV$  calculated for PH cell immediately after the blast is equal to about 20% and it increased at 29% when considering measurements 10 days after the blast. This indicates that plasticity may have occurred around PH cell, at only 15 m distance from the excavation, and that plastic deformations

increased with time. This is confirmed by the unstable trend observed in PH measurements which suggests plastic behaviors until around March 2016 (Fig. 4.21), thus along the whole duration of stage 2. In terms of comparison, the *COV* calculated for PD cell for the same strain shift is in the order of 7%.

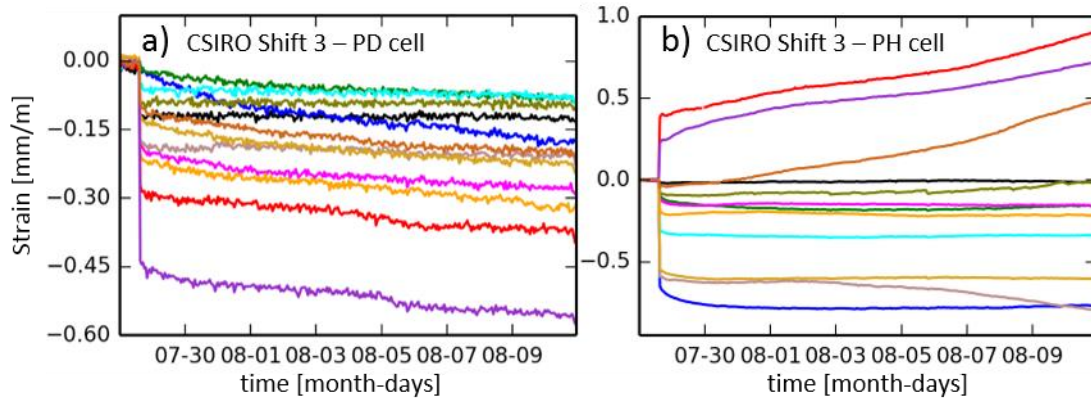


Fig. 4.23 - Strain measurements at PD (a) and PH (b) cells during Shift 3.

In agreement with the temporal behavior of strains measured at PH, the related seismic sequence ( $S_1$ ) shows a persistent activity along several days, with an immediate increase of seismicity rate following the blast, which is gradually reducing in the following days (Fig. 4.8b). When comparing temporal behaviors of MSE and measured strains, similarities in the trends are quite well visible (Fig. 4.28a), implying that seismic activity is decaying proportionally to the decaying rate of induced deformations. The latter observation is in agreement with studies (e.g. Bourouis and Bernard, 2007; Perfettini and Avouac, 2004) about coupled mechanisms of seismic and aseismic slip driven by creep. The model proposed by these authors assumes that some faults, or some segments of faults, obey a velocity-strengthening frictional law which leads to a stable silent creep (i.e. slip without seismic activity). Ruptures (i.e. seismicity) occur along locked segments of the faults which are gradually charged by the aseismic creep around them. It has been shown that, once earthquakes are triggered on the seismic parts of the fault, the aftershocks decay rate is driven by creep, thus, seismicity decays proportionally to the slip rate.

The second strain shift (Shift 4) recorded during the second stage is due to the first-round blast at level 1207 of Stope 13. Related strains are significant and evolving in time, especially at PH cell (Fig. 4.24a), while no seismic activity was recorded. If this indicate silent slip of aseismic rock volumes, as already observed during the first stage, it can also indicate that only part of the induced stress within the stiff rock masses surrounded by weak lenses was released, leaving these areas under overstressed conditions. After this major shift, other three minor shifts (see Tab. 2.5) were recorded at PH cell in the last days of August 2015 which may have contributed to further increase the stress state in the area of Stope 13. Then, due to the occurrence of the third-round blast at level 1207 of Stope 13, seismicity rose again with seismic sequence  $S_2$ , which was unfortunately missed by strain cells because of a malfunctioning of the system. However, this PB was well detected by the downward extensometer located in a suitable position with respect to the blasted area. The extensometer measured an immediate maximum displacement of 21 mm, reaching more than 25 mm one week after the blast (Fig. 4.21). Displacements of similar intensity would generally correspond to a magnitude 1.5 earthquake, with fault length of several meters. However, the biggest

event observed during  $S_2$  had a magnitude of 0, indicating that part of the deformation was due to aseismic processes.

With the time passing, other stopes are excavated, and this probably contribute to further increase the stress state around Stope 13, which may start becoming overstressed. One evidence for this hypothesis is the occurrence of a strain shift (Shift 5) related to a DB, which was recorded on the 18<sup>th</sup> December 2015 (red line on the third panel of Fig. 4.21), when the excavation advancement in Stope 13 was at the 84%. It is the first time that a small excavation (~100 kg of explosive for drifting the gallery of Stope 13 level 1157) have the potential to influence the stress state in the adjacent Stope 14, where stress and strains start increasing progressively. Indeed, the shift recorded at PH is almost neglectable immediately after the DB, for then becoming important around 5 hours later. As visible in Fig. 4.24b, creeping phenomenon is observed in the measurements, with strains gradually evolving within the following ten days.

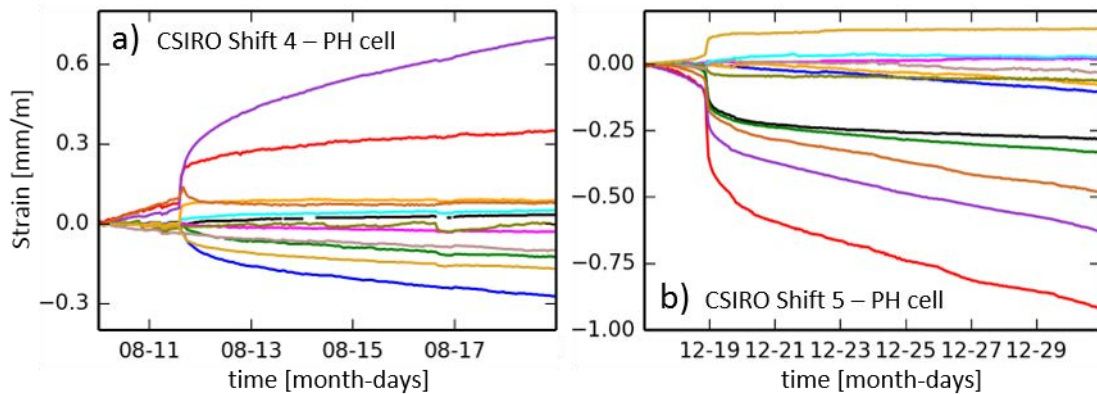


Fig. 4.24 - Strain measurements at PH cell during Shift 4 (a) and Shift 5 (b).

The third stage starts with the first-round blast at level 1182 of Stope 13, which is now reaching the 88% of its complete excavation. Related strains are important at both PD and PH cells (Shift 6), which measured maximum strains of 600  $\mu\text{m}/\text{m}$  and 635  $\mu\text{m}/\text{m}$ , respectively, immediately following the blast.

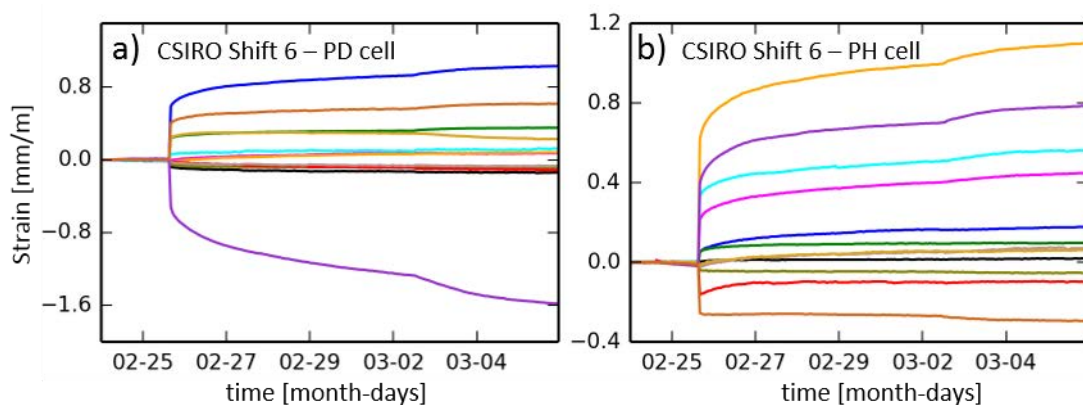


Fig. 4.25 - Strain measurements at PD (a) and PH (b) cells during Shift 6.

This shift is so far the highest recorded since the installation of the system, discarding strain Shift 3 at PH cell, while the volume of extracted rock mass is the lowest. This suggests that the stiff rock mass around Stope 13 is becoming progressively unstable. However, only few events ( $S_3$ ) were recorded in coincidence with this PB, indicating that the rock mass is still able to charge additional load without

the occurrence of significant fractures but with important aseismic deformations. Temporal trend of this shift is particularly interesting (Fig. 4.25). Indeed, strains increase fast at the beginning, keeping rising more slowly in the following days. Seven days after the blast a new low strain increase is observed at both cells, which is followed by a new rise of seismicity rate (Fig. 4.28b). Even if this delayed reactivation is small both in terms of number of MSE and strain intensity, it indicates that deformations and cracks start propagating without any additional external inducing force.

The entire system becomes progressively unstable and it starts also to be influenced by production occurring outside Stope 13. Indeed, in stages 1 and 2, major strain shifts were only linked with excavations in Stope 13 (Tab. 4.2), while during stage 3, even if Stope 13 production is not progressing, its local stress state starts to be influenced by PB in stopes 11, 15 and 17, which induced major strain changes at both PH and PD cells (Fig. 4.21 and Tab. 4.2). Of these latter strain shifts the last is of particular interest (Shift 9). Strains recorded at PH show a trend characterized by three distinct phases (Fig. 4.26b). A first small and immediate decrease (or increase, depending on considered gauges) followed by a slow strain increase (decrease) persistent over two days and, finally, a new more rapid increase (decrease). Similar trends are observed at PD (Fig. 4.26a), where the immediate shift appears more pronounced. Indeed, contrary to what has been so far observed, the immediate strain shift is much higher at PD compared to PH. However, at longer time scales, PH shows larger strain variations which reached  $-380 \mu\text{m}/\text{m}$  five days after the blast, while PD records strain variations of only  $50 \mu\text{m}/\text{m}$  in 5 days. This suggests that, at short time scales, production in Stope 17 mainly influenced the area where PD cell is installed, while for longer time scales the effect of production is mostly reflected in the adjacent Stope 14, where PH measured increasing deformations during time.

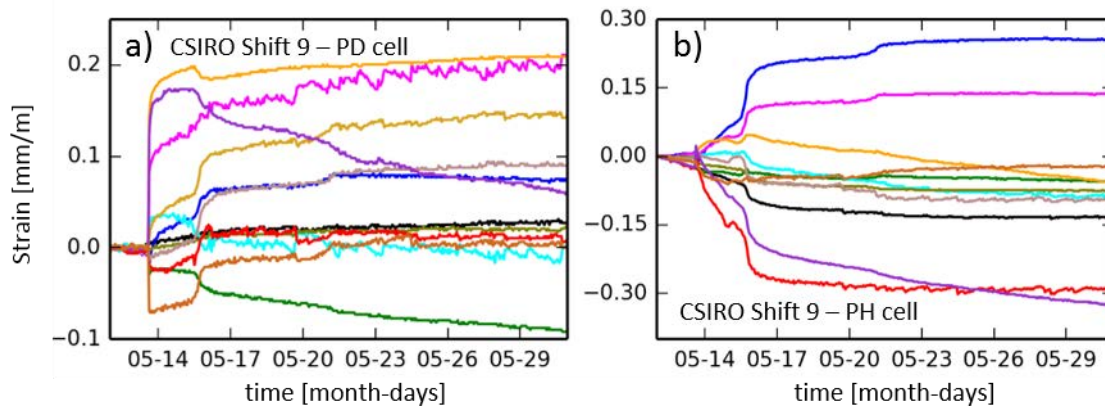


Fig. 4.26 - Strain measurements at PD (a) and PH (b) cells during Shift 9.

Three MSE, with  $M_w \leq -0.8$ , were recorded immediately after the blast, which are all located between stopes 14 and 13 around level 1157, at more than 60 m distance from the blast and close to PH cell. No event was detected around the excavation. Two days after, the self-triggered seismic sequence occurred ( $S_4$ ) with events localized in the same area which started breaking after the blast and, additionally, in the upper area of the mine (Fig. 4.9a). When comparing the temporal trend of strains and MSE located around CSIRO cells, the correlation is clearly evident (Fig. 4.28c). This is particularly true starting from the 15<sup>th</sup> of May, thus from the beginning of  $S_4$ , and for the delayed reactivation, which occurred at the same time for microseismic sequence and measured strains. This means that the non-blasts related seismic sequence was triggered by gradual deformation, i.e. creep, occurring around Stope 14, which was initiated by production in Stope 17. Stress variation

immediately after the blast, was probably not strong enough for triggering several ruptures within the stiff rock masses surrounded by creeping areas. With the time passing, deformations are gradually intensified as well as stresses, until they exceed the strength of the stiff rock mass which starts breaking with a seismic rate proportional to the deformation velocity. The described mechanism explains why  $S_4$  occurred with two days of delay from the blast in Stope 17 and why its temporal behavior is significantly different from that of the other seismic sequences.

In addition, during the reactivation of  $S_4$ , which occurred about 4 days after its beginning, a migration of seismic activity toward the upper area of 1250 block was observed (Fig. 4.9a). This implies that creeping is acting at large scales, influencing the local stress state at important distances from the area where the stress change was induced. This hypothesis is even more convincing considering that remote MSA in the upper level of the mine was already observed during  $S_1$  and  $S_3$ , which also showed proportionality of their temporal decay with that of induced strains. It can be suggested that fractures induced by creeping mostly occur within areas of the mine already under overstressed conditions, notably around the central area of Stope 13 and in the upper level of the mine. Indeed, as already discussed in the current section, stresses within the former zone are progressively increasing as the excavation progress in and around Stope 13. At the same time, the upper area of 1250 block is constituted by a 20 meters sill pillar, which divides the upper level of the study area (at -1107 m) from the bottom (at -1080 m) of the previous mining zone. High stress states within the sill pillar are expected as stresses induced by blasting within the upper and lower mining areas are here concentrated.

The last stage (stage 4) identified in Fig. 4.21 is distinguished by the intense microseismic activity which characterizes the beginning of the strong rock mass response period, with remote triggering of MSE in the RC area. Indeed, as production was resumed in Stope 13, for the final steps of its exploitation, important strain shifts are recorded by CSIRO cells, followed by intense MSA both in CC and RC (Fig. 4.21 and Tab. 4.2). The first strain shift (Shift 10), due to the second-round blast at level 1182 of Stope 13, presents larger strain at PD compared to PH, as it was already observed during Shift 9.

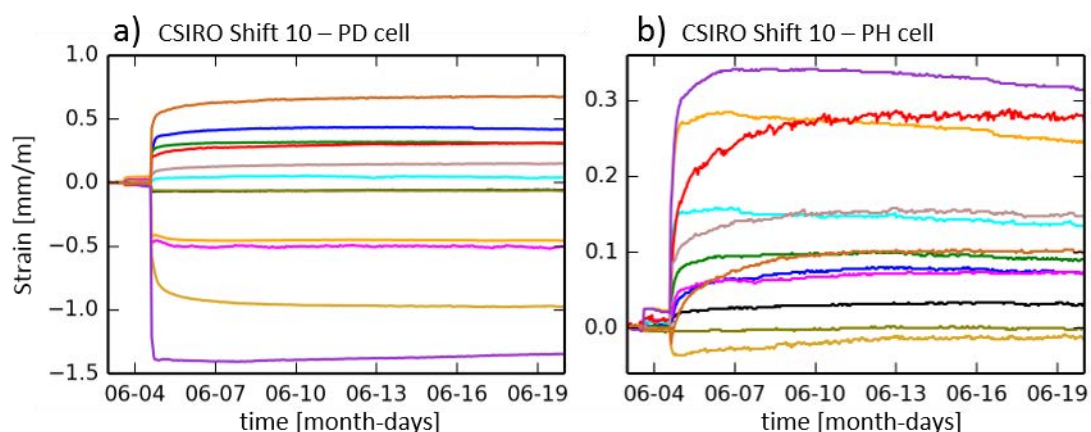


Fig. 4.27 - Strain measurements at PD (a) and PH (b) cells during Shift 10.

Thus, it is unlikely that the observed trend is due to the smaller distance of PD cell from the blasted area during shift 10. It can rather be suggested that induced strains were preferentially redistributed in the area of PD cell, which corresponds with the last rock mass volume not yet mined out in the entire column 13. Induced strains in the adjacent secondary stope were much lower. As a result,

displacements measured by the extensometer, also located within Stope 14, were important but not extremely high. In addition, contrary to the observation made for Shift 9, during Shift 10 the temporal evolution of strains is similar at both cells, with a variation of  $177 \mu\text{m}/\text{m}$  and  $192 \mu\text{m}/\text{m}$  for PD and PH cells, respectively, within four days following the blast.

The strain shift observed at PD is the largest recorded since the installation of the cells, showing an immediate drop following the blast of  $-1181 \mu\text{m}/\text{m}$ . Such large induced strains may be due to the overstressed condition of the mined zone before the blast. Indeed, when the void is performed the large strain energy stored within the mined volume is released and abundant fractures (seismic sequence  $S_5$ ) start propagating quickly in the surrounding rock masses. For the same reason, when Stope 13 was completely mined out two months later, PD cell was destroyed, and PH recorded the largest strain shift (Shift 13), which reached  $2561 \mu\text{m}/\text{m}$  immediately following the blast. During the last shift, stresses retrieved by mean of inversion from measured strains, allow determining a principal stress of around 52 MPa (indicating traction) immediately following the blast. Stresses in this order of magnitude are comparable with the major principal stress due to the overburden weight at the depth of the cell. This means that the area around PH was completely destressed after completion of production in Stope 13. It appears clearly that such a massive amount of induced stresses needed to be redistribute elsewhere after the blasts, influencing the local stress field of the RC area, where fractures start propagating fast immediately following the blasts, but with a slower temporal rate compared to fractures propagation within CC area (Fig. 4.11).

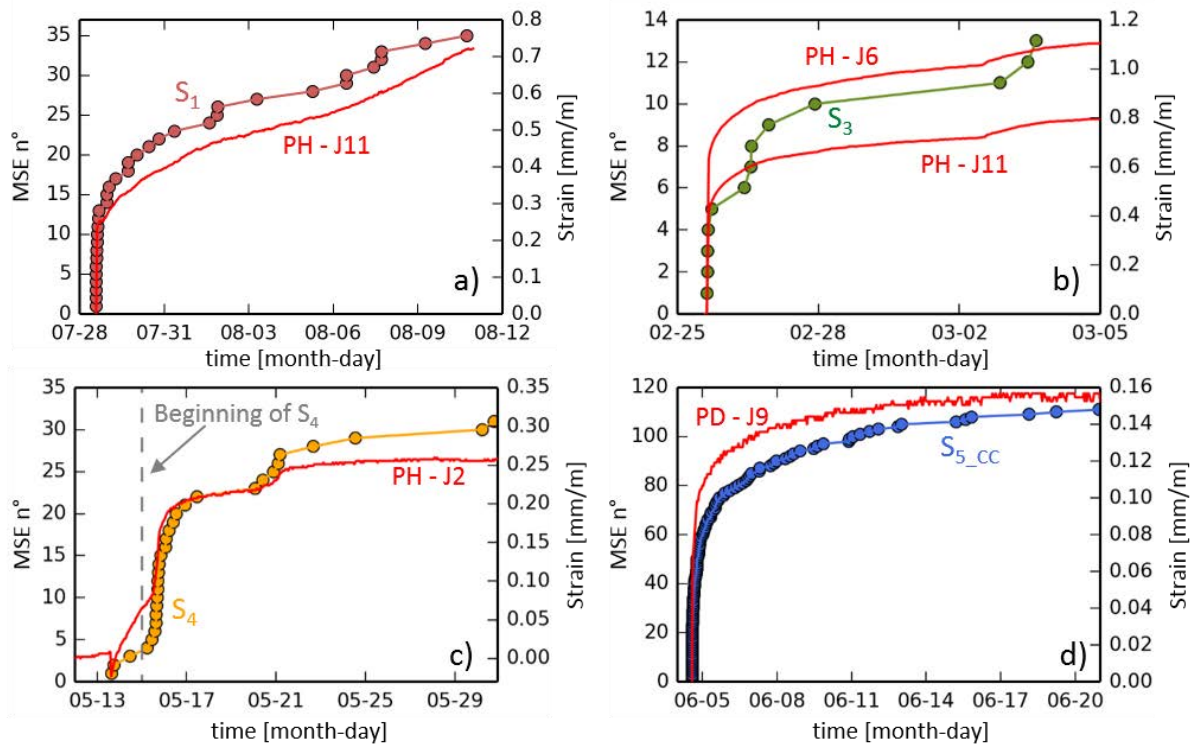


Fig. 4.28 - Comparison between strain measurements by CSIRO cells and cumulative number of MSE for  $S_1$  (a),  $S_3$  (b),  $S_4$  (c) and  $S_5$  (d). Red lines indicate the measured strains at some gauges of CSIRO cells.

It is interesting to observe that the temporal decay of MSE within the CC during  $S_5$  is nicely proportional to the decaying rate of the induced deformation measured at PD cell during Shift 10 (Fig. 4.28d). On the contrary, deformations grow much faster during Shift 13 than MSA did within the CC for  $S_6$  (Fig. 4.29a). Temporal trend of displacements measured by ED agrees well with MSE decay

(Fig. 4.29b), even if this is only valid for the first 15 days. After this period, a new important acceleration of seismicity rate is observed, which is although not visible neither in the strain or in the displacement measurements.

Seismicity rate appears remaining at important levels until the end of Stage 3, while no other strain shifts were recorded by PH cell. Despite many other stopes were produced, the following shift observed at PH cell was recorded only one year later, on the 5<sup>th</sup> June 2017, after a PB in Stope 15. This confirms that the end of production in Stope 13 resulted in destressing the surrounding rock mass volume, which appear only poorly influenced by new blasting in the other stopes.

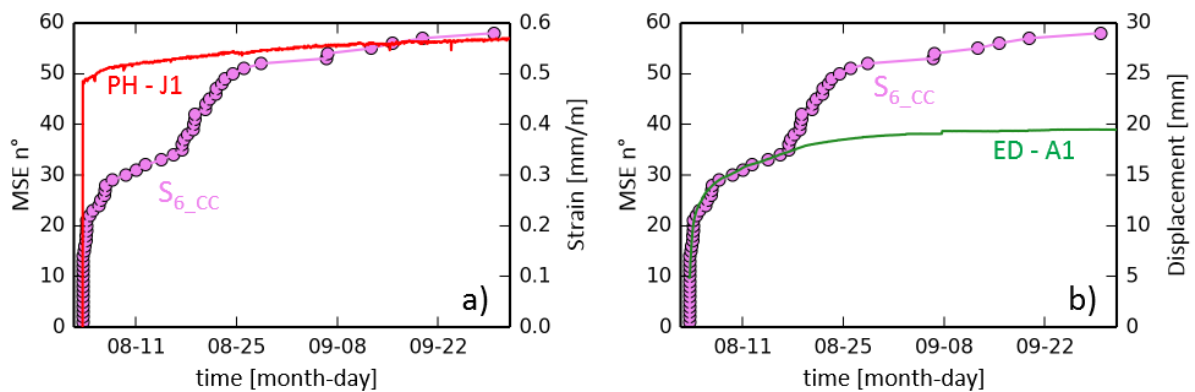


Fig. 4.29 - Comparison between strain measured at PH cell (a) and displacements observed at the downward extensometer (ED) (b) with cumulative number of CC events during S6.

## 4.5 Summary and discussion

In this chapter Lappberget MSA for the period 2015-2016 was analyzed and compared with spatiotemporal characteristics of mining activities (Section 4.1). It has been shown that PB play a primary role in the generation of the induced seismicity and that MSA is strongly dependent on the chosen mining sequence, rather than to the volume of extracted rock mass. As a result, the most important seismic sequences occurred during the two-years period analyzed are all linked with the final stages of production in Stope 13 (Fig. 4.3).

Seismicity rate significantly changed during time, showing a first period characterized by weak rock mass response to mining (until May 2016), followed by an overall increase of the seismicity rate during a second period of strong response to mining (Fig. 4.2). Clustering of MSE highlighted two seismically active regions: the CC, near the main production area, and the RC, near a major weak geological zone (Fig. 4.5).

Spatiotemporal analysis of MSE together with mine production enabled understanding that RC became an intense source of seismicity only during the period of strong rock mass response to mining, when distant PB performed in Stope 13 resulted in a remote seismicity within this area of the mine. This means that, during the final stages of Stope 13 exploitation, stress changes induced by blasting do not have any more a local behavior, triggering seismicity at more than 70 m distance from the excavations and preferentially within the RC area, where geological structures start having an important influence on MSE distribution.

To better understand the mechanisms that lead to this remote seismicity, how geological properties influence the seismicity pattern and why Stope 13 production plays a primary role in MSA generation, characteristics of the recorded induced seismicity have been deeper investigated, looking for possible differences between CC and RC seismicity. Tab. 4.3 reports a summary of the major results which are discussed in the following.

Tab. 4.3 - Summary of major differences observed between CC and RC seismicity. Except for b-value, for all the other parameters the median value is given. Reported p-values of the Omori law are those computed for S5 and S6 considering separately CC and RC events.

	<b>CC</b>	<b>RC</b>
b-value	1.2	1.8
Source radius [m]	3.6	0.9
Energy [J]	25	195
Stress drop [MPa]	0.6	17.3
Apparent stress [MPa]	0.01	0.2
Interevent time	shorter	larger
p-value Omori law	~0.8	~0.6

At first, the analysis of seismic source parameters (Section 4.2) highlighted that distinct geological regions of the mine (i.e. CC and RC) have seismic response characterized by significantly different dynamics and a different distribution of the local stress state. This has been explained considering the strong geological heterogeneities of the eastern area of the mine, where stiff rock masses are interbedded with weak plastic lenses. Geological heterogeneities strongly influence rupture propagation within the RC, where fractures are stopped before growing into bigger events, due to the presence of the weak areas at direct contact with the breaking stiff rock mass. Consequently, RC events are characterized by smaller fracture dimensions (Fig. 4.13) and by higher b-value (Fig. 4.12) than events nucleated within the CC area. In addition, due to inhomogeneous geological properties, the local stress field is heterogeneously distributed in the RC, with high stress levels within the stiff rock masses surrounded by weak geological areas. As a result, RC events are, on average, more energetic (Fig. 4.14a) than CC ones. Higher apparent stress and stress drop values for RC events (Fig. 4.15 and Fig. 4.16) confirm distinct stress states within these two areas of the mine. If the local stress state is already at important levels, even stress changes induced by distant blasts have the potential to further increase stresses in the RC area, until they exceed the strength of the rock mass and cracks start propagating quickly.

Based on these results, CC and RC populations can be classified as two distinct types of induced seismicity. Both are directly induced by blasting but, if CC events are mostly characterized by a short and local response to the induced stress change, RC events are also influenced by geological heterogeneities present in the area and are most probably occurring along pre-existent geological structures, such as fractures or contact zones between materials with different mechanical properties. It can be, thus, excluded that RC activity represents a type of the so-called triggered seismicity (Dahm et al., 2013; Hudyma, 2009; Richardson and Jordan, 2002; Stec, 2007), frequently observed in seismicity related to anthropogenic activity. Indeed, RC events are not occurring along tectonically active faults and, thus, they would not be present without any mining. Rather, these events are related to global stress field changes induced by long term mining, due to the geological



setting of the area. The strong influence of geological structures on seismicity pattern is clearly evident when considering seismicity recorded between 2015 and 2016 in the whole Lappberget orebody, until level 500 below ground surface (Fig. A.4). Most of the events are localized in the eastern area of the mine along the entire height of the orebody, even if mine sequencing is different between mine blocks. This confirms that, in addition to mining, geological structures have a primary role in MSA distribution.

The analysis of interevent time distribution (Section 4.3) enabled distinguish between two separated components of seismicity. The first is driven by the immediate rock mass response to stress changes induced by blasting, where, like in an aftershock sequence, events which directly follow the blast (i.e. the mainshock) are characterized by smaller interevent times. While, the second component is slower and more persistent after the blast. Even if is not possible to clearly separate these types of seismicity between CC and RC, CC activity appears on average characterized by shorter interevent times, with a probable interaction between consecutive events (Fig. 4.18). Based on the models proposed in the literature on seismic burst or seismic swarms triggering, the second type of seismicity has been associated with the silent creep of some areas of the mine, which slowly load seismic asperities bringing them to the rupture. This mechanism has also been considered responsible for the delayed reactivations of seismicity rate observed in most of the analyzed seismic sequences (Section 4.1.1). A model solely driven by self-triggering between events has been excluded based on some considerations: (i) seismicity rate is not linked with events magnitude; (ii) similarly, the spatial extent of MSA is not driven by events size; (iii) delayed reactivations of seismicity rate do not occur necessarily at same locations as of previous activity and (iv) they are mainly observed after steady rates of seismic activity or after periods where no events occurred.

The analysis of geotechnical measurements (Section 4.4) gave more consistency to a mechanism driven by silent creep. Evidence for creeping phenomenon is clearly observed at both CSIRO cells and extensometer measurements, which show evolving strains and displacements with time. Moreover, strains measured by CSIRO cells highlight that most of the stopes were produced without inducing seismic activity (i.e. fractures). If this trend is due to high triggering thresholds which limit the detection of small seismic events, one would have expected a proportionality between strains intensity and seismicity rate, which is not the case (Tab. 4.2). It seems clear that aseismic slip occurs in Lappberget area and that induced rock mass deformations are gradually evolving in time. Creeping phenomenon is most probably occurring within weak geological areas which load the interbedded stiff rocks. Stress changes due to blasting induce aseismic slip within weak zones, which results in increasing the local stress state of stiff rock masses. Here, if the induced stress change exceeds the strength of the rock, fractures start propagating. Otherwise, the blast will only result in aseismic deformations and in the overall intensification on the local stress state.

Similarities within temporal trend of MSE and measured strains have been observed for all the analyzed seismic sequences (Fig. 4.28), except for  $S_6$  (Fig. 4.29). This implies that seismic activity decays proportionally to the decaying rate of induced deformations and this is consistent with models obeying velocity-strengthening frictional laws, which drives silent creep phenomenon. In other words, the observed proportionality between seismicity rate and the temporal evolution of measured strains is a strong evidence for the proposed model of coupled aseismic and seismic phenomenon, where seismicity is driven by creeping. This is even more convincing when considering that most of the observed delayed reactivations of seismic activity are also visible in strain curves.

Which means that the delayed increases of seismicity rate are most probably induced by intensification of the slip around the breaking zone.

The picture given by strain measurements also highlighted that stress state at the location of the cells gradually increased as the excavation within Stope 13 progressed. This is well visible considering seismic activity and measured strains characteristics in the four temporal stages identified in Fig. 4.21, which can be related with the mining sequence chosen for Stope 13.

In the first stage, seismic activity is almost neglectable and measured strains are rather small. Seismicity starts rising in the second stage when also plastic deformations started to be observed at PH cell (Fig. 4.23b). Measured strains appear higher than in the previous stage and for the first time a strain shift induced by DB, rather than PB, occurred. This is interpreted as a gradual increase of stress state around CSIRO cells location, where even small blasts start to influence the local stress field. After the occurrence of  $S_1$  and  $S_2$ , during stage 2, Stope 13 was already almost entirely excavated and refilled with paste, leaving only a rock volume, between levels 1157 and 1182, which was acting as a pillar (Fig. 4.3b). When the first part of this final volume of Stope 13 was taken out, at the beginning of stage 3, high stress states were induced in the surrounding rock masses of CC, where CSIRO cells recorded the highest strain shift (Shift 6) since their installation, despite the extracted rock mass volume was rather small. After this shift, even if production is not evolving in Stope 13 (Fig. 4.21), the local stress state starts to be influenced by production in the adjacent stopes (Tab. 4.2). It can be, then, supposed that the last volume of Stope 13 started becoming progressively overstressed. Indeed, this last block is the only one able to stand any additional load in the entire column 13, as all the other levels were already excavated and refilled with paste (Fig. 4.3b). Evidences for increasing stresses in this area come from CSIRO cells which measured strains progressively more elevated at PD than to PH during stage 3 (Tab. 4.2). This is also confirmed by the temporal evolution of b-value (Section 4.2.1), which shows a gradual decrease between  $S_3$  and  $S_4$ , in coincidence with Stage 3. Indeed, gradual b-value decrease has been interpreted as a gradual stress increase within CC. In this phase, which is not characterized by important seismic activity, additional aseismic deformations due to production around Stope 13 contribute to further increase the stress state within this area of the mine. The occurrence of  $S_4$ , which was triggered by creeping phenomenon initiated two days earlier by production in Stope 17, is another evidence for the unstable condition of this area of the mine. Indeed, rock mass are not able to resist deformation under increasing stresses and cracks propagate fast.

The strong MSA triggered in the RC during stage 4 can be explained considering the heterogeneous geological setting of the RC area, creeping phenomenon and overstressed conditions within and around the last block of Stope 13. Indeed, when also this final part of the stope is mined out (Shift 10 and Shift 13), the large quantity of strain energy stored is released and needs to be redistributed in the surrounding rock masses. Here, the large induced strains have the potential to further increase creep within weak rock masses, which now acts at significant larger scales, influencing the local stress state of stiff rock masses within the eastern side of the mine (i.e. RC). Probably, under smaller strain release after the blasts, such intense seismic activity would have not occurred in the RC area.

In addition, seismicity induced by creep seems to mostly occur in areas where the initial stress state is already at important levels, such as in the sill pillar above block 1250 and in the RC area. This is not surprising as stiff rock masses are gradually loaded by creep of the surrounding weak zones. The

higher the initial stress state in the seismic zone, the lower the stress variation needed to induce fractures.

Further analyses are currently under development to deeper understand the proposed model of seismicity driven by aseismic creep. Indeed, even if it has been demonstrated that creep occurs at Lappberget mine and that seismicity is strongly related to induced deformations, the mechanism is so far only poorly understood. Ongoing studies focus on the analysis of multiplets found within the Lappberget microseismic catalogue based on waveform similarities, which are interpreted as repeated ruptures of the same seismic zone loaded by aseismic creep around it.

All these results strongly highlight the importance of merging seismic data and geotechnical measurements analysis for better constraint and deeper understanding of the mechanisms induced by mining excavations. This is currently only poorly done in operational monitoring of deep underground mines, where microseismic networks and geotechnical measurements are generally employed, but conceived as separated tools. It is demonstrated that a multi-parameter approach, which also takes into account information about mining practices and geological settings, can be a powerful tool for the improvement of short-term and long-term hazard prevention in deep mines.

# Chapter 5

## Numerical modelling

The analysis of geophysical data and geotechnical measurements, presented in the previous chapter, have highlighted the occurrence of aseismic phenomena in response to excavations, in addition to fractures propagation within the surrounding rock masse. It has been shown how merging geophysical analysis with geotechnical data, one can get a deeper understanding of rock mass mechanical response to mining. However, strain measurements and extensometer data provide only local information at the location where the sensors are installed. This means that we can achieve a complete characterization of rock mass response to mining only in a small region compared to the whole extension of 1250 block. To overcome this issue, numerical modelling can be a powerful tool for a better understanding of rock mass behavior at a larger scale. The aim of this chapter is, thus, to present and describe the numerical model built for simulating the mining sequence performed in the studied area between February 2015 and December 2016. The model aims at establishing the spatial extent and the amount of stress and strain variations induced by excavations in the surrounding rock masse within the whole block 1250. Moreover, attention will be given at the analysis of weak geological zones influence on stress and strain paths, as well as on the extension of predicted damaged zones.

This chapter has the following structure: first, numerical modelling techniques are briefly presented (Section 5.1), for then discussing modelling objectives together with the chosen modelling strategy (Section 5.2). In Section 5.3 the proposed numerical model will be described, focusing on: geometry (Section 5.3.1) and model meshing (Section 5.3.2), as well as on initial and boundary conditions (Section 5.3.3), constitutive laws and assumed mechanical properties (Section 5.3.5). The model will then be compared with extensometer and strain cells shifts (Section 5.4) recorded in block 1250 during the study period, as discussed in the previous section. Finally, model results will be presented in Section 5.5. The analysis will focus on the influence of mining sequence on predicted strain, stress field and damaged zone extensions, as well as on the mechanical role of weak geological zones.

### 5.1 Numerical modelling techniques

Numerical modelling is a flexible approach to disparate purposes and requirements. Jing (2003) presented a detailed and extensive review of numerical modelling techniques applied to the field of rock mechanics and rock engineering. Based on this review, Tab. 5.1 provides a summary of numerical modelling approaches and methods, together with some of the most widely used constitutive laws. The first main differentiation among modelling approaches can be done between continuous and discontinuous methods. Basically, in the former approach rock masses are considered as continuous media, whose elements remain connected to each other, thus, they cannot be broken in smaller pieces. On the contrary, when performing a discontinuous model, the material is modelled as an assemblage of particles or blocks and the contact pattern is constantly changing with the deformation process (Jing, 2003), making it possible to explicitly model fractur processes (Cai et al., 2007). Due to this inherent differentiation in approaching the rock mass system, distinct

methods exist in the literature for mathematically solve continuous and discontinuous rock mechanics models (Tab. 5.1). It is behind the scope of this thesis to describe them all, for which the reader is referred to Jing (2003).

Tab. 5.1 - Numerical modelling techniques and constitutive models.

Numerical modelling approaches	Numerical modelling methods	Constitutive models
Continuous	Finite Difference Method (FDM) Finite Element Method (FEM) Boundary Element method (BEM)	<ul style="list-style-type: none"> <li>• Elastic (Hooke's law)</li> <li>• Plastic and elasto-plastic (e.g. Mohr-Coulomb, Hoek-Brown criteria)</li> <li>• Rock fractures models</li> <li>• Rheology effects (e.g. creep)</li> <li>• Dynamic loading (e.g. earthquakes)</li> <li>• Coupled thermo-hydro-mechanical models</li> </ul>
Discontinuous	Discrete Element Method (DEM) Discrete Fracture Network (DFN)	
Hybrid continuous/discontinuous	Hybrid FEM/BEM Hybrid FEM/DEM Hybrid FDM/DEM	

Continuous and discontinuous approaches have each clear advantages and drawbacks, of which the most significant is that discontinuous models are much more computational intensive than continuous ones (Cai et al., 2007). This makes them less suitable for large scale modelling of highly fractured rock masses. Generally, in the field of deep underground hard-rock mines, it is a common approach to make use of continuous modelling, particularly when one wants to investigate stresses and strains at the mine-wide extension. As an example, Shnorhokian et al. (2015) built a large scale numerical model (1.15 million zones) to determine the best mining scenario to adopt in a deep mine, based on some instability indicators. They used a continuous approach based on the finite difference method and assuming a perfect elastoplastic behavior of the rock mass, with a Mohr-Coulomb failure criterion.

Even when the objective of numerical modelling is the evaluation of mining-induced stresses in small areas, the model needs to be built at a larger scale. This must be done, on one hand, to avoid openings influences on model boundaries and, on the other hand, to take into account all the excavations which may have influenced the local stress state in the area of interest. Thus, continuous models are as well applied to the analysis of mining-induced stresses at specific underground locations. Bruneau et al. (2003) made a large-scale numerical model, simulating the excavation of 208 stopes, to assess the influence of mining and large faults on mine shaft stability. They make use of a continuous elastic mechanical model, combining the displacement discontinuity technique (Gordeliy and Detournay, 2011) with the boundary element method.

Thanks to the advancement of computer technology, discontinuous models have started to be employed in the field of rock mechanics. However, due to the large computational requirement of this methodologies, large-scale 3D discontinuous numerical models are often avoided. For this reason, it is a common approach to make use of hybrid numerical methods, with the aim of coupling continuous and discontinuous techniques. Cai et al. (2007) presented a numerical approach which combines the finite difference method (continuous) with the distinct element technique

(discontinuous), for simulating acoustic emissions induced by the excavation of a large underground cavern. The rock mass surrounding acoustic emission sensors is modelled with the discontinuous approach, while the entire cavern is modelled based on the continuous method. In this manner, continuous model predicts stresses induced by excavations, which are then used by the discontinuous model for simulating cracks nucleation and propagation. However, with this approach only acoustic events localized in close proximity to the sensors can be modelled, discarding those occurring at greater distances.

Besides scientific literature, mining industry makes a large use of numerical modelling, particularly for choosing the appropriate mining sequence to adopt in a range of possible sequencing scenarios. As these models are used as an aid for decision-making, they must be rather simple to build and quick to run. Therefore, continuous models, based on the simplistic assumption of an elastic rock mass behavior, are often employed. However, as it will be later discussed (Section 5.6), errors on stress estimates due to the elastic assumption may be significant, especially when large volumes of rock masses have been extracted. This leads to another important aspect of numerical modelling, which is the choice of the constitutive laws to be adopted. Constitutive laws basically define the mechanical behavior of modelled rock mass. The simplest approach is that of considering the rock mass as an elastic material, where strain increments generate stress increments based on the linear and reversible Hook's law. When this assumption is undertaken, the constitutive law is completely characterized by two distinct material properties, namely the Young's modulus ( $E_Y$ )<sup>1</sup> and the Poisson coefficient ( $\nu$ ). Linear elastic mechanical behaviors are largely adopted in numerical models (Jing, 2003), not only in mining industry but also in the scientific literature.

On the other hand, models based on plastic or elastoplastic theory are as well largely employed for numerical modelling of hard rocks. In these cases, it is assumed that the modelled rock mass undergoes irreversible (i.e. inelastic) deformations, once the imposed failure criterion has been reached. This phase corresponds to the plastic response of the rock mass, when damage occur. Most commonly used failure criteria are the Mohr-Coulomb and the Hoek-Brown criteria. In the case of underground excavations, such as mines, elastoplastic models make it possible to estimate the extension of the excavation damaged zone (EDZ), which develops around underground openings. The development of such zone strictly depends on the imposed failure criterion or, in other word, on the constitutive law chosen for modelling rock mass mechanical behaviors.

Elastic and elastoplastic constitutive models, so far discussed, are only able to simulate the immediate response of rock masses to excavations, thus, temporal effects are not taken into account. As reported in Tab. 5.1, time-dependent mechanisms which influence the physical behavior of rock masses are mainly related to rheology effects, such as in the case of creep mechanisms, or to dynamic loading conditions, for example induced by blasting or seismic events (Jing, 2003). Numerical models which simulate the latter physical behavior of rock masses, belong to the category of dynamic modelling and could, thus, be used for simulating the occurrence of rockbursts. However, due to the complexity of these phenomena, their application is limited to the laboratory scale (e.g. Li

---

<sup>1</sup> In this thesis the Young's modulus is reported with the subscript Y ( $E_Y$ ), to distinguish it from the seismic source energy (E).

et al., 2008) or to 2D numerical simulations at the scale of one single underground opening (Zhu et al., 2014, 2010). Similarly, for creeping phenomena, even if many constitutive laws have been developed (e.g. Jaeger et al., 2009; Patton and Fletcher, 1998), the literature does not provide many applications on large-scale 3D numerical models of deep underground excavations, except in the case of long-term stability investigations, such as for radioactive waste underground storage.

## 5.2 Model choice and strategy

Considering the number of available numerical modelling approaches, the choice of one or more methods to adopt needs to be driven by modelling strategies and objectives. In other words, before choosing the methodology, one must think at the reason why a numerical model is demanded and what are the characteristics of the rock mass process that one wants to investigate. As already discussed in the introduction of the current Chapter, we want to use numerical modelling for a deeper comprehension of the rock mass response to mining in the whole 1250 block and considering the complete excavation sequence applied in this area of the mine within the two-years period analyzed (from February 2015 to December 2016). Then, we want to compare numerical modelling results with microseismic data analysis. The required numerical code must, thus, be able to handle (i) complex 3D geometries (ii) on a large scale (model with several millions of zones), (iii) simulating numerous step-by-step excavations. Based on these considerations and taking into account the lack of information about size, orientation and spatial distribution of eventual major discontinuities, a continuous approach has been chosen for modelling rock mass behaviors in Lappberget orebody. The code which has been used at this scope is the Fast Lagrangian Analysis of Continua (FLAC3D). FLAC3D utilizes the explicit finite difference method for mathematically solving rock mechanic problems by means of partial differential equations. The resolution process consists in discretizing the model space in meshes (ore zones) with assigned material properties that are connected by nodes (and faces in some cases).

In the FLAC3D software, differential equations are solved in subsequent computation stages, under defined initial and boundary conditions. At each stage, forces, velocities and displacements are computed at the nodes, and values of stress and strain are retrieved within model zones, each previously divided in ten sub-zones. Stresses and strains are then averaged. The final solution is obtained when the model is in a state of equilibrium, which means that the resultant force at each grid point reaches a threshold value imposed by the user. By default, the software considers the equilibrium is reached when the ratio between the maximum unbalanced force of the model and the mean force applied at each node is smaller than  $10^{-5}$ .

Assuming that neither thermal, nor hydraulic effects occur, rock masses in the proposed numerical model have been modelled assuming a purely mechanical elastoplastic constitutive law (Souley et al., 2018), which takes into account the brittle behavior observed in hard rocks, like Lappberget orebody. The assumed constitutive model will be further discussed in Section 5.3.5.

Short-term temporal effects, such as dynamic loading due to seismic events, are not considered in the model we propose. One can argue that, when aiming at comparing modelling with geophysical field observations, dynamic phenomena must be considered. However, the objective here is neither to simulate the nucleation and propagation of seismic waves, nor to analyze the rock mass response due to its dynamic loading. In other words, we want to examine if the predicted static (equilibrium)

strain and stress fields redistribution induced on rock masses by mining excavations can explain the occurrence of seismic activity and its pattern. In addition, it must be considered that MSE recorded in block 1250 are characterized by low moment magnitudes, not higher than 0.8. Thus, it is plausible to suppose that their dynamic effect on neighboring rocks can be neglected.

Long-term temporal effects, such as creep, are neither considered in the proposed numerical model. In the previous chapter it has been shown that creep may occur in block 1250, probably within talc-schists zones, influencing seismicity pattern and stress field redistribution. However, these phenomena need long computation time to be modelled and require a previous calibration for characterizing the appropriate constitutive law to be adopted. The talc-schist unit observed in Lappberget orebody have been only poorly studied by mine geologists and only elastic properties are available (more details are provided in Section 5.3.5), which hinders the feasibility of modelling creep phenomena at this stage. In addition, before performing a time-dependent numerical model, a better understanding of rock mass behavior, of the influence of weak geological zones and of their response to mining, needs to be achieved, which is the aim of the proposed numerical model. Time dependent modelling will be included in subsequent studies to investigate the possible effect of creep.

## 5.3 Description of the model

Before running a 3D numerical model for simulating underground excavations some aspects need to be carefully defined: (i) model extension and computation time; (ii) geometry and mesh of model elements; (iii) initial and boundary conditions; (iv) constitutive laws, which describe the mechanical behavior of rock masses; and (v) rock mass characterization, i.e. rock mass mechanical properties. In this section, all these aspects will be discussed considering choices made for building-up the numerical model proposed in this work.

### 5.3.1 Model geometry and boundaries

Numerical model proposed in this thesis has been built in order to reconstruct, as accurately as possible, the geometry of excavations and the geological setting of block 1250 (Fig. 5.1 on the left), which constitutes our area of interest. Elements which have been reconstructed are the orebody profile, weak and very weak zones geometries, as well as mine galleries and stopes within block 1250. Only the ramp has not been considered. Because of the considerable volume of extracted rock mass within the shallower mining areas, their influence cannot be neglected. This is demonstrated by stress measurements performed in block 1250 in December 2014 (Chapter 2, Section 2.2.2), at a time when excavations of the upper mine levels were already at advanced stages. Measurements results showed strong differences, both in horizontals and vertical stresses, from the computed virgin state of stress (before any mining), highlighting the influence of upper levels excavations on the actual stress field in block 1250. For this reason, upper levels, which extend from -578 m to -1088 m, were introduced into the model (Fig. 5.1 on the left), as well as the orebody profile in the same vertical range (Fig. 5.1 in the middle). This latter was finally extruded until the ground surface, as its real geometry is not precisely described by mine geologists for depths shallower than 435 m. The geometry of upper levels excavations (i.e. galleries and stopes) was built based on a previous work by Souley et al. (2018), where each zone was reshaped by cuboids approximately equal to the volume of excavated areas (Fig. 5.1 on the left).



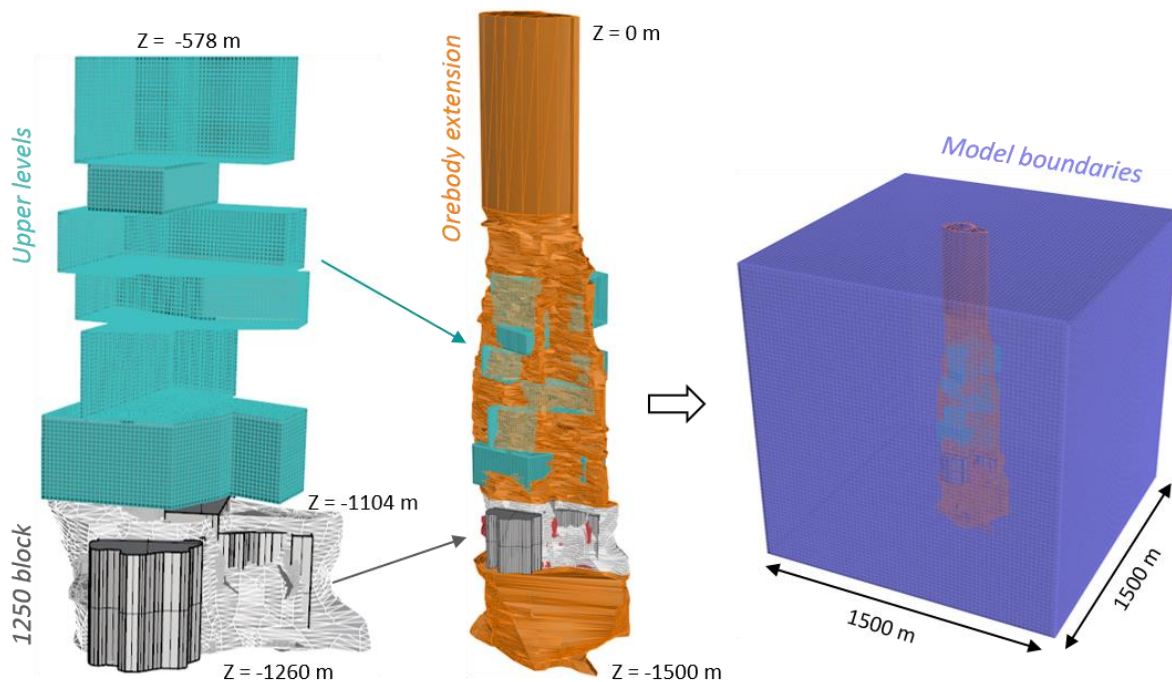


Fig. 5.1 - Model geometry. Upper levels profiles and block 1250 (on the left); the whole model extension along depth (in the middle) and model boundaries (on the right).

To avoid the influence of excavations on the model boundaries, the lower boundary of the model has been fixed at -1500 m (Fig. 5.1 in the middle), which equates to 240 m distance from the bottom of 1250 block. At such distance, displacements on the lower boundary are not influenced by excavations within block 1250. The overall model has, thus, a total vertical extension of 1500 m, starting from the ground surface. To limit the horizontal extension and to avoid influences on the boundaries, lateral limits of the model have been fixed at a distance equal to about three times the width of excavations within 1250 block (~200 m) on each side. This restricts the extension of the model to a box of 1500 m side, where orebody, block 1250 and upper levels are placed in the middle (Fig. 5.1 on the right). The described geometry has been reconstructed with the Rhino software (v5.0), which also allowed a preliminary surface meshing of some elements of the model, as it will be later discussed.

The whole orebody shape (between 435 m and 1500 m depths) has been provided by mine geologist. On the contrary, the geometry of the excavations (i.e. galleries and stopes), as well as that of weak and very weak geological zones within block 1250 required an accurate and intensive work for their 3D reconstruction. A detailed description of the approach used for galleries and stopes reconstruction within block 1250 is provided in Annex B. Similarly, Annex C presents the approach used for building the 3D shape of weak and very weak geological zones.

Final result of galleries and stopes reconstruction is presented in Fig. 5.2. Stopes excavated between 2014 and December 2016 are color coded in function of the level to which they belong. In order to be as accurate as possible, and to avoid overestimations or underestimations of the volume of reconstructed stopes, several information, such as 3D laser scanner of mine voids, as well as drill holes coordinates for blasting design, have been used to refine stope geometries (see Annex B). In addition, stopes excavated between 2017 and 2018, as well as stopes which will be excavated in the future, have been added to the model (in gray in Fig. 5.2). In this manner, the here reconstructed

geometry will be also suitable for analyzing future scenarios of mine sequencing, which is although out of the scope of this thesis.

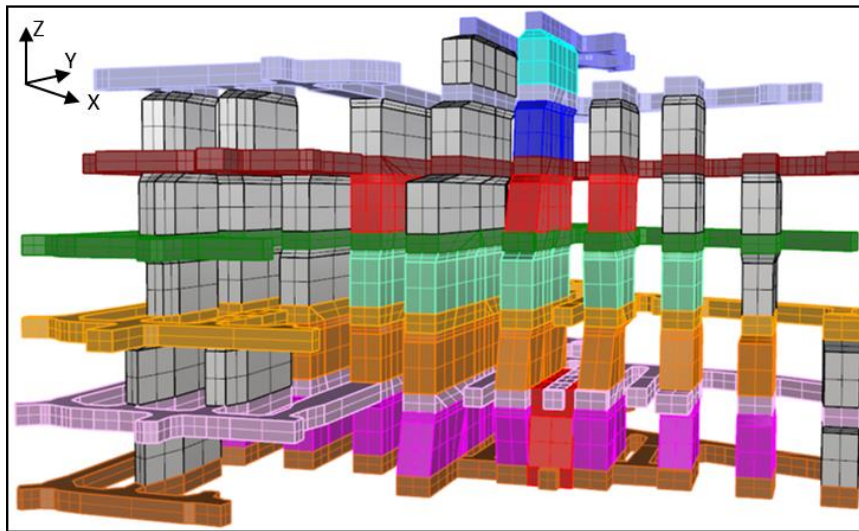


Fig. 5.2 - Galleries and stopes reconstruction in block 1250. See text for stopes color coding.

Weakness zones are modelled by mine geologists as 2D layers at each level of block 1250 (see Fig. 2.4 in Chapter 2). Therefore, the major difficulty in their reconstruction is that of building 3D profiles where no information is given on their extension in the vertical direction. As described in Annex C, weakness zones reconstruction was mainly aimed at reconnecting each weak lens between consecutive levels of block 1250, treating separately weak and very weak zones. The approach followed for the reconstruction had the objective of maximizing weak and very weak zones volumes, keeping their 2D shapes at each level of the mine as similar as possible to that proposed by mine geologists. The final result of 3D weakness zone geometry is presented in Fig. 5.3.

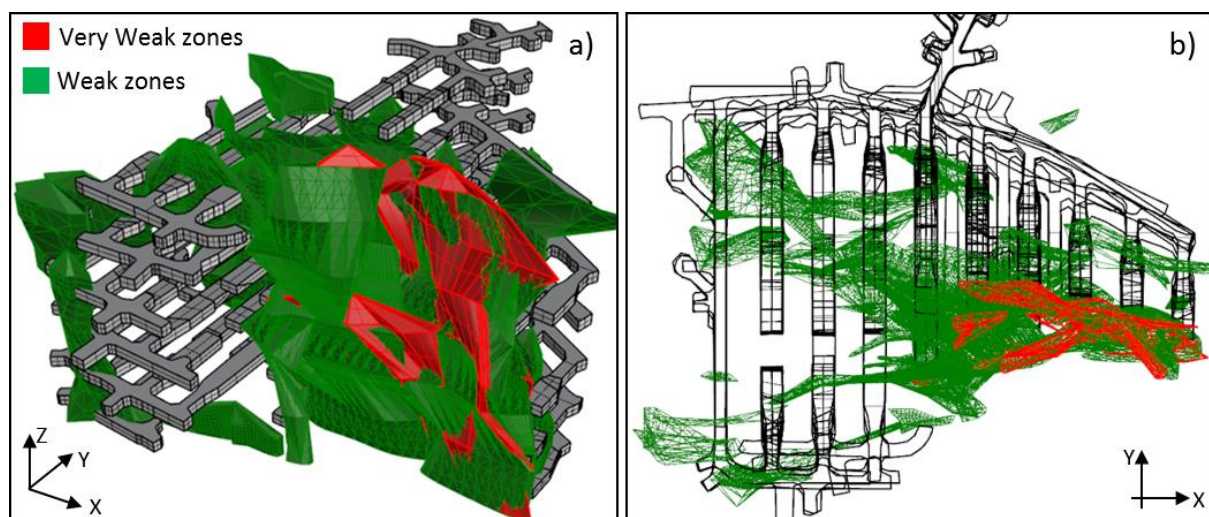


Fig. 5.3 - Weakness zones reconstruction in block 1250. (a) 3D view, (b) horizontal profile in the X-Y plane.

The proposed 3D geometry of weak and very weak zones is certainly a simplification of reality. However, based on the available geological information, this is the best possible approximation that can be done at this stage, and which is mandatory for running a 3D numerical model. It must be considered that 2D layers of weak and very weak zones are constantly updated by mine geologists

(Chapter 2). In this thesis, we refer to the geometry updated on October 2017 discarding any further change to this configuration.

### 5.3.2 Model meshing

Once the geometry of the model is finalized, model volume needs to be discretized, i.e. sub-divided in smaller elements (or meshes) needed for solving the partial differential equations. For this purpose, an automatic approach has been chosen by using the mesh generator Rhino plug-in *Griddle* (Dzik et al., 2017), which is more suitable than a manual FLAC3D meshing when many different elements with complex geometries are considered. A detailed description of automatic meshing procedure is provided in Annex D. Model mesh has been built at varying degrees of details. This means that the mesh has a high resolution (i.e. a small size) within the area of interest (i.e. block 1250) and it becomes coarser (i.e. larger) further away. Indeed, given the whole dimension of the numerical model, and considering computing time and memory needed for the storage of model results, it would not have been possible to maintain the same small mesh size for the whole model. This is neither necessary considering that the focus of the numerical model is on block 1250, where stress and strain induced by step-by-step stopes excavation need to be evaluated.

Based on these considerations, a maximum mesh size of 1 m has been chosen for discretizing the model in block 1250, which includes galleries and stopes (close-up of Fig. 5.4), as well as weak and very weak zones (close-up of Fig. 5.5).

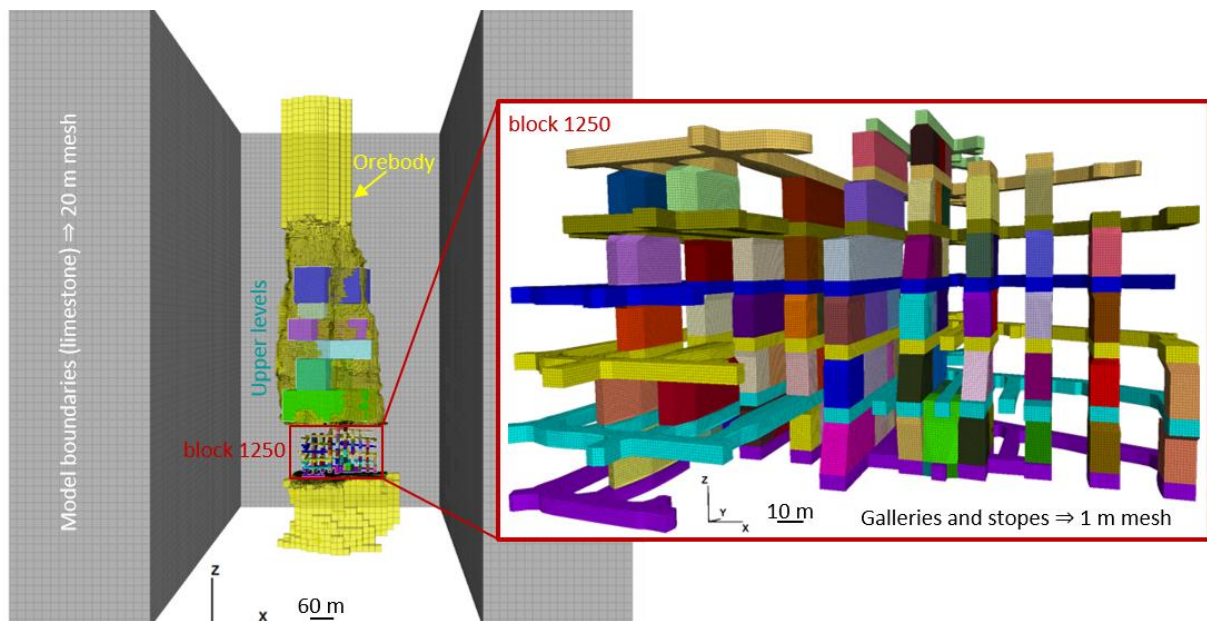


Fig. 5.4 - Final volumetric mesh of the whole numerical model. Note that, for a better visualization, the orebody, as well as weak and very weak zones, within block 1250 have been removed from the figure. The close-up shows geometry and mesh of 1250 block.

On the contrary, a 5 m mesh size has been chosen for the upper levels of the mine (Fig. 5.5), while the remaining model volume has been meshed at 20 m (Fig. 5.4). As it will be shown in Section 5.3.6, the adopted meshing strategy ensures a good resolution of model results within the area of interest, where discretization is small enough, and it guarantees reasonable computing time for running step-by-step simulations. The final 3D volumetric mesh consists of about 13.3 million elements, of which

more than the 98% is constituted by hexahedrons. This highlights a good mesh quality as hexahedral meshes ensures a better accuracy of model results with respect to tetrahedral meshes.

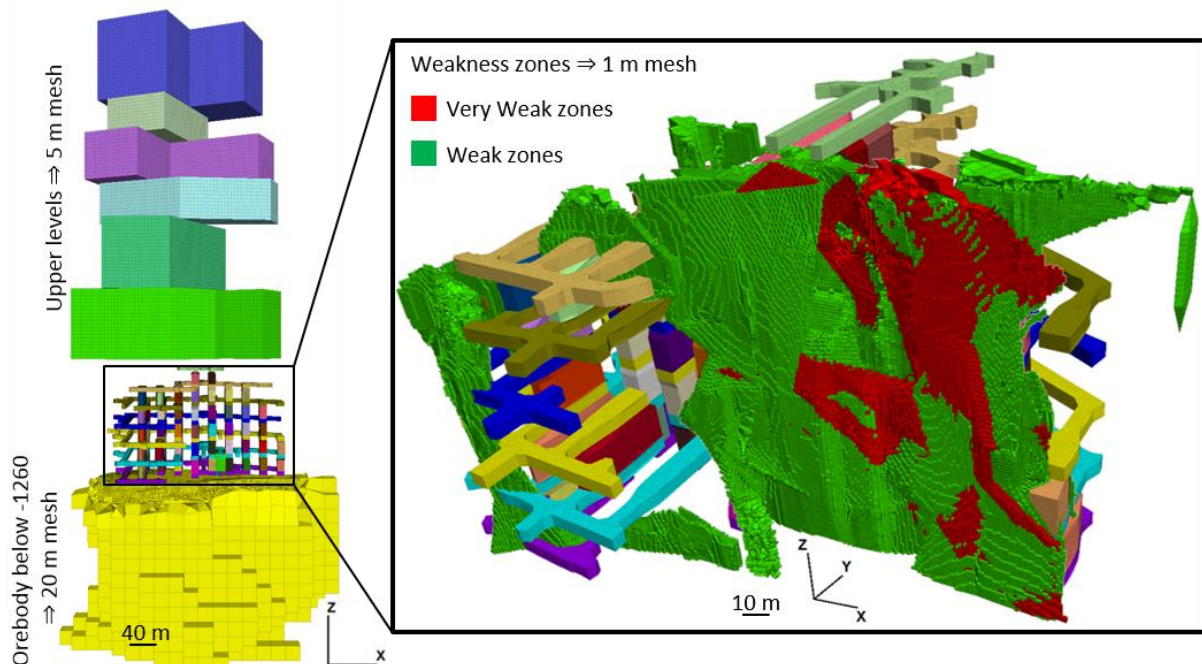


Fig. 5.5 - Upper levels, block 1250 and orebody (yellow) below -1260 m. The close-up shows weak and very weak zones meshes within block 1250.

### 5.3.3 Initial and boundary conditions

Initial and boundary conditions have a strong influence on model results and need to be carefully defined. Boundary conditions define constraints on the boundary nodes (or elements) of the numerical model, which need to be satisfied when solving the partial differential equations. In the framework of mechanical modelling, boundary constraints are generally defined in terms of stresses or displacements. Normal null boundary conditions have been chosen. This means that horizontal displacements within nodes located on the lateral limits of the model are fixed at zero, while, it is imposed that no vertical displacement can occur along the lower horizontal boundary. In additions, model borders have been designed far enough from the excavated area (Fig. 5.1) in such a way that boundaries do not have any effect on stress and displacement fields after each excavation.

Initial conditions refer to the in situ stress state before any excavation. This virgin state of stress is not easy to determine as it is specific for each site and dependent on numerous parameters like depth, density and mechanical properties of rock masses, as well as surrounding geological structures. Measurements of virgin stress are difficult and expensive as they have to be done at various locations and, preferentially, prior to underground excavation of large rock volumes. For these reasons, empirical relationships have been developed to determine virgin stresses at large scales both in terms of magnitude and orientation.

The most common approach used to determine the vertical stress ( $\sigma_v$ ), which is assumed to be one of the principal components of the stress tensor, relies on the hypothesis that, in the vertical direction, stresses are only influenced by the overburden weight. Based on this assumption, the vertical stress at a depth  $z$  within a rock mass of density  $\rho$  will be defined as:

$$\sigma_v = \rho g z \quad (5.1)$$

where  $g$  is the gravity.

Brown and Hoek (1978), by comparing measured vertical stresses across the world, showed that the vertical stress is on average varying linearly with depth, with a constant factor of 0.027 MPa/m and assuming an average specific weight ( $\rho g$ ) of the rock equals to 27 kN/m<sup>3</sup>. However, at shallower depths they observed a significant scatter of the measurements around the linear trend. Even though this theoretical model may not always be valid, it is widely employed in many fields of rock mechanics, thus, it will be adopted for Lappberget numerical model.

Horizontal stresses are much more difficult to estimate and cannot be calculated in general. However, assuming that the vertical stress is a principal component of the stress tensor, the other two principal directions must be horizontal and orthogonal to each other. Generally, horizontal stresses are expressed as a function of the vertical stress by the constants  $k_x$  and  $k_y$ , such that:

$$\sigma_h = k_x \sigma_v = \rho g k_x z \quad (5.2)$$

$$\sigma_H = k_y \sigma_v = \rho g k_y z \quad (5.3)$$

This means that horizontal stresses are as well a function of the depth. Numerous authors (e.g. Brown and Hoek, 1978; Sheorey, 1997; Terzaghi and Richart, 1952) worked on empirical relationships able to define the constants  $k_x$  and  $k_y$ , thus the ratios  $\sigma_h/\sigma_v$  and  $\sigma_H/\sigma_v$ . It is out of the scope of this work to present a wide literature on this argument, however, what is important to point out is that, when virgin stress measurements are available at a given underground location, stresses at other depths and in other proximal areas can be retrieved based on equations 5.1, 5.2 and 5.3, only knowing the rock mass density. Even if these equations are based on simplifying assumptions, they allow to initialize the stress state in the numerical model, which will be, thus, linearly variable with depth.

As described in Chapter 2, no direct measurement of the virgin stress state is available for Lappberget orebody, as the measurement campaigns took place after the beginning of mine excavations. For this reason, the virgin stress state adopted in the model is the one which was back-computed with numerical modelling by Souley et al. (2018), based on stress measurements carried out in December 2014 at a depth of -1155 m (Chapter 2, Section 2.2.2). This inverse problem approach allowed deriving a virgin stress state that is reminded in Tab. 5.2.

Tab. 5.2 - Back-computed virgin state of stress. This has been retrieved for a depth of -1155 m (Souley et al., 2018) and then initialized into the model.

$\sigma_1 (\sigma_y)$	$\sigma_2 (\sigma_x)$	$\sigma_3 (\sigma_z)$
47.3 MPa	44.4 MPa	34.3 MPa

The virgin stress state was retrieved by imposing a vertical stress equal to the overburden weight, in accordance with equation 5.1. The other two principal stress directions are horizontals, with the major and the intermediate stress oriented parallel and perpendicular to mine's drifts, respectively. These principal stress directions are in agreement with the ones determined during the Ineris stress measurement campaign at H2 cell (see the right side of Fig. 2.6, Chapter 2).

Based on the considered virgin stress state and according to equations 5.2 and 5.3, the constants  $k_x$  and  $k_y$ , which define the ratios between horizontal and vertical stresses, are taken equal to 1.38 and 1.29 along Y and X direction, respectively. This represents the stress gradient which will be initially set up into the model, prior to any excavation.

### 5.3.4 Modelled elements and mechanical effect of paste fill

Besides initial and boundary conditions, each model mesh needs to be described by specific mechanical properties. For doing so, each model mesh has to be prior assigned to a specific lithology. This has already been done by reconstructing and discretizing the orebody, as well as weak and very weak geological zones (Section 5.3.2). In addition, we assume that all the zones within the model which do not belong to the ore, neither to weak geological materials, are considered as limestone. Thus, the number of modelled geological structures is reduced to four: (i) the limestone, (ii) the ore, (iii) the weak zone and (iv) the very weak zone. Each lithological type considered in the model is assumed to be isotropic and characterized by homogeneous mechanical properties. Chosen properties per each modelled material will be presented and discussed in Section 5.3.5.

In addition to geological elements, large volumes of paste fill are present in block 1250, as well as in the upper levels of Lappberget orebody. Indeed, once primary stopes are excavated and mucked-out entirely, a slurry composed by waste rock and cement is pumped into the mined-out area. As illustrated in Tab. 5.3, the Young's modulus of this paste is much smaller than that of the excavated rock mass (i.e. the ore). This means that backfill mechanical influence could probably be neglected.

Tab. 5.3 - Elastic properties and density of paste fill and orebody.

Material	Young's modulus [MPa]	Poisson ratio	Density [kg/m <sup>3</sup> ]
Paste fill	500	0.2	2000
Orebody	66000		3030

To validate this assumption, a very simple model was built. Description and results of this model are presented in the following section.

#### 5.3.4.1 Mechanical effect and numerical modelling of paste fill

The excavation sequence of primary and secondary stopes was simulated, considering three primary stopes alternated by two secondary stopes, all laying at the same mine level (Fig. 5.6). An arbitrary depth of -1250 m was chosen for the lower level of the stopes, which are 25 m high and 10 m to 15 m wide for primary and secondary stopes, respectively (Fig. 5.6 on the right). Height and width have been chosen according to real stope dimensions. Along Y direction stopes have a length of 60 m which is equivalent to typical lengths of stopes in the central area of block 1250, such as for example Stope 13. Model boundaries have been fixed at a distance of 300 m on both sides along X direction, for a total length of 660 m. For simplicity, the same total extension has been chosen along Z and Y directions (Fig. 5.6 on the left). Model mesh within the stopes is fixed at 2 m and is gradually increasing with a ratio of 1.08 (of geometric progression) moving toward the boundaries (Fig. 5.6 on the left).

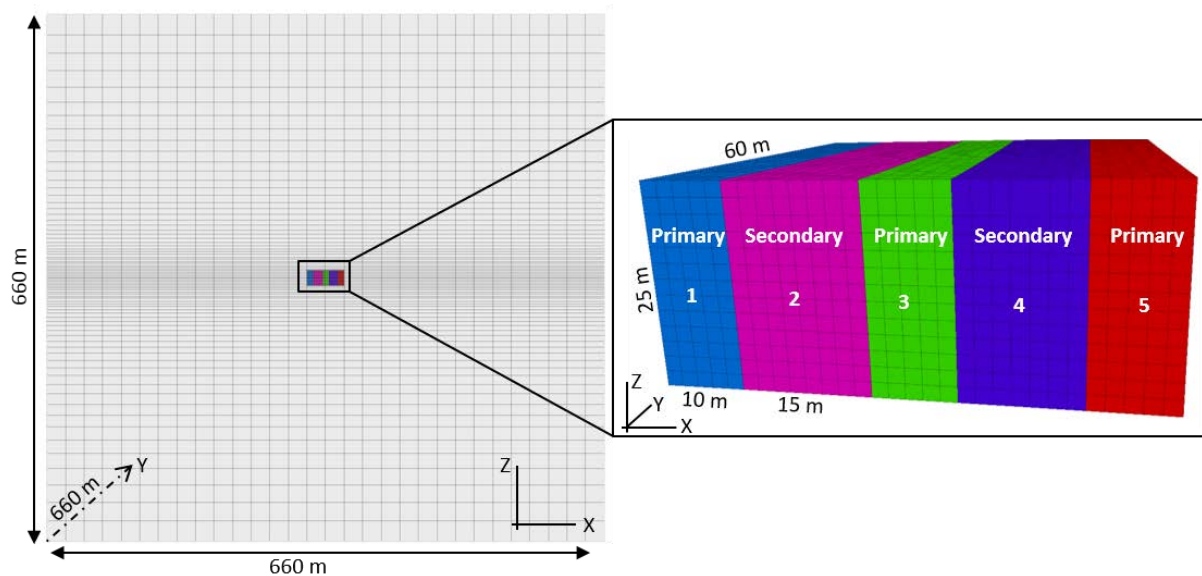


Fig. 5.6 - Geometry and mesh of the elementary model for paste fill influence evaluation. The whole model until the boundaries (on the left) and a close-up (on the right) showing the excavations.

The model simulates five excavation phases following a 1-3-5 sequence where primary stopes (1, 3 and 5) are excavated first, followed by secondary stopes (2 and 4). The complete sequence is summarized in Tab. 5.4, where, for each modelled step, the material that fills each stope is indicated. Basically, at each step, a stope is excavated, and the previous mined-out area is paste-filled (see for example step b in Tab. 5.4).

Tab. 5.4 - Summary of modelled mining sequence. “Void” means that the corresponding stope is excavated during the corresponding step, while “paste” indicates that the stope has been paste filled. “Rock” refers to not yet mined stopes.

Steps	Stope 1	Stope 2	Stope 3	Stope 4	Stope 5
a	void	rock	rock	rock	rock
b	paste	rock	void	rock	rock
c	paste	rock	paste	rock	void
d	paste	void	paste	rock	paste
e	paste	paste	paste	void	paste

To evaluate the influence of paste fill, two models have been run, considering different orebody types: a stiff one, which has same mechanical properties as the real orebody in block 1250 (Tab. 5.3), and a softer one, for which a 10-times smaller Young’s modulus ( $E_Y = 6.6$  GPa) has been chosen. Density is assumed the same for stiff and soft orebodies and is equal to  $3030 \text{ kg/m}^3$ .

Normal null displacements are prescribed to all boundaries, except the top where vertical stresses are imposed (compatible with initial stress state). The assumed initial state of stress is the one presented in Chapter 2 and which has been described in Section 5.3.3. This corresponds to a vertical principal stress of 36.75 MPa, at a depth of -1225 m, due to the overburden on top of the model. Maximum and intermediate horizontal principal stresses at the same mine depth equate to 50.2 MPa (along Y) and 46.55 MPa (along X), respectively.

Paste-fill is modelled assuming a linear elastic behavior based on Hooke's law, while for the orebody an elastoplastic constitutive law has been adopted, as proposed by Souley et al. (2018). This law is the one that will be adopted in the large-scale numerical model (Section 5.3.5).

Results of the two numerical models are summarized in Tab. 5.5. The table reports the mean maximum principal stress ( $\hat{\sigma}_1$ ), calculated within the paste-fill of primary stopes at the end of the excavation sequence, and its percentage increase with respect to the initial stress state, considering the two models and, thus, the two orebody types separately.

Tab. 5.5 - Summary of model results. See text for description. Blue color indicates results of the model where a stiff orebody has been considered, while red refers to the model with a soft orebody. Negative sign denotes compression.

Type of ore		Stope 1	Stope 3	Stope 5
Stiff ore	$\hat{\sigma}_1$ [MPa]	-0.37	-0.62	-0.31
Soft ore		-3.25	-5.46	-2.52
Stiff ore	$\hat{\sigma}_1/\sigma_1^{ini}$	0.7%	1.2%	0.6%
Soft ore		6.6%	10.8%	5%

Looking at the results, it appears that stress load within the paste fill directly depends on the stope walls convergence. The stiffer the orebody, the smallest the load in the paste fill. When a softer ore is considered, stresses in the paste fill increase significantly, where a difference of a factor of 10 in the stiffness of the orebodies implies a ratio of 7 on the stresses within the paste. Thus, in block 1250, where the orebody is characterized by stiff properties, the influence of stress field on the paste can be neglected. Based on these considerations, paste fill will not be taken into account when modelling excavations within block 1250. Once excavated, stopes will be considered as voids. Similar considerations have been made by other authors in the literature. As an example, Ziegler et al. (2015) neglected the presence of paste fill when simulating the stope-by-stope excavation in a deep gold mine, considering that the stiffness of the backfill is negligible compared to that of mined-out rocks.

### 5.3.5 Constitutive laws and mechanical properties

Boliden company has carried out numerous laboratory tests in order to characterize the mechanical parameters of the limestone and the ore. However, due to the observed heterogeneity of these formations, values can be extremely different from one measurement to the other, as reported in Tab. 5.6. On the contrary, material properties for weakness zones are only poorly known. It has to be reminded that weakness zones are quite complex to define from a geological point of view, as they cannot be referred to a single specific lithology or mineral type (see Chapter 2 for more details). Roughly, these areas can be considered as schist lenses with a large amount of soft minerals, such as talc. The sole study that reports some mechanical parameters of the talc is the work of van Koppen (2008), whose results are summarized in Tab. 5.6.

Based on the available data, it is challenging to choose consistent mechanical parameters which can describe the rock mass properties in a large-scale numerical model. Thus, some assumptions must be made. Firstly, it has been decided to adopt mean values for the reported mechanical parameters of limestone and ore. Then, the available parameters for the talc have been affected to the weak zones



of the model. Considering that very weak zones can be defined as weak zones where the amount of schist and talc is much higher, these areas will be characterized by stronger foliation and lower stiffness than weak zones. For this reason, and based on the available talc properties, we have assumed a Young's modulus ( $E_V$ ) of very weak zones 10 times smaller than that reported for the talc, a three-time smaller compressive strength ( $\sigma_c$ ) and a Poisson's ratio ( $\nu$ ) higher of a factor of 1.3 (Tab. 5.7). This is in accordance with compressive strength values reported by Hoek and Brown (1997), who estimates  $\sigma_c < 25$  MPa for very weak rock types. Similarly, the authors report  $E_V$  values significantly lower than 10 GPa for poor-quality rock masses.

Tab. 5.6 - Variability in material properties as retrieved from Boliden analysis. Note that biaxial test results presented in Chapter 2 are as well considered in this table.

<i>Materials</i>	<i>Young's modulus <math>E_V</math> [GPa]</i>	<i>Poisson's ratio <math>\nu</math></i>	<i><math>\sigma_c</math> [MPa]</i>	<i>Density <math>\rho</math> [kg/m<sup>3</sup>]</i>
Ore	44 - 90	0.15 - 0.25	175 - 200	3000 - 3331
Limestone	55 - 60	0.12 - 0.25	100 - 120	2714 - 2722
Talc	20	0.3	30	-

It would have been suitable to perform a parametric analysis on rock mass properties, to evaluate the effects of their variations on model results. However, due to the complexity of the model and, thus, the time needed for the computation, this analysis has been discarded at this stage.

Tab. 5.7 - Retained mechanical parameters for numerical modelling.

<i>Materials</i>	<i><math>\sigma_c</math> [MPa]</i>	<i>Density <math>\rho</math> [kg/m<sup>3</sup>]</i>	<i>Elastic parameters</i>		<i>Hoek-Brown parameters</i>	
			<i>Young's modulus <math>E_V</math> [GPa]</i>	<i>Poisson's ratio <math>\nu</math></i>	<i><math>m</math></i>	<i><math>s</math></i>
Ore	188	3030	66	0.2	10	0.112
Limestone	110		57	0.18	10	0.112
Weak	30		20	0.3	1	0.001
Very weak	10		2	0.4	0.63	0.00024
Pastefill	-	2000	0.5	0.2	-	-

Where  $\sigma_c$  is the rock mass compressive strength, while  $m$  and  $s$  are the constants which define the Hoek and Brown failure criterion.

The density in the model has been assumed the same for all the considered geological materials and equals to the ore density (Tab. 5.7). This assumption, which is obviously in disagreement with the real volumetric mass of rocks, is purely motivated by numerical issues. Indeed, having imposed a homogenous stress gradient (Section 5.3.3), variations in the rock mass density would result in local variations of the vertical stress (equation 5.1) and, in turn, of the horizontal stresses (equations 5.2 and 5.3). Thus, the model will not be at the equilibrium prior to simulated excavations and it would require an additional modelling step to reach an initial equilibrium. The assumption of a constant density for the whole modelled elements avoid this numerical issue and this only poorly impacts the rock mass behavior after each simulated excavation, where the heterogeneity of the rock mass is taken into account thanks to the other mechanical parameters, which are significantly different for each geological element.

A first test model was run assuming a linear elastic behavior of all the materials in the model. Then, in a second model, we assumed two different plastic constitutive laws: (i) a perfectly plastic law with a parabolic failure criterion (Hoek and Brown, 1997) and (ii) an elastoplastic law which takes into account the brittle behavior of rocks (Souley et al., 2018).

The Hoek and Brown failure criterion can be described by the following equation:

$$\sigma_1 = \sigma_3 + \sigma_c \sqrt{m \frac{\sigma_3}{\sigma_c} + s} \quad (5.4)$$

where  $\sigma_1$  and  $\sigma_3$  are the major and the minor principal stresses, respectively, while  $\sigma_c$  is the uniaxial compressive strength of the intact rock and  $m$  and  $s$  are rock mass constants. These latter constants can be assessed based on the following empirical relations (Hoek and Brown, 1997):

$$m = m_i \exp\left(\frac{GSI - 100}{28}\right) \quad (5.5)$$

$$s = \exp\left(\frac{GSI - 100}{9}\right) \quad (5.6)$$

where  $m_i$  is the Hoek-Brown constant and  $GSI$  is the Geological Strength Index. Note that equations 5.5 and 5.6 are only valid for  $GSI > 25$ . The  $m_i$  constant for Lappberget materials has been chosen based on the values provided by Hoek (2001), who listed this parameter for different rock types (Tab. A.4). Similarly, the  $GSI$  has been estimated based on Tab. A.5, where parameter values are listed as a function of rock mass structure and heterogeneity. Chosen values of these latter parameters are reported in Tab. 5.8, while  $\sigma_c$  and the resultant values of  $m$  and  $s$  are listed in Tab. 5.7 for each modelled material.

Tab. 5.8 - Chosen values of  $m_i$  and  $GSI$  for modelled materials.

<i>Materials</i>	$m_i$	$GSI$
Ore	20	80
Limestone		
Weak	9	38
Very weak		25

Based on the estimated parameters and following equation 5.4, the parabolic failure criterion for ore, limestone, weak and very weak zones (seen as rock masses and not as rock types) is presented in Fig. 5.7.

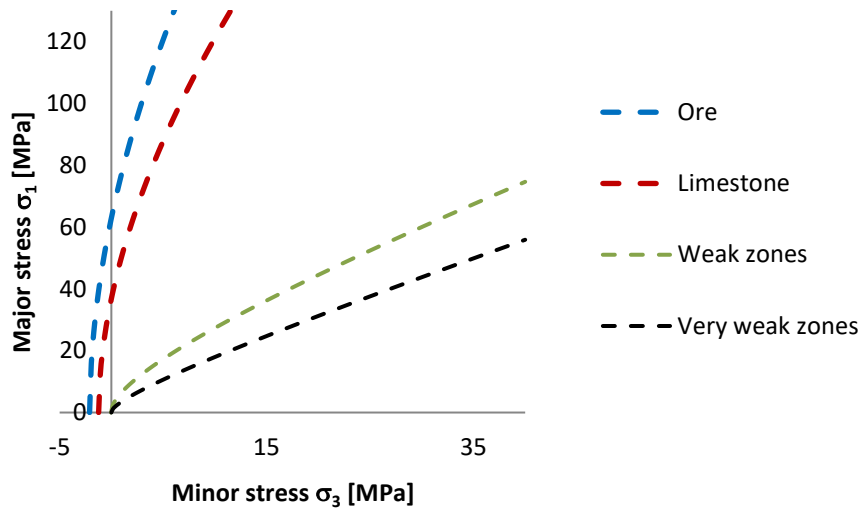


Fig. 5.7 - Hoek and Brown failure criterion for Lappberget modelled materials.

Lappberget ore is a stiff rock mass and a brittle behavior in the post-failure phase can be expected. According to Hoek and Brown (1997) and as illustrated in Fig. 5.8, this type of good quality rocks deviate from the elastic behavior for higher stress levels (Fig. 5.8c) compared to soft (Fig. 5.8a) or “average quality” (Fig. 5.8b) rocks but, once the peak-stress reached, rock strength decreases dramatically and fractures occurs without any prior plastic strain. When a residual strength is reached, plastic flow occurs at constant stresses.

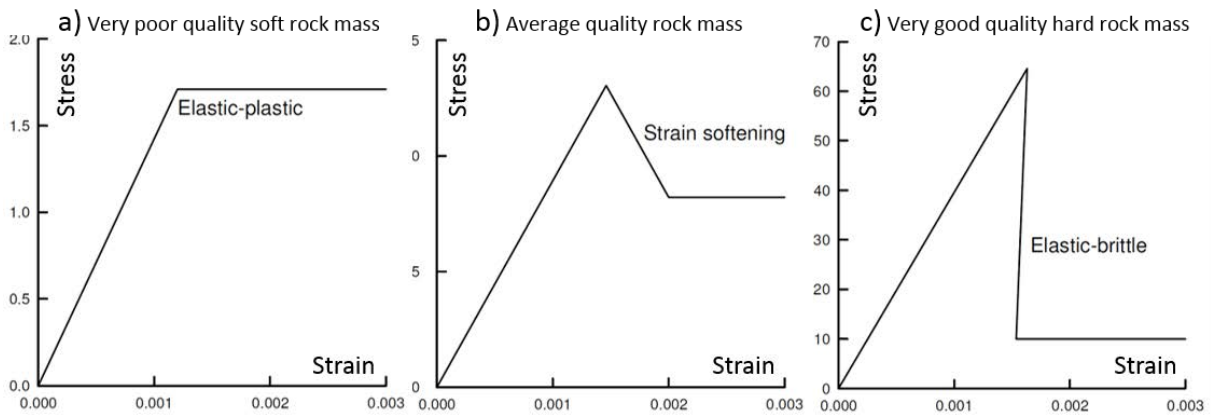


Fig. 5.8 - Illustration of post-failure behaviors for different rock mass qualities (after Hoek and Brown, 1997).

Souley et al. (2018) have developed a non-linear constitutive model which modifies the Hoek and Brown criterion by means of the stress tensor invariants ( $J_1, J_2, J_3$ ), more precisely considering the mean stress ( $p$ ), the deviatoric stress ( $q$ ) and the Lode’s angle ( $\theta$ ). The failure criterion ( $F_s$ ) proposed by these authors is, thus, written as follow:

$$F_s = \frac{4 \cos^2 \theta}{3} \frac{q^2}{\sigma_c} - m \left( \frac{\cos \theta}{\sqrt{3}} - \frac{\sin \theta}{3} \right) q + mp - s\sigma_c \quad (5.7)$$

where  $\theta = \frac{1}{3} \arcsin \left( \frac{-3\sqrt{3}}{2} \frac{J_3}{J_2^{3/2}} \right)$ ,  $p = \frac{tr(\sigma)}{3}$  and  $q = \sqrt{3J_2}$ , with  $tr(\sigma)$  the trace of the stress tensor  $\bar{\sigma}$ .

The described constitutive law was tested and applied by Souley et al. (2018) to the case of Garpenberg mine, with a small-scale 2D numerical model and a large-scale 3D model which focused

on the area of block 1250, but which was 3 times smaller than the 3D numerical model built in this thesis. The authors clearly showed that the proposed law is able to better predict strains and plastic zones localizations around simulated excavations than a classical Hoek and Brown law. This represents a clear advantage for identifying the extent of damaged zones induced by mining and thus for a better accuracy of model results. For this reason, it has been decided to adopt the constitutive law proposed by Souley et al. (2018) for modelling the orebody behavior in the elastoplastic numerical model. In contrast, limestone, weak and very weak zones will be modelled by the Hoek and Brown failure criterion. Additional parameters needed for applying the described constitutive model are listed in Tab. 5.9 together with the selected values for Lappberget ore as suggested by Souley et al. (2018).

Tab. 5.9 - Additional parameters needed for the constitutive law applied to Lappberget ore. For a detailed description of each parameter and selected values, the reader should refer to Souley et al. (2018).

<i>Materials</i>	$m_r$	$\sigma_3^{b-d}$ [MPa]	$s_r$	$\xi_r$	$b_1$	$\beta_m$
Ore	2	$\sigma_c \sqrt{s}$	$s * 10^{-5}$	0.0025	$\tan(15^\circ)$	750

Note that  $\sigma_c$  and  $s$  values are listed in Tab. 5.7

As already discussed in Section 5.3.4.1, the influence of paste fill is neglected within modelled excavations of block 1250. However, due to the large amount of extracted rock mass above block 1250 (Fig. 5.1 and Fig. 5.5), it has been preferred to refill the upper levels with paste, rather than leave them as voids. The paste fill is then treated like an elastic material. Elastic parameters for the paste, which are reported in Tab. 5.7, were retrieved from previous studies provided by Boliden (van Koppen, 2008). In this case, we have assumed a different density for the paste with respect to that of the other materials, because paste is not present prior to excavations and does not have any influence on the mechanical equilibrium of the model during the consolidation phase.

### 5.3.6 Simulated mining sequence

As already discussed, numerical modelling aims at analyzing the impact of stopes production in block 1250 on surrounding rock masses. In addition, we are as well interested in comparing modelling results with microseismic data analysis. For these reasons, the mining sequence applied in this area of the mine, from the installation of the microseismic monitoring network (February 2015) until the end of December 2016, was reproduced in the model in a step-by-step excavation sequence. This corresponds to a total of 52 excavated stopes which were simulated as many modelling stages.

As shown in Chapter 4, galleries excavation has only little impact on the induced seismicity, thus, it is reasonable to think that their influence on stress redistribution is neglectable and limited to galleries walls. This was already demonstrated by Souley et al. (2018) who reported a maximum extension of the plastic zone induced by galleries excavation of 20 and 30 cm at the roof and the floor of galleries, respectively. For this reason, in a first attempt, the excavation of mine galleries within block 1250 was simulated in a single initial step of the modelling. However, when dealing with the elastoplastic model, this resulted in numerical errors which caused crashing of the computation. This particularly occurs when galleries are excavated within geological elements characterized by different mechanical properties (e.g. orebody and weak zones), which results in large strains along the borders between dissimilar materials. This introduces geometry errors when the displacement of a given grid point exceeds the mesh size of the element to which it belongs. Moreover, when mine galleries are all excavated in a single step, large stress changes are imposed instantaneously. This in turn

generates large strains and displacements, which results in bad geometries and thus in the crashing of the computation. To avoid these issues without including any additional step to the model, galleries excavations were simulated within the aforementioned 52 modelling steps, in function of the date of their excavation. Thus, each step considers one excavated stope and the galleries developed during the time between the actual step and immediately before the next step. Fig. 5.9 shows the step-by-step excavation simulation where each stope and slice of galleries are color coded as a function of the step to which they belong.

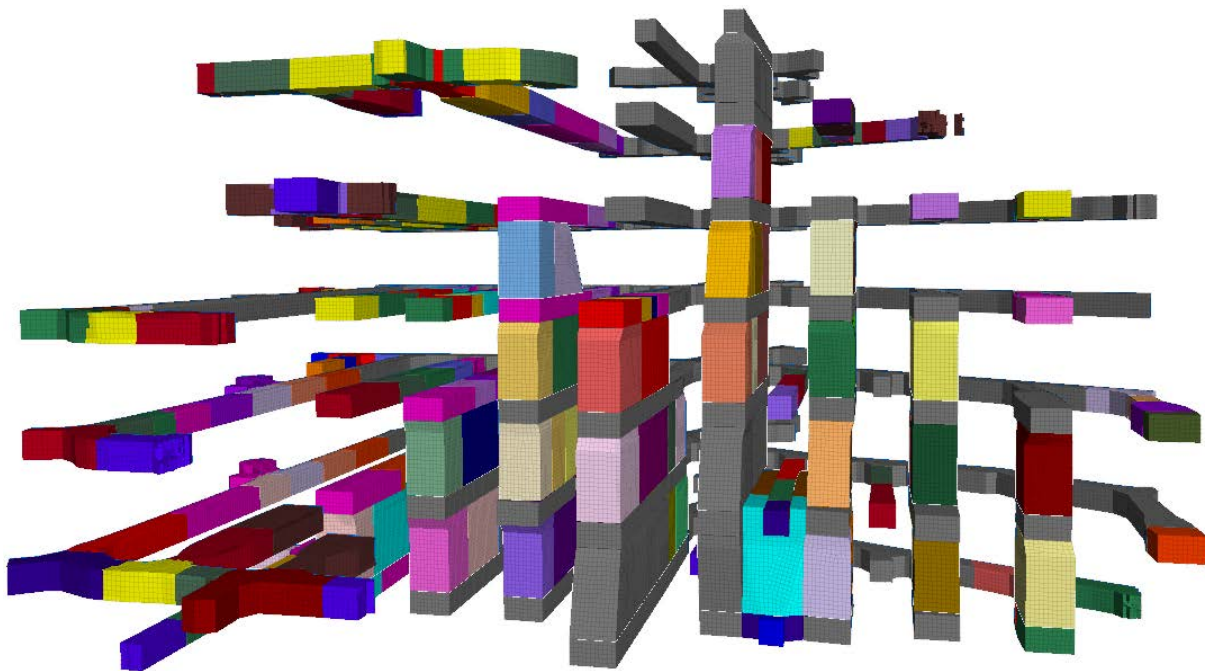


Fig. 5.9 - Step-by-step galleries and stopes excavation in the numerical modelling. Dark gray stopes and galleries refer to excavation performed before February 2015.

The modelling sequence is characterized by 14 additional steps executed prior to the 52 already described steps. At step 0.0, the model is consolidated by initializing the stress gradient, as discussed in Section 5.3.3. In addition, at the same step, the upper levels are excavated block by block and then backfilled with paste. Steps from 0.1 to 0.13 simulate the excavation of stopes and galleries mined-out in block 1250 before February 2015. This corresponds to the excavation of 13 sub-stopes (within Stope 13 and Stope 15) and a large volume of galleries, which are reported in dark gray in Fig. 5.9. Then follow the 52 steps of excavation within block 1250. The complete simulated mining sequence is summarized in Tab. A.6, where the list of stopes excavated at each step is reported together with the corresponding volume of extracted rock.

With the described modelled mining sequence, four different mechanical models were performed. First, a test model was run, considering a linear elastic constitutive law for all materials. This was needed for testing model geometry, to ensure that no gaps or overlaps between elements were introduced. Then, three elastoplastic mechanical models were performed with the following differences (see also table Tab. 5.10):

- Plastic Model #1  $\Rightarrow$  the area of interest (block 1250) is meshed at 2 m and same mechanical properties are applied to very weak and weak zones, assuming weak zones properties as reported in Tab. 5.7.

- Plastic Model #2 ⇒ different mechanical properties have been assumed for weak and very weak materials (see Tab. 5.7), while mesh size has been kept at 2 m.
- Plastic Model #3 ⇒ the mesh of the area of interest has been reduced to 1 m, considering mechanical properties assumed for Plastic Model 2.

Tab. 5.10 - Differences between performed plastic models.

	Plastic Model #1	Plastic Model #2	Plastic Model #3
Mesh size	2 m	2 m	1 m
Mechanical properties	Same properties for weak and very weak zones	Different properties for weak and very weak zones	Different properties for weak and very weak zones
Total n° of zones	3 378 262		13 334 776
Computing time	~5 days		~10 days
Storing capacity	461 Go		1.7 To

As summarized in Tab. 5.10, with the area of interest meshed at 2 m (plastic models #1 and #2), the whole model presents a total of 3 378 262 zones with 2 458 165 nodes, for a computation time of about 5 days and a hard drive space for storing results of 461 Go. In contrast, when the area of interest is meshed at 1 m (Plastic Model #3), the whole model is characterized by 13 334 776 zones with 9 995 828 nodes, which takes about 10 days of computation and 1.7 To of storing capacity. It appears evident that the last model is much more computational-intensive than that meshed at 2 m. However, when comparing results, Plastic Model #3 appears much more accurate than Plastic Model #2. To give an example, Fig. 5.10 shows the deviatoric strain, or Von Mises equivalent strain, computed at the last step of the simulated mining sequence (Step 52) on a vertical section at  $y = 460$  m for plastic models #2 (Fig. 5.10a) and #3 (Fig. 5.10b). It is here reminded that the deviatoric strain is a scalar which depends on the principal strains ( $\epsilon_1$ ,  $\epsilon_2$  and  $\epsilon_3$ ):

$$\epsilon_q = \frac{2}{3} \sqrt{\frac{1}{2} [(\epsilon_1 - \epsilon_2)^2 + (\epsilon_1 - \epsilon_3)^2 + (\epsilon_3 - \epsilon_2)^2]} \quad (5.8)$$

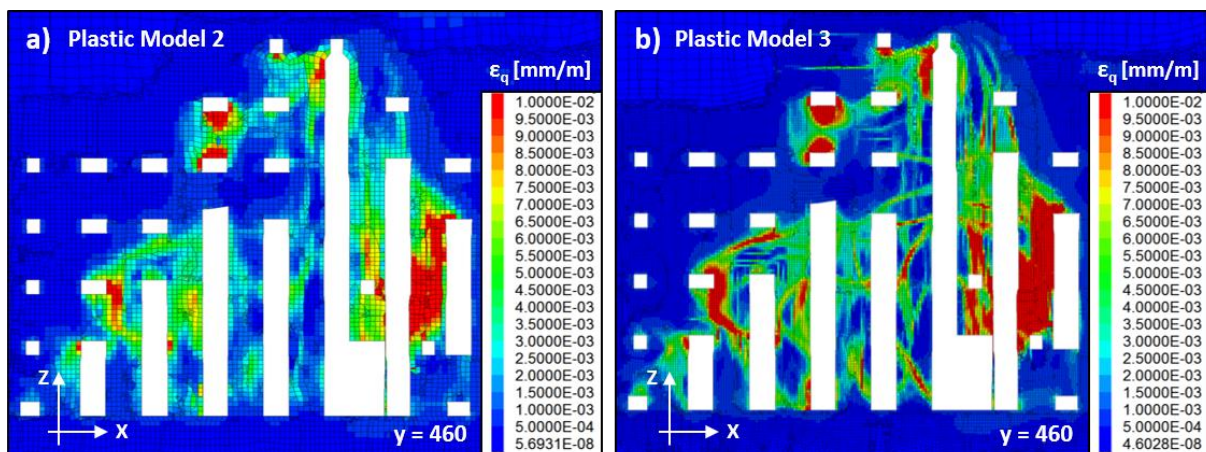


Fig. 5.10 - Comparison between Plastic Model #2 and #3. (a) Von Mises equivalent strain ( $\epsilon_q$ ) on a vertical section ( $y = 460$  m) computed at Step 52 for Plastic Model #2. (b) The same as in (a) but for Plastic Model #3.

For both models, higher strains are observed in secondary stopes between major excavated zones, but Plastic Model #3 clearly shows bands of strain localizations which are not visible in Plastic Model

#2. The effect of mesh size is thus extremely important for the identification and the estimation of the excavation damaged zone (EDZ), which appears much more defined when a finer mesh is considered. For this reason, analysis and interpretation of numerical modelling results, which are presented in Section 5.5, will be only referred to Plastic Model #3 that allows a better resolution.

## 5.4 Comparison with in situ geotechnical measurements

To verify the consistency of our numerical model with field observations, results of Plastic Model #3 were compared with stress shifts measured by CSIRO cells, as well as with extensometer data, both presented in Chapter 2 (Sections 2.4.1 and 2.4.2) and discussed together with microseismic activity in Chapter 4 (Section 4.4).

For doing a quantitative comparison between model results and measured strain shifts, at each simulated step of the model, strain and stress tensors were retrieved from the model zones coincident with the location of PH and PD cells. Then, as strain and stress changes are measured by CSIRO cells, cartesian components of stress and strain tensors at a given excavation step are subtracted from those of the previous stage. This exercise has been done for all model steps in coincidence of which strain shifts were recorded by CSIRO cells, resulting in comparing 15 model steps at PH location and 14 at PD. Results are reported in Fig. 5.11 in terms of mean stress ( $p$ ), for measured and modelled stress shifts at PD (Fig. 5.11a) and PH (Fig. 5.11b). The choice of the mean stress as variable for the comparison is simply motivated by its easier graphical representation, where all normal stresses can be analyzed together.

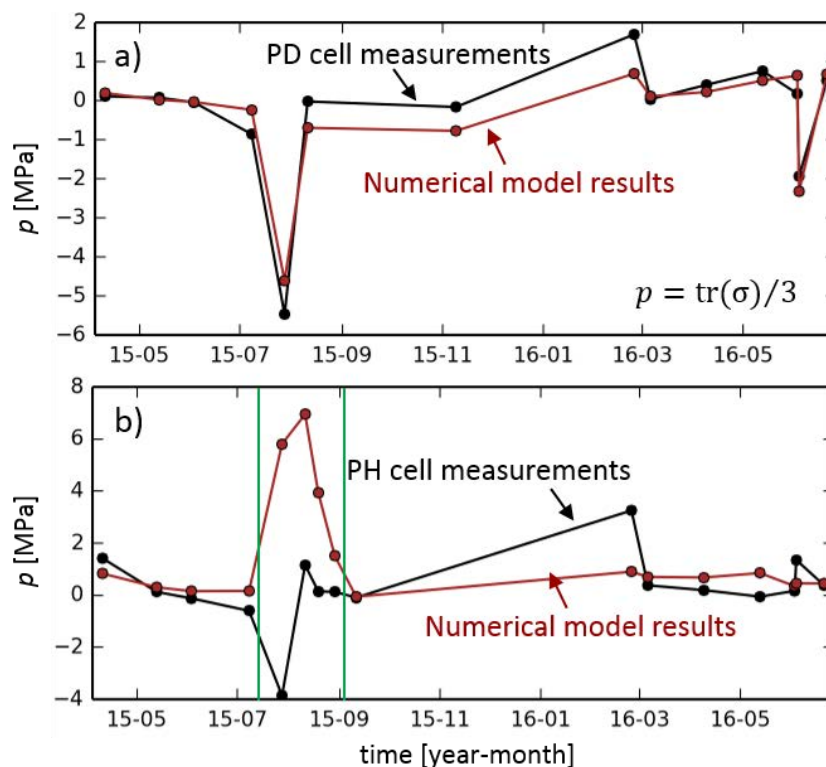


Fig. 5.11 - Comparison between model and CSIRO cells data. Values are reported in term of mean stress for model (in red) and measured (in black) stress shifts at PD (a) and PH (b). Green rectangle in (b) underlines 4 modelled steps which present larger differences between model estimates and measured stresses.

Model results are strongly consistent with measurements at PD cell location (Fig. 5.11a), which demonstrate a very good agreement between model estimates and field measurements. This is as well observed when considering separately each normal stress, or when comparing principal stresses (not shown). The average difference (Frobenius norm<sup>2</sup>) between model and measured stresses at PD is of 1.5 MPa. On the other hand, a larger scatter is observed for model results at PH cell location (Fig. 5.11b), particularly for four modelled steps between the end of July and August 2015 (highlighted by a rectangle in Fig. 5.11b). Similarly, the stress shift recorded at the end of February 2016 (Fig. 5.11b) appears underestimated by the model, which gives a means stress of 0.9 MPa with respect to 3.25 MPa measured at PH cell. On average, the difference (Frobenius norm) between model and measurements at PH cell location is of about 7 MPa. These results highlight a better accuracy of model estimates at PD cell location with respect to PH. Possible explanations for this trend may include model geometry oversimplifications in proximity of PH cell, in term of mechanical parameters and/or weak geological zones reconstruction. In addition, this could also be explained by the presence of geological structures near PH cell, not considered in the model, causing local variation of the stress field. Finally, inaccuracies of PH measurements, and/or of stresses retrieved by inversion, must also be considered. Indeed, as observed in Chapter 4 (Fig. 4.21), PD measurements showed a good stability throughout the analyzed period, while PH presented an unstable trend starting from July 2015 and with a progressive stabilization from March 2016, indicating the occurrence of plastic strains. The 5 modelled steps which show larger differences with respect to PH data (Fig. 5.11b) are in coincidence with this period of unstable measurements. If plastic strains occur, the elastic assumption made for determining the stress tensor from strains measured at PH (see Chapter 2, Section 2.4.2) is not valid, and larger uncertainties are introduced in the stress estimation. This means that stresses retrieved from PH measurements must be regarded with caution and that PD stress estimates are more reliable, indicating a good consistency of model results with field data.

To further validate model accuracy, results were also compared with extensometer data. For doing so, coordinates of extensometer anchors have been introduced into the model, determining their relative displacement with respect to the extensometer head at each modelled step. Then, extensometer readings have been compared with model estimates. Results are presented in Fig. 5.12 for the anchors at 2.5 m, 8 m and 14 m from extensometer head. Globally we observe a good match of model data with field observations. Best results are obtained for central anchors, as the one at 8 m (Fig. 5.12b). This measuring point reached the same displacement as field data at the end of the analyzed period, showing a total displacement of 28.5 mm, which is strongly in agreement with the measured displacement of 29.07 mm. This indicate that model results are coherent with field observations, especially at distances from about 8 m to 10 m from gallery walls. Results for the anchor at 2.5 m (Fig. 5.12a), which is closer to the gallery, show a slight overestimation of model results with respect to displacements observed at the extensometer. This is particularly observed at Step 21 (indicated by an arrow in Fig. 5.12a), where the displacement calculated by the model is more than three times larger than that observed on the measurements. A possible explanation for

---


$$^2 \text{ Frobenius norm} = \sqrt{(\Delta\sigma_{max}^{model} - \Delta\sigma_{max}^{measure})^2 + (\Delta\sigma_{int}^{model} - \Delta\sigma_{int}^{measure})^2 + (\Delta\sigma_{min}^{model} - \Delta\sigma_{min}^{measure})^2}$$



the observed trend may be the presence of reinforcements (e.g. bolts) in the mine, which reduce displacements in proximity to galleries, that are although not considered in the model. On the contrary, model results for the anchor at 14 m (Fig. 5.12c) are underestimated with respect to extensometer readings. At the end of the analyzed period, model displacements are almost two times smaller than real observations. A possible explanation for the observed trend may be the close position of the considered measurement point from Stope 13 (see figure Fig. 5.12d), where large voids are created due to production. The effect of voids is thus much more important at smaller distances, where fractures within the rock mass can occur, and is reduced with the distance from production area. The proximity to Stope 13 have a direct impact on measured displacements that, at the end of the analyzed period, are almost three time larger at anchor 14 (located at less than 5 m from Stop 13) than that observed at anchor 2.5. Displacements calculated by the model are also increasing with the distance from the extensometer head, but less significantly.

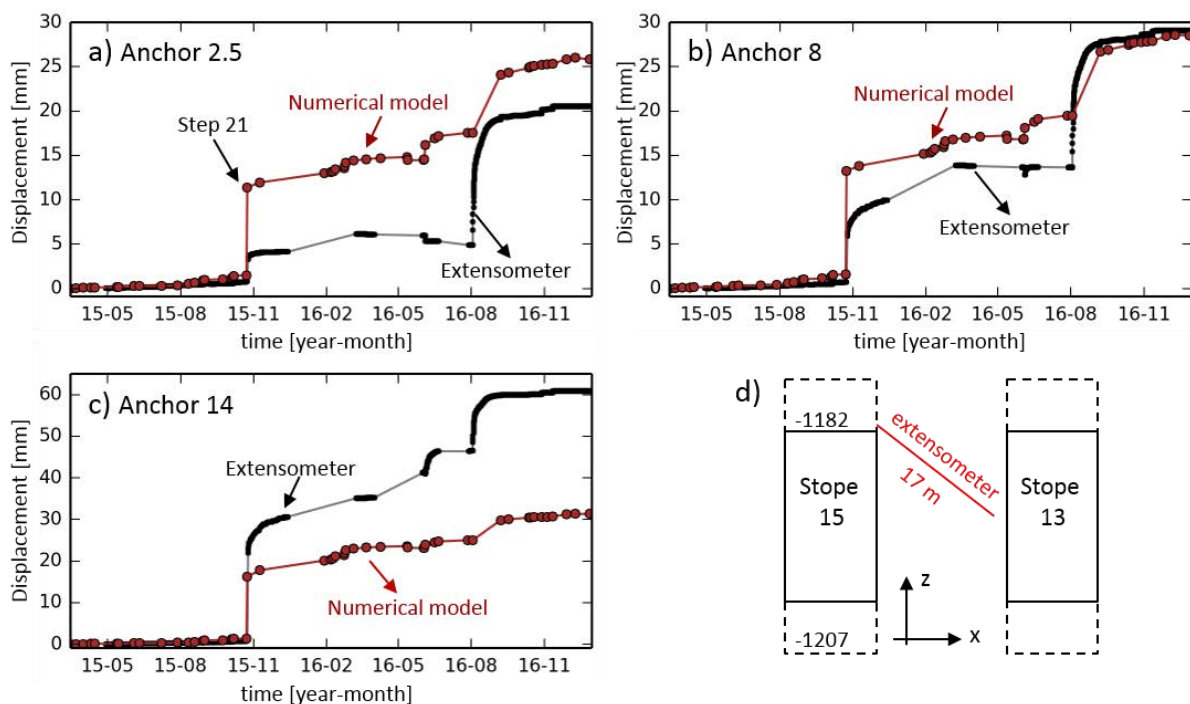


Fig. 5.12 - Comparison between model and extensometer data. (a) Displacements retrieved by numerical modelling and measured by the extensometer for the anchor at 2.5 m. (b) The same as in (a) but for the anchor at 8 m. (c) The same as in (a) but for the anchor at 14 m. (d) Schematic vertical profile showing the position of the extensometer between stopes 13 and 15. Dashed rectangles represent galleries. The extensometer has a total length of 17 m.

## 5.5 Model results and interpretations

When performing large scale numerical models, the analysis of results is not straightforward due to the enormous amount of available data. This is even more problematic when the objective of modelling is the comprehension of the rock mass response to mining for several exploitation stages and at the scale of a whole mine block. Moreover, the complexity of the excavation geometry in Lappberget orebody imposes to analyze data in 3D and to consider their evolution with time. This means that a detailed analysis of model results at each of the 52 simulated steps and for each of the 7 levels of 1250 block is clearly unrealistic. For these reasons, we will particularly focus on some

selected exploitation stages at some selected levels of the mine, analyzing stresses, strains and plastic deformation calculated by numerical modelling.

It is here reminded that each step of the model corresponds to the excavation of a single stope's block. Tab. 5.11 reports dates and extracted stopes for some steps of the model which will be discussed in the current section. For the complete list of extracted stopes and corresponding model steps, the reader is referred to Tab. A.6.

Tab. 5.11 - Some selected model steps and mined-out stopes.

Date	Model step	Mined-out stope
2015-02-07	Step 0.13	13_1257 #3
2015-07-28	Step 11	13_1157 #3
2015-08-31	Step 15	17_1232 #1
2015-10-24	Step 21	13_1207 #3
2016-02-09	Step 25	19_1232 #1
2016-02-25	Step 29	13_1182 #1
2016-05-13	Step 34	17_1207 #2
2016-06-21	Step 39	15_1207 #2
2016-08-03	Step 41	13_1182 #3
2016-12-28	Step 52	17_1182 #2

As a reminder, and for helping in the comprehension of the figures which will be shown in the current section, Fig. 5.13 shows the position of extracted stopes for two model steps. At the time of Step 0.13 (Fig. 5.13a) the seismic monitoring network was not yet operational and only few stopes were already mined-out. While, Step 52 (Fig. 5.13b) corresponds to the last modelled step at the end of the study period.

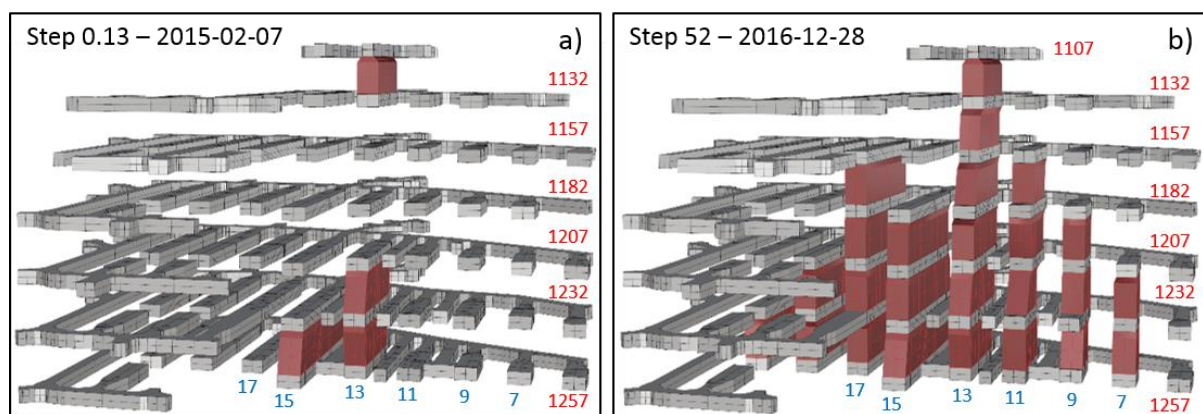


Fig. 5.13 - Mining sequence at model step 0.13 and 52. Red blocs indicate excavated stopes. Blue numbers refer to stope names, while red number indicate mine levels.

### 5.5.1 Analysis of stress distribution

Fig. 5.14a shows the distribution of the  $\sigma_{XX}$  component of the stress tensor (hereafter called “horizontal stress”) at the end of Step 0.13, when only few stopes were excavated in block 1250. Stresses are presented for a vertical section at  $y = 460$  m, which is approximately in the middle of block 1250. Excavation results in the relaxation of the horizontal stress within secondary stopes on

the sides of mined-out primary stopes. Stresses are predominantly compressive (negative sign indicates compression), even if some areas with tensile values are observed close to stope walls and within secondary stopes that have not been extracted yet. The highest compressive stresses, which reach more than 100 MPa, are observed at the top and at the bottom of extracted stopes and galleries.

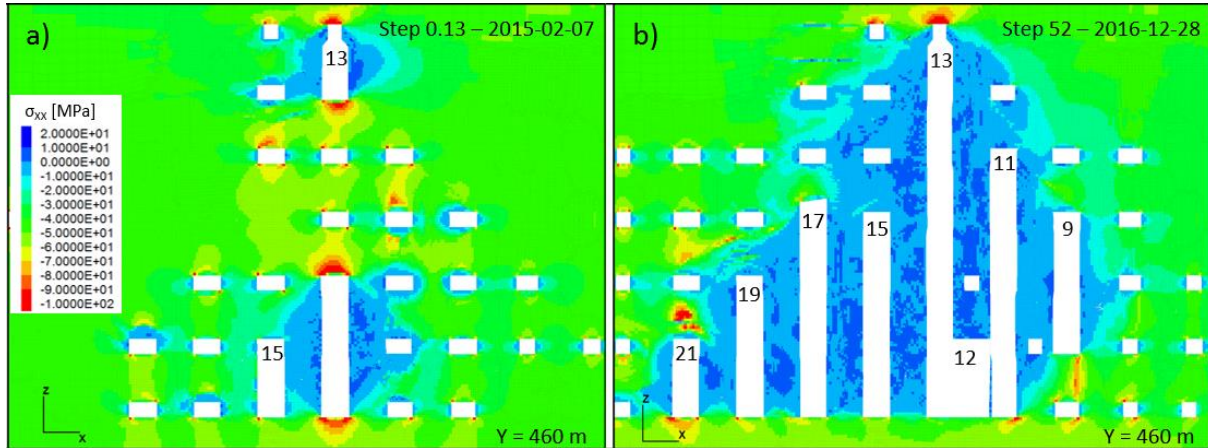


Fig. 5.14 - Contour plot of XX-stress. (a) Excavation step 0.13 (b) Excavation Step 52 (b). Numbers in (a) and (b) indicate stope names.

As the volume of extracted rock mass increases, zones of horizontal stress relaxation become wider (Fig. 5.14b). This is clearly visible at the final analyzed production stage (Step 52) when block 1250 appears almost completely destressed between stopes 11 and 15 and along its entire height, with large zones characterized by tensile horizontal stresses (Fig. 5.14b). Higher compressive stresses are, thus pushed to the sides of the analyzed area and within the sill pillars just above Stope 13. In addition to variation in stress magnitude, excavations also result in changes of the stress tensor orientation. This is visible in Fig. 5.15 which shows the principal stress tensor along a horizontal section at Step 52. Due to large excavated volumes between stopes 11 and 17, stress field is redistributed on the sides and particularly toward stopes 19 and 9.

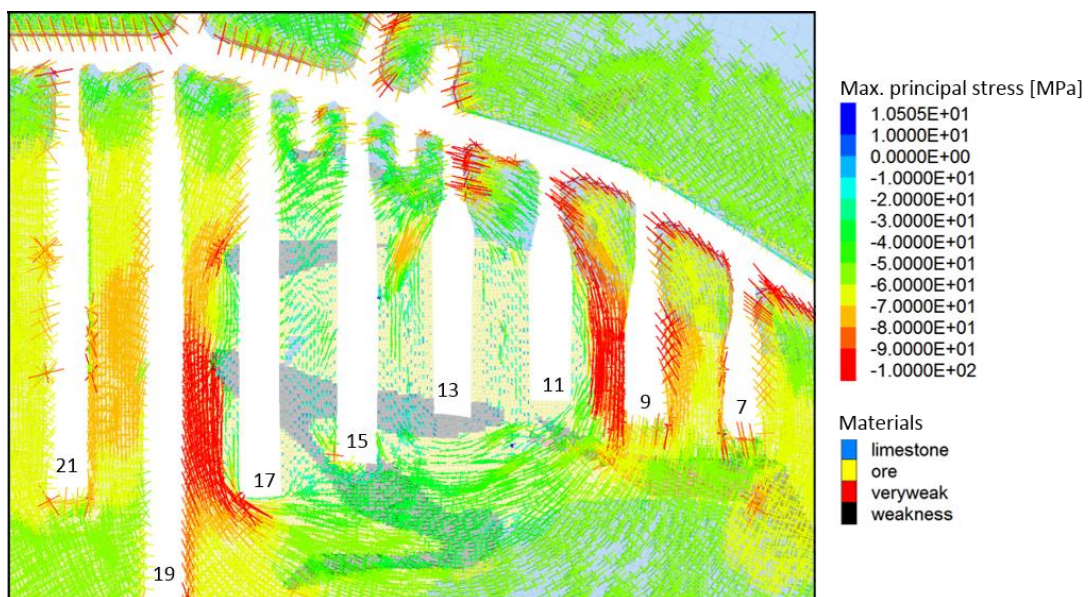


Fig. 5.15 - Principal stress tensor orientation at Step 52. The stress tensor is shown along a horizontal section at level 1157. Vectors are colored in function of the maximum principal stress magnitude.

The relaxation in the central zone of block 1250, and the consequent increase of compressive stresses toward the borders, is gradually evolving with the excavation advancement. This is demonstrated by the evolution of deviatoric stress ( $q$ ) distribution for distinct mining stages (Fig. 5.16). The deviatoric stress, also referred to as Von Mises equivalent stress, is written as follow:

$$q = \sqrt{3J_2} = \sqrt{\frac{1}{2}[(\sigma_1 - \sigma_2)^2 + (\sigma_1 - \sigma_3)^2 + (\sigma_3 - \sigma_2)^2]} \quad (5.9)$$

where  $\sigma_1$ ,  $\sigma_2$  and  $\sigma_3$  are the major, the intermediate and the minor principal stresses, respectively.

Fig. 5.16 shows that destressed zones are gradually increasing around mined-out areas during time (i.e. for different model steps), following a pyramid shape, as mining sequence do. Contemporarily, areas of increased deviatoric stress are enlarged toward the borders as the excavation progresses.

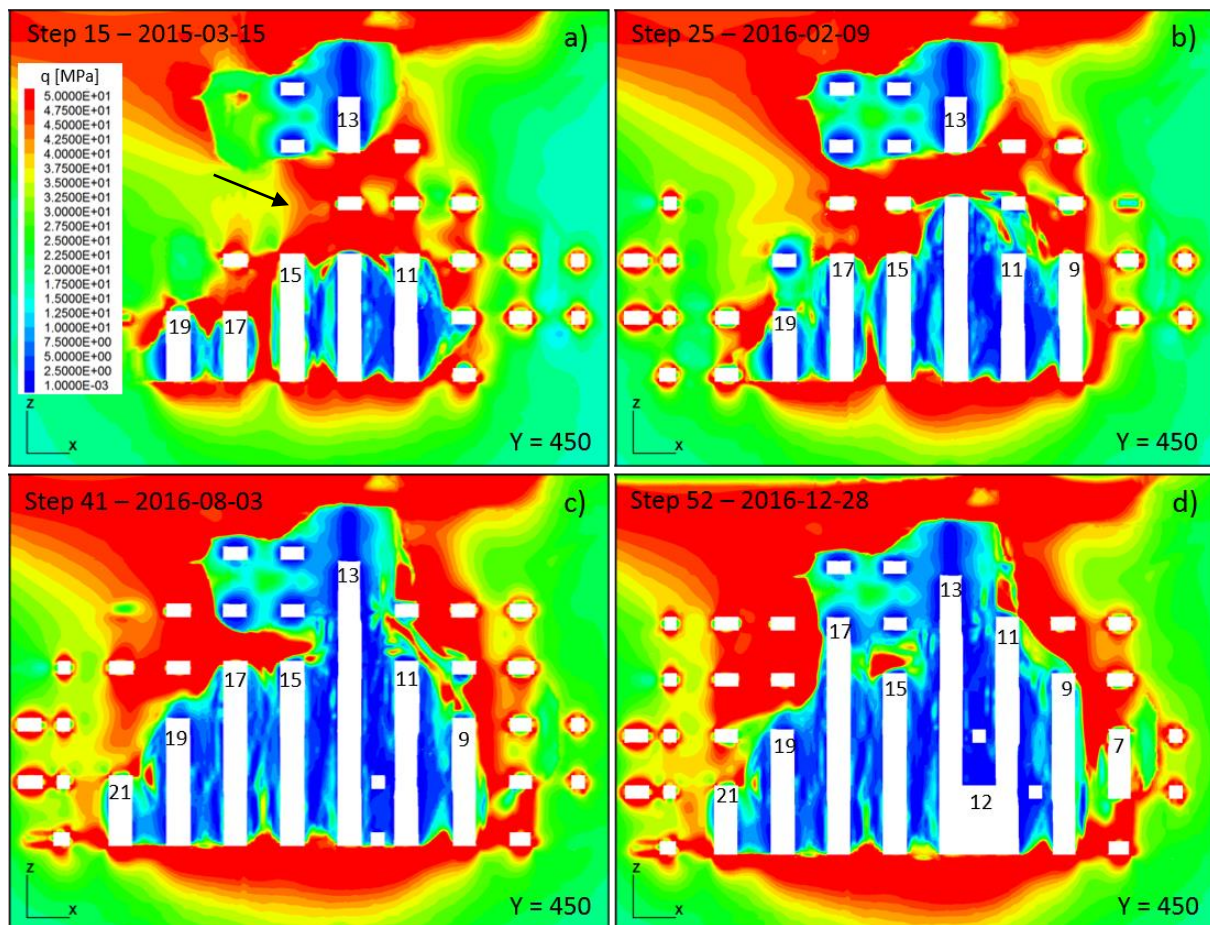


Fig. 5.16 - Contours of deviatoric stress along a vertical section. Four distinct mining steps are considered. Contour plots are calculated by volumetric averaging on model zones.

Below block 1250, the area characterized by high deviatoric stresses has doubled its maximal extension along the vertical direction in less than one year, increasing from about 10 m at Step 15 to 20 m at the final stage of the exploitation (Step 52). Moreover, the chosen mining sequence, which advances both bottom-up and top-down within Stope 13, results in two distinct zones characterized by lower stresses around mined volumes, interrupted by an area (indicated by an arrow in Fig. 5.16a), where deviatoric stresses are higher. Indeed, stresses induced at the bottom and at the top of

the excavated zones are gradually “pushed” toward the central area of the block. This is particularly visible in Fig. 5.16a and b, at steps 15 and 25, when the lower and the upper excavation areas of Stope 13 have not yet been connected. In this central zone, the deviatoric stress reaches 50 MPa which means an increase of more than 4 times with respect to its initial value (equals to 11.6 MPa at the average depth of -1182 m).

Deviatoric stresses in the horizontal plane are presented in Fig. 5.17 for the same excavation stages as in Fig. 5.16.

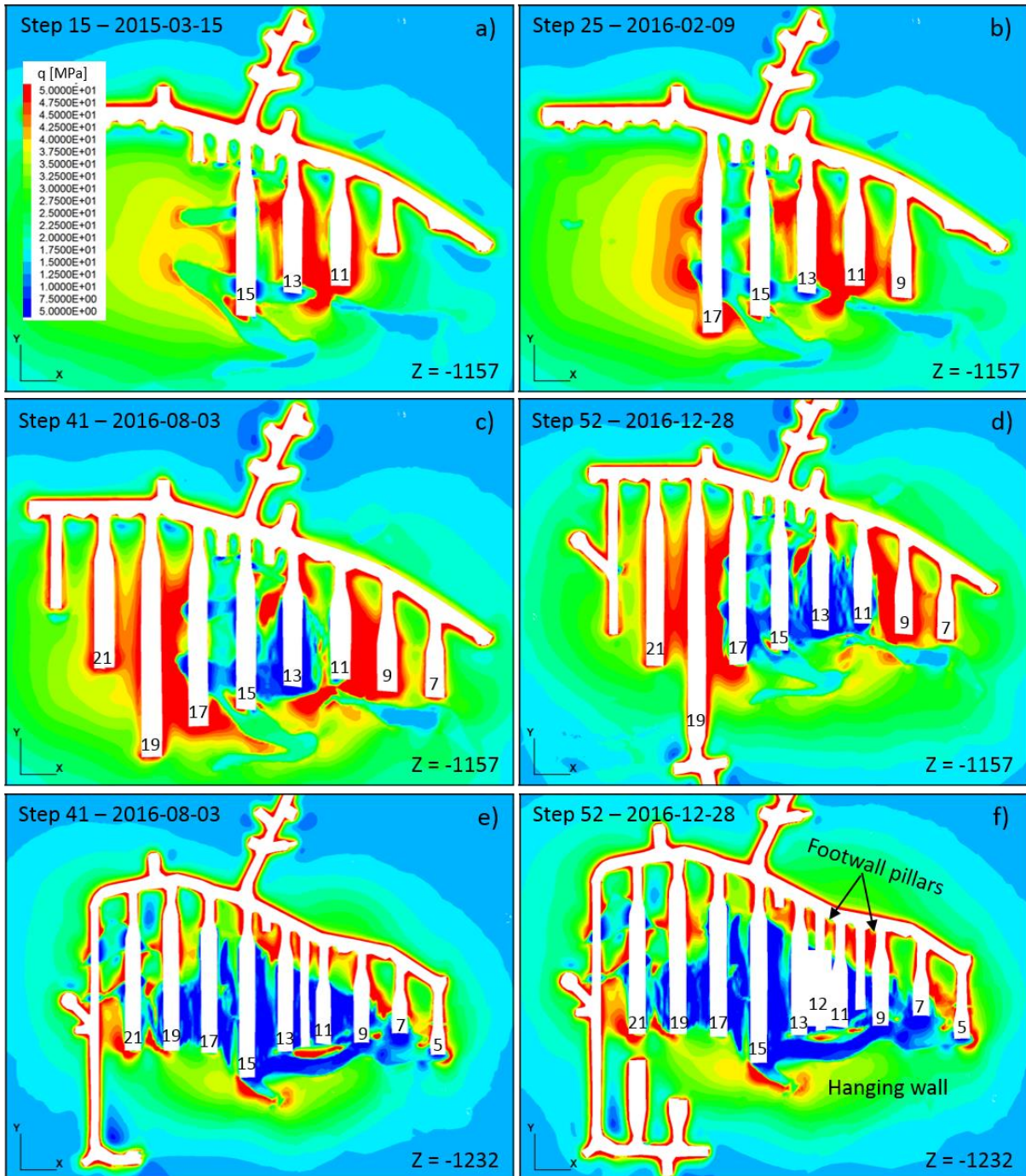


Fig. 5.17 - Contour of deviatoric stress along the horizontal plane. Horizontal sections are taken at levels 1157 (a, b, c, d) and 1232 (e, f). Four distinct excavation steps are considered. Stress contours are calculated as in Fig. 5.16. Note that figures may not be in the same scale between them.

Similarly to what has been previously observed, as the excavation progresses in Stope 13 and in the adjacent primary stopes, the central area of the block appears to be gradually distressed. It is interesting to observe the difference in stress redistribution at distinct levels of block 1250. Fig. 5.17e and f show the contour of deviatoric stress for a deep level of the block (-1232 m) at Steps 41 and 52. At these stages, all primary stopes have already been excavated, resulting in a significant reduction of the stress state in all the adjacent secondary stopes, almost for the entire width of the level. Deviatoric stresses are significantly lower in comparison with the configuration at level 1157 during the same stages (Fig. 5.17c and d). However, higher stress states are observed at the hanging wall contact, in some localized areas, and more particularly toward footwall pillars between stopes 13 and 9 (Fig. 5.17f). High stress levels in these zones must be considered with attention, firstly, because these pillars are extremely important for the stability of the footwall gallery and, secondly, because they represent the access area for the future development of secondary galleries.

To analyze the extension of the zone influenced by step-by-step production, stress variations between some subsequent exploitation steps was computed by simply calculating the change in deviatoric stress ( $\Delta q$ ) between Step<sub>*i*</sub> and Step<sub>*i-1*</sub>. Results are presented in Fig. 5.18, focusing on steps related to production in Stope 13 and reported in Tab. 5.11. Warm colors (from yellow to red) highlight model zones with  $\Delta q > 0$ , thus, the areas where stresses were mostly transferred during a given Step<sub>*i*</sub>. Induced stresses at Step 11 (Fig. 5.18a and b) appear to be mostly redistributed in zones near the excavation. High stresses are observed at the lower production level and in the adjacent secondary stopes. Overall the blast appears having an area of influence of about 15 m from each side of the excavation along the horizontal plane. Step 21 shows a wider influence area (Fig. 5.18c and d). Indeed, induced stresses are redistributed in the level immediately above the excavation (1182), within the last remaining block of Stope 13 and in the adjacent secondary pillars 12 and 14. However, at the production level (1207), stresses appear to be pushed at more than two stope wide distance (~25 m), and particularly toward the eastern side of the mine, from stopes 10 to 8 (Fig. 5.18c). At this level, stresses in secondary stopes on the side of blasted area are only concentrated toward the footwall drift (Fig. 5.18c), while the rock mass in contact with the excavated stope does not charge large loads. As a result, stresses appear to be more heterogeneously redistributed with respect to the previously analyzed case (Step 11), presenting an extension of influenced area larger than 25 m in the horizontal direction and of more than 50 m along the vertical direction. As the excavation progresses within Stope 13, the zone influenced by production is progressively enlarged. This is clearly visible at Step 41 (Fig. 5.18e and f), where large stresses are redistributed at more than 50 m distance from the blasted area.

As highlighted by these results, excavations have the effect of gradually reducing stresses in secondary stopes as the amount of extracted rock mass increases within primary ones. In addition, the analysis of stress variation between consecutive steps demonstrates that zones where higher stresses are induced due to blasting are gradually extending further away from the excavated area. This trend is most probably linked with the extension of the damaged zone (i.e. plasticity) induced in surrounding rock masses due to production. Indeed, as excavation progresses in primary stopes, fractures are induced in adjacent secondary pillars, reducing their stiffness. As it will be shown in Section 5.5.3, the extent of damaged zones gradually increases with the excavation advancement, influencing larger areas. These zones, characterized by reduced stiffness, are not able to charge load

and, when new stress changes are induced by blasting, the stress field is redistributed at larger distances from production area, where the rock mass is stiffer.

In addition, even if production follows a quite regular pattern, deviatoric stresses appear quite inhomogeneous along mine levels, presenting some bands of lower stresses surrounded by higher stress zones (Fig. 5.17). This trend indicates that besides mining sequence, other factors influence the stress field redistribution, as it will be later discussed in Section 5.5.3.

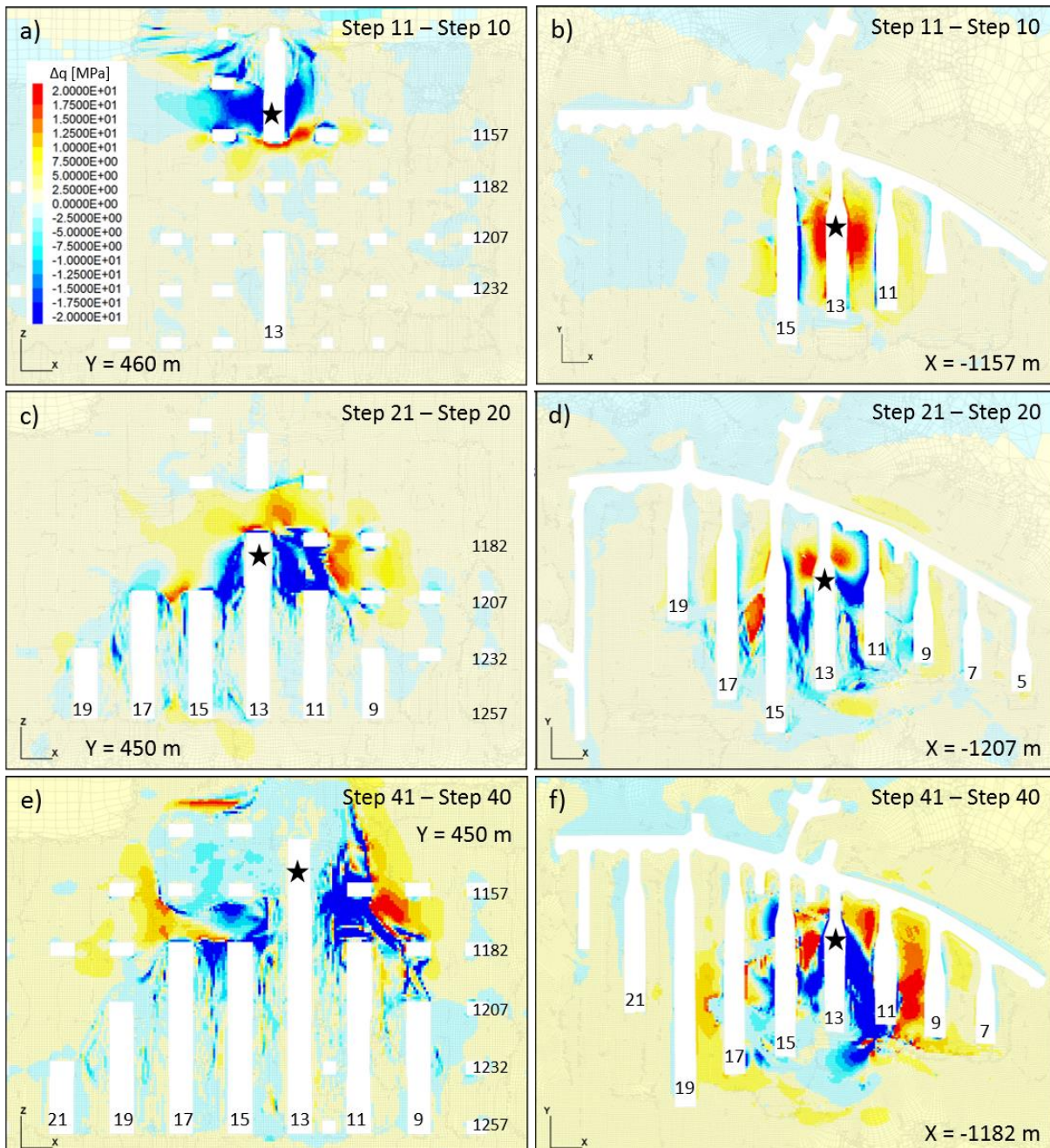


Fig. 5.18 - Difference in computed deviatoric stress between subsequent excavation steps. Results are presented along the vertical section for  $y = 450$  m (left panel) and on the horizontal profile for  $z = -1182$  m (right panel). Stars indicate the approximate position of mined-out area per each analyzed step. Numbers on the right side of left panel images denote mine levels.

### 5.5.2 Analysis of strain distribution

To analyze the distribution of induced strains, we focus on the same mining steps discussed in the previous section, looking at deviatoric strains (see equation 5.8). From the analysis of Fig. 5.19, we observe bands of strain localization which appear in secondary pillars between excavated primary stopes, especially at the lower levels of 1250 block. Damage and failures in rocks are usually accompanied by localization of the deformation and of plastic zones (Zhang et al., 2013), therefore, it is important to analyze their pattern. As visible in Fig. 5.19, these bands are almost vertical and parallel to stope walls, even if in some cases, we observe a slight curvature which is driven from primary stope walls toward the heart of secondary pillar. Thus, fractures may be initiated at opening walls and then propagate following the orientation of strain localization bands. As primary stopes are excavated at new levels (Fig. 5.19c ad d), strain localization bands become enlarged and deviatoric strain magnitude is increased.

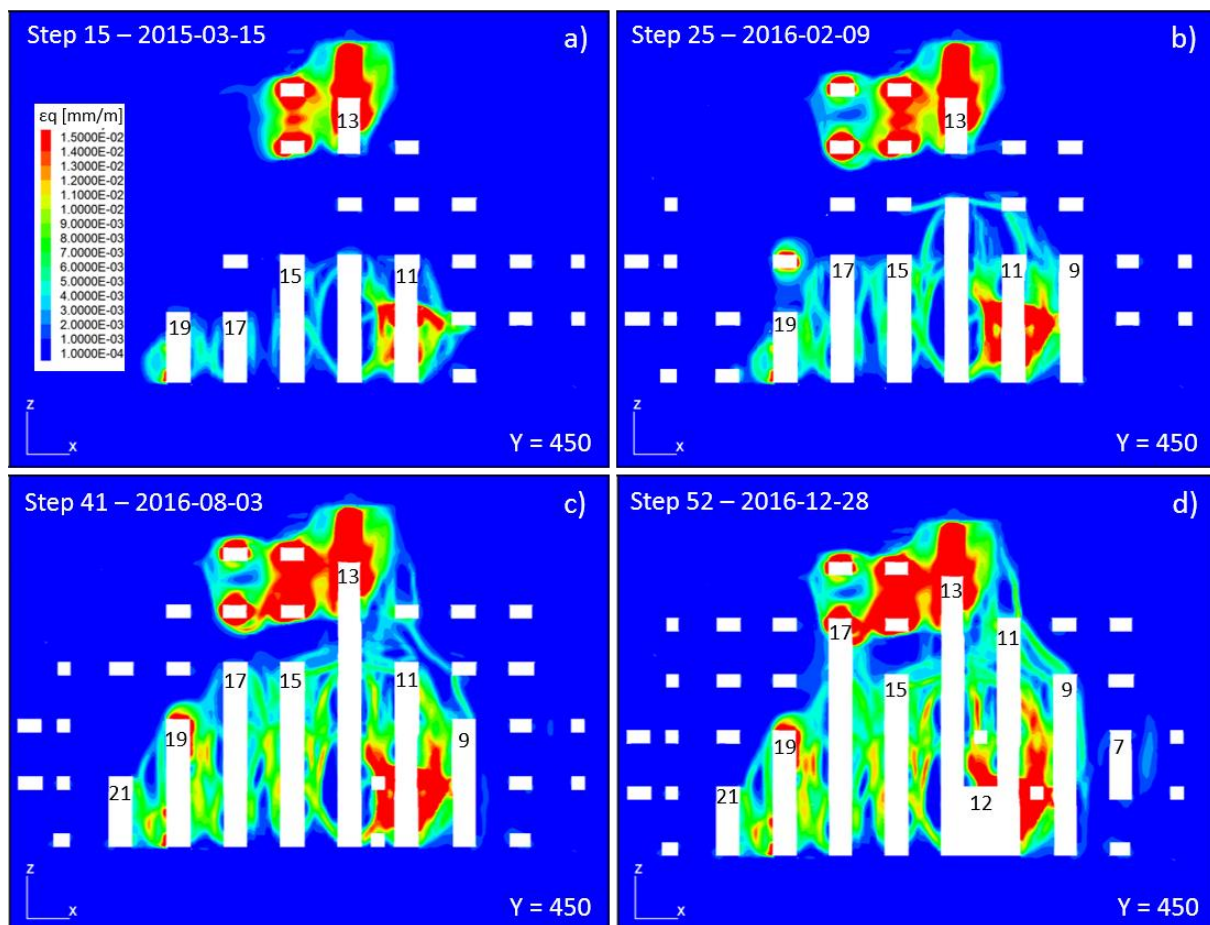


Fig. 5.19 - Contours of deviatoric strains along a vertical section. Four distinct mining steps are considered. Contour plots are calculated by volumetric averaging on model zones.

In the upper part of the block, one can observe a large deformed area, between levels 1107 and 1132 (Fig. 5.19), which appears disproportioned both in terms of intensity and extension if compared with the rather small production here performed. Similarly, a large strained area is observed in secondary stopes at the sides of Stope 11 (Fig. 5.19). This zone is limited between around levels 1232 and 1257 at the beginning of the mining sequence (Fig. 5.19a and b), for then extending until level 1182 at the final analyzed stage of the exploitation (Fig. 5.19d). The occurrence of this largely strained area



cannot be explained easily by the excavation pattern. Indeed, mining sequence is almost symmetrical on the eastern and western sides of Stope 13, with only few more stopes exploited in the western area. Thus, one would have expected a symmetrical distribution of the strain pattern or, at least, higher strains in the western area rather than the contrary. As it will be later discussed (Section 5.5.3), strain distribution is strongly influenced by the geological setting.

Contours of deviatoric strains on the horizontal plane are presented in Fig. 5.20.

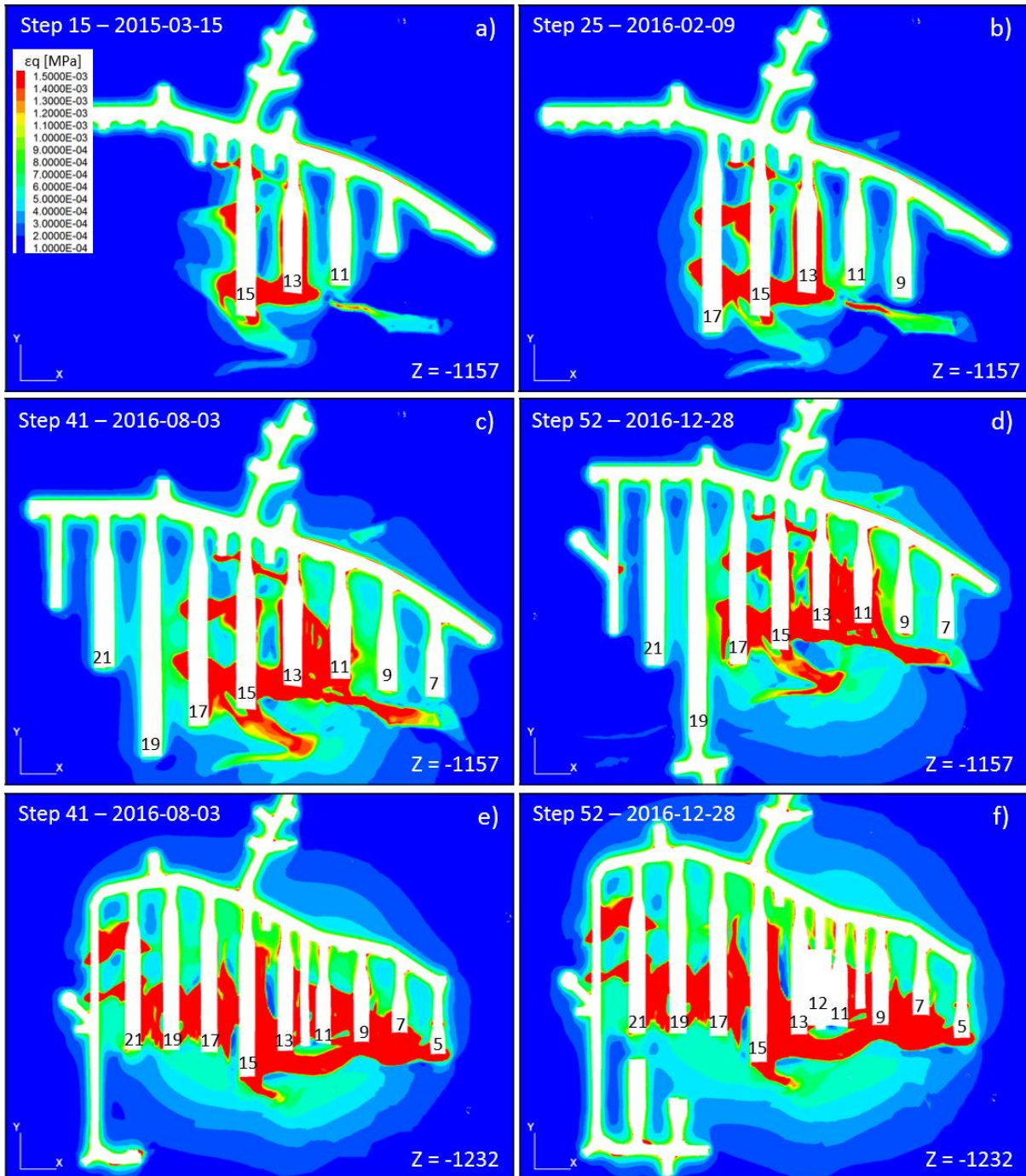


Fig. 5.20 - Contours of deviatoric strains along horizontal planes. Horizontal sections are taken at levels 1157 (a, b, c, d) and 1232 (e, f). Four distinct excavation steps are considered. Note that figures may not be in the same scale between them. Strain contours are calculated as in Fig. 5.19.

Large deviatoric strains are observed around Stope 13 and they are gradually enlarging with the exploitation advancement. Deeper levels (Fig. 5.20e and f) of the block present larger strains along the entire width, at the final stages of the mining sequence. The hanging wall appears here largely deformed, particularly between stopes 5 and 15. Smaller highly-strained areas are as well observed in coincidence with footwall pillars. As observed for the deviatoric stress, deviatoric strains are as well quite heterogeneously distributed particularly on the horizontal plane.

### 5.5.3 Analysis of plastic zones and influence of weak geological materials

Similarly to strain localization bands, the analysis of plastic zones allows determining the extent of the excavation damaged zone, based on the applied constitutive law. The distribution of plastic zones is presented in Fig. 5.21 for a vertical section at four distinct stages of the exploitation. As discussed in Section 5.3.5, the orebody has been modelled with a different constitutive law in comparison with limestone and weakness zones. Therefore, two distinct states of failure are predicted for the ore: (i) brittle failures in the post-peak phase (indicated as softening in Fig. 5.21) and (ii) ductile failures when the residual threshold is reached (indicated as residual in Fig. 5.21). Plastic zones within the orebody are, thus, the zones failed with a strength value between the peak and the residual (Souley et al., 2018). All the other materials, which follow the Hoek and Brown criterion, fail in shear.

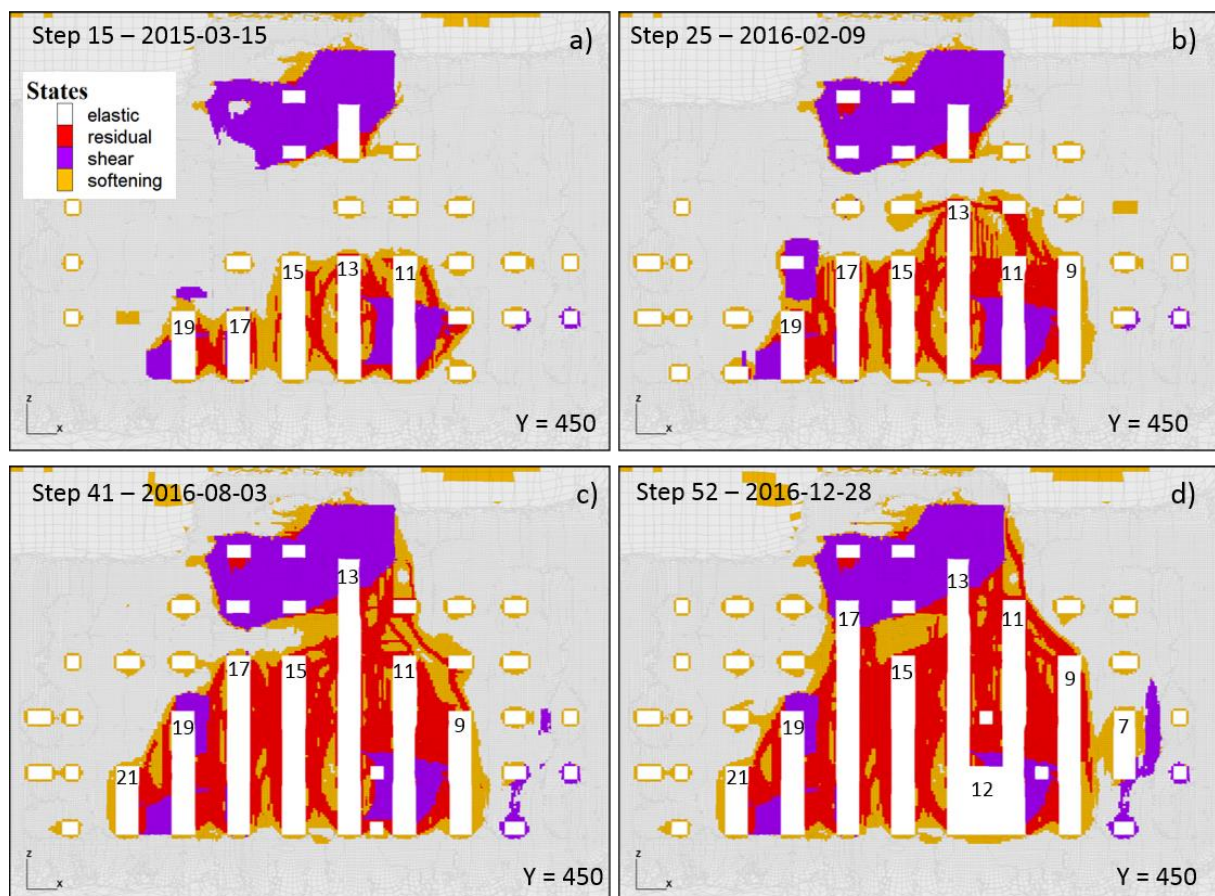


Fig. 5.21 - Distribution of predicted plastic zones along a vertical section. Four different steps of the excavation sequence are considered.

Geometry of damaged zones (Fig. 5.21) is consistent with deviatoric strain distribution (Fig. 5.19). Indeed, within the orebody, plasticity (softening and residual states in Fig. 5.21) is mostly occurring in secondary stopes between excavated primaries and following the shape of previously observed

bands of strain localization. The size of damaged zones is gradually increasing with the excavation advancement, moving in the vertical direction toward the central levels of block 1250. Plasticity is as well observed at the edges of excavations, i.e. around galleries profiles. At the end of the analyzed mining sequence large areas of secondary stopes appear reaching the residual strength (Fig. 5.21d). Violet areas in Fig. 5.21 are the failure zones predicted by the Hoek and Brown criterion. Most of these latter zones are as well characterized by large deformations as already observed in Fig. 5.19. These zones appear to all occur in coincidence with weak geological materials, which thus play a primary role in the distribution of plastic zones. To deeper analyze the effect of weakness zones on predicted plasticity, Fig. 5.22a and b compare the position of weak zones at level 1157 (Fig. 5.22a) with the profiles of plastic areas during Step 25 (Fig. 5.22b). Weak zones in contact with excavations are subjected to plasticity, as it is visible between stopes 13 and 17 (Fig. 5.22b), and this also influence plasticity within the orebody. Depending on weak zone dimension, plastic lenses are not entirely plasticized in one time. This is better visible in Fig. 5.23, where the extension of plastic zones at level 1157 is shown for Steps 15 and 25. Indeed, at Step 15, plasticity occurring in coincidence with the large weak lens at the hanging wall has an extension of about 10 m from the western side of drift 15 (Fig. 5.23a). At Step 25, once drift 17 has been excavated, the plastic zone extension appears enlarged (Fig. 5.23b) within the weak geological lens.

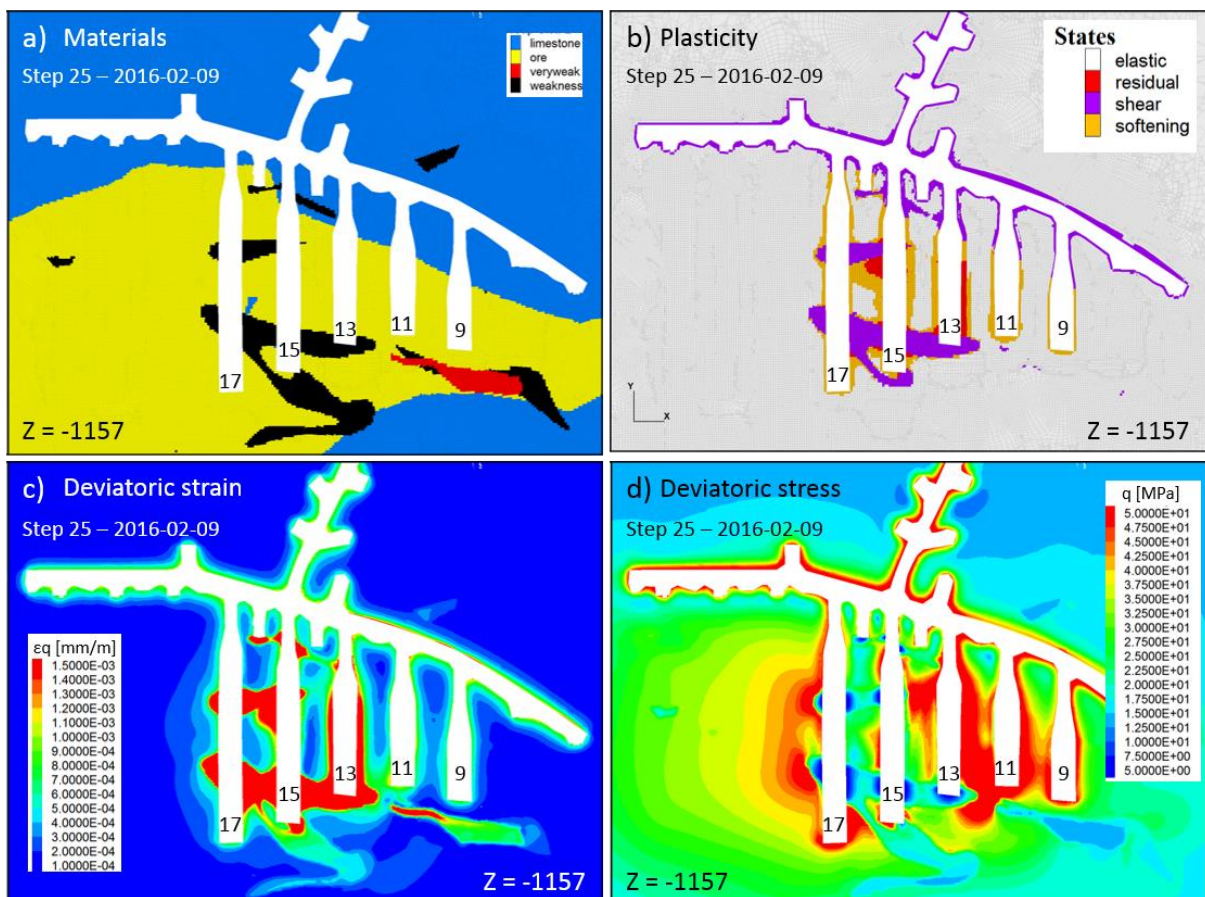


Fig. 5.22 - Effect of weak zones on plasticity, stress and strain distribution. (a) Horizontal profile at level 1157 showing the different geological elements. (b) Plastic zones at Step 25 along the horizontal profile at level 1157. (c) Contour plot of deviatoric strains at Step 25 for the horizontal profile at level 1157. (d) Contour plot of deviatoric stresses at Step 25 for the horizontal profile at level 1157.

Plasticity within weak materials appears also influencing strains and stresses in surrounding rocks. This can be seen in Fig. 5.22, where the distribution of deviatoric stress (Fig. 5.22d) and strain (Fig. 5.22c) is compared with plastic regions (Fig. 5.22b) and weak zones location (Fig. 5.22a). As expected, the areas subjected to plasticity are characterized by large strains (Fig. 5.22c), with typical values in the order of  $1.5 \mu\text{m}/\text{m}$ , and low stresses (Fig. 5.22d), which can go down to 5 MPa. These areas follow the contour of the weak zones and explains the heterogeneous distribution of stress and strain fields observed in Fig. 5.17 and Fig. 5.20. Indeed, the stress field is redistributed in the surrounding rock mass where high stresses are encountered within the ore at the edges of the weak zones (Fig. 5.22d). Consequently, overstressed areas can be observed at a certain distance from excavations. This is visible in Fig. 5.22d where highly stressed areas are distributed at about 20 m distance from the western wall of drift 17. In terms of comparison, the high stress state region around drift 9, which is not influenced by the presence of weak zones, appears homogeneously distributed with a maximum extension of about 3 m from gallery walls.

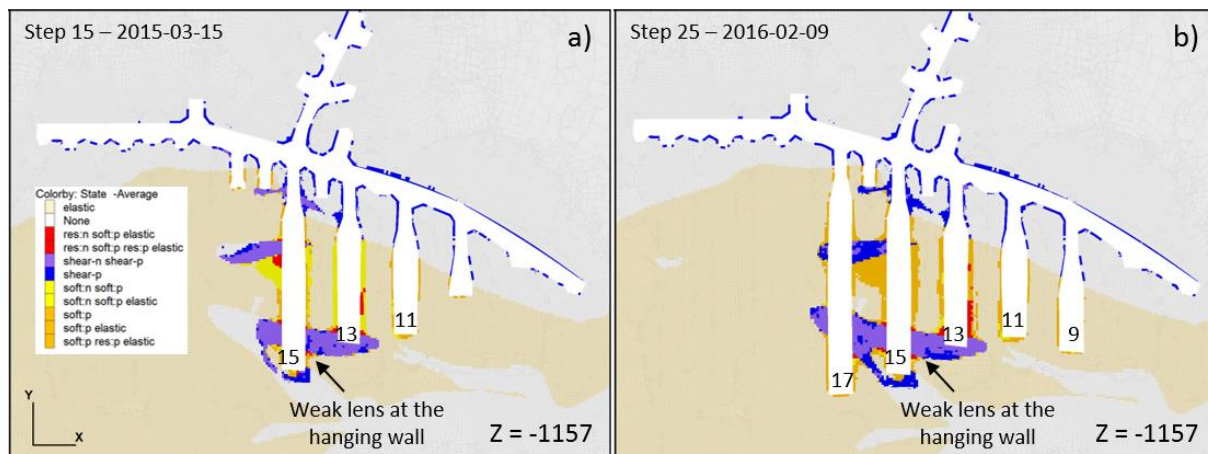


Fig. 5.23 - Variation in plastic zone extension during time. (a) Predicted plasticity at level 1157 during Step 15. (b) The same as (a) during Step 25.

#### 5.5.4 Temporal evolution of model parameters

To better analyze the temporal evolution of model results, mean values of deviatoric stresses and induced strains, as well as of plastic zones volume, have been calculated in the whole area of interest at each simulated mining step (from 1 to 52). As visible from Fig. 5.24, these parameters appear gradually growing in the two-year period analyzed, together with the excavation advancement. If the mean deviatoric stress presents locally some small decreases, mean strains keep rising during the whole period until the end of December 2016. Overall, the trend of the curves appears regular, without any major acceleration in time. Nevertheless, some minor jumps can be observed in the curves, of which the most significant are recorded in coincidence with steps 21, 29 and 41 (see Tab. 5.11 for more details). In coincidence with these excavation stages, the mean deviatoric stress within the area of interest increased, respectively, of 0.21 MPa, 0.08 MPa and 0.11 MPa with respect to the previous steps. Similarly, the mean deviatoric strain has increased of  $39 \mu\text{m}/\text{m}$ ,  $23 \mu\text{m}/\text{m}$  and  $41 \mu\text{m}/\text{m}$ , respectively. In addition, a slight slope variation is visible in plastic volume and deviatoric strain from Step 34, with an acceleration of plastic volume and induced strains growth, until Step 39. During this period, the mean strain increases of  $150 \mu\text{m}/\text{m}$ , while the volume of plastic zones riced of about 9%. On the contrary, in the same period, mean deviatoric stresses appear having a smaller variation.

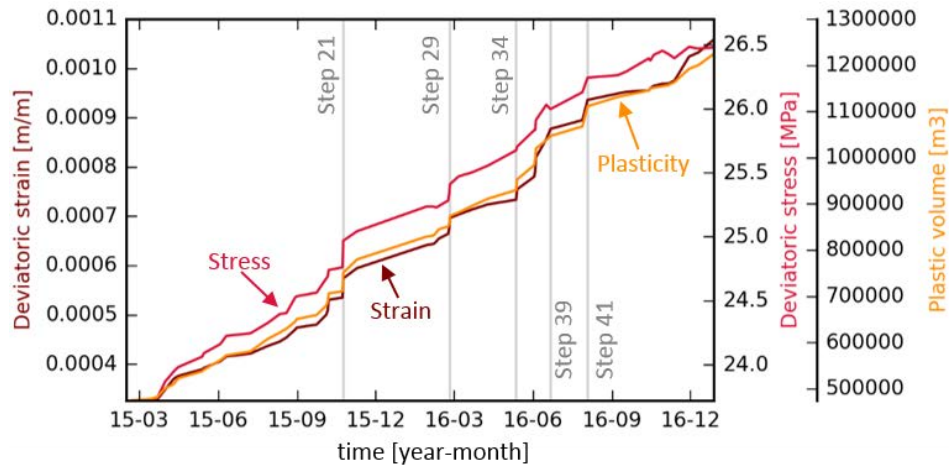


Fig. 5.24 - Temporal evolution of model parameters. Stress, strains and plastic volume are computed as average values for all the zones within the area of interest at each model step. Vertical gray lines denote some simulated steps of the excavation.

What is interesting to underline in the curves presented in Fig. 5.24 is that the three major observed changes in stress, strain and plasticity are all related to production in Stope 13 at levels 1207 and 1182 (see Tab. 5.11). Related PB are as well responsible for the triggering of seismic sequences  $S_2$ ,  $S_3$  and  $S_6$ , and for the detection of major strain and displacement shifts recorded by the extensometer and CSIRO cells, as discussed in Chapter 4. This observation underlines, once again, the key role played by Stope 13 production, which appears influencing rock mass state in the whole block 1250. Moreover, this result demonstrates that numerical results are in good agreement with field observations, making it possible to qualitative and quantitative compare model results with field data.

## 5.6 Discussion and conclusion

In this chapter, the mine-wide 3D numerical model of Lappberget orebody has been presented together with the analysis of its results. Several assumptions have been made for the construction of the proposed numerical model. Of these, one of the most important is related to weak and very weak zones characterization. These areas are only poorly studied by mine geologists both in terms of geometry and mechanical properties, thus their introduction in the numerical model is problematic due to a lack of data. On the other hand, it has been demonstrated in Chapter 4 that these geological elements have a strong influence on the seismicity path and on microseismic events dynamics. Therefore, it is important to analyze the influence played by these zones on the rock mass mechanical behavior in response to mining. In addition, as demonstrated by Souley et al. (2018), the introduction of weak zones in the numerical model of Lappberget orebody proposed by these authors significantly reduced the gap between stress measurements and computed stresses. For these reasons, in this thesis an accurate 3D reconstruction of weak zones geometries has been proposed. Even if this results in simplifying the real geological setting, the proposed approach remains the best possible approximation based on the available data. If new models will be built in the future, one will have to refer to the most recent available improvement made by mine geologists regarding weak and very weak zones characterization.

Another important assumption is that of considering each of the four modelled geological units (limestone, ore, weak and very weak zones) as isotropic and characterized by homogeneous mechanical properties. It has been shown that the real geological setting is locally heterogeneous even within same lithologies (see Chapter 2). Therefore, the use of constant mechanical properties may result in oversimplifying rock mass characterization at local-scale. On the other hand, mechanical properties cannot be directly measured at larger scales, thus, the simplifying hypothesis of homogeneous geological units is necessary and acceptable when rock masses need to be characterized at large-scale.

Finally, we have assumed a continuous medium for which no discontinuities have been considered. As already pointed out at the beginning of this chapter, this was a forced choice as no indication is given by mine geologists about fractures location, intensity nor orientation.

Despite the inherent simplifications in the proposed numerical model, results appear to be in good agreement with field data. This has been demonstrated by comparing displacements and stresses measured by the extensometer and CSIRO cells, respectively, with displacements and stresses calculated by numerical modelling. Therefore, the proposed model provides a good approximation of the rock mass mechanical behavior, at least close to production areas, where geotechnical instruments were installed. In addition, defining a fine mesh within the area of interest, model accuracy has been significantly improved. This has been shown comparing results of two identical plastic models, characterized by different mesh sizes (Section 5.3.6). It must be underlined that large numerical models (with more than 10 million zones), as the one proposed in this thesis, are seldom found in the literature. This is because such large models are more difficult to build and manage and require larger computing times. However, our study demonstrates how model results can be more precise when high resolution meshes are adopted.

Beside the application of a fine mesh, the accuracy of the proposed numerical model is also determined by the assumed elastoplastic constitutive laws. The choice of the appropriate constitutive model to adopt, together with rock properties characterization, are key aspects of numerical models which determine their successfulness in approximating real rock mass behaviors. As already discussed in Section 5.1, beside mining industry, numerous examples can be found in the scientific literature where rocks are assumed to follow a simple elastic behavior (e.g. Bruneau et al., 2003; Ziegler et al., 2015) for numerical modelling purposes. It can, thus, be interesting to assess and quantify the error on stress estimation due to the elastic assumption. For doing so, the elastic model performed in the framework of this thesis has been compared with the Plastic Model #1 (see Section 5.3.6 and Tab. 5.10), which both have the area of interest meshed at 2 m. Elastic and elastoplastic models have been compared in terms of deviatoric stress ( $q$ , see equation 5.9). More precisely, we calculated the difference ( $\Delta q$ ) between deviatoric stress resulting from the elastic model ( $q^{elas}$ ) and that of the plastic model ( $q^{plas}$ ), having considered all zones within the area of interest. Differences in deviatoric stress are in some areas bigger than 50 MPa, if the last step of the exploitation (Step 52) is considered, implying a clear overestimation of stresses predicted by the elastic model. To have an idea of the spatial extension of this stress overestimation, Fig. 5.25 shows model zones where  $\Delta q = q^{elas} - q^{plas} > 2q^{ini}$ , where  $q^{ini}$  is the deviatoric stress before any excavation, which is equal to 11.6 MPa at a mean depth of 1182 m. At Step 1, when only few stopes are excavated,  $\Delta q$  exceeds the threshold value of  $2q^{ini}$  only in zones located at the edges of the excavations (Fig. 5.25a, b), where higher stresses are localized in the elastic model. If we consider that the influence of mine voids on

stress variation can be neglected at few radii of distance from the excavated area, we can assume that the elastic approximation is reliable only if few stopes have been extracted. However, when the excavated volume increases, stopes become mechanically dependent on each other, and stress variation starts to be important also at a certain distance from the excavation. This is clearly visible in Fig. 5.25c and d where the difference between elastic and plastic deviatoric stress is calculated at the last step of the excavation sequence (Step 52). In this case, errors in stress estimation due to the elastic assumption are distributed almost within the entire area of interest. This observation highlights that modelling results should be considered with caution when a purely elastic behavior is assumed, especially at advanced stages of the exploitation when elastoplastic models appear to be more reliable.

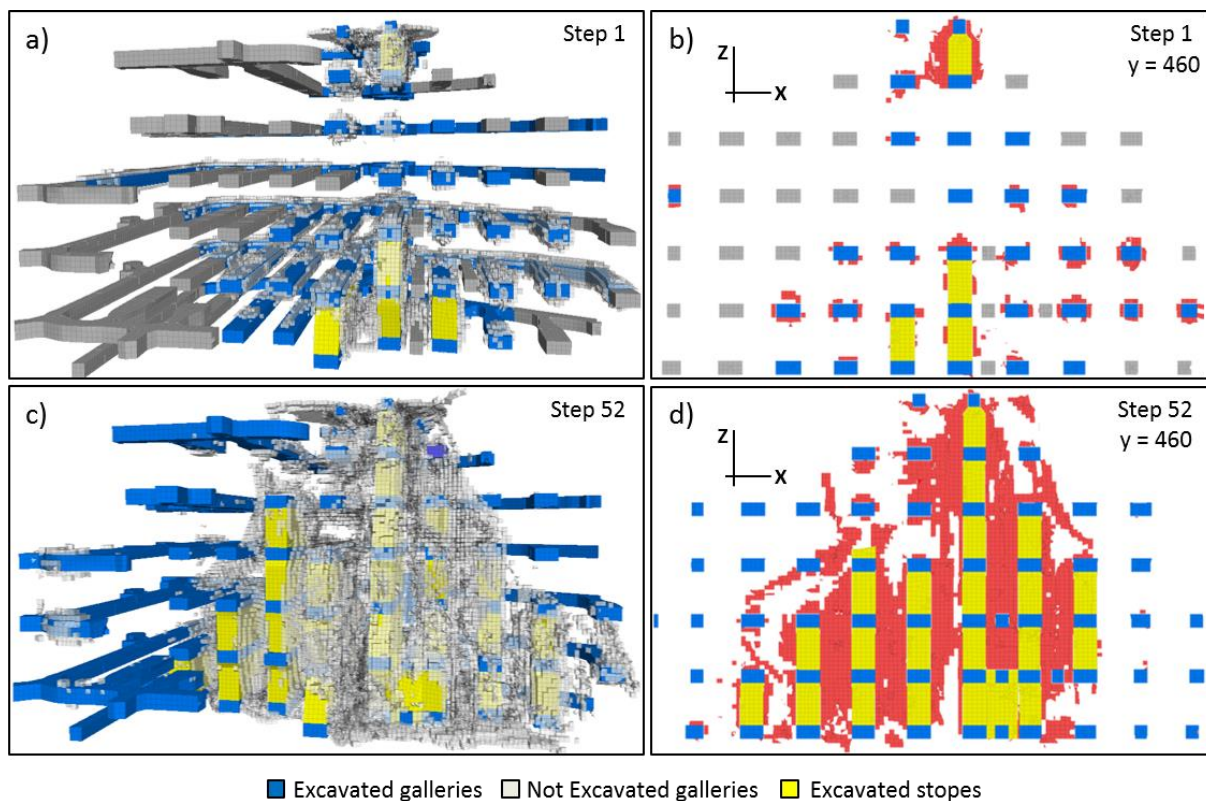


Fig. 5.25 - Comparison between elastic and elastoplastic models. (a, b) 3D view and vertical profile showing model meshes where  $\Delta q > 2q^{ini}$  at Step 1. (c, d) Same as in (a, b) but at Step 52. See text for more details.

Numerical modelling results presented in Section 5.5 show that distribution of stresses and strains, as well as that of plastic zones, is strongly influenced by mining sequence, on one hand, and by the presence of weak geological zones, on the other hand. Primary stopes excavation results in gradually distressing adjacent secondary stopes, where large strains and plasticity are observed. Some tensile stresses can occur, even if most of the induced stress is in compression. Numerical modelling clearly shows the effects on stress field redistribution due to the mining sequence chosen for Stope 13. Indeed, as mining follow a simultaneous bottom-up and top-down sequence, two zones of lower stresses but increasing strains are observed in the northern and southern area of block 1250, which are encompassed by zones of higher stresses in the middle of the block and along its boundaries (see Fig. 5.16). In other words, the chosen mining sequence results in gradually increasing stresses within the last remaining level of Stope 13 and in neighboring rocks. This result is strongly consistent with field observation and discussion made in Chapter 4, where the overstressed condition of this area of

the mine was already pointed out. Globally, the model shows that, as mining progresses, stresses are gradually pushed toward lateral drifts, while plasticity and strains increase within unmined secondary stopes.

Bands of strain localization have been observed in secondary stopes, whose orientation is mostly vertical and parallel to excavated stope walls (see Fig. 5.19). As soon as stopes are excavated at new levels, strain localization bands become larger, propagating along the vertical direction, and strain magnitude is increased. The extension of predicted damaged zones (i.e. plasticity) is consistent with that of strain distribution, following the shape of strain localization bands (see Fig. 5.21). Moreover, plasticity appears to be strongly influenced by weak geological materials (talc-schist). Indeed, when weak zones are intersected by or in contact with excavations, they are immediately subjected to plasticity over large areas. This is reflected on stress redistribution in surrounding rock masses, where large stresses are encountered at the edges of weak areas (see Fig. 5.22 and Fig. 5.23). Indeed, weak materials, which are not able to carry large stresses, impose a mechanism of stress transfer toward surrounding rock masses. Overall, the presence of this talc-schist lenses results in enlarging the extensions of highly-stressed regions from mine openings of about a factor 7. The role of weakness zones on stress field redistribution was already discussed in Chapter 4, based on strain measurements and induced seismicity patterns. Now, numerical modelling results give more constraints to this assumption, confirming the mechanism of stress transfer imposed by the presence of weak geological materials.

Temporal variation of model parameters computed on the whole area of interest, underlined the primary role played by Stope 13 production on the whole 1250 block. In particular, it has been demonstrated that model steps resulting in larger stress and strain changes, as well as in plastic volume variations, are the same steps for which seismicity rate increased and major seismic sequences were recorded. Moreover, the slight intensification of strain and plasticity observed between Steps 34 and 39 (Fig. 5.24) may be interpreted as a period of increasing damage in 1250 block. This is strongly consistent with observations made on the field where major damage started to be observed in the second half of May 2016, which agrees with the timing of Step 34. Indeed, as discussed in Chapter 2, in this period cracks and, then, a roof failure took place in Stope 13 level 1157, in a zone which started showing roof spalling and deterioration of the opening back in the previous months. However, these are only preliminary results that need further investigations. Deeper analysis on the correlation between numerical modelling results together with field data and observations are the subject of the next chapter, where the combined analysis between seismicity and numerical modelling is presented.



# Chapter 6

## Combined analysis of seismicity and numerical modelling

As pointed out in the introduction of this thesis, seismic monitoring in underground mines is nowadays a common tool to assess seismic hazard induced by mining and to prevent seismic risk. Similarly, in the previous chapter (Chapter 5), it has been shown that numerical modelling techniques are widely used as an aid to decision making, for planning long-term mining strategies and for defining the optimal mining sequence. Therefore, these techniques, even if largely applied, are generally regarded as separated tools with distinct objectives.

The aim of this chapter is, on one hand, to investigate whether qualitative and quantitative correlations can be found between seismic parameters and numerical modelling outputs, and, on the other hand, to show that numerical modelling can give additional insights in the characterization of Lappberget induced seismicity. Indeed, model results presented in the previous chapter indicate a strong influence of Stope 13 exploitation on surrounding rock masses, as well as a primary role played by the presence of weak geological zones on induced strains and stresses. These results agree with field observations analyzed in Chapter 4 and, thus, look promising for a deeper investigation of the rock mass mechanical response to mining by means of numerical modelling. Relating seismic data analysis with numerical modelling, and finding possible links, may allow gaining additional insights into failure processes, with the aim of improving short-term and long-term prevention.

Based on this idea, this chapter intends to compare results discussed in Chapter 4, based on seismic data analysis, with the previously analyzed numerical modelling results. The chapter is organized as follow: first, a short bibliographic review presents the most common methodologies used by other authors for relating mining-induced seismicity with geomechanical numerical modelling (Section 6.1). Then, the different strategies of comparison adopted in the current work are presented (Section 6.2) and discussed in detail together with their results in Section 6.3 and Section 6.4.

### 6.1 Relating induced seismicity with geomechanical modelling

Mining-induced seismicity has been widely studied in the literature, providing disparate methodologies for its analysis and interpretation (see Chapter 1). Similarly, the scientific literature presents a large documentation of numerical modelling techniques (see Chapter 5) with examples on many different applications. In contrast, there is a more limited research for the application of numerical modelling to the study of induced seismicity, even if some attempts have been done in the past and are still the subject of recent works. In this section, a review of methodologies applied for relating seismic analysis with numerical modelling is presented, focusing only on static mechanical models, which have the objective of calculating states of mechanical equilibrium, without paying attention to transient states. Indeed, as discussed in Chapter 5, we are interested in examining whether induced seismicity can be explained and characterized by the analysis of static strain and stress field redistribution due to mining. If interested in dynamic models, aimed at modelling

rockburst occurrence and seismic wave propagation, readers are mainly referred to He et al. (2016) and Zhu et al. (2014, 2010). Modelling approaches which explicitly reproduce rock fracture phenomena by means of discrete elements methods or their coupling with finite element methods (e.g. Cai et al., 2007) are as well discarded from this review.

In the framework of static numerical models, some authors have qualitatively compared MSE localization with the extension of stress accumulation zones predicted by modelling. Snelling et al. (2013) proposed a 2D discontinuous numerical model (distinct element code) to assess the influence of faults networks on remote seismicity and stress redistribution at the Creighton mine (Canada). The authors concluded that shear zones (faults) within the mine do not trigger seismicity by fault-slip, but they do influence stress field redistribution around excavations, and in turn the seismicity pattern. Indeed, zones characterized by intense seismic activity are consistent with areas where the maximum principal stress and the shear stress are higher. Similarly, Abdul-Wahed et al. (2006) compared the seismicity pattern induced by a longwall coal mine in France with zones of increasing stresses predicted by modelling. Based on a 3D homogeneous elastic boundary element model, the authors simulated five steps of longwall face advancement, each representing 20 m of panel excavation. Then, they determined the extension of the rock volume influenced by mining, imposing a threshold value to the ratio between the computed vertical stress and the initial vertical stress. The increasing extension of the computed volume of influence at subsequent modelled steps is found to be in good correlation with the spatial migration of MSE as the face advances. However, having simulated a single panel excavation, authors were only able to describe seismicity occurring in close proximity to the advancing panel. Vatcher et al. (2014) qualitatively estimated the spatial extension of seismic clusters with that of predicted plastic zones as retrieved by a large-scale continuous model of Kirunavaara Mine (Sweden). Plastic zones positions were found to corresponded well with the extension and localization of microseismic events, however a good match between seismic events and plastic zones could be achieved either in the footwall or in the hanging wall, but not in both zones simultaneously. Authors concluded that geological structures, not considered in the model, influence the rock mass response.

Another approach for the analysis of mining-induced seismicity through numerical modelling is based on the estimation of the excess shear stress (*ESS*), initially introduced by Ryder (1988):

$$ESS = |\tau| - \mu\sigma_n \quad (6.1).$$

This parameter, calculated on a given fault and for a given slip direction, is defined as the difference between the absolute value of the shear stress ( $\tau$ ) prior to slip and the normal stress ( $\sigma_n$ ) multiplied by the internal friction coefficient ( $\mu$ ). Based on this parameter, areas of the model where the *ESS* has a positive value indicate potential sources of seismicity. Due to its formulation, the *ESS* can be employed when one wants to evaluate seismicity along a preferential plane, but the friction coefficient remains difficult to estimate. An example of *ESS* application to the analysis of mining-induced seismicity is provided by the work of Hofmann et al. (2012), who intended to investigate whether a large seismic event ( $M_w = 2.1$ ) that occurred in a dyke of Mponeng Gold Mine (South Africa) was induced by stress changes due to mining. The authors developed a 3D elastic boundary element model, where the simulation of the slip along the fault is permitted by the introduction of a displacement discontinuity surface. They found that rupture plane is coincident with high *ESS* zones, with an average *ESS* value of 2.7 MPa prior to the event. The author concluded that stress changes

induced by mining were high enough for triggering the analyzed event. Very similar to *ESS* is the estimation of changes in the Coulomb failure stress ( $\Delta CFS$ ). The mechanism of static stress transfer is largely employed in natural seismology to evaluate if increasing stresses along a fault may bring it close to failure or not. Aftershocks along a fault can be triggered by the stress change induced by preceding mainshock, in accordance to the Coulomb failure criterion (King et al., 1994; King, 2007; Stein, 1999; Utkucu et al., 2013). The formulation of Coulomb stress changes is similar to that of *ESS* and can be written as follow:

$$\Delta CFS = \Delta\tau - \mu\Delta\sigma_n \quad (6.2),$$

where  $\tau$ ,  $\mu$  and  $\sigma_n$  take same meanings as in equation 6.1, but these are calculated as the difference between two consecutive steps of the model.

This criterion was successfully applied by Ziegler et al. (2015) who modelled the same event that occurred within a dyke at Mponeng Gold Mine already studied by Hofmann et al. (2012). Based on the modelled distribution of  $\Delta CFS$ , the authors concluded that the area around the  $M_w$  1.9 seismic event was brought close to failure due to stress changes induced by mining. In addition, Ziegler et al. (2015) also assessed the seismic hazard due to excavation advancement toward the dyke, based on the variation of computed  $\Delta CFS$ . Results showed a significant stress increase in the last 50 m from the dyke, however, authors pointed out the difficulty in assessing the level at which the  $\Delta CFS$  becomes critical.

*ESS* and  $\Delta CFS$  can be used when one wants to investigate the potential for induced seismicity along a preferential rupture plane. Thus, when these planes are not known or when the aim is to analyze the induced seismicity widespread within the whole area of interest, other approaches have to be used. Shnorhokian et al. (2014) constructed cubes in FLAC3D centered at the location of 24 major seismic events where they investigated the potential for mining-induced seismicity based on some differential stress ( $\sigma_1 - \sigma_3$ ) related indicators, namely the maximum shear stress, the brittle shear ratio (*BSR*) and the continuous change in differential stress (*CC-DS*). They found an abrupt increase in *CC-DS* prior or during the temporal occurrence of major events. Martin et al. (1999) proposed to use the Hoek-Brown criterion with parameters  $m = 0$  and  $s = 0.11$  to predict the depth of brittle failures around underground openings, highlighting good agreement with field observations.

Beside comparing stress related-parameters retrieved by modelling with the location of induced seismicity, other approaches are based on energy estimation. In this framework, a numerically-computed parameter is the energy release rate (*ERR*) (Cook et al., 1966), which is basically a measure of stress accumulation (Jager and Ryder, 1999). This parameter has been mostly applied to assess the rockburst proneness of mine layouts by numerical simulations. However a case where *ERR* was compared with overall induced seismicity is available in the study of Spottiswoode et al. (2008). The authors computed the *ERR* by numerical modelling for two deep (more than -3000 m) South African mines, in terms of the ratio between released strain energy and mined area. Then, these latter quantities were qualitatively compared with some seismic parameters, such as number of events, seismic moment and radiated energy, from events located in the same modelled area. Results shown a better proportionality between seismicity and released strain energy rather than with mined area, leading the authors to conclude that microseismic activity increases with increasing levels of *ERR*. The major problem in applying energy estimates to compare seismicity with modelling is that numerically-calculated energy is not easy to correlate with seismic energy. Indeed, during a failure, only a minor amount of the elastic released strain energy is radiated in the form of seismic energy.

The remaining part (more than 90 % according to Jager and Ryder, 1999) is released under aseismic processes. This represents a clear inherent constraint in the use of *ERR* for describing seismicity.

Finally, a work which is worth mentioning is that of Mercer and Bawden (2005a, 2005b), who attempted to statistically correlate model outputs and seismic parameters. The authors collected a large seismic dataset (about 1150 events) from the deep copper-nickel Creighton Mine (Canada), recorded over three months, and used seismic source parameters as input data for a quantitative correlation with numerical model outputs. In order to obtain model outputs at the location of the events, a linear-elastic and a non-linear-plastic model were run, simulating five successive mining steps. Then, through multivariate statistical techniques, model stress-related variables were quantitatively correlated with seismic source parameters. Beside the inherent difficulty in relating seismic and model variables, which required an intense filtering of the seismic dataset, the authors concluded that, even if relatively highly correlated relations can be found, it is a challenge to meaningfully interpret them in order to gain valuable insights into ongoing failure processes. In addition, predicting the potential for seismicity from such relationships is challenging and not straightforward, and this was not achieved by the authors.

## 6.2 Strategy of comparison in our work

As underlined in the previous section, it is challenging to apply valuable strategy of comparison, especially when the objective is to analyze data from a qualitative and quantitative point of view and at the scale of an entire mine block. The first difficulty is due to the inherent difference in spatial distribution between seismic and model outputs: the formers are given at specific point locations within the whole area of interest, while the latter are widespread within the whole space with a spatial distribution which is given by the size of model mesh zones and a temporal frequency which is related to the different modelled stages. The most intuitive approach of comparison would suggest analyzing seismic and model parameters at the location of each seismic source. However, as will be later shown in this section, this procedure is strongly influenced by location errors of seismic events, which are unavoidable and generally larger than mesh size in the model, at least when a fine mesh (smaller than 5 m) is employed. A second issue is related to temporal aspects. Indeed, when time-dependent effects (such as creep) are not considered in numerical modelling, results only reflect the instantaneous response of rock masses due to neighboring excavations. In contrast, seismicity is clearly time-dependent. This has been shown in Chapter 4 by analyzing different seismic sequences and observing that seismicity rate can take several weeks before going back to the steady state after the immediate stress change induced by blasting. Finally, a third issue, which is strictly related to the seismic dataset analyzed in this work, is the relatively small amount of available events and the limited number of seismic sequences, with respect to the number of excavated stopes.

Based on these considerations and taking into account that spatiotemporal differences between seismic and model outputs cannot be adjusted, we decided to adopt a strategy of comparison at different spatial scales. First, we will perform a qualitative analysis considering the whole 1250 block, comparing seismic events localization with the volume and the position of predicted plastic and potentially damaged zones. Then, to be able to analyze relationships between modelling and seismicity from a quantitative point of view, we will investigate data at a smaller scale, considering punctual measures at seismic source locations and cumulated measures within spheres centered on

the location of the events. The latter analysis will be focused on various seismic source parameters which will be compared with stress- and strain-related variables, as well as with predicted plasticity retrieved by modelling. Finally, results retrieved by smaller scale analysis will be used for a deeper interpretation of the rock mass response to mining throughout the study period.

### 6.3 Qualitative comparison at large-scale

The comparison between seismic data and model results at the scale of the whole 1250 block will focus on some key steps of the exploitation (steps 11, 21, 34, 37 and 41) which resulted in the major seismic sequences ( $S_1$ ,  $S_2$ ,  $S_4$ ,  $S_5$  and  $S_6$ ) described in Chapter 4. Characteristics of the selected steps are summarized in Tab. 6.1. The aim is to investigate whether seismicity path is comparable with the spatial distribution of some model variables, namely the predicted plastic zones and stress variations. These latter will be analyzed based on some instability criteria taken from natural seismicity and rock mechanics literature.

Tab. 6.1 - Some selected model steps and mined-out stopes.

Date	Model step	Seismic sequence	Mined-out stope
2015-07-28	Step 11	$S_1$	13_1157 #3
2015-10-24	Step 21	$S_2$	13_1207 #3
2016-05-13	Step 34	$S_4$	17_1207 #2
2016-06-04	Step 37	$S_5$	13_1182 #2
2016-08-03	Step 41	$S_6$	13_1182 #3

#### 6.3.1 Plastic zone and seismic activity

Plastic zones within the model indicate areas where the yield criterion is reached based on the assumed constitutive laws. Plastic zones give, thus, indication on the extension and the volume of predicted damaged zones due to mining, where fractures can be expected. Therefore, it is interesting to compare the volume and location of plastic zones with the seismicity path at different model steps. For doing so, we selected four excavation steps (steps 11, 21, 34 and 41), which resulted in four major seismic sequences ( $S_1$ ,  $S_2$ ,  $S_4$  and  $S_6$ ), as discussed in Chapter 4. At each of these steps, we considered all the events related to the corresponding seismic sequence and that occurred between the current step ( $step_i$ ) and immediately prior to the subsequent step ( $step_{i+1}$ ). For what concerns plasticity, only model zones which become plastic during the current examined step are included in the analysis, discarding all zones which were already under plastic conditions at previous stages.

Results of this approach are presented in Fig. 6.1. Plastic zones calculated by modelling appear to be widespread in space for each of the analyzed steps, extending over larger areas as the excavation progresses. At step 11 (Fig. 6.1a), in coincidence with seismic sequence  $S_1$ , plasticity close to mined-out stope (indicated by a blue star) is mostly occurring on the walls of the excavated zone and within the roof of the underneath stope. Except for few microseismic events localized close to excavation walls, all the others are not in good agreement with the spatial extent of plastic zones. This means that numerical modelling at the analyzed step cannot explain the distribution of seismic events (i.e. fractures) by means of predicted plastic damage. A possible explanation for the observed trend may

be that the assumed failure criterion (i.e. the assumed constitutive law) within the model is not representative of the mechanism which drives seismicity at the analyzed step. On the other hand, inaccuracy in weak and very weak geological zones reconstruction at local scale may also be responsible for the observed trend. Finally, location errors of seismic events, should also be taken into account.

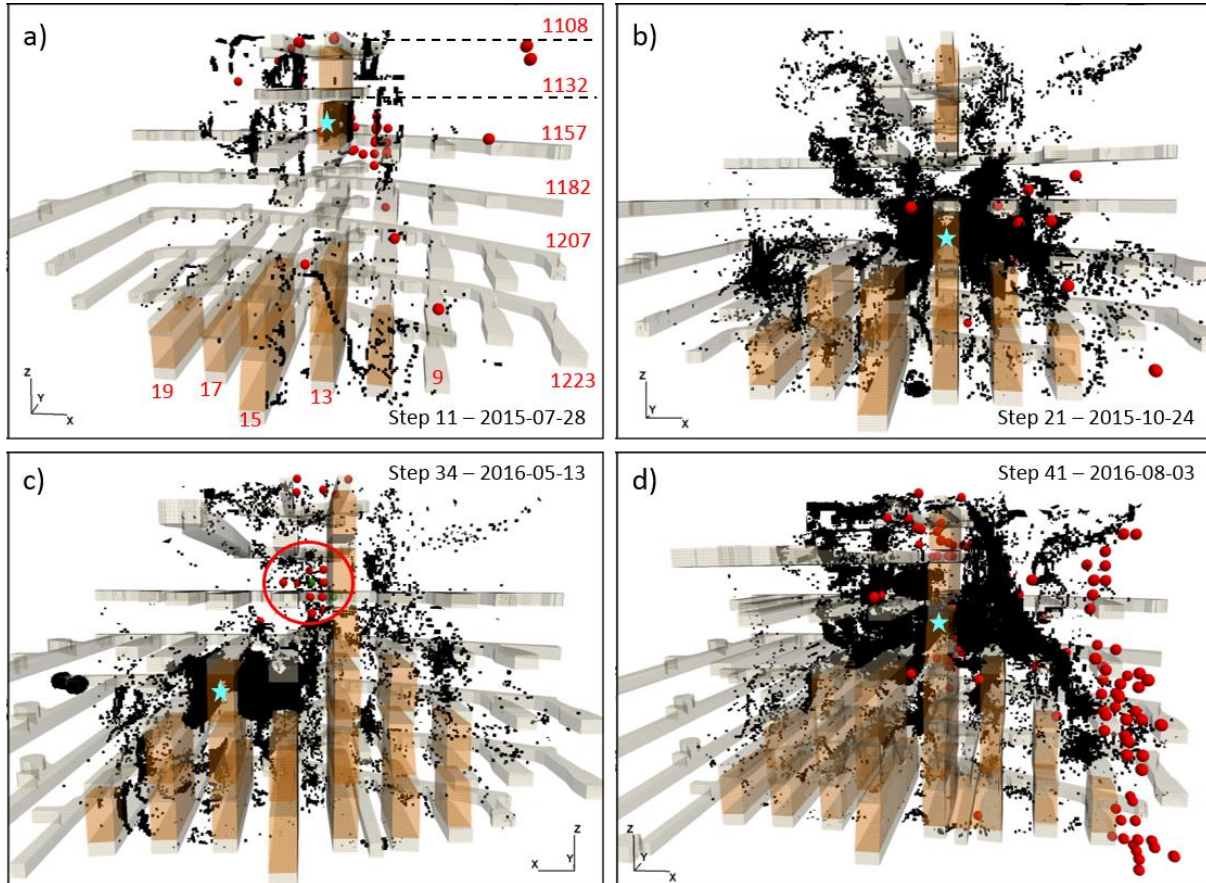


Fig. 6.1 - Comparison between plastic zones and microseismic events. Plastic zones are indicated by black cuboids, while red spheres represent microseismic events. Four modelled steps are considered (a, b, c, d) which are reported on each figure. Stars indicate blast position at each step. Mine levels and primary stoppe names are reported in (a) on the right side and at the bottom of the figure, respectively.

At Step 21 (Fig. 6.1b), plasticity influenced a larger volume with respect to the previously analyzed step. Plastic zones are observed around the excavated stope and extend for about 20 m on the western side and more than 50 m on the eastern side, affecting stopes 12, 11, 10 and 9. This is strongly congruent with the seismicity path, which shows that most of the events are located between stopes 9 and 11 at the depth of the excavation. However, considerable plastic volumes are as well observed in areas where no seismicity occurs. A possible explanation for this trend is that computed plasticity does not take into account the difference between seismic and aseismic damage. Therefore, it is reasonable to have larger plastic zones than the extension of seismically active areas. Note that large plastic zones are as well encountered within the hanging wall of the mine, where a large weak rock mass is present. This trend is observed for all the analyzed mining steps. However, almost no seismicity is located there and, thus, for a better visualization, these zones have been removed from Fig. 6.1 (except in Fig. 6.1a).

As discussed in Chapter 4, seismic sequence  $S_4$  was detected two days after the excavation of Stope 17 at level 1207 (see Tab. 6.1 and Fig. 6.1c). After the blast, no seismicity was detected around the excavation, while two events were located within Stope 14, in the same area which become seismically active two days after, with the occurrence of sequence  $S_4$  (indicated by a circle in Fig. 6.1c). At this step, plasticity is mostly localized around the excavation (indicated by a star in Fig. 6.1c). However, few plastic zones are as well observed in coincidence with the seismically active area, within Stope 14. The observed trend may confirm the hypothesis addressed in Chapter 4, according to which the blast in Stope 17 initiated damage in the area of Stope 14, which was then intensified by time dependent effects (i.e. creep).

At step 41 (Fig. 6.1d) Stope 13 was completely mined-out. This resulted in inducing an intense seismic activity (seismic sequence  $S_6$ ) both in the Central Cluster (CC) and in the Right Cluster (RC). Within CC, seismic events are mostly distributed from the production level (1182) toward shallower depths (Fig. 4.10f). This is congruent with computed plastic zones which are mainly observed in the upper mining levels of block 1250 (Fig. 6.1d). Therefore, seismicity appears to be in good agreement with plastic zones within the CC area. On the contrary, the spatial extent of computed plastic zones does not coincide with that of induced microseismic events in the RC area. When analyzing Step 37 (not shown), in coincidence of which seismic sequence  $S_5$  occurred, we observed a similar trend. CC events are quite well correlated with the spatial extent of plastic zones within the same area of the mine, while no correlation is found for RC seismicity. This discrepancy between CC and RC may indicate that assumed mechanical properties are not able to explain the rock mass mechanical behavior at large-scale. In other words, it could be possible that different parameters should be used for characterizing geological materials of RC area. Further analysis will be needed to investigate this aspect, for example by performing a parametric study based on seismic events localizations. In addition, as shown in Chapter 4, creep phenomenon may be responsible for triggering remote seismicity within RC. This means that the purely mechanical constitutive laws assumed in the model are probably not representative of the mechanisms driving seismicity in the RC area.

### 6.3.2 Instability criteria and seismic activity

Beside plastic zones predicted by modelling based on the assumed constitutive laws, stress-related damage can be as well assessed imposing threshold values of stresses. This topic has been widely studied in the field of rock mechanics applied to underground mining, and various criteria exist in the literature that attempt to predict potential instabilities (e.g. Castro et al., 2012; Martin et al., 1999, 2003; Shnorhokian et al., 2018), as well as rockburst occurrence (e.g. Cai, 2016; Jiang et al., 2010; Miao et al., 2016; Mitri et al., 1999; Xiao et al., 2016).

Generally, seismic events are induced by shear movements along preexistent or newly-formed fracture planes. However, as discussed in Chapter 4, based on S-wave to P-wave energy ( $E_s/E_p$ ) ratio for Lappberget microseismic catalogue, tensile mechanisms cannot be excluded. Numerical modelling results have as well demonstrated the presence of tensile stresses, particularly near stope walls and toward the heart of secondary pillars (Chapter 5). Therefore, it is important to evaluate correlation between seismicity path and instability criteria based on both shear and tensile mechanisms.

A criterion that attempts to describe shear failures, and which is recognized as a good indicator of induced seismicity (Shnorhokian et al., 2018), is based on the differential stress ( $\sigma_1 - \sigma_3$ ) and its

distance from the uniaxial compressive strength of the intact rock mass ( $\sigma_c$ ). This criterion, also known as brittle shear ratio (*BSR*), can be formulated as follow (Castro et al., 2012; Shnorhokian et al., 2018):

$$BSR = \frac{(\sigma_1 - \sigma_3)}{\sigma_c} \quad (6.3)$$

Damage and thus seismicity have been recognized to occur for *BSR* ranging from 0.4 and more than 0.7 (Castro et al., 2012), with higher levels of damage for increasing values of the ratio. However, these thresholds, which are generally retrieved from elastic numerical models, need to be adjusted for plastic models that are more conservative in terms of stress values. A recent study (Switala, 2016) conducted on real damage observed in block 1250 of Lappberget orebody, and based on elastoplastic numerical model, indicates differential stress of 83 MPa as threshold value for failure initiation. This means that potential damage are deemed to occur when the differential stress exceeds 40% of the  $\sigma_c$  of Lappberget orebody, assumed at 188 MPa (see Chapter 5). Thus, the lower limit for the *BSR* criterion has been imposed at 0.4. It can be argued that  $\sigma_c$  is not constant within block 1250 due to the presence of weak and very weak geological zones. However, as already discussed in Chapter 4, MSE are more likely to occur within the ore rather than in weak zones. Thus, it is reasonable to compare the seismicity path with a *BSR* criterion only based on the orebody.

The coulomb failure criterion (equation 6.2) presented in Section 6.1, is commonly used in the field of natural seismicity to assess whether stress changes are likely to bring faults close or far away from failure. This criterion has been as well used to compare major seismic events in underground mines with numerical modelling results (see Section 6.1). However, the use of equation 6.2 requires the knowledge of fault slip planes which are not known for Lappberget. As proposed by Boltz (2014), a simplification of this criterion would simply consider the maximum shear stress variation, discarding the normal stress (see equation 6.2) and thus avoiding the need for fault plane orientation. In natural seismology very small stress changes, in the order of 0.1 MPa, are already sufficient to bring faults toward failure (Stein, 1999). However, due to the rather small seismicity observed in Lappberget and considering that shear stress changes estimated by modelling present values not higher than 40 MPa, a higher threshold of 5 MPa has been imposed for the shear stress change criterion, which is computed between successive excavation stages.

Finally, to evaluate potential instabilities due to tensile mechanisms, zones of the model where the minor principal stress ( $\sigma_3$ ) is higher than 0 have been analyzed and compared with seismic events distribution (using the FLAC3D convention with tension considered as positive). This conservative approach, which ignores the tensile strength of the rock, has been used, following Shnorhokian et al. (2018) and considering that rock masses present, generally, low resistance to traction.

We define “unstable regions” the zone of the model where threshold values of the selected criteria are exceeded and thus where damage can be expected. These areas are then compared with the spatial extent of the induced seismicity at some model stages.

### 6.3.2.1 Predicted shear instabilities

Fig. 6.2 displays model zones where the *BSR* exceeds the threshold value of 0.4. Based on this criterion, a large “unstable region” is predicted for all the analyzed steps within the sill pillar. This was expected due to high stresses within this area of the mine, where stresses induced by



excavations in block 1250 and within the above mining region are concentrated. In addition, “unstable zones” are as well observed at lower levels of the block, following galleries and excavated stopes profiles, particularly at the hanging wall contact, but also within secondary stopes. The observed irregular shape of predicted “unstable regions” based on *BSR* criterion appears to be influenced by the presence of weak geological zones, in addition to stress changes induced by mining. Indeed, “unstable regions” are particularly observed within the orebody in areas surrounded by weak lenses and where excavations have been performed. As weak zones are not able to carry important loads, stress redistribution after the formation of new voids mainly occurs within stiff rocks where the *BSR* exceeds the selected threshold. This mechanism also explains the large “unstable region” within the sill pillar, where in addition to high induced stresses, a massive weak area is encountered.

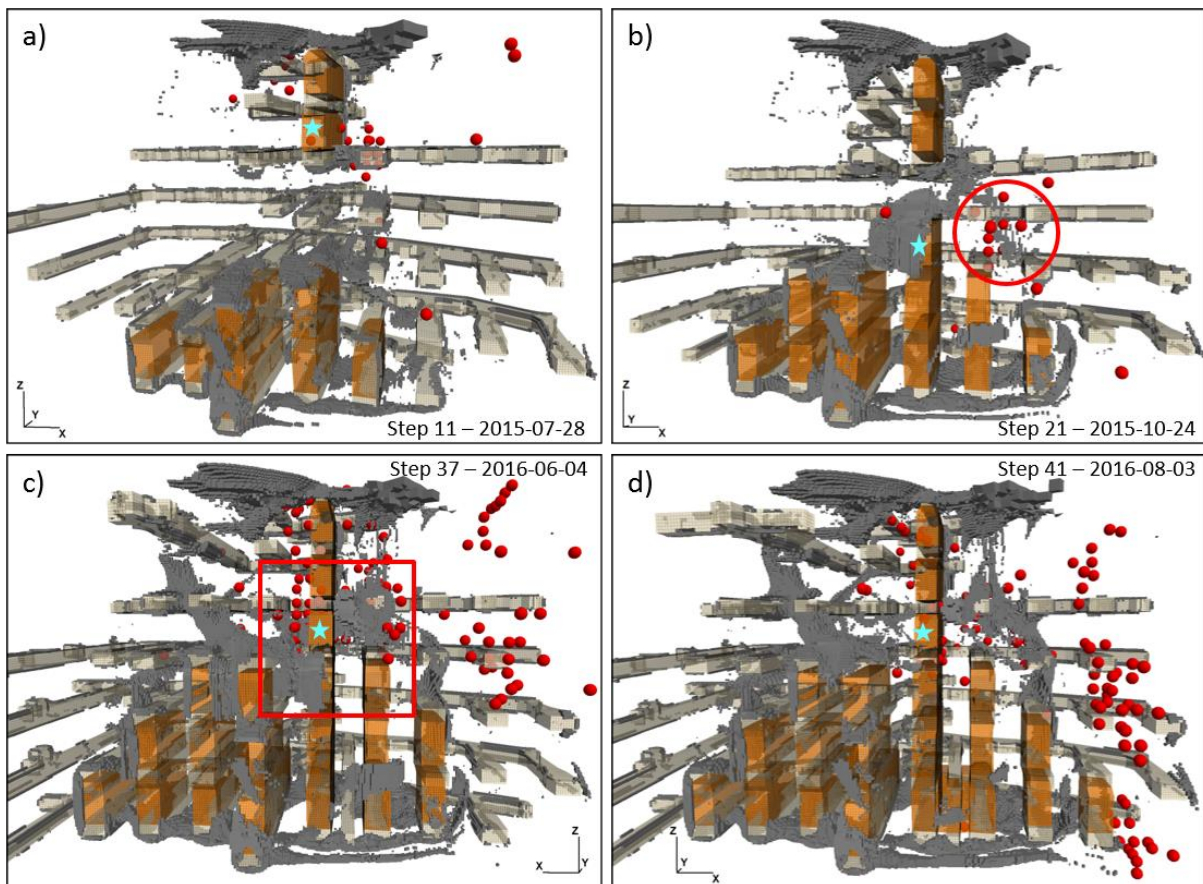


Fig. 6.2 - Predicted “unstable regions” based on *BSR* criterion ( $BSR \geq 0.4$ ). Stars indicate blast position at each model step. The reader is referred to Fig. 6.1 for mine levels and stope names.

At Step 11 (Fig. 6.2a), “unstable regions” are observed at the back of the excavation (indicated by a blue star), as well as in the roof of the underneath stope, similarly to failures predicted by plastic zones analysis (Fig. 6.1a). Therefore, apart from MSE located at the opening back and within the sill pillar, predicted unstable zones do not match with seismic active regions. “Unstable zones” predicted at Step 21 (Fig. 6.2b) are more deployed at the hanging wall contact rather than at the back of the excavation. These areas occur within the orebody in the zone of separation between the mined-out stope and a massive very weak area, highlighting again the strong influence of geological heterogeneities on stress field redistribution and, thus, on the *BSR* criterion. Almost no damage is predicted within secondary stopes adjacent to the excavation. A smaller “unstable area” is observed

where most of seismic events are located at the analyzed step (indicated by a circle in Fig. 6.2b). Even if only few zones are brought to failure in this area compared with other regions of block 1250 and even if events are not located in exactly the same model mesh elements, the correlation between seismicity path and predicted instabilities is satisfying.

It is interesting to compare the distribution of predicted “unstable regions” between steps 37 and 41 (Fig. 6.2c and d). Indeed, the “unstable regions” predicted in secondary stopes 12 and 14 at Step 37 (indicated by a rectangle in Fig. 6.2c), disappear almost completely at Step 41, when Stope 13 was totally mined-out. This indicates that these zones have probably reached or are close to the residual strength during Step 41, in agreement with stress measurement performed in Stope 14 (PH cell) that indicated an almost complete destressing at this stage of the excavation (see Chapter 4). In addition, the observed trend is in accordance with seismicity path which at Step 41 shows a significant decrease of MSE around Stope 13 with respect to Step 37. It can, thus, be concluded that predicted unstable zones at the last two examined steps are well correlated with the spatial extent of MSE around Stope 13 (i.e. CC). Nevertheless, this is not the case for RC seismicity, where the *BSR* criterion never exceeds the imposed threshold at any of the analyzed stages, except in very localized regions at galleries edges (Fig. 6.2). The main reason for this lack of correlation is the absence of mined-out stopes within the RC area. Indeed, as observed for the previously analyzed stages, the *BSR* criterion appears to be strongly influenced by excavations and presence of weak zones. Their mutual geometry defines zones within the ore where stresses are concentrated and the *BSR* exceeds the imposed threshold. This behavior is accentuated within the central region and in the eastern area of the mine when closer voids become mechanically dependent each other, and stress redistribution is widespread over larger areas. Therefore, for a modelling point of view, the only presence of weak lenses within RC is not sufficient to account high stress states induced by distant excavations. Even if weak materials in this region of the mine may present high strain values (due to plasticity), as discussed in Chapter 5, the stress state within surrounding stiff rocks remain at relatively lower levels as only poorly influenced by adjacent excavations.

### 6.3.2.2 Variation of maximum shear stress

At step 11 (Fig. 6.3a), “unstable regions” based on maximum shear stress variation are punctually located around the excavation. This appears to be in good agreement with the seismic sequence ( $S_1$ ) induced at the analyzed mining stage, where events are mainly located on the eastern side of the excavated stope.

At step 21 (Fig. 6.3b) a significantly larger volume is brought to failure according to shear stress change criterion. The “unstable region” is located around the mined-out stope and particularly on its eastern area, in accordance with the zone where most of seismic events are observed.

As observed in the case of *BSR* criterion, the analysis of maximum shear stress variation cannot account for the induced seismicity within the RC (Fig. 6.3c, e and d). In addition, at steps 37 and 41, the maximum shear stress criterion appears to be poorly correlated even with CC seismicity, except for the events located toward the eastern side of the excavation.

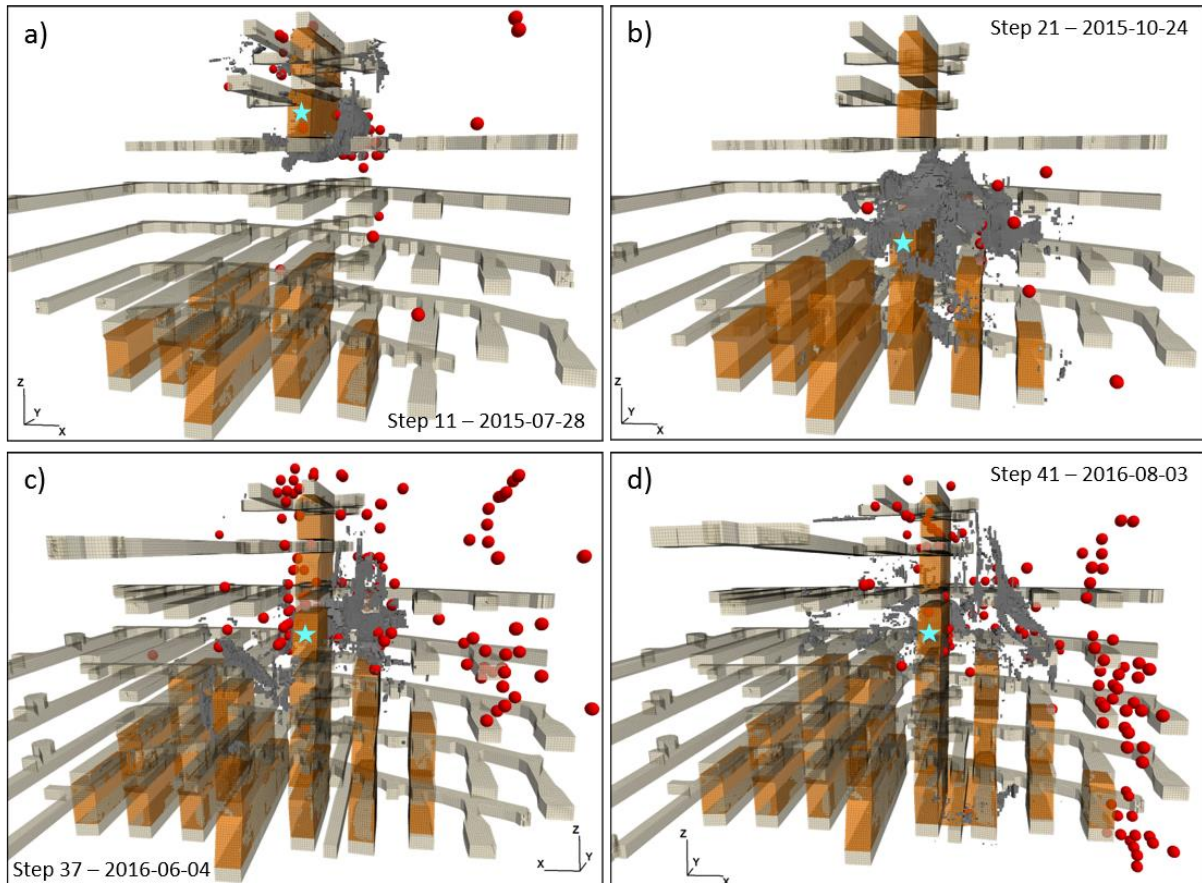


Fig. 6.3 - Predicted “unstable regions” based on maximum shear stress variation criterion ( $\Delta\tau \geq 5$  MPa). Stars indicate blast position at each model step. The reader is referred to Fig. 6.1 for mine levels and stope names.

### 6.3.2.3 Tensile instabilities

Results of tensile criterion analysis are presented in Fig. 6.4. As expected for considerations addressed in Chapter 5, tensile stresses are locally observed within secondary stopes where primaries have already been mined-out, in close proximity to the excavation walls. Few tensile zones are as well encountered at the hanging wall contacts. These areas are gradually enlarging as the volume of voids is increasing, such that the central region of block 1250 appears to be the most affected. Overall, areas characterized by tensile stresses do not correlate well with the seismicity path for any of the analyzed steps, apart from events occurring at stope walls and particularly at Step 41 (Fig. 6.4d).

Even if this criterion may not be suitable for predicting seismically active areas, the distribution of expected tensile stresses is in good agreement with results of  $E_S/E_P$  ratio presented in Chapter 4. Indeed, it has been observed that CC seismicity is characterized by smaller  $E_S/E_P$  ratios than the RC population, indicating a larger occurrence of events driven by tensile mechanisms for the former cluster rather than for the latter. Therefore, this is congruent with numerical modelling results, where tensile stresses are mostly occurring in the central region of the mine, while no tension is observed within the RC area.

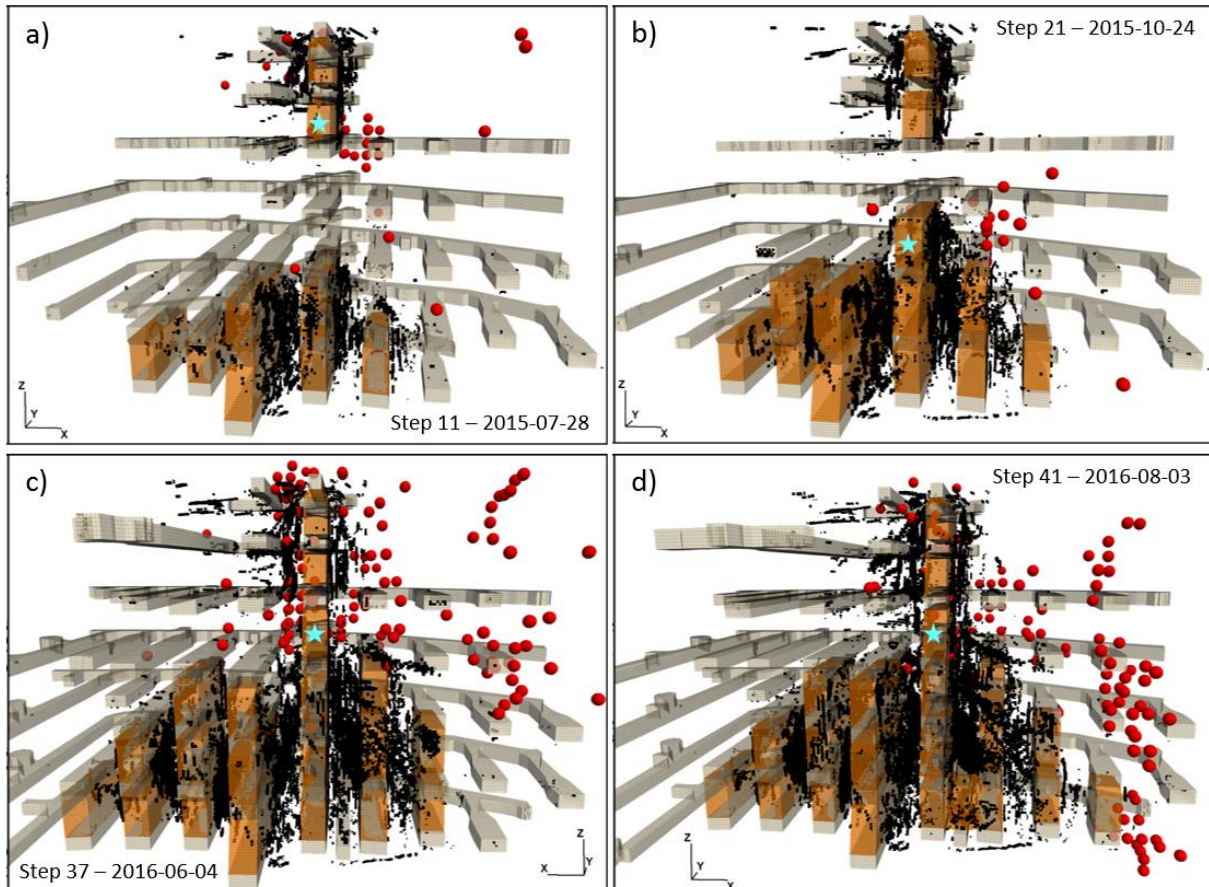


Fig. 6.4 - Predicted “unstable regions” based on tensile criterion ( $\sigma_3 > 0$ ). Stars indicate blast position at each model step. The reader is referred to Fig. 6.1 for mine levels and stope names.

## 6.4 Quantitative comparison at small-scale

The analysis conducted at the scale of the whole area of interest demonstrates that spatial correlations can be found between predicted damaged in the CC area. On the contrary, RC seismicity is only poorly explained by numerical modelling, especially when considering stress-based criteria, because stress changes calculated by the model appear not large enough to induce the high seismicity rates observed in situ. Nevertheless, large-scale comparison is qualitative and restricted to few modelled mining steps, thus, further investigations are needed.

In order to quantitatively compare model and seismic parameters, it is necessary to solve the spatial problem between model and seismic variables, which are given in the whole space and at certain point locations, respectively. Model space needs, thus, to be restricted around source location of MSE to be able to compare model and seismic parameters within seismically active areas throughout the study period. In this framework, two approaches have been chosen. The first consists in analyzing model and seismic variables at the location of MSE, to investigate whether quantitative correlations can be found. While, the second is based on the selection of a sub-volume within the whole area of interest of the model identified by spheres centered at event localizations. Inside this selected sub-volume, some model outputs as well as seismic variables can be cumulated throughout the study period, to investigate possible correlations in their reciprocal temporal trend.

Before data comparison, the whole microseismic catalogue, characterized by 762 MSE, required some filtering. Firstly, events localized in model voids (galleries and/or mined-out stopes), probably due to location errors or because of their proximity to gallery and stope walls, were removed from the catalogue. Then, to handle the problem of events with identical location or falling within same model mesh elements, the event with higher energy was selected discarding the others. These operations reduced our initial catalogue to a total of 552 events which determines point representing source locations within the mechanical model. Each of these points can be identified by selecting the corresponding or the closest mesh element of the model, which will be then characterized by a number of seismic and model variables according to events source parameters and model results. Fig. 6.5a depicts the identified model meshes according to the selected 552 event locations, which are color-coded as a function of the geological unit to which they belong.

Once model meshes in seismically active regions are selected, a FISH-language code is used to build 10 m radius spheres around source event locations (Fig. 6.5b). This determine a sub-space within the whole area of interest identified by spheres position. When spheres are located at the boundary between different geological units, they will comprise portions of different geological formations. Moreover, due to the close position between MSE in some regions, spheres can overlap each other. The choice of sphere radius dimension is simply motivated by MSE source location errors, which show mean values lower than 14 m (see Chapter 3).

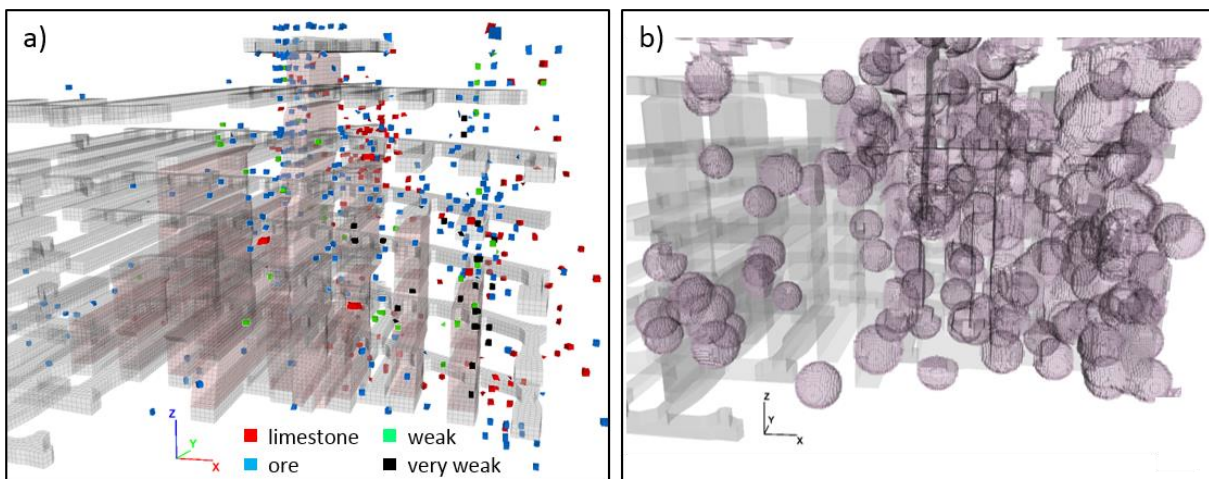


Fig. 6.5 - Point sources locations and spheres. (a) Model zones in coincidence or closest to event source locations, colored as a function of the geological unit to which they belong. (b) Selection of the sub-space within the whole area of interest based on 10 m radius spheres drawn from MSE hypocenters.

#### 6.4.1 Model and seismic parameters at punctual locations

Model results vary in space and as a function of the considered excavation step. This means that model parameters can change at each considered steps within the 552 selected meshes. On the other hand, microseismic events are recorded at specific instants of time which can be related with the temporal occurrence of excavations and thus with that of model steps. For this reason, a temporal criterion has been chosen to associate each microseismic event (i.e. each model meshes) to a particular excavation phase among the 52 simulated excavations. As schematically represented in Fig. 6.6, for each modelled step (i), which corresponds to a production blast (i), all events recorded at the time of a given blast (i) and immediately prior to blast (i+1) are associated to the current Step(i).

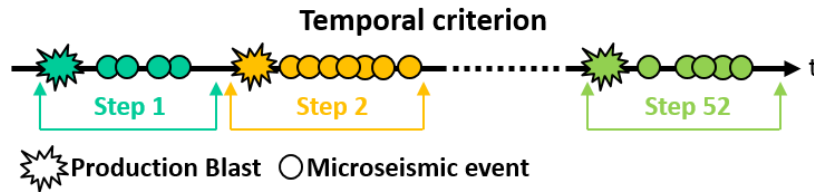


Fig. 6.6 - Schematization of temporal criterion chosen to associate each MSE to a singular modelled excavation step.

As a function of the modelled step to which it belongs, each selected model mesh is characterized by a number of model outputs and seismic variables as listed in Tab. 6.2.

Tab. 6.2 - Model outputs and seismic parameters considered for comparison.

Model outputs		Seismic parameters
<i>Stress parameters [MPa]</i>	<i>Strain parameters [m/m]</i>	
$\sigma_1$ - max. principal stress	$\epsilon_1$ - max. principal strain	$M_0$ - seismic moment [J]
$\sigma_2$ - int. principal stress	$\epsilon_2$ - int. principal strain	$E$ - radiated seismic energy [J]
$\sigma_3$ - min. principal stress	$\epsilon_3$ - min. principal strain	$r$ - source radius [m]
$\sigma_{ij}$ - stress tensor components	$\epsilon_{ij}$ - strain tensor components	$\sigma_a$ - apparent stress [MPa]
$\tau$ - maximum shear stress	$\gamma$ - maximum shear strain	$\Delta\sigma$ - stress drop [MPa]
$q$ - deviatoric stress	$\epsilon_q$ - deviatoric strain	$f_c$ - corner frequency [Hz]
<i>Elastic parameters [J]</i>	<i>Plastic parameters [J]</i>	$V_a$ - apparent volume [m <sup>3</sup> ]
Volumetric elastic energy	Volumetric energy dissipated by plasticity	
Shear elastic energy	Shear energy dissipated by plasticity	
Total elastic energy	Total energy dissipated by plasticity	
	Plastic volume [m <sup>3</sup> ]	

Given the number and the nature of selected variables, a multivariate statistical approach has been chosen to be able to simultaneously investigate relations between more than two variables within the model and seismic database. In this context, the principal component analysis (PCA) has been adopted. The aim of this statistical technique is to convert a set of  $n$  observations in a smaller set of values called principal components, based on the variance of the initial observations. The first advantage of PCA is its ability to find correlations between observations without assuming any dependent variable. In addition, a second advantage is its graphical output, which allows to easily identify variables having stronger correlations. However, to perform a consistent analysis, it is preferable to analyze data which are not dependent on each other. This means that parameters chosen for the statistical analysis, as listed in Tab. 6.2, cannot be evaluated all together, as among seismic and model datasets, many parameters are between them interlinked. For this reason, groups of independent parameters within model and seismic datasets have been isolated and then analyzed by means of PCA. The first two selected groups are reported in Tab. 6.3 and contain three independent seismic variables and one model variable each. These groups have been chosen first as they relate parameters whose eventual correlations may be better explained from a physical point of view.

Tab. 6.3 - Selected groups of model and seismic parameters and variables transformations.

Groups of model and seismic parameters	Variables transformations
$q; E; f_c; M_0$	$1/q; q^2; \sqrt{q}$
$\varepsilon_q; E; f_c; M_0$	$1/\varepsilon_q; \varepsilon_q^2; \sqrt{\varepsilon_q}$

As visible from Tab. 6.3, identified variables have been previously transformed before proceeding with the statistical analysis. Indeed, PCA only accounts for linear correlations among parameters, while we do not have any indication for a preferential linear relationship between model and seismic variables. Transformations, which were only applied to model parameters, have been thought to overcome the describe linear correlation approach of PCA technique. When PCA was applied to the first two selected groups, only poor correlations could be found. As an example, results of PCA for the first selected group of parameters are reported in Fig. 6.7. The two axes represent the principal components on which variables are projected as a function of their variance, such that parameters laying on the same axis have a strong correlation, while not being correlated with parameters closer to the second axis. Based on this criterion, Fig. 6.7 shows that a correlation exists between deviatoric stress and corner frequency (that is inversely proportional to seismic source radius), while no correlation can be found with seismic moment ( $M_0$ ) nor with seismic energy ( $E$ ), which are however correlated between them. Nevertheless, as reported in Fig. 6.7, the strength of the correlation is extremely low.

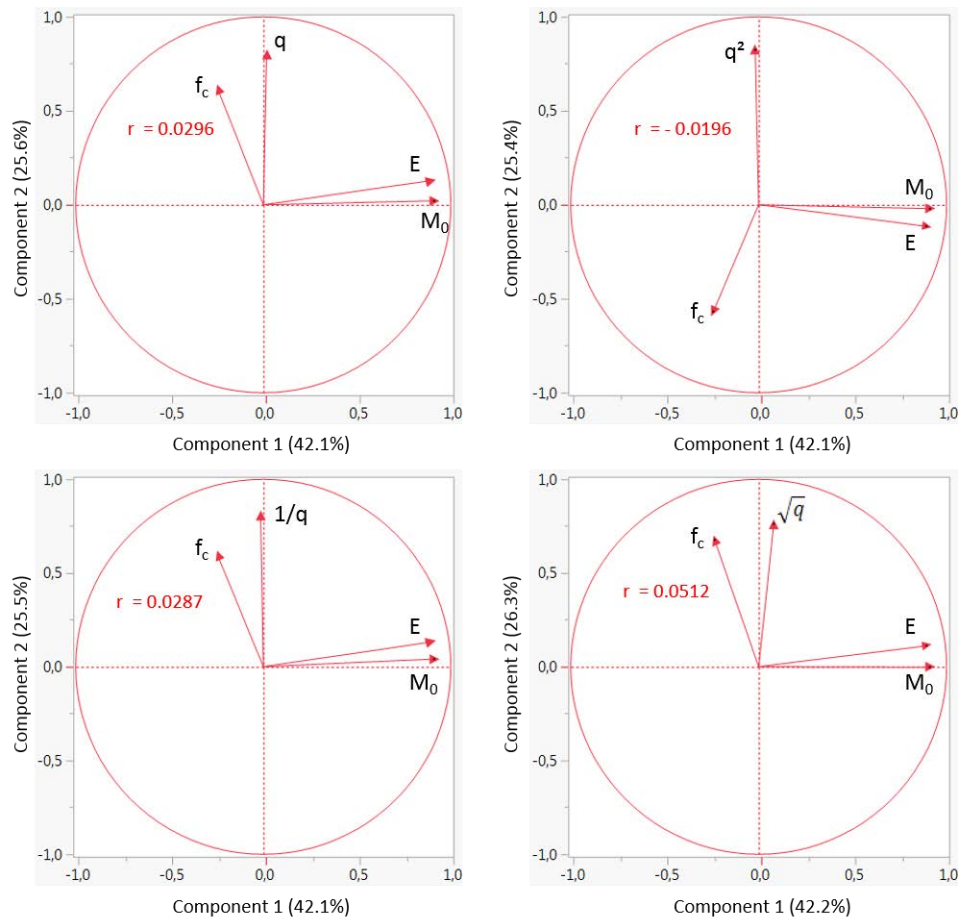


Fig. 6.7 - PCA results for the first selected group of parameters. The coefficient of correlation reported in each graph is referred to the correlation between the corner frequency ( $f_c$ ) and the deviatoric stress ( $q$ ) or one of its transformations.

In an attempt of improving correlations, the contribution of CC was separated from that of RC events and these two subsets have been evaluated separately, still considering groups of parameters reported in Tab. 6.3. Indeed, RC seismicity has already shown only a poor qualitative correlation with the spatial extent of plastic zones. Nevertheless, this separation did not result in any significant improvement of the correlation.

A reason for these poor correlations may be related to seismic and model uncertainties, such as approximation in the geometry reconstruction of geological formations, as well as errors in microseismic events localization. To give an example, Fig. 6.8 reports contour maps of apparent stress (see equation 4.3) and deviatoric stress as retrieved at the locations of the 552 selected meshes of the model and considering each modelled excavation step. It appears that the area characterized by a larger apparent stress, as retrieved from seismic source parameters, is not located in coincidence with the area characterized by large deviatoric stresses retrieved from numerical modelling (both indicated by a circle in Fig. 6.8). When trying to find quantitative correlations, the observed difference in the location of seismic and model parameters plays a dominant role. It inevitably reduces the strength of the correlation.

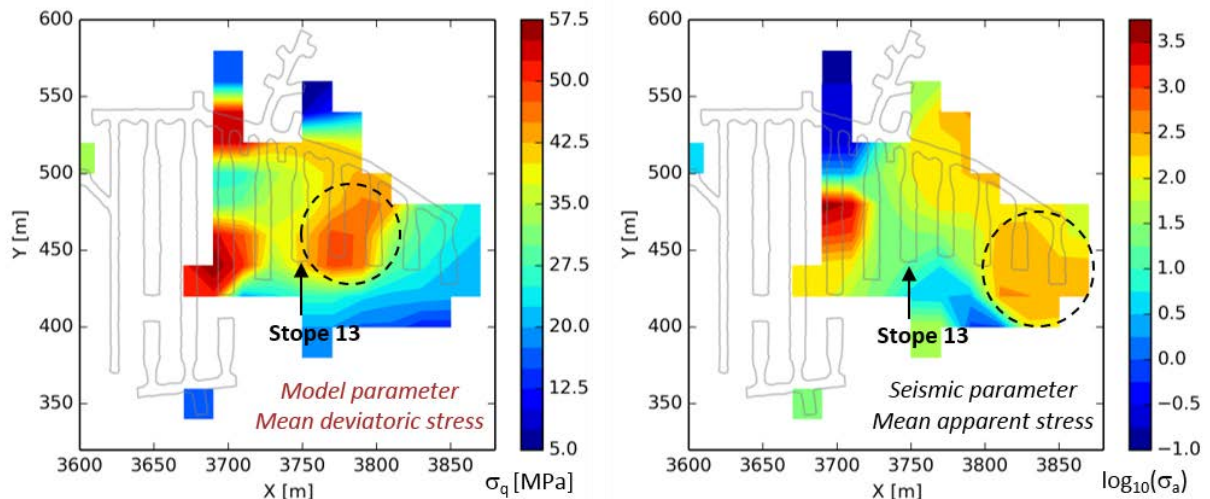


Fig. 6.8 - Contour maps of mean deviatoric stress (on the left) and mean apparent stress (on the right) for the identified 552 source point locations. Note that, the average of apparent stress and deviatoric stress have been computed considering all source points discarding their depth. The apparent stress is reported in logarithmic scale for a better visualization.

As already demonstrated by Mercer and Bawden (2005a), to find statistically significant multivariate correlations between seismic and model variables, a preliminary intense filtering of both datasets is needed. The author found that the strength of the relations is enhanced when considering only “background” seismicity, which they defined as the seismicity randomly distributed in time and generated under relatively stable stress conditions. However, the aim of the current thesis is not that of working on background seismicity, rather that of finding possible relations between model and seismic parameters for describing seismicity strictly related to the mining process.

The compared statistical analysis between seismic and model parameters has not been further evaluated in this thesis. However, the here proposed procedure for data analysis give a methodology and a starting point for future studies.



### 6.4.2 Model and seismic parameters at spheres location

Another way to partially solve the spatial problem between seismic and model variables is to consider model parameters over a larger area, rather than at the source location of MSE. This has been done by considering sub-volumes consisting of 10m-radius spheres, as previously described. The entire spheres sub-volume is thus considered as a new smaller volume of interest with respect to the whole 1250 block. Selecting average or cumulative values of model outputs at each modelling step, it is possible to follow temporal variations of model results within the spheres, looking for differences between seismically quiet and active periods. At the same time, temporal variation of model parameters within the spheres can be compared with that of seismic variables, to look for correlations.

As discussed in Chapter 4, RC and CC seismicity appears behaving differently. RC events present energy, stress drop and apparent stress values higher than the CC population, which is, on the contrary, characterized by larger source radii. In addition, if CC is seismically active throughout the whole analyzed period, RC becomes a significant source of seismicity only in the second half of 2016, when the local seismic activity started being influenced by final exploitation stages in the distant Stope 13 (steps 37 and 41). Based on cross-analysis between seismic data and geotechnical measurements (Chapter 4), RC seismicity has been explained considering: i) the heterogeneous geological setting of the area, ii) the probable occurrence of aseismic slip induced by blasting and iii) the overstressed conditions within and around the last block of Stope 13. All these observations make the distinction between CC and RC a phenomenon we wanted to analyze by means of numerical modelling. For doing so, the spheres of CC and RC were analyzed separately. To avoid misunderstanding, CC and RC regions identified by spheres sub-space will be thereafter reported with the subscript M (i.e.  $CC_M$  and  $RC_M$ ) to indicate their belonging to numerical model space.

Stresses, strains and plastic volumes have been monitored at each modelled mining step within the spheres, and therefore in  $CC_M$  and  $RC_M$  regions, and then compared with timings of major seismic sequences observed during the studied period. As a reminder, the list of seismic sequences is reported in Tab. 6.4, together with the corresponding model step and the mined-out stope. For stope position, the reader is referred to Fig. 5.13.

Tab. 6.4 - Seismic sequences and model steps. Note that  $S_4$  is a self-triggered seismic sequence occurred two days after Step 34. This latter step has been thus added in the table.

Seismic sequence	Date	Model step	Mined-out stope
$S_1$	2015-07-28	Step 11	13_1157 #3
$S_2$	2015-10-24	Step 21	13_1207 #3
$S_3$	2016-02-25	Step 29	13_1182 #1
-	2016-05-13	Step 34	17_1207 #2
$S_4$	2016-05-15	-	-
$S_5$	2016-06-04	Step 37	13_1182 #2
$S_6$	2016-08-03	Step 41	13_1182 #3

Results are presented in Fig. 6.9 and Fig. 6.10 in terms of deviatoric stress, deviatoric strain and plastic volume, which are reported together with the excavation advancement in Stope 13. Mean values of stresses and strains retrieved at each simulated step within the spheres have been

subtracted from mean values computed at Step 0.13, right before the installation of seismic monitoring network in Lappberget orebody. In this manner, it is possible to analyze variation of model parameters in the same temporal span as seismic activity.

In terms of deviatoric strain (Fig. 6.9a), we observe a gradual increase within  $CC_M$  region (in red in Fig. 6.9a) for a total variation of 1.7 mm/m at the end of the analyzed period. Strains are punctually increased by excavations of nearby stopes, showing four major jumps, which occur in coincidence with seismic sequences  $S_2$ ,  $S_3$ ,  $S_5$  and  $S_6$ , while no significant change is observed at the time of sequence  $S_1$  (see Tab. 6.4 and Fig. 6.9a). Production of Stope 17 at step 34 also resulted in a smaller but still visible increase of induced strains within  $CC_M$  (Fig. 6.9a).

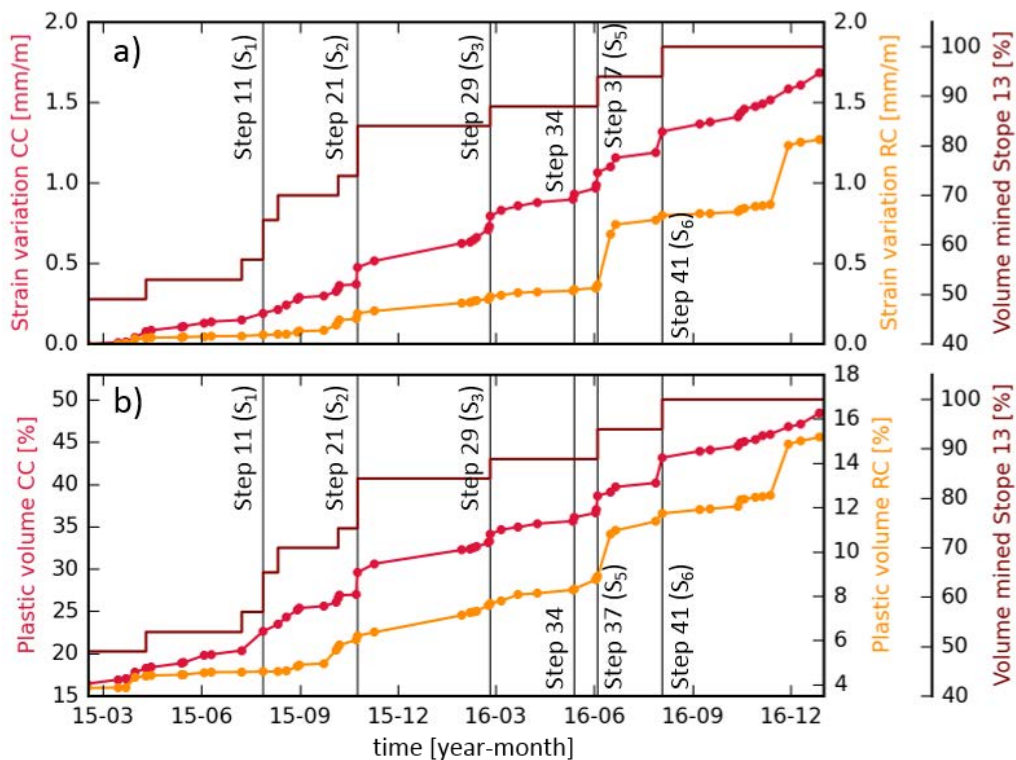


Fig. 6.9 - Mean deviatoric strain and plastic volume within spheres. (a) Mean deviatoric strain variation within model spheres for  $CC_M$  (in red) and  $RC_M$  (in yellow). (b) Percentage of plastic zones within spheres for  $CC_M$  (in red) and  $RC_M$  (in yellow). Vertical black lines indicate modelled mining steps which lead to major seismic sequences (see Tab. 6.4). Note that in (b) plastic volumes for CC and RC do not have same scale. The brown curve represents the percentage of excavation advancement in Stope 13 along time.

Strains in  $RC_M$  region (in yellow in Fig. 6.9a) appear to be strongly influenced by mining in RC area, as visible from the two larger increments in June and November 2016 that are linked with Stope 7 exploitation. However, small strain changes can be as well observed in coincidence with exploitation stages which resulted in the major seismic sequences (steps 21, 29, 37 and 41) and related with Stope 13 production. Even if very low, these strain increments demonstrate that the model can account for strain variation even at certain distance from the excavation and that Stope 13 production influenced strain in  $RC_M$  all along its excavation sequence. However, strain changes do not variate significantly from one step to another, thus, they are not large enough to explain the remote triggering of seismicity in the RC occurred at steps 37 and 41. Overall,  $CC_M$  and  $RC_M$  curves present a similar trend which indicates a similar mechanical response to mining. As a result,  $RC_M$  and  $CC_M$  have a comparable rate of strain increase.

The temporal variation of predicted plasticity within  $CC_M$  and  $RC_M$  is reported in Fig. 6.9b as the percentage of plastic volume with respect to the total number of zones belonging to each region. Overall, these curves present a temporal trend strongly comparable with that of strain variation. However, at the end of the study period, the 49% of the zones within  $CC_M$  were under plastic conditions, while plasticity in  $RC_M$  accounts only for the 15% of the whole region.

The temporal trend of mean deviatoric stresses within model spheres is illustrated in Fig. 6.10a and b. This is reported in terms of variation with respect to the reference Step 0.13 (Fig. 6.10a) and as mean absolute values (Fig. 6.10b) at each modelled step.

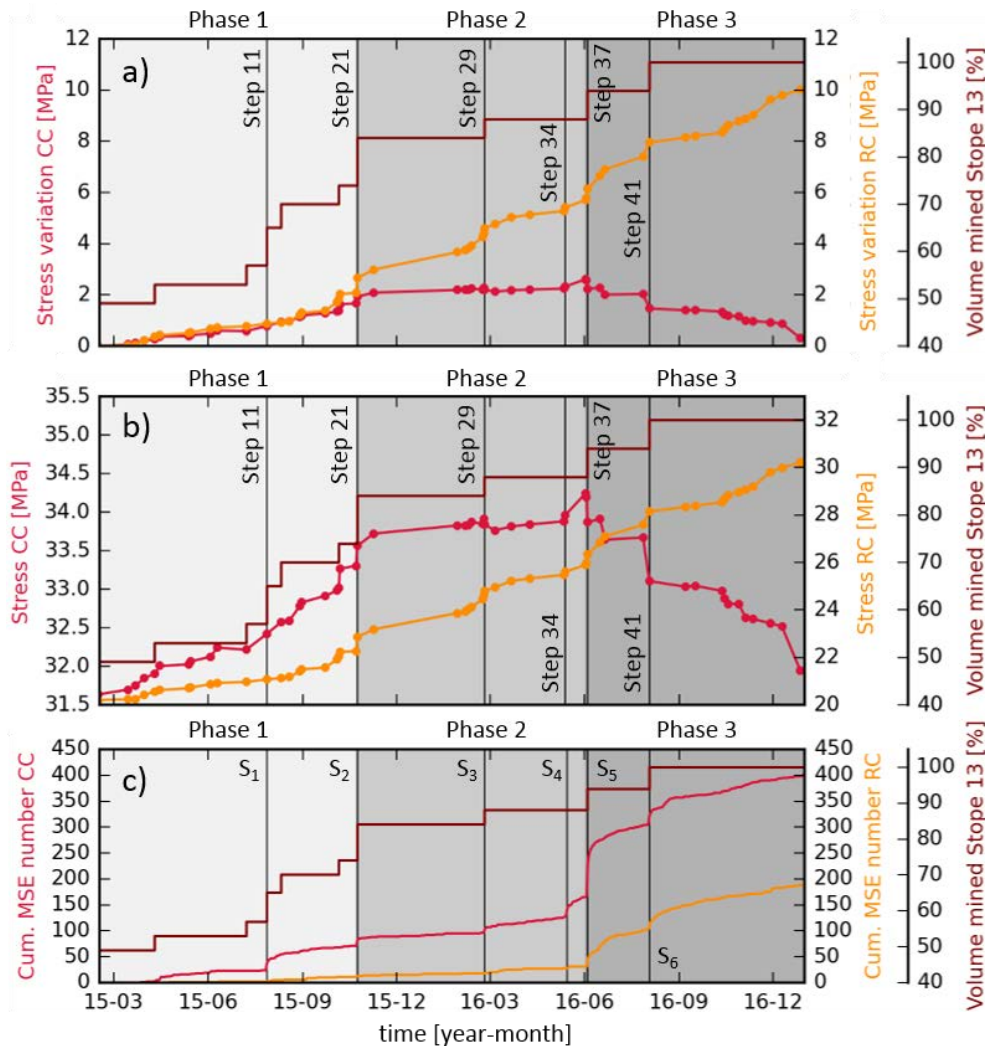


Fig. 6.10 - Mean deviatoric stress within spheres and temporal evolution of seismic activity. (a) Mean deviatoric stress variation with respect to the reference Step 0.13 within  $CC_M$  (in red) and  $RC_M$  (in yellow). (b) Average deviatoric stress values at each modelled mining step within  $CC_M$  (in red) and  $RC_M$  (in yellow). (c) Cumulative number of MSE in CC and RC. Note that in (b) deviatoric stress within  $CC_M$  and  $RC_M$  do not have same scale. Background colors mark three distinct temporal phases which are named on top of the graphs (see text for more details). The brown curve represents the percentage of excavation advancement in Stope 13 along time.

Trends of  $CC_M$  and  $RC_M$  clearly indicate significantly different behaviors. Mean stresses within  $RC_M$  are gradually increasing, reaching 10 MPa difference at the end of the study period, while  $CC_M$  has a more complex trend characterized by smaller stress changes, with a maximum increase of about 2.6 MPa (Fig. 6.10a). Overall, mean stresses remain higher within  $CC_M$ , ranging from a minimum of 31.6

MPa to a maximum of 34.2 MPa (Fig. 6.10b). However, the difference in the stress state between the two regions is gradually reduced as excavations progress and due to the increase of stress state within  $RC_M$  and the concurrent stress decrease in  $CC_M$ . At the end of the analyzed period, mean stresses are comparable within these two regions of the mine (Fig. 6.10b).

Three distinct phases can be identified in Fig. 6.10, which are marked with different background colors. At the beginning of the analyzed period and until Step 21 (Phase 1),  $CC_M$  and  $RC_M$  regions present similar rates of stress increase (Fig. 6.10a). Then, when the excavation advancement within Stope 13 reaches 84% (Step 21) and until Step 36 (Phase 2), when the mined-out volume is at 88%, stress remains almost constant within  $CC_M$  at the highest level, while it increases significantly in the  $RC_M$ . Finally, after Step 37 (Phase 3), thus, in coincidence with the two last stages of Stope 13 exploitation, stress state in  $CC_M$  starts dropping until the end of the study period, while stresses within  $RC_M$  keep rising. For comparison, the cumulative number of MSE within CC and RC is reported in Fig. 6.10c. The intense seismic activity within RC ( $S_5$  and  $S_6$  in Fig. 6.10c) takes place immediately after a period where stresses in the major production area (i.e.  $CC_M$ ) remain almost constant around the highest level, while they continue growing in the future seismic active region (i.e.  $RC_M$ ). At the same time, as observed in Fig. 6.9, strain and plastic volume are gradually increasing in both  $CC_M$  and  $RC_M$  throughout the analyzed period.

#### 6.4.2.1 Excavations, rock mass response and remote seismicity

To be able to understand the mechanical origin of seismicity, rock mass response to mining as retrieved by numerical modelling needs to be analyzed throughout the study period and considering responses of  $CC_M$  and  $RC_M$ . As proposed by some authors (e.g. Andrieux et al., 2008; Cotesta et al., 2014; Fairhurst, 2004), the strain-softening response of rock masses solicited by external forces (e.g. blasting) can be divided into 5 regions (Fig. 6.11), which can be related with different seismicity rates.

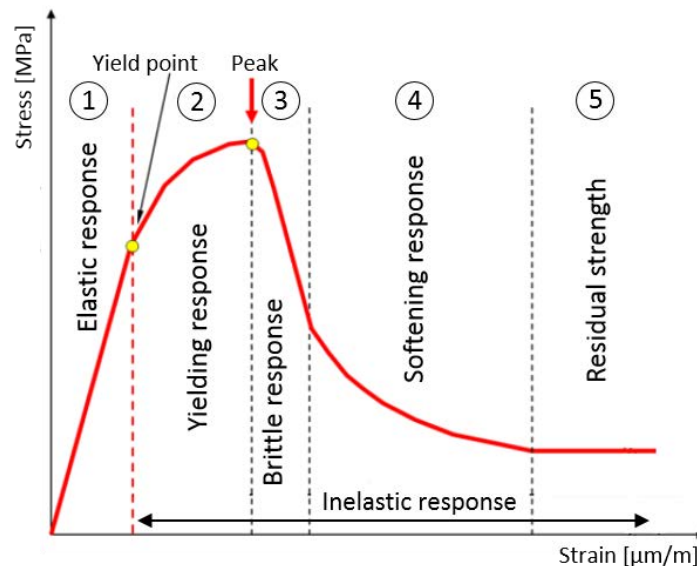


Fig. 6.11 - Five regions of the strain-softening response for a moderately jointed rock mass (modified after Cotesta et al., 2014).

The first region in Fig. 6.11, corresponding to the elastic response, is primarily aseismic as no permanent damage occur within the rock mass. Nevertheless, low level of microseismic activity can be associated with this response. After the yield point, fractures can occur, and the seismicity rate is

accelerating with a more pronounced seismic activity after blasts (Andrieux et al., 2008). During the yielding phase, stresses are gradually increasing until reaching the peak strength. Immediately after, the brittle phase takes place, where damage and rock mass deterioration can be observed, accompanied with larger seismic events. From this stage, and until reaching the residual strength, the rock is gradually destressed as deformation progresses. During the softening response phase, some seismicity can still occur, while the residual phase is generally characterized by aseismic deformations as the rock mass is not anymore able to store sufficient strain energy.

Strain-softening curves are valid for rock samples during laboratory tests. However, the different regions of the strain-softening response, as described from Fig. 6.11, could be used to characterize rock mass response that occurred within CC and RC during the studied period. Fig. 6.12 reports average deviatoric strains in function of the average deviatoric stress both computed within sphere sub-space. The curves are shown separately for  $CC_M$  (Fig. 6.12a) and  $RC_M$  (Fig. 6.12b) and are compared with the three phases previously identified in Fig. 6.10.

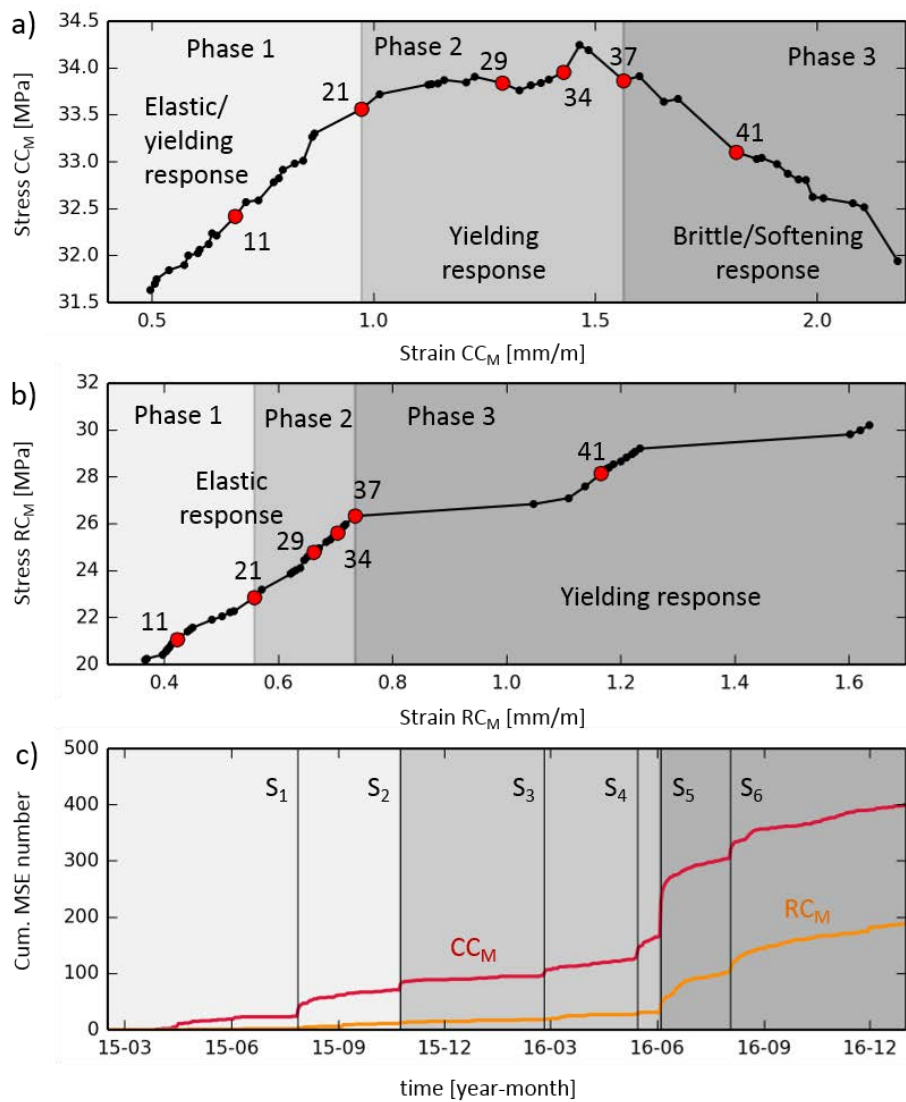


Fig. 6.12 - Average deviatoric strains versus average deviatoric stresses as retrieved by numerical modelling. Average values are determined on sphere sub-space for  $CC_M$  (a) and  $RC_M$  (b). Red dots correspond to mining

steps which resulted in seismic sequences. These are indicated according to the number of the corresponding step. (c) Cumulative MSE number.

Considering  $CC_M$  region (Fig. 6.12a), Phase 1 may cover the elastic and the yielding response, when stresses, strains and seismic activity (Fig. 6.12c) are gradually increasing as excavation progresses. At the beginning of Phase 2,  $CC_M$  region is brought close to peak strength. Subsequent excavations within neighboring stopes contribute to further increase strains within this area of the mine, while the stress is slightly fluctuating around a mean value of 33.7 MPa until Step 29. This latter mining step corresponds to the first excavation within the last block of Stope 13 (see Tab. 6.4) when large strain changes were recorded by CSIRO cells (see Fig. 4.21). Peak strength appears to be reached immediately after Step 34 and due to production in Stope 15. However, no strains were recorded by CSIRO cells in coincidence with this excavation, thus, model results may be probably overestimated at this stage. Consequently, peak strength may have been reached in coincidence with Step 34, when a significant strain shift was detected (Tab. 4.2). Finally, Phase 3, starting with Step 37, corresponds to the brittle response, with a large seismic response, a rapid stress decrease and consequent increasing strains.

This means that intense remote seismicity within RC started when the CC entered in its brittle/softening phase, thus, when additional loads induced by blasting cannot be redistributed around the excavations and are transferred toward the RC. The idea of stress transfer toward RC area due to an incapacity of CC to sustain additional load was already proposed in this thesis. However, except for the strong seismicity triggered in RC, there were no additional evidences for this mechanism. Numerical modelling results, demonstrate the occurrence of a significant stress drop during the last two blasts in Stope 13 (Step 37 and Step 41), giving more consistence to the proposed model.

On the other hand, the stress-strain curve of  $RC_M$  region presents a linear increase of strain with increasing stresses, lead thinking to a linear-elastoplastic behavior. Yield point has been probably reached in coincidence with Step 37, when seismicity occurred (Fig. 6.12c). Deviation from the linear trend are due to production in Stope 7. This latter results in large strain increase with almost no significant stress variations. This peculiar trend, which was already visible in Fig. 6.9a and b, may be due to the large amount of weak and very weak zones present in this area which are not able to sustain large stresses and are thus subjected to significant large deformations. Some seismic events were recorded in the RC area in coincidence with these blasts.

#### 6.4.2.2 Temporal trends of model results and induced seismicity

To deeper investigate relationships between model and seismic observations, the cumulative seismic moment is compared with plastic energy, plastic volume and deviatoric strain. These latter have been obtained by cumulating model results between each modelled mining step within the spheres. Curves are presented in Fig. 6.13 for CC. Results obtained considering the whole spheres sub-space and the entire Lappberget microseismic catalogue present very similar trends to that of CC.

Independently from the model parameter chosen, CC curves present interesting trends (Fig. 6.13). Until Step 34, thus until the final stages of the yielding response, seismic moment and model parameter curves present similar trends, which indicate a comparable increase between model and seismic variables. In other words, model results and seismic activity respond similarly to mining excavations. Nevertheless, in coincidence with Step 34 seismic moment presents a significant

increase, which is not followed by an equal increment in model curves. This means that, at this mining step, the chosen model outputs are not capable to account for seismicity changes.

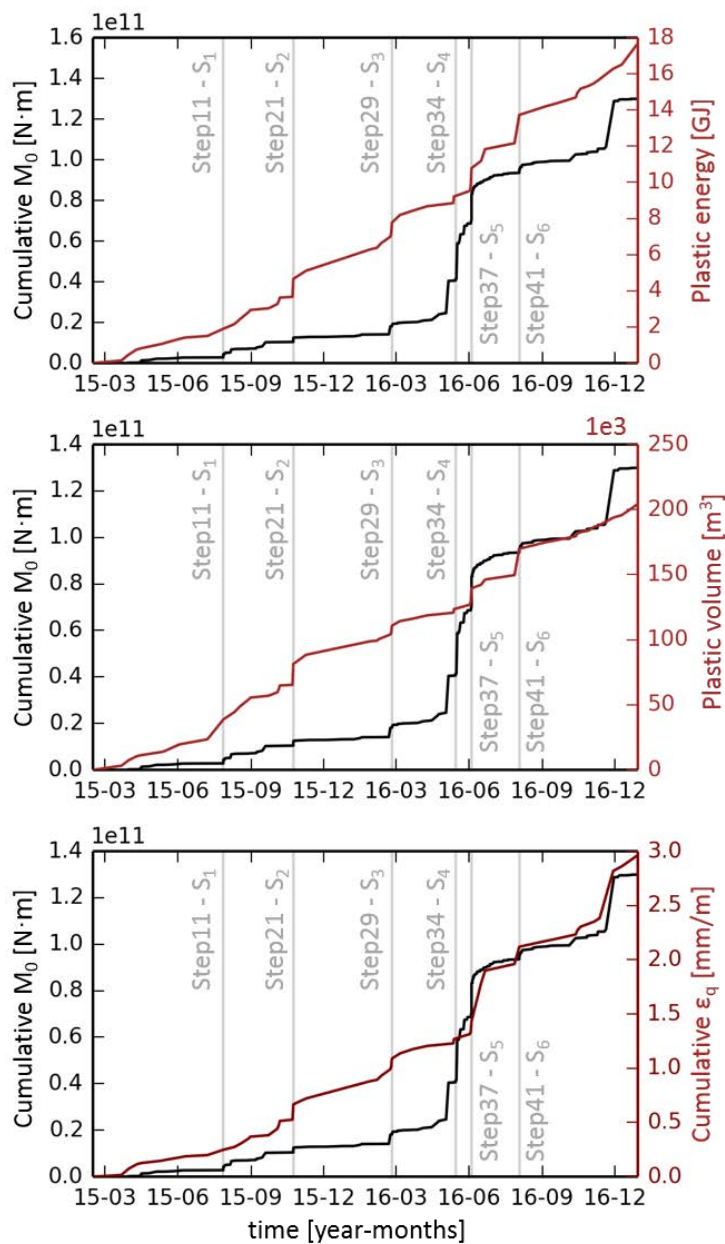


Fig. 6.13 - Temporal variation of seismic moment within CC (black) related to temporal variation of some model parameters within  $CC_M$  (red). Vertical gray lines depict the temporal occurrence of some major mining steps which lead to seismicity.

When comparing stresses and strains computed by the model with that measured by PD cell at Step 34, we found a very good agreement between model results and field data. This is visible from Fig. 6.14, which reports changes in predicted and measured principal stresses and strains immediately after the blast. However, as described in Chapter 4, most of seismicity related to Step 34 was delayed of two days with respect to the blast and persisted for more than 15 days, during which measured strains kept increasing (see Fig. 4.26). This means that, starting from Step 34, aseismic processes as well as time-dependent mechanisms are enhanced within the mine and drive seismicity. Seismic sequence  $S_4$  is a direct result of these mechanisms and is the sole sequence not directly induced by

blasting. This means that the observed difference between model and seismic parameters at Step 34 is due the lack of additional mechanisms within numerical modelling.

As expected, poor correlations are found when comparing temporal variation of model outputs and seismic parameters in the RC area (not shown).

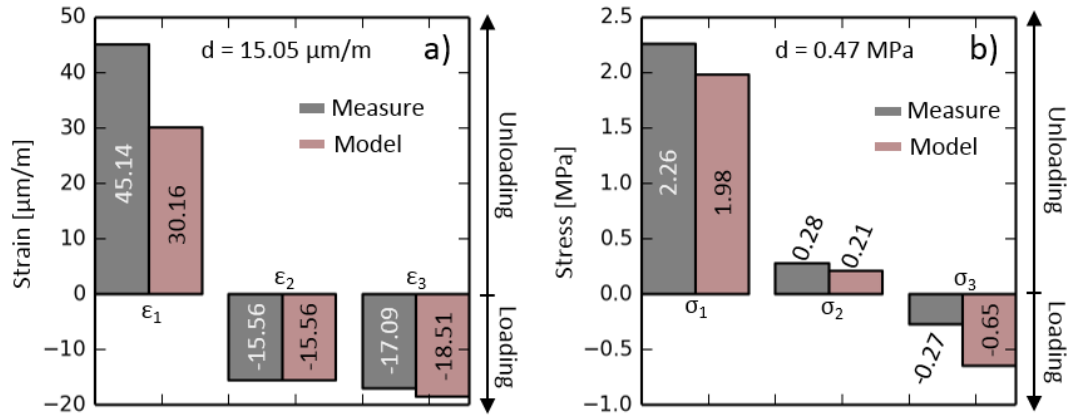


Fig. 6.14 - Principal strains (a) and stresses (b) at Step 34 measured by PD cell and predicted by modelling.

Where  $d = \sqrt{(\sigma_1^{model} - \sigma_1^{measure})^2 + (\sigma_2^{model} - \sigma_2^{measure})^2 + (\sigma_3^{model} - \sigma_3^{measure})^2}$ .

These results demonstrate that a proportionality between model outputs and seismic parameters exist for CC seismicity, at least when MSE are in majority driven by stress redistribution induced by blasting. This is the case during the period of weak rock mass response to mining (until Step 34), when seismicity was found to have a local and temporally short behavior, which was interpreted as the immediate response to local stress changes induced by blasting (Chapter 4). On the contrary, additional mechanisms are overlapping to blast-induced seismicity during the period of strong rock mass response to mining (from Step 34), as a result seismicity is long lasting over time and widespread in space (i.e. CC and RC). The introduction of these triggering mechanisms in the numerical model would probably result in improving the proportionality between seismic and model parameters also in the second half of the studied period.

## 6.5 Summary and conclusion

In this chapter, it was attempted to make a comparison between numerical model results and seismic data, based on different methods. The aim was, on one hand, to investigate whether qualitative and quantitative correlation exists, and, on the other, to better constrain differences observed between seismicity of CC and RC area.

The qualitative analysis conducted at the whole scale of 1250 block underlined an inherent difficulty in relating RC seismicity with the calculated plastic volumes and with the extension of “unstable regions” determined based on some instability criteria. On the other hand, a better correlation could be found for CC seismicity. Different aspects can be considered for finding an explanation to the observed trend. A first cause can be linked with geological properties chosen for weak and very weak materials. Indeed, as discussed in Chapter 2, these materials have been only poorly characterized by mine geologists and few information exist on their properties (and on their geometry). A way of improvement may be that of testing new material properties and calibrate the model including



information coming from microseismic activity. Indeed, as no instrument has been so far installed in the RC area, the strong seismicity located there could be an important indicator for plasticity and stress redistribution. In addition to material properties, differed strain mechanisms can be responsible for stress redistribution at larger distances and, thus, on the spatial extent of plastic zones. Therefore, deeper investigation of this supposed mechanism should be done in future works based on seismic data analysis. When phenomena will be better constrained, it will then be possible to consider their introduction in the numerical model. On the other hand, plastic zones correspond well with the localization of seismic events within the CC area. As already pointed out, this may probably indicate that geological heterogeneities between CC and RC should be taken into account by assuming different mechanical properties in these areas of the mine.

The analysis conducted at the scale of the spheres strongly highlighted the importance and the potential of reducing the model investigated area around seismic active regions. Indeed, analyzing separately CC and RC areas, it has been demonstrated that the model is actually able to account for stress, strain and plasticity changes in RC region due to Stope 13 production (see Fig. 6.9 and Fig. 6.10). It has been shown that production stages responsible for induced seismicity are also coincident with major stress changes not only in CC but also in RC, which strongly agrees with MSA. In addition, this give additional information about the rock mass response in these areas of the mine. Indeed, stress changes induced in the RC by distant Stope 13 production are visible along the whole analyzed period and not only at steps 37 and 41, when intense seismicity was triggered in this area. This may indicate the occurrence of aseismic processes within RC, caused by remote production which contribute to gradually increase stresses and strains in the area. The occurrence of aseismic processes could so far be demonstrated only in the major production area (i.e. the CC) thanks to strain measurements. While, even if these processes have been supposed to occur also within the RC, no proves were available. Numerical modelling results give now much consistence to this hypothesis.

In addition, it has been found that, when Stope 13 was almost completely mined out and only its central level still had to be blasted (Step 21), this region of the mine become close to the peak strength (see Fig. 6.12). Subsequent excavations only poorly influenced the already elevated stress which remained almost constant until when Stope 13 was completely mined out. This phase has been interpreted as a final stage of the yielding response, when plastic strains occur even for small stress changes and the seismicity rate increases. Due to excavation of the last remaining block in Stope 13, the  $CC_M$  entered in its brittle response, with a strong seismic activity recorded, sharp stress drops and increasing strain and plasticity. The remote seismicity in  $RC_M$  occurred in coincidence with the beginning of the brittle response in  $CC_M$ .

These results, which strongly agree with considerations made in Chapter 4, based on merged analysis of seismic data and strain measurements, can be seen as indicators for overstressed conditions within production area, as well as precursors of induced seismicity within RC. More precisely, three major concurrent aspects seem to be indicators for potential remote damage (see Fig. 6.12): (i) a rather null stress variation within production volume (i.e. CC), with mean stationary stresses close to the peak strength; (ii) a constant stress increase within potential seismogenic regions (i.e. RC); and (iii) the almost complete production within a stope (i.e. Stope 13). When knowing where the most seismic active regions are located, a well calibrated numerical model can track temporal evolutions of stress changes and potentially predict the occurrence of remote seismicity based on stress and

strain variation within production area. An analysis only based on stress variations within  $RC_M$  would not have been sufficient to explain the intense seismicity occurred in this region at steps 37 and 41. Indeed, even if predicted stresses are influenced by distant blasts, their variation is small and rather constant along time, such that no distinction can be done between stress changes which lead to seismicity (i.e. steps 37 and 41) within the RC, and those which did not result in any observable or measurable fracturing (i.e. 21 and 29).

The analysis conducted in Section 6.4.2.2 highlighted the difficulty in finding correlations between model outputs and seismic parameters when seismicity is not only driven by stress changes induced by blasting. This has been shown thanks to the comparison between temporal variations in model results and seismic moment (Fig. 6.13), demonstrating that proportionality exist at least when MSE are mostly a direct response to stress changes induced by blasting. If a good correlation cannot be found when other triggering mechanisms, such as creep, are overlapping, the compared analysis of trends in seismic and model variables could be used as an indicator for the occurrence of additional mechanisms not solely related to blasting. This can be a powerful analysis especially when mechanisms which lead to seismicity have not been yet understood.

# Chapter 7

## Summary, conclusions and perspectives

In order to improve our understanding of the mechanical phenomena which induce seismicity in underground mines, we propose to study the rock mass response to mining by means of seismic and geotechnical data, along with 3D numerical modelling and considering mining sequence and geological setting. The methodology has been applied to the case study of the deep Lappberget orebody (1250 block) in Garpenberg mine (Sweden), where polymetallic ore is extracted by sublevel stoping method with backfilling. The study focuses on a two-year period, between 2015 and 2016, during which mining-induced seismicity has been monitored by a seismic network, while stress and displacement changes have been measured by two strain cells and an extensometer, all installed underground. Along the study period, 52 stopes were extracted of which Stope 13 was completely mined-out, giving the unique opportunity to follow the rock mass response as excavations progress.

Seismic data recorded within the study period have been analyzed considering their spatiotemporal characteristics with respect to mine production, for then interpreting the rock mass response based on seismic source parameters and other microseismic events attributes. Then, seismic data analyses have been compared and further interpreted along with geotechnical measurements, as summarized in Section 7.1. Subsequently, a large-scale, densely-meshed, elastoplastic 3D numerical model has been built and run considering a precise reconstruction of the 4 different lithological units and of the virgin stress state. The model simulates the mining sequence, which allows analyzing rock mass response in terms of induced stresses and strains within the whole area of interest, as well as other mechanical parameters. Finally, model results have been compared with seismic data analysis to investigate whether correlations exist between each other. This combined analysis is summarized and discussed in Section 7.2.

It is important to underline that this thesis work has been done in concomitance with the operational monitoring carried out by Ineris in Lappberget orebody, thanks to which the geophysical and geotechnical networks have been installed underground. Therefore, an important part of this work has also been dedicated to the improvement of the routine seismic data processing in semi-real time, for the recognition and the selection of MSE among all recorded signals and for their localization. Major difficulties encountered in these operations are due to waveform similarities between real MSE (due to cracks in the rock mass) and signals related to mine workings and blasting, which make challenging their differentiation, but also to P and S-wave picking that can be arduous when events are emergent and characterized by short delays between P and S-phase arrivals. Based on these considerations, a back-analysis of seismic signals recorded from February 2015 to June 2016 was carried out, to evaluate and correct phase arrivals picking, and to remove from the database all recordings erroneously classified as MSE.

For the future, other improvements can be done to further enhance semi real-time acquisition and treatment. First, a continuous acquisition of seismic signals will be carried out which is preferable than the actual based on triggered data (See Chapter 3). This will significantly enhance the number of potentially recordable events. Moreover, disposing of continuous data, further analysis will be

performed on signals, such as for example ambient seismic noise correlation for monitoring wave velocity changes after blasts (e.g. Olivier et al., 2015). In addition to data acquisition, MSE detection and localization will be done based on automatic approaches. This will reduce location errors of MSE, as well as erroneous signals classifications. Ineris, in collaboration with IPGP, has already studied the feasibility of applying some of the proposed improvements to Lappberget microseismic data, such that continuous recording and automatic localization will be soon implemented on a routine base.

## 7.1 Microseismic and geotechnical data analysis and interpretation

A first result obtained by studying the Lappberget microseismic catalogue is that production blasts (PB) play a primary role in the generation of the induced seismicity and that MSA is strongly dependent on the mining sequence, rather than on the blasted volume. In particular, Stope 13, which was completely mined-out during the study period, strongly influenced the seismicity rate. We observe a first period (until May 2016) characterized by a weak rock mass response to mining, followed by an overall increase of seismic activity during a second period of strong response to mining. Events clustering highlights two major seismically active regions: the Central Cluster (CC), near the main production area, and the Right Cluster (RC), near a major talc-schist zone, in the eastern side of the mine. CC is seismically active throughout the study period, while RC becomes an intense source of seismicity only in the second half of 2016, during the period of strong rock mass response to mining. Overall, Lappberget induced seismicity presents rather small magnitudes if compared with other deep hard-rock mines (e.g. Fritschen, 2010; Kgarume et al., 2010; Kubacki et al., 2014; Vallejos and McKinnon, 2011). Indeed, moment magnitudes within the analyzed dataset vary in the range  $-2 \div 0.8$ . Events characterized by  $M_w \geq 0$  represent only a small portion of the whole dataset and are mainly encountered within CC.

Seismicity seems to primarily result from the direct response of rock masses to stress changes induced by blasting, where sudden seismic rate increases are observed immediately after the blasts, like in a mainshock-aftershock sequence. Five out of six analyzed seismic sequences are related with production in Stope 13. This is valid both for CC and RC, such that RC events are spatially remote from mined areas but temporally in coincidence with blasts. Remote seismicity triggered in RC has been interpreted considering various concomitant factors such as: (i) overstressed conditions of the CC area in the last phases of Stope 13 exploitation; (ii) large strain energy released in coincidence with the two last blasts in Stope 13, and (iii) the heterogeneous distribution of stress field in the RC area due to local lithological heterogeneities. Indeed, as the excavation progresses within the CC area, neighboring rock masses experience high stress states and seismicity rate increases fast. When new PB are performed, the large amount of stresses within the blasted rock needs to be redistributed in the surrounding rock mass, influencing the local stress field in the RC area. Here, due to inhomogeneous lithology, the local stress field is heterogeneously distributed, with high stresses in the stiff rocks surrounded by weak geological lenses. Due to this peculiar configuration, even small stress changes induced by distant blasts (in Stope 13) have the potential to trigger seismicity in the RC area, where the rock mass is close to its peak strength, and fractures are propagating fast. In addition to blasting, geological heterogeneities play a primary role on stress field redistribution and, thus, on the seismicity path within RC. It has been postulated that fractures in RC are most probably nucleated within stiff rocks and are, then, stopped before growing into bigger events, because of the

presence of weak lenses at direct contact with the breaking rock mass. As a result, RC events present higher  $b$ -values and smaller source radii compared to the CC population. Moreover, because of a heterogeneous local stress field, RC events are on average more energetic and characterized by higher apparent stress and stress drop when compared to seismicity occurring in CC.

In addition to the blast-aftershock effect, a second overlapped mechanism seems to be driving seismicity both in CC and RC. It is characterized by a slower response, persisting after the blasts. This latter component of seismicity has been considered responsible for the delayed reactivations of seismicity rate observed in most of the analyzed seismic sequences, as well as for sequence  $S_4$ , which is not related to any blast and is recorded at the beginning of the strong rock mass response period. Rather than being driven by self-triggering between consecutive MSE, this second type of seismicity has been associated to creep phenomena induced by blasting. Indeed, many evidences have been found which lead to exclude a mechanism solely driven by self-triggering through stress transfer. Firstly, seismicity rate is not linked with event magnitudes, such that delayed reactivations observed in many analyzed seismic sequences are not induced by larger MSE. The same happens for  $S_4$ , which cannot be considered as an aftershock-like sequence as larger events do not appear first. In addition, reactivations do not occur necessarily at same location than previous seismic activity, indicating that a larger-scale mechanism is involved. Finally, delayed reactivations of seismicity are mainly observed after periods of steady seismic activity or after periods where no events occurred. All these observations imply that more than a simple cascade of MSE which triggers additional events is involved, and a model driven by coupled aseismic and seismic slip has been proposed. More precisely, it is believed that mining induces aseismic deformation by creep-like phenomena within soft rocks, that slowly load surrounding seismic asperities until they break.

The latter proposed model is in part confirmed by strain measurements performed in the area of Stope 13 during the study period. Indeed, their analysis highlights, on one hand, that most of the stopes were produced without inducing seismic activity but large aseismic stains. On the other hand, induced strains are evolving and long-lasting in time, which implies the occurrence of creep phenomena. A strong evidence for a combined effect between silent creep and seismic activity is given by the observed proportionality between seismicity rate and evolution of measured strains with time. This implies that seismic activity decays proportionally to the decaying rate of induced aseismic strains, and this is consistent with models proposed in the literature (e.g. Bourouis and Bernard, 2007; Naoi et al., 2015) where seismic asperities are loaded and forced to rupture by creeping around them. Further analyses, currently ongoing, confirm the proposed model, showing the occurrence of multiplets families (i.e. events with highly similar waveforms) within Lappberget microseismic catalogue. These repeating events represent fractures occurring along neighboring asperities loaded by aseismic creep. Thanks to waveforms similarities, events within each family can be relocated by cross-correlation. Resulting uncertainties on relative location are estimated in the order of 1 m, which significantly improves location errors. Finally, as a further improvement of Lappberget microseismic data analysis, a moment tensor solution will be needed for determining focal mechanism of recorded MSE.

## 7.2 Numerical modelling and mining-induced seismicity

The objective of the numerical model developed in this thesis was, on one hand, to deeper characterize the rock mass response to mining within the whole 1250 block and, on the other hand, to investigate correlations between model results and the analyzed induced seismicity.

As a first result, the proposed numerical model highlights the influence of weakness geological zones on stress, strain and plastic zones distribution. Indeed, these areas, characterized by significantly lower mechanical properties with respect to the orebody, are not able to carry large loads. Consequently, stresses are transferred to surrounding stiff rock masses, resulting in enlarging the extent of high stress regions, particularly at weak zones edges. As a result, the stress field appears heterogeneous around excavations and large strains are observed within talc-schist lenses.

As a second important result, numerical modelling underlines the strong influence of mining sequence on stress (re)distribution. In particular, it has been shown that, due to the coupled bottom-up and top-down sequence chosen for Stope 13, the last central block of this stope experienced high stress levels. Stresses are gradually intensified as the excavation progresses within Stope 13. This observation strongly agrees with measured seismicity, found to be intensified in coincidence with last stages of Stope 13 exploitation, as well as with geotechnical measurements, which indicate increasing induced strains as the excavation progresses.

Even if most of the results of numerical modelling seem to be in good agreement with field observations, there are some aspects of the induced seismicity that the model cannot fully explain. Firstly, there is an inherent difficulty in correlating model results with RC seismicity. This is obvious when looking for correlations between spatial extension of high-stress areas and failed zones in the model with MSE localizations. RC is characterized by rather low plastic volumes and zones where plasticity occurs are not in coincidence with seismically active areas. Similarly, induced stresses and stress changes appear to be not strong enough to justify such elevated levels of induced seismicity in RC area, which remains too far from excavations. On the other hand, when analyzing numerical model results at a smaller scale, i.e. within spheres centered at seismic source locations, we do observe an influence of Stope 13 production on stress changes within RC area. This demonstrates that the model can account for stress changes induced in RC by distant production blasts, though stress variations are similar in intensity from one step to another, such that no clear distinction can be done between stress changes which lead to seismicity and those which did not result in any recorded event. In other words, by only looking at model results within RC no indication for the occurrence of the observed seismicity can be given.

Major reasons for the observed discrepancy between model results and RC seismicity should be sought in the mechanisms that can drive remote seismicity but that are not included in the model. Based on seismic data analysis, RC seismicity is assumed to be strongly driven by geological heterogeneities, which result in regions where stresses are “accumulated” and where seismicity induced by distant blasts is preferentially nucleated. Heterogeneities in the geological setting of RC area have been attributed to the large volumes of weak and very weak materials that are more abundant in this region of the mine than in the central area and in the western side. However, in the numerical model, the sole presence of weak materials seems not to be sufficient for inducing higher stresses and in turn large seismic activity within RC. This suggests that something is missing in the model. A first cause can be related to the mechanical properties chosen for weak and very weak

zones, which have not been characterized by lab tests. Also, the orebody has been considered as a homogeneous material characterized by same properties throughout the model. However, as discussed in Chapter 2, the ore in the eastern area is distinguished by massive sulfides interbedded within the host rock (i.e. limestone/dolomite). On the contrary, as we move toward the western side, the geology becomes more homogeneous, where mineralization occurs within veins networks hosted in a mica-quartzite unit. Probably, ore heterogeneities should be taken into account within the model to be able to reproduce more realistic geological settings and in turn more suitable conditions for remote seismicity. In addition to a mechanism driven by stress changes induced by distant blasts, RC seismicity appears to be as well influenced by silent creep. Therefore, improvements could probably be achieved by considering a constitutive law which considers the occurrence of creep for weak zones (only), which would probably induce stress transfers over larger distances. However deeper investigations should be done previously to determine the most appropriate constitutive law to be applied and to choose one or more lithologies to which it will be assigned.

Better results have been achieved for CC seismicity. This is particularly true when analyzing stress, strain and plasticity changes during time, averaged within spheres centered on the hypocenters of CC events (Fig. 6.12). This analysis highlights the occurrence of a period where stresses computed by modelling within CC are only slightly fluctuating around their higher value, while strains and plasticity keep increasing. Stresses then significantly drop in coincidence with mining steps which also resulted in triggering the most significant seismic sequences ( $S_5$  and  $S_6$ ). This latter period has been interpreted as the brittle response of the rock mass within CC. The observed trend in modelled stresses within this latter period is consistent with major seismicity being related to de-stressing of rock mass. Additionally, this is also consistent with the idea that remote seismicity within RC is being triggered when CC is not anymore able to charge additional loads. As a result, stress drops within production area may also be used as an indicator for the occurrence of remote seismicity. However, the proposed approach, which only considers stress changes within the major production area, does not give any indication on the region were remote seismicity will be triggered. On the other hand, when knowing where the most seismically active regions are located, a well calibrated numerical model can track temporal evolutions of stress changes and potentially predict the occurrence of remote seismicity based on stress variation within production area.

Finally, a good proportionality has been found between the temporal trend of cumulative seismic moment of CC events and the temporal variation of some model outputs (i.e. plastic energy, plastic volume and deviatoric strain), cumulated within the spheres. However, proportionality can only be achieved when seismicity is mostly driven by stress changes directly induced by blasting. As soon as additional mechanisms not considered in the model (i.e. creep) are involved in seismicity generation, seismic and model parameters are not anymore increasing at similar rates. Despite this inherent constrain, this result looks promising for possible quantitative correlations between model and seismic variables and underlines the importance of considering in the model all the mechanisms which contribute to trigger seismicity. On the other hand, at this stage, the comparison between temporal trends in seismic and model variables could be used as an indicator for additional mechanisms driving seismicity overlapping a mechanism driven by immediate stress changes induced by blasting.

### 7.3 General perspectives

Results of this thesis demonstrate that a combined approach which associates seismic and geotechnical data with numerical modelling can significantly improve our understanding of the rock mass response to mining. This is particularly true when one wants to analyze not only the seismic behavior, but also aseismic processes induced by underground excavations. However, geotechnical measurements are generally not performed at large-scale, thus induced aseismic strains are only poorly investigated. As demonstrated in this thesis, the aseismic component of the rock mass response to mining should not be discarded, as it gives not only a deeper comprehension of the rock mass behavior, but also because it can be fundamental to better understand seismic processes. Adding numerical modelling results to geophysical and geotechnical data may reduce the need for large-scale strain measurements. One of the major strengths of a combined approach lies in the inherent complementarity between geophysical data, geotechnical measurements and numerical modelling. As an example, Tab. 7.1 lists major advantages and disadvantages of the three methodologies, as arisen from the case study of Lappberget orebody. The combination of these methodologies in an integrated approach can significantly reduce their straightforward limitations, which appears evident when these instruments are considered separately.

Tab. 7.1 - Non-exhaustive list of major advantages and disadvantages of geophysical monitoring, geotechnical measurements and numerical modelling. Note that the table is valid for large-scale numerical models.

MICROSEISMIC MONITORING		GEOTECHNICAL MEASUREMENTS		NUMERICAL MODELLING	
Advantage	Disadvantage	Advantage	Disadvantage	Advantage	Disadvantage
<ul style="list-style-type: none"> <li>• Real time monitoring</li> <li>• Large-scale monitoring</li> <li>• Insight into fracture dynamics</li> <li>• Indication of stress state where fractures are nucleated</li> <li>• Failure mechanisms monitoring</li> </ul>	<ul style="list-style-type: none"> <li>• Monitor only seismic processes</li> <li>• Monitor only seismogenic regions</li> <li>• Uncertainties in detection and localization</li> <li>• Interpretation needed for stress state evaluation</li> <li>• Uncertainties in source parameter estimation</li> </ul>	<ul style="list-style-type: none"> <li>• Monitor quasi-static stress transfer in real time</li> <li>• Monitor rock mass behavior from both seismic and aseismic processes</li> <li>• Monitor changes in rock mass behaviors</li> <li>• Indication of stress and strain orientation</li> <li>• Allow numerical modelling calibration</li> </ul>	<ul style="list-style-type: none"> <li>• Local measurements</li> <li>• Assume elastic rock mass behavior for inversion</li> <li>• Measurements accuracy depending on the instrument</li> </ul>	<ul style="list-style-type: none"> <li>• Mine-wide analysis</li> <li>• Long-term prediction</li> <li>• Simulation of different excavation sequences</li> <li>• Analysis of seismic and aseismic processes</li> </ul>	<ul style="list-style-type: none"> <li>• Choice of constitutive laws</li> <li>• Computational extensive</li> <li>• Large memory for data storage</li> <li>• Mechanical parameters and their uncertainties</li> <li>• Dependent on chosen constitutive law</li> <li>• Geometry reconstruction and simplification</li> </ul>



As a prospective for future investigations and in order to presents some examples of how strengths of singular methodologies may enhance limitations of the others, the proposed integrated approach can be seen as a workflow where geophysical data, geotechnical measurements and numerical modelling are connected by a mutual exchange of data. As evidenced from results of this theses one of the aspects of the induced seismicity that the model cannot fully explain is the remote seismicity of the RC. This may be due to the mechanical parameters used as input data in the model, as well as due to the applied constitutive models. In this context, once uncertainties in localization of seismic data will be improved, a calibration of the model based on seismic events can be envisaged. This needs to be done to compensate the lack of geotechnical instruments in this area of the mine. Therefore, materials parameters could be adjusted within the model until high stress zones reasonably fit the extension of seismic regions. In addition, the ongoing work on multiplet families within Lappberget catalogue will allow determining small structures defined by events relocation within each family. Identified rupture segments could then be introduced into the model for constructing fracture networks based on real data. Also, Coulomb stress changes could be analyzed in the model along the planes defined by multiplets, to verify which conditions may bring them to rupture. All these improvements will allow to better understand the rock mass response to mining, as well as to provide a better calibrated numerical model which, together with well-located MSE and a larger microseismic catalogue, will provide better quantitative correlations between seismic and model variables.

# Bibliography

- Abdul-Wahed, M., Senfaute, G., Piguet, J.P., 2001. Source location estimation using single three-component seismic station, in: Proceedings of ISRM Regional Symposium. Presented at the Eurock, Espoo, Finland.
- Abdul-Wahed, M.K., Al Heib, M., Senfaute, G., 2006. Mining-induced seismicity: Seismic measurement using multiplet approach and numerical modeling. *International Journal of Coal Geology* 66, 137–147.
- Ahmadi, O., Juhlin, C., Malehmir, A., Munck, M., 2013. High-resolution 2D seismic imaging and forward modeling of a polymetallic sulfide deposit at Garpenberg, central Sweden. *Geophysics* 78, B339–B350.
- Ake, J., Mahrer, K., O'Connell, D., Block, L., 2005. Deep-injection and closely monitored induced seismicity at Paradox Valley, Colorado. *Bulletin of the Seismological Society of America* 95, 664–683.
- Alcott, J.M., Kaiser, P.K., Simser, B.P., 1998. Use of microseismic source parameters for rockburst hazard assessment. *Pure and Applied Geophysics* 153, 41–65.
- Allen, R., Bull, S., Ripa, M., Jonsson, R., 2003. Regional Stratigraphy, Basin Evolution, and the Setting of Stratabound Zn-Pb-Cu-Ag-Au Deposits in Bergslagen, Sweden (Final report SGU-FoU project 03-1203/99).
- Amadei, B., Stephansson, O., 1997. Rock stress and its measurement. Springer Science & Business Media.
- Amitrano, D., Grasso, J.R., Senfaute, G., 2005. Seismic precursory patterns before a cliff collapse and critical point phenomena. *Geophysical Research Letters* 32.
- Amorese, D., 2007. Applying a change-point detection method on frequency-magnitude distributions. *Bulletin of the Seismological Society of America* 97, 1742–1749.
- Andrieux, P.P., Hudyma, M.R., O'Connor, C.P., Li, H., Cotesta, L., Brummer, R.L., 2008. Calibration of large-scale three-dimensional non-linear numerical models of underground mines using microseismic data, in: Proceedings of the First International FLAC/DEM Symposium, Minneapolis. pp. 25–27.
- Bath, M., 1965. Lateral inhomogeneities of the upper mantle. *Tectonophysics* 2, 483–514.
- Bischoff, M., Cete, A., Fritschen, R., Meier, T., 2010. Coal mining induced seismicity in the Ruhr area, Germany. *Pure and applied geophysics* 167, 63–75.
- Boettcher, M.S., Kane, D.L., McGarr, A., Johnston, M.J., Reches, Z., 2015. Moment tensors and other source parameters of mining-induced earthquakes in TauTona Mine, South Africa. *Bulletin of the Seismological Society of America* 105, 1576–1593.
- Boltz, S.M., 2014. Mining-induced seismicity and FLAC3D modeling at the Trail Mountain Mine (Master thesis). University of Utah.
- Bouffier, C., Lahaie, F., Bigarré, P., 2015. Stress measurement campaign and stress monitoring experiment in the Lappberget mining area, at Garpenberg mine, Boliden (Technical note No. DRS-15-127363-05867A). Ineris.
- Bourouis, S., Bernard, P., 2007. Evidence for coupled seismic and aseismic fault slip during water injection in the geothermal site of Soultz (France), and implications for seismogenic transients. *Geophysical Journal International* 169, 723–732.
- Brown, E.T., Hoek, E., 1978. Trends in relationships between measured in-situ stresses and depth. *International Journal of Rock Mechanics and Mining Sciences & Geomechanics Abstracts* 15, 211–215.
- Brown, L., Hudyma, M., 2017. Identification of stress change within a rock mass through apparent stress of local seismic events. *Rock Mechanics and Rock Engineering* 50, 81–88.
- Brune, J.N., 1970. Tectonic stress and the spectra of seismic shear waves from earthquakes. *Journal of geophysical research* 75, 4997–5009.

- Bruneau, G., Hudyma, M.R., Hadjigeorgiou, J., Potvin, Y., 2003. Influence of faulting on a mine shaft—a case study: part II—numerical modelling. *International Journal of Rock Mechanics and Mining Sciences* 40, 113–125.
- Cai, M., 2016. Prediction and prevention of rockburst in metal mines—A case study of Sanshandao gold mine. *Journal of Rock Mechanics and Geotechnical Engineering* 8, 204–211.
- Cai, M., Kaiser, P.K., Morioka, H., Minami, M., Maejima, T., Tasaka, Y., Kurose, H., 2007. FLAC/PFC coupled numerical simulation of AE in large-scale underground excavations. *International Journal of Rock Mechanics and Mining Sciences* 44, 550–564.
- Castro, L.A.M., Bewick, R.P., Carter, T.G., 2012. An overview of numerical modelling applied to deep mining. *Innovative numerical modelling in geomechanics* 393–414.
- Chatelain, J., 1978. Étude fine de la sismicité en zone de collision continentale à l'aide d'un réseau de stations portables: la région Hindu-Kush-Pamir (PhD thesis). Université Paul Sabatier, Toulouse.
- Cichowicz, A., 1993. An automatic S-phase picker. *Bulletin of the Seismological Society of America* 83, 180–189.
- Contrucci, I., Klein, E., 2018. Knowledge review concerning hazards and risks related to Anthropogenic Seismicity, [Ineris DRS-18-171539-05280A](#).
- Contrucci, I., Klein, E., Bigarre, P., Lizeur, A., Lomax, A., Bennani, M., 2010. Management of post-mining large-scale ground failures: blast swarms field experiment for calibration of permanent microseismic early-warning systems. *Pure and applied geophysics* 167, 43–62.
- Cook, N.G.W., 1976. Seismicity associated with mining. *Engineering Geology* 10, 99–122.
- Cook, N.G.W., Hoek, E., Pretorius, J.P., Ortlepp, W.D., Salamon, M.D.G., 1966. Rock mechanics applied to study of rockbursts. *Journal of the Southern African Institute of Mining and Metallurgy* 66, 436.
- Corral, Á., 2006. Dependence of earthquake recurrence times and independence of magnitudes on seismicity history. *Tectonophysics* 424, 177–193.
- Corral, Á., 2004. Long-term clustering, scaling, and universality in the temporal occurrence of earthquakes. *Physical Review Letters* 92, 108501.
- Cotesta, L., O'Connor, C.P., Brummer, R.K., Punkkinen, A.R., 2014. Numerical modelling and scientific visualisation - integration of geomechanics into modern mine designs, in: *Proceedings of the Seventh International Seminar on Deep and High Stress Mining*. Hudyma M. and Potvin Y., Sudbury, Canada, pp. 377–395.
- Dahm, T., Becker, D., Bischoff, M., Cesca, S., Dost, B., Fritschen, R., Hainzl, S., Klose, C.D., Kühn, D., Lasocki, S., 2013. Recommendation for the discrimination of human-related and natural seismicity. *Journal of seismology* 17, 197–202.
- De Santis, F., Contrucci, I., Kinscher, J., Bernard, P., Renaud, V., Gunzburger, Y., 2018. Impact of Geological Heterogeneities on Induced-Seismicity in a Deep Sublevel Stopping Mine. *Pure and Applied Geophysics*, 1-21.
- De Santis, F., Contrucci, I., Lizeur, A., Tonnellier, A., Matrullo, E., Bernard, P., Nyström, A., 2017. Numerical approach for evaluating microseismic array performances: case study of a deep metal mine monitoring network. In *Proceedings of the 9<sup>th</sup> international symposium on rockbursts and seismicity in mines*.
- Dineva, S., Boskovic, M., 2017. Evolution of seismicity at Kiruna Mine, in: *8th International Conference on Deep and High Stress Mining*, Perth, 28-30 March 2017. Australian Centre for Geomechanics, pp. 125–140.
- Durrheim, R.J., 2010. Mitigating the risk of rockbursts in the deep hard rock mines of South Africa: 100 years of research. *Extracting the Science: a century of mining research*, Brune J (eds), Society for Mining, Metallurgy, and Exploration, Inc 156–171.
- Durrheim, R.J., Anderson, R.L., Cichowicz, A., Ebrahim-Trollope, R., Hubert, G., Kijko, A., McGarr, A., Ortlepp, W.D., Van der Merwe, N., 2006. The risks to miners, mines, and the public posed by large seismic events in the gold mining districts of South Africa.

- Dzik, E., Detournay, C., Cundall, P., 2017. A Practical Approach to Challenges in Meshing Mining Models. *Procedia Engineering*.
- Eshelby, J.D., 1957. The determination of the elastic field of an ellipsoidal inclusion, and related problems, in: *Proceedings of the Royal Society of London A: Mathematical, Physical and Engineering Sciences*. The Royal Society, pp. 376–396.
- Fairhurst, C., 2004. Nuclear waste disposal and rock mechanics: contributions of the Underground Research Laboratory (URL), Pinawa, Manitoba, Canada. *International Journal of Rock Mechanics and Mining Sciences* 41, 1221–1227.
- Feustel, A.J., 1998. Seismic attenuation in underground mines: a comparative evaluation of methods and results. *Tectonophysics* 289, 31–49.
- Foulger, G.R., Wilson, M., Gluyas, J., Julian, B.R., Davies, R., 2018. Global review of human-induced earthquakes. *Earth-Science Reviews* 438–514.
- Fritschen, R., 2010. Mining-induced seismicity in the Saarland, Germany. *Pure and applied geophysics* 167, 77–89.
- Ge, M., 2005. Efficient mine microseismic monitoring. *International Journal of Coal Geology* 64, 44–56.
- Ghasemi, Y., 2012. Numerical studies of mining geometry and extraction sequencing in Lappberget, Garpenberg (Master thesis). Luleå University of Technology, Luleå.
- Gibowicz, S.J., 2009. Seismicity induced by mining: Recent research, in: *Advances in Geophysics*. Elsevier, pp. 1–53.
- Gibowicz, S.J., 1995. Scaling relations for seismic events induced by mining. *pure and applied geophysics* 144, 191–209.
- Gibowicz, S.J., Kijko, A., 1994. *An Introduction to Mining Seismology*. Academic Press.
- Glowacka, E., Kijko, A., 1989. Continuous evaluation of seismic hazard induced by the deposit extraction in selected coal mines in Poland. *Pure and Applied Geophysics* 523–533.
- Goertz-Allmann, B.P., Goertz, A., Wiemer, S., 2011. Stress drop variations of induced earthquakes at the Basel geothermal site. *Geophysical Research Letters* 38.
- Gordeliy, E., Detournay, E., 2011. Displacement discontinuity method for modeling axisymmetric cracks in an elastic half-space. *International Journal of Solids and Structures* 48, 2614–2629.
- Grigoli, F., Cesca, S., Priolo, E., Rinaldi, A.P., Clinton, J.F., Stabile, T.A., Dost, B., Fernandez, M.G., Wiemer, S., Dahm, T., 2017. Current challenges in monitoring, discrimination, and management of induced seismicity related to underground industrial activities: A European perspective. *Reviews of Geophysics* 55, 310–340.
- Gutenberg, B., Richter, C.F., 1944. Frequency of earthquakes in California. *Bulletin of the Seismological Society of America* 34, 185–188.
- Hainzl, S., Fischer, T., 2002. Indications for a successively triggered rupture growth underlying the 2000 earthquake swarm in Vogtland/NW Bohemia. *Journal of Geophysical Research: Solid Earth* 107, ESE–5.
- Hasegawa, H.S., Wetmiller, R.J. and Gendzwil, D.J., 1989. Induced seismicity in mines in Canada: An overview. *Pure and applied geophysics*, 129(3-4): 423-453.
- He, B.-G., Zelig, R., Hatzor, Y.H., Feng, X.-T., 2016. Rockburst generation in discontinuous rock masses. *Rock Mechanics and Rock Engineering* 49, 4103–4124.
- Hoek, E., 2001. Rock mass properties for underground mines, in: *Underground Mining Methods: Engineering Fundamentals and International Case Studies*. W. A. Hustrulid and R. L. Bullock.
- Hoek, E., Brown, E.T., 1997. Practical estimates of rock mass strength. *International journal of rock mechanics and mining sciences* 34, 1165–1186.
- Hofmann, G., Ogasawara, H., Katsura, T., Roberts, D., 2012. An attempt to constrain the stress and strength of a dyke that accommodated a ML 2.1 seismic event, in: *Southern Hemisphere International Rock Mechanics Symposium SHIRMS*. pp. 1–15.
- Holmgren, J., 2015. Induced seismicity in the Dannemora mine, Sweden (Master thesis). Uppsala University, Uppsala.

- Hudyma, M., Potvin, Y., Allison, D., 2008a. Seismic monitoring of the Northparkes Lift 2 block cave- Part I undercutting. *Journal of the Southern African Institute of Mining and Metallurgy* 108, 405–419.
- Hudyma, M., Potvin, Y., Allison, D., 2008b. Seismic monitoring of the Northparkes Lift 2 block cave- Part 2 production caving. *Journal of the Southern African Institute of Mining and Metallurgy* 108, 421–430.
- Hudyma, M., Potvin, Y.H., 2010. An engineering approach to seismic risk management in hardrock mines. *Rock mechanics and rock engineering* 43, 891–906.
- Hudyma, M.R., 2009. Analysis and interpretation of clusters of seismic events in mines (PhD thesis). University of Western Australia Perth.
- Hudyma, Y., Potvin, Y., 2004. Seismic hazard in Western Australian mines. *Journal of the Southern African Institute of Mining and Metallurgy* 104, 265–275.
- Jaeger, J.C., Cook, N.G., Zimmerman, R., 2009. *Fundamentals of rock mechanics*. John Wiley & Sons.
- Jager, A.J., Ryder, J.A. (Eds.), 1999. *A handbook on rock engineering practice for tabular hard rock mines*. Safety in Mines Research Advisory Committee (SIMRAC), Johannesburg.
- Jansson, N., 2011. The origin of iron ores in Bergslagen, Sweden, and their relationships with polymetallic sulphide ores (PhD thesis). Luleå University of Technology.
- Jiang, Q., Feng, X.-T., Xiang, T.-B., Su, G.-S., 2010. Rockburst characteristics and numerical simulation based on a new energy index: a case study of a tunnel at 2,500 m depth. *Bulletin of engineering geology and the environment* 69, 381–388.
- Jing, L., 2003. A review of techniques, advances and outstanding issues in numerical modelling for rock mechanics and rock engineering. *International Journal of Rock Mechanics and Mining Sciences* 40, 283–353.
- Julià, J., Nyblade, A.A., Durrheim, R., Linzer, L., Gök, R., Dirks, P., Walter, W., 2009. Source mechanisms of mine-related seismicity, Savuka mine, South Africa. *Bulletin of the Seismological Society of America* 99, 2801–2814.
- Julià, J., Nyblade, A.A., Durrheim, R.J., Linzer, L.M., Gok, R., Walter, W., Spottiswoode, S.M., Dirks, P., 2009. A Wadati filter for mine-induced seismicity. *South African Journal of Geology* 112, 371–380.
- Kaiser, P.K., Tannant, D.D., McCreath, D.R., Jesenak, P., 1992. Rockburst damage assessment procedure. *Rock support in mining and underground construction* 639–647.
- Kanamori, H., 1977. The energy release in great earthquakes. *Journal of geophysical research* 82, 2981–2987.
- Kgarume, T.E., Spottiswoode, S.M., Durrheim, R.J., 2010. Statistical properties of mine tremor aftershocks. *Pure and applied geophysics* 167, 107–117.
- Kijko, A., 1986. Theoretical model for a relationship between mining seismicity and excavation area. *Acta Geophysica Polonica* 33, 231–241.
- King, G.C., Stein, R.S., Lin, J., 1994. Static stress changes and the triggering of earthquakes. *Bulletin of the Seismological Society of America* 84, 935–953.
- King, G.C.P., 2007. Fault interaction, earthquake stress changes, and the evolution of seismicity.
- Kinscher, J.L., 2015. The analysis and interpretation of microseismicity induced by a collapsing solution mining cavity: A contribution for progress in hazard assessment of underground cavities (PhD thesis). Université de Lorraine.
- Kubacki, T., Koper, K.D., Pankow, K.L., McCarter, M.K., 2014. Changes in mining-induced seismicity before and after the 2007 Crandall Canyon Mine collapse. *Journal of Geophysical Research: Solid Earth* 119, 4876–4889.
- Kwiatek, G., Ben-Zion, Y., 2013. Assessment of P and S wave energy radiated from very small shear-tensile seismic events in a deep South African mine. *Journal of Geophysical Research: Solid Earth* 118, 3630–3641.

- Kwiatek, G., Plenkers, K., Dresen, G., Group, J.R., 2011. Source parameters of picoseismicity recorded at Mponeng deep gold mine, South Africa: Implications for scaling relations. *Bulletin of the Seismological Society of America* 101, 2592–2608.
- Langenbruch, C., Dinske, C., Shapiro, S.A., 2011. Inter event times of fluid induced earthquakes suggest their Poisson nature. *Geophysical Research Letters* 38.
- Larsson, K., 2004. Mining induced seismicity in Sweden (Licentiate Thesis). Luleå University of Technology, Luleå.
- Lasocki, S., 2005. Probabilistic analysis of seismic hazard posed by mining induced events, in: *Proc. Sixth Int. Symp. on Rockburst and Seismicity in Mines "Controlling Seismic Risk.* pp. 9–11.
- Leśniak, A., Isakow, Z., 2009. Space–time clustering of seismic events and hazard assessment in the Zabrze–Bielszowice coal mine, Poland. *International Journal of Rock Mechanics and Mining Sciences* 46, 918–928.
- Li, T., Cai, M.F., Cai, M., 2007. A review of mining-induced seismicity in China. *International Journal of Rock Mechanics and Mining Sciences* 44, 1149–1171.
- Li, X., Zhou, Z., Lok, T.-S., Hong, L., Yin, T., 2008. Innovative testing technique of rock subjected to coupled static and dynamic loads. *International Journal of Rock Mechanics and Mining Sciences* 45, 739–748.
- Linde, A.T., Gladwin, M.T., Johnston, M.J., Gwyther, R.L., Bilham, R.G., 1996. A slow earthquake sequence on the San Andreas fault. *Nature* 383, 65.
- Liu, J., Feng, X., Li, Y., Sheng, Y., 2013. Studies on temporal and spatial variation of microseismic activities in a deep metal mine. *International Journal of Rock Mechanics and Mining Sciences* 60, 171–179.
- Lizurek, G., Rudziński, \Lukasz, Plesiewicz, B., 2015. Mining induced seismic event on an inactive fault. *Acta Geophysica* 63, 176–200.
- Lomax, A., Virieux, J., Volant, P., Berge-Thierry, C., 2000. Probabilistic earthquake location in 3D and layered models, in: *Advances in Seismic Event Location.* Springer, pp. 101–134.
- Ma, X., Westman, E.C., Fahrman, B.P., Thibodeau, D., 2016. Imaging of temporal stress redistribution due to triggered seismicity at a deep nickel mine. *Geomechanics for Energy and the Environment* 5, 55–64.
- Madariaga, R., 1976. Dynamics of an expanding circular fault. *Bulletin of the Seismological Society of America* 66, 639–666.
- Malek, F., Leslie, I., 2006. Using seismic data for rockburst re-entry protocol at INCO's Copper Cliff North Mine, in: *Golden Rocks 2006, The 41st US Symposium on Rock Mechanics (USRMS).* American Rock Mechanics Association.
- Marsan, D., Bean, C.J., Steacy, S., McCloskey, J., 1999. Spatio-temporal analysis of stress diffusion in a mining-induced seismicity system. *Geophysical Research Letters* 26, 3697–3700.
- Martin, C.D., Kaiser, P.K., Christiansson, R., 2003. Stress, instability and design of underground excavations. *International Journal of Rock Mechanics and Mining Sciences* 40, 1027–1047.
- Martin, C.D., Kaiser, P.K., McCreath, D.R., 1999. Hoek-Brown parameters for predicting the depth of brittle failure around tunnels. *Canadian Geotechnical Journal* 36, 136–151.
- Matrullo, E., Lizeur, A., 2015. Practical guide to assess seismic array performances, Ineris DRS-127366-06061B.
- Mayeda, K., Gök, R., Walter, W.R., Hofstetter, A., 2005. Evidence for non-constant energy/moment scaling from coda-derived source spectra. *Geophysical research letters* 32.
- McGarr, A., 1976. Seismic moments and volume changes. *Journal of geophysical research* 81, 1487–1494.
- McGarr, A., Simpson, D., Seeber, L., Lee, W., 2002. Case histories of induced and triggered seismicity. *International Geophysics Series* 81, 647–664.
- Mendecki, A.J., Van Aswegen, G., Mountfort, P., 1999. A guide to routine seismic monitoring in mines. *A handbook on rock engineering practice for tabular hard rock mines* 35.

- Mercer, R.A., Bawden, W.F., 2005a. A statistical approach for the integrated analysis of mine-induced seismicity and numerical stress estimates, a case study—Part I: developing the relations. *International Journal of Rock Mechanics and Mining Sciences* 42, 47–72.
- Mercer, R.A., Bawden, W.F., 2005b. A statistical approach for the integrated analysis of mine induced seismicity and numerical stress estimates, a case study—Part II: evaluation of the relations. *International Journal of Rock Mechanics and Mining Sciences* 42, 73–94.
- Miao, S.-J., Cai, M.-F., Guo, Q.-F., Huang, Z.-J., 2016. Rock burst prediction based on in-situ stress and energy accumulation theory. *International Journal of Rock Mechanics and Mining Sciences* 86–94.
- Milev, A.M., Spottiswoode, S.M., 2002. Effect of the rock properties on mining-induced seismicity around the Ventersdorp Contact Reef, Witwatersrand Basin, South Africa, in: *The Mechanism of Induced Seismicity*. Springer, pp. 165–177.
- Milne, W.G., Berry, M.J., 1976. Induced seismicity in Canada. *Engineering Geology* 10, 219–226.
- Mitri, H.S., Tang, B., Simon, R., 1999. FE modelling of mining-induced energy release and storage rates. *Journal-South African Institute of Mining and Metallurgy* 99, 103–110.
- Molchan, G., 2005. Interevent time distribution in seismicity: a theoretical approach. *Pure and applied geophysics* 162, 1135–1150.
- Müller, B., Zoback, M.L., Fuchs, K., Mastin, L., Gregersen, S., Pavoni, N., Stephansson, O., Ljunggren, C., 1992. Regional patterns of tectonic stress in Europe. *Journal of Geophysical Research: Solid Earth* 97, 11783–11803.
- Nadeau, R.M., Johnson, L.R., 1998. Seismological studies at Parkfield VI: Moment release rates and estimates of source parameters for small repeating earthquakes. *Bulletin of the Seismological Society of America* 88, 790–814.
- Nanjo, K.Z., Schorlemmer, D., Woessner, J., Wiemer, S., Giardini, D., 2010. Earthquake detection capability of the Swiss Seismic Network. *Geophysical Journal International* 181, 1713–1724.
- Naoui, M., Nakatani, M., Igarashi, T., Otsuki, K., Yabe, Y., Kgarume, T., Murakami, O., Masakale, T., Ribeiro, L., Ward, A., 2015. Unexpectedly frequent occurrence of very small repeating earthquakes ( $-5.1 \leq M_w \leq -3.6$ ) in a South African gold mine: Implications for monitoring intraplate faults. *Journal of Geophysical Research: Solid Earth* 120, 8478–8493.
- Naoui, M., Nakatani, M., Yabe, Y., Kwiatak, G., Igarashi, T., Plenkers, K., 2011. Twenty thousand aftershocks of a very small ( $M 2$ ) earthquake and their relation to the mainshock rupture and geological structures. *Bulletin of the Seismological Society of America* 101, 2399–2407.
- Nuannin, P., Kulhanek, O., Persson, L., Askemur, T., 2005. Inverse correlation between induced seismicity and b-value, observed in the Zingruvan Mine, Sweden. *Acta Geodynamica et Geomaterialia* 2, 5.
- Olivier, G., Brenguier, F., Campillo, M., Roux, P., Shapiro, N.M., Lynch, R., 2015. Investigation of coseismic and postseismic processes using in situ measurements of seismic velocity variations in an underground mine. *Geophysical Research Letters* 42, 9261–9269.
- Orlecka-Sikora, B., Lasocki, S., Lizurek, G., Rudziński, \Lukasz, 2012. Response of seismic activity in mines to the stress changes due to mining induced strong seismic events. *International Journal of Rock Mechanics and Mining Sciences* 53, 151–158.
- Ortlepp, W.D., 1997. Rock fracture and rockbursts: an illustrative study. *South African Institute of Mining and Metallurgy*.
- Ortlepp, W.D., Stacey, T.R., 1994. Rockburst mechanisms in tunnels and shafts. *Tunnelling and Underground Space Technology* 9, 59–65.
- Pasolini, C., 2008. The attenuation of seismic intensity (PhD thesis). Università di Bologna.
- Patton, T.L., Fletcher, R.C., 1998. A rheological model for fractured rock. *Journal of structural geology* 20, 491–502.
- Pechmann, J.C., Arabasz, W.J., Pankow, K.L., Burlacu, R., McCarter, M.K., 2008. Seismological report on the 6 August 2007 Crandall Canyon mine collapse in Utah. *Seismological Research Letters* 79, 620–636.

- Perfettini, H., Avouac, J.-P., 2004. Postseismic relaxation driven by brittle creep: A possible mechanism to reconcile geodetic measurements and the decay rate of aftershocks, application to the Chi-Chi earthquake, Taiwan. *Journal of Geophysical Research: Solid Earth* 109.
- Potvin, Y., Hudyma, M.R., 2001. Seismic monitoring in highly mechanized hardrock mines in Canada and Australia, in: *Keynote Address in the Proceedings of the Fifth International Symposium on Rockburst and Seismicity in Mines (RaSiM 5)*. pp. 267–280.
- Richardson, E., Jordan, T.H., 2002. Seismicity in deep gold mines of South Africa: Implications for tectonic earthquakes. *Bulletin of the Seismological Society of America* 92, 1766–1782.
- Romano, M.A., Nardis, R. de, Garbin, M., Peruzza, L., Priolo, E., Lavecchia, G., Romanelli, M., 2013. Temporary seismic monitoring of the Sulmona area (Abruzzo, Italy): A quality study of microearthquake locations. *Natural Hazards and Earth System Sciences* 13, 2727–2744.
- Ryder, J.A., 1988. Excess shear stress in the assessment of geologically hazardous situations. *Journal of the Southern African Institute of Mining and Metallurgy* 88, 27–39.
- Schoenball, M., Davatzes, N.C., Glen, J.M., 2015. Differentiating induced and natural seismicity using space-time-magnitude statistics applied to the Coso Geothermal field. *Geophysical Research Letters* 42, 6221–6228.
- Scholz, C.H., 1968. The frequency-magnitude relation of microfracturing in rock and its relation to earthquakes. *Bulletin of the seismological society of America* 58, 399–415.
- Schorlemmer, D., Woessner, J., 2008. Probability of detecting an earthquake. *Bulletin of the Seismological Society of America* 98, 2103–2117.
- Sheorey, P.R., 1997. *Empirical rock failure criteria*. AA Balkema.
- Shnorhokian, S., MacNeil, B., Mitri, H.S., 2018. Volumetric analysis of rock mass instability around haulage drifts in underground mines. *Journal of Rock Mechanics and Geotechnical Engineering* 10, 60–71.
- Shnorhokian, S., Mitri, H.S., Moreau-Verlaan, L., 2015. Stability assessment of stope sequence scenarios in a diminishing ore pillar. *International Journal of Rock Mechanics and Mining Sciences* 74, 103–118.
- Shnorhokian, S., Mitri, H.S., Moreau-Verlaan, L., 2014. Analysis of microseismic cluster locations based on the evolution of mining-induced stresses, in: *Conference: 7th International Conference on Deep and High Stress Mining-Deep Mining 2014*, Sudbury, Canada. pp. 709–722.
- Sileny, J., Milev, A., 2008. Source mechanism of mining induced seismic events - Resolution of double couple and non double couple models. *Tectonophysics*, 465(1-2), 3-15.
- Snelling, P.E., Godin, L., McKinnon, S.D., 2013. The role of geologic structure and stress in triggering remote seismicity in Creighton Mine, Sudbury, Canada. *International Journal of Rock Mechanics and Mining Sciences* 58, 166–179.
- Souley, M., Renaud, V., Al Heib, M., Bouffier, C., Lahaie, F., Nyström, A., 2018. Numerical investigation of the development of the excavation damaged zone around a deep polymetallic ore mine. *International Journal of Rock Mechanics and Mining Sciences* 106, 165–175.
- Spottiswoode, S.M., Linzer, L.M., Majiet, S., 2008. Energy and stiffness of mine models and seismicity, in: *Southern Hemisphere International Rock Mechanics Symposium SHIRMS*. Y. Potvin, J. Carter, A. Dyskin, and R. Jeffrey, Perth, Australia, pp. 693–707.
- Srinivasan, C., Arora, S.K., Yaji, R.K., 1997. Use of mining and seismological parameters as premonitors of rockbursts. *International Journal of Rock Mechanics and Mining Sciences* 34, 1001–1008.
- Stabile, T.A., Iannaccone, G., Zollo, A., Lomax, A., Ferulano, M.F., Vetri, M.L.V., Barzaghi, L.P., 2012. A comprehensive approach for evaluating network performance in surface and borehole seismic monitoring. *Geophysical Journal International* 192, 793–806.



- Stec, K., 2007. Characteristics of seismic activity of the Upper Silesian Coal Basin in Poland. *Geophysical Journal International* 168, 757–768.
- Stein, R.S., 1999. The role of stress transfer in earthquake occurrence. *Nature* 402, 605.
- Stephansson, O., 1988. Ridge push and glacial rebound as rock stress generators in Fennoscandia. *Bulletin of the Geological Institutions of the University of Uppsala* 14, 39–48.
- Stork, A.L., Verdon, J.P., Kendall, J.-M., 2014. The robustness of seismic moment and magnitudes estimated using spectral analysis. *Geophysical Prospecting* 62, 862–878.
- Switala, J., 2016. Mining sequence for Lappberget 1250 (Master thesis). Delft University of Technology, Netherlands.
- Tarantola, A., Valette, B., 1982. Generalized nonlinear inverse problems solved using the least squares criterion. *Reviews of Geophysics* 20, 219–232.
- Teyssoneyre, V., Feignier, B., Silény, J., Coutant, O., 2002. Moment tensor inversion of regional phases: Application to a mine collapse, in: *The mechanism of induced seismicity*, pp. 111–130, Springer.
- Terzaghi, K., Richart, F.E.J., 1952. Stresses in rock about cavities. *Geotechnique* 3, 57–90.
- Tierney, S.R., Morkel, I.G., 2017. The optimisation and comparison of re-entry assessment methodologies for use in seismically active mines, in: *Eighth Int. Conf. on Deep and High Stress Mining*. Deep Mining, Perth, Australia.
- Tonnellier, A., Bouffier, C., Renaud, V., Bigarré, P., Mozaffari, S., Nyström, A., Fjellström, P., 2016. Integrating microseismic and 3D stress monitoring with numerical modeling to improve ground hazard assessment, in: *Proceedings of the 8th International Symposium on Ground Support in Mining and Underground Construction*. Presented at the 8th International Symposium on Ground Support in Mining and Underground Construction, Luleå.
- Tornos, F., Peter, J.M., Allen, R., Conde, C., 2015. Controls on the siting and style of volcanogenic massive sulphide deposits. *Ore Geology Reviews* 68, 142–163.
- Urbancic, T.I., Trifu, C.-I., 2000. Recent advances in seismic monitoring technology at Canadian mines. *Journal of Applied Geophysics* 45, 225–237.
- Utkucu, M., Durmus, H., Yalçin, H., Budakoglu, E., Isik, E., 2013. Coulomb static stress changes before and after the 23 October 2011 Van, eastern Turkey, earthquake (MW= 7.1): implications for the earthquake hazard mitigation. *Natural Hazards and Earth System Sciences* 13, 1889.
- Utsu, T., Ogata, Y., Matsu'ura, R.S., 1995. The centenary of the Omori formula for a decay law of aftershock activity. *Journal of Physics of the Earth* 43, 1–33.
- Vallejos, J.A., Estay, R.A., 2018. Seismic Parameters of Mining-Induced Aftershock Sequences for Re-entry Protocol Development. *Pure and Applied Geophysics* 175, 793–811.
- Vallejos, J.A., McKinnon, S.D., 2011. Correlations between mining and seismicity for re-entry protocol development. *International Journal of Rock Mechanics and Mining Sciences* 48, 616–625.
- Vallejos, J.A., McKinnon, S.D., 2010. Omori's law applied to mining-induced seismicity and re-entry protocol development. *Pure and applied geophysics* 167, 91–106.
- Van Aswegen, G., Butler, A.G., 1993. Applications of quantitative seismology in South African gold mines, in: *Proceedings of the 3rd International Symposium on Rockbursts and Seismicity in Mines*. Rotterdam: AA Balkema. pp. 261–266.
- van Koppen, M., 2008. Estimation of the Risk for Mine Induced Seismicity in Large Scale Mining in the Garpenberg Mine (Master thesis). Delft University of Technology, Netherlands.
- Vatcher, J., McKinnon, S.D., Sjöberg, J., 2014. Mine-scale numerical modelling, seismicity and stresses at Kiirunavaara Mine, Sweden, in: *International Conference on Deep and High Stress Mining: 16/09/2014-18/09/2014*. Australian Centre for Geomechanics, pp. 363–376.
- Vidale, J.E., Shearer, P.M., 2006. A survey of 71 earthquake bursts across southern California: Exploring the role of pore fluid pressure fluctuations and aseismic slip as drivers. *Journal of Geophysical Research: Solid Earth* 111.
- Wadati, K., 1933. On the travel time of earthquake waves, Part II. *Geophysical Magazine* 7, 101–111.

- Wang, H., Ge, M., 2008. Acoustic emission/microseismic source location analysis for a limestone mine exhibiting high horizontal stresses. *International Journal of Rock Mechanics and Mining Sciences* 45, 720–728.
- Wilkie, J., Gibson, G., 1995. Estimation of seismic quality factor Q for Victoria, Australia. *AGSO Journal of Geology & Geophysics* 15, 511–517.
- Wilson, M.P., Foulger, G.R., Gluyas, J.G., Davies, R.J., Julian, B.R., 2017. HiQuake: The human-induced earthquake database. *Seismological Research Letters* 88, 1560–1565.
- Woessner, J., Wiemer, S., 2005. Assessing the quality of earthquake catalogues: Estimating the magnitude of completeness and its uncertainty. *Bulletin of the Seismological Society of America* 95, 684–698.
- Wuestefeld, A., Kendall, J.M., Verdon, J.P., van As, A., 2011. In situ monitoring of rock fracturing using shear wave splitting analysis: an example from a mining setting. *Geophysical Journal International* 187, 848–860.
- Wyss, M., Brune, J.N., 1968. Seismic moment, stress, and source dimensions for earthquakes in the California-Nevada region. *J. Geophys. Res.* 73, 4681–4694.
- Xiao, Y.X., Feng, X.T., Li, S.J., Feng, G.L., Yu, Y., 2016. Rock mass failure mechanisms during the evolution process of rockbursts in tunnels. *International Journal of Rock Mechanics and Mining Sciences* 174–181.
- Yamada, T., Mori, J.J., Ide, S., Abercrombie, R.E., Kawakata, H., Nakatani, M., Iio, Y., Ogasawara, H., 2007. Stress drops and radiated seismic energies of microearthquakes in a South African gold mine. *Journal of Geophysical Research: Solid Earth* 112.
- Zhang, H., Huang, G., Song, H. and Kang, Y., 2013. Experimental characterization of strain localization in rock. *Geophysical Journal International*, 194(3), pp.1554-1558.
- Zhao, H., Ma, F., Xu, J., Guo, J., 2012. In situ stress field inversion and its application in mining-induced rock mass movement. *International journal of rock mechanics and mining sciences* 53, 120–128.
- Zhu, W.C., Li, Z.H., Zhu, L., Tang, C.A., 2010. Numerical simulation on rockburst of underground opening triggered by dynamic disturbance. *Tunnelling and Underground Space Technology* 25, 587–599.
- Zhu, W.C., Wei, J., Zhao, J., Niu, L.L., 2014. 2D numerical simulation on excavation damaged zone induced by dynamic stress redistribution. *Tunnelling and Underground Space Technology* 43, 315–326.
- Ziegler, M., Reiter, K., Heidbach, O., Zang, A., Kwiatak, G., Stromeyer, D., Dahm, T., Dresen, G., Hofmann, G., 2015. Mining-Induced Stress Transfer and Its Relation to a Mw 1.9 Seismic Event in an Ultra-deep South African Gold Mine. *Pure and Applied Geophysics* 172, 2557–2570.

# Annex A

## Supplementary figures and tables

Tab. A.1 - Rock type list as reported by mine geologists (June 2017). Codes may not be in numerical order.

Code	Description	Code	Description	Code	Description	Code	Description
1	quartzite	54	nepheline syenite	119	metabasite	175	massive sulphide-fes
2	arenite	55	monzonite	120	granulite	176	massive sulphide-feass
3	quartz sandstone	56	diorite	121	amphibolite	179	actinolite skarn
4	feldspathic quartzite	57	gabbro	125	pegmatite	180	garnet skarn
5	dolomite	58	tonalite	126	aplite	181	tremolite skarn
6	siltstone	60	ultramafic rock	127	qu.carbonate	182	diopside skarn
7	conglomerate	61	hyperite	128	carbonate rock	183	hornblende skarn
8	arkose	62	anorthosite	129	greenstone	184	skarn-dolomite breccia
9	tillite	63	dunite	131	lamprophyre	186	above ground
10	sedimentary breccia	64	peridotite	132	diabase	187	Soil
11	turbidite	65	pyroxenite	133	hyperite	188	core loss
12	greywacke	66	hornblendite	135	dike	190	limestone breccia
13	argillite	67	serpentinite	136	quartz	191	single mineral rock
14	shale/phyllite	75	mylonite	138	alteration rock	193	Sandstone
15	limestone-dolomite	76	shear breccia	139	amphodelite quartzite	200	phlogopite shale
16	chert	77	breccia	140	sericite-chlorite quartzite	201	mica talc shale
17	clastic sediment	78	hornfels	141	chlorite quartzite	202	phlogopite quartzite
18	tuffite	80	gneiss	142	zoisite quartzite	203	phlogopite-sericite quartzite
19	pumice	81	augen gneiss	143	cordierite quartzite	204	cordierite-mica quartzite
20	tuff	82	banded gneiss	144	andalusite quartzite	245	shale-greywacke
21	lapilli tuff	83	mica gneiss	145	andalusite-biotite quartzite	246	tuff-lava
22	agglomerate	84	amphib.gneis	146	chlorite-biotite quartzite	247	agglomeratic lava
23	pyroclastic rock	85	garnet gneiss	147	biotite quartzite	248	tuffs and shales
24	tufficite	86	supracrustal gneiss	148	mica quartzite	249	cinerites shales
25	ignimbrite	87	amphibolite gneiss	149	garnet-biotite quartzite	251	mass-med bd
26	mass-flow	88	sedimentary gneiss	150	unidentifiable rock type	270	cordierite-sericite
27	sedimentary rock	89	sedimentary vein gneiss	151	tremolite-talc schist	273	calcite ore
30	rhyolite	90	vein gneiss	152	talc schist	274	massive calcite alteration
31	quartzlatite	91	migmatite	153	garnet-biotite schist	275	unidentifiable alteration rock
32	dacite	94	metasedimentary rock	154	schist (alteration rock)	276	sericite porphyroblast
33	trachyte	95	metavolcanic rock	155	sericite schist	277	amphibo-magnetite-ilmenite
34	andesite	97	gneiss granite	156	sericite-quartz schist	278	Amphibo. extreme alteration
35	basalt	98	granitic gneiss	157	sericite-andalusite schist	279	amphibole-magnetite
36	clastic volcanic / volcaniclastic rock	99	hällflinta/flint	158	sericite-chlorite schist	271	biotite spotted alteration rock
37	volcanic rock	100	leptite	160	sericite-cordierite schist	280	chlorite-biotite-sericite
38	lava	101	felsite	161	chlorite schist	325	feldspar-epidote zone
39	coherent volcanic rock / non-clastic volcanic rock	102	greenstone	162	chlorite-talc schist	272	hydrothermal dike with calcite-magnetite-ilmenite
40	porphyry	105	ore quartzite	163	chlorite-andalusite-schist	301	quartz-eye rhyolite
41	quartz porphyry	106	sericite quartzite	164	chlorite-quartz-schist	302	quartz-porph.-rhyolite
42	quartz keratophyre	107	fels	165	chlorite-biotite-schist	303	rhyolite quartz porphyry
43	quartz-feldspar porphyry	108	phyllite	166	weathering product	304	rhyolite-dacite
44	feldspar porphyry	109	skarn	169	massive oxides	305	basaltic andesite
45	porphyrite	114	graphitic shale	170	massive sulphide	306	diabase dyke
50	granite	115	mica schist	171	massive sulphide-cufes2	307	semi-massive sulphide
51	granodiorite	116	biotite schist	172	massive sulphide-fes2		
52	quartz diorite	117	chlori.schis	173	massive sulphide-zns		
53	syenite	118	limestone	174	massive sulphide-pbs		

Tab. A.2 - Seismic probes position and orientation. Coordinates are expressed in meters and angles in degrees.

AU Level	Probe name	Probe type	Probe coordinates			X sensor		Y sensor		Z sensor	
			X	Y	Z	Az.	Dip	Az.	Dip	Az.	Dip
1108	A02	3C	3690	551	-1106	56	-65	56	25	326	-0.7
	A03	1C	3815	519	-1102					195	-2.6
	A04	1C	3714	446	-1106					214	-1.6
1182	B05	3C	3593	631	-1206	250	12	160	4	234	-78.3
	B06	3C	3891	557	-1192	208	25	118	3	202	-64.8
	B07	1C	3620	429	-1169						+90
	B08	1C	3836	475	-1168						+90
1257	C09	3C	3674	446	-1245	317	0	47	0		+90
	C10	3C	3722	589	-1276	185	-11	95	-16	312	-72.4
	C11	1C	3660	529	-1246						+90
	C12	1C	3786	489	-1246						+90

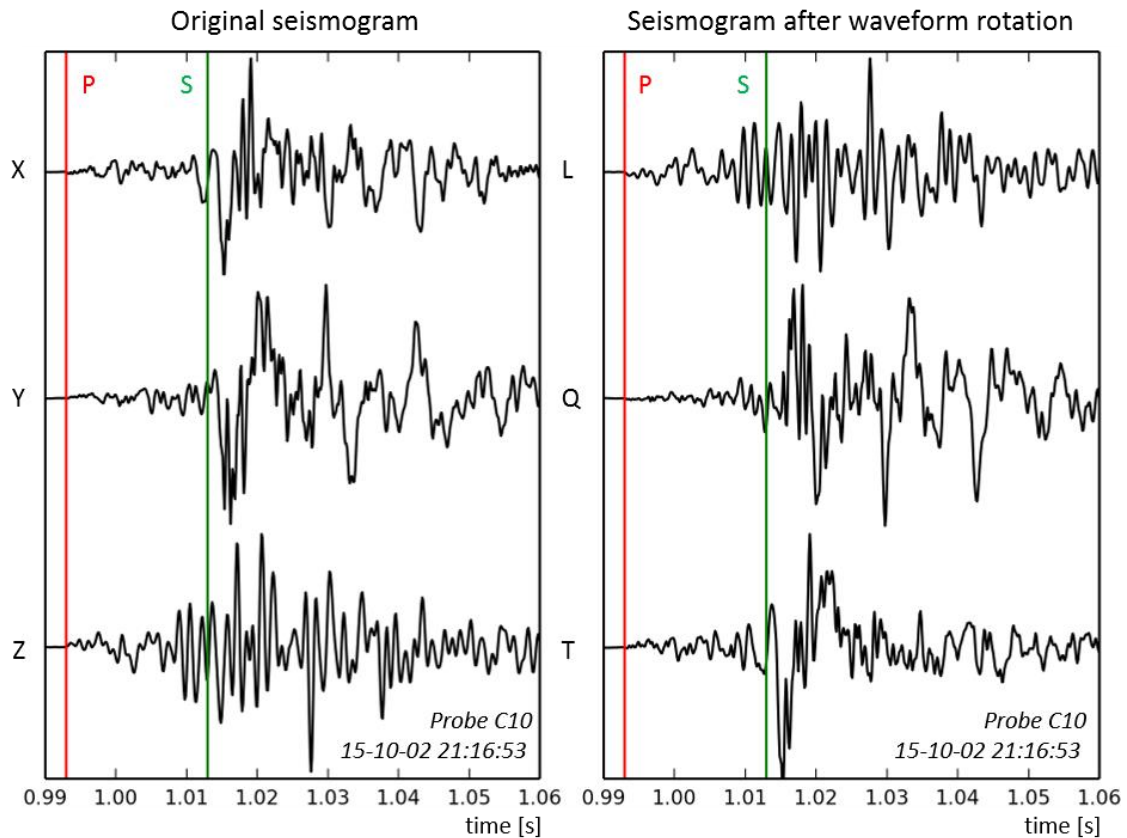


Fig. A.1 - Example of waveform rotation from the probe coordinate system (X, Y, Z - on the left) to the wave polarization direction (L, Q, T - on the right). One can observe a significant reduction of P phase, along Q- and T-components after waveform rotation (on the right). Red and green lines represent the P- and S-wave arrivals, respectively, as retrieved by manual picking.

Tab. A.3 - Characteristics of MSE selected for amplitude ratio technique.

Date & time	X [m]	Y [m]	Z [m]	$M_L$
04/06/2016 14:04	3740.625	478.125	-1171.875	-2.3
04/06/2016 14:04	3746.875	446.875	-1153.125	-2.4
04/06/2016 14:04	3784.375	428.125	-1153.125	-2.7
04/06/2016 14:04	3759.375	465.625	-1171.875	-2.6
04/06/2016 14:07	3740.625	471.875	-1165.625	-2.1
04/06/2016 14:15	3734.375	459.375	-1165.625	-2.1
04/06/2016 14:17	3778.125	446.875	-1165.625	-2.6
04/06/2016 14:24	3740.625	471.875	-1165.625	-2.0
04/06/2016 14:38	3740.625	478.125	-1165.625	-2.2
04/06/2016 14:42	3781.25	431.25	-1168.75	-2.6
04/06/2016 14:42	3778.125	459.375	-1146.875	-2.6
04/06/2016 14:53	3759.375	484.375	-1165.625	-2.8
04/06/2016 14:55	3740.625	471.875	-1165.625	-2.1
04/06/2016 14:59	3740.625	478.125	-1159.375	-2.3
04/06/2016 15:27	3734.375	471.875	-1165.625	-2.1
04/06/2016 15:31	3759.375	503.125	-1159.375	-2.8
04/06/2016 15:38	3734.375	459.375	-1171.875	-1.8
04/06/2016 15:58	3765.625	503.125	-1146.875	-2.6
04/06/2016 15:59	3734.375	471.875	-1165.625	-2.6
04/06/2016 16:43	3740.625	478.125	-1153.125	-2.0
04/06/2016 17:00	3740.625	478.125	-1153.125	-2.1

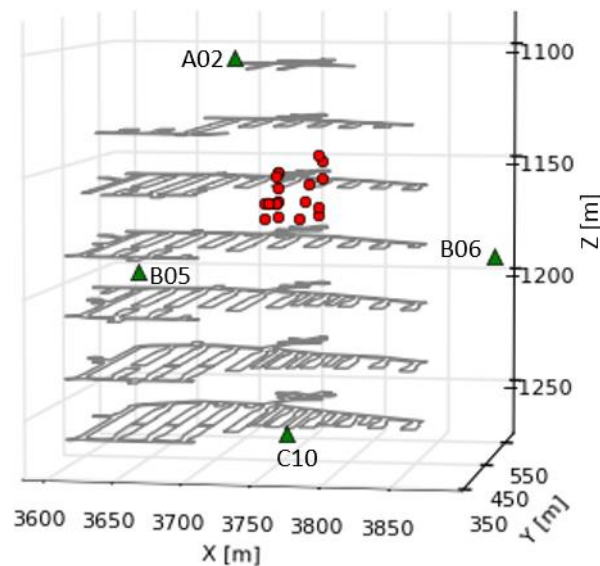


Fig. A.2 - Localization of MSE selected for amplitude ratio technique. Green triangles indicate the position of 3C probes used for amplitude ratio calculation.

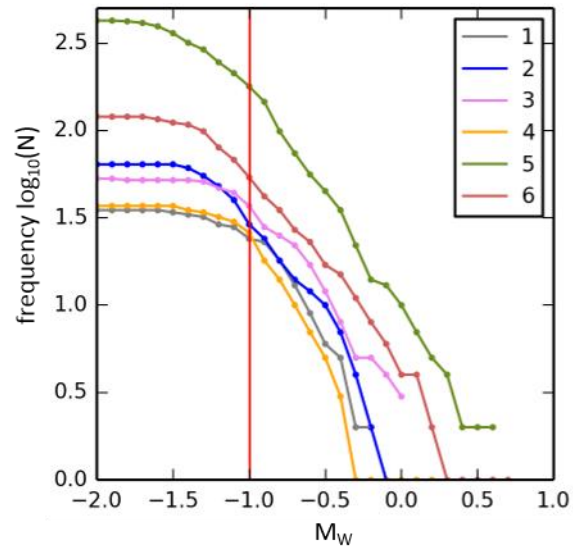


Fig. A.3 - Frequency-magnitude relationship for 6 different periods of time between February 2015 and December 2016. The vertical red line indicates the magnitude of completeness which matches all the analyzed periods. Temporal intervals have been chosen accordingly to variations in seismic network configuration and are organized as follows: 1) 15-02-14 00:00:00 ÷ 15-06-10 02:01:00; 2) 15-06-10 02:02:00 ÷ 15-09-12 07:57:00; 3) 15-09-12 07:58:00 ÷ 15-11-25 16:19:00; 4) 15-11-25 16:20:00 ÷ 16-03-07 07:01:00; 5) 16-03-07 07:02:00 ÷ 16-08-22 20:12:00; 6) 16-08-22 20:13:00 ÷ 16-12-23 23:59:00.

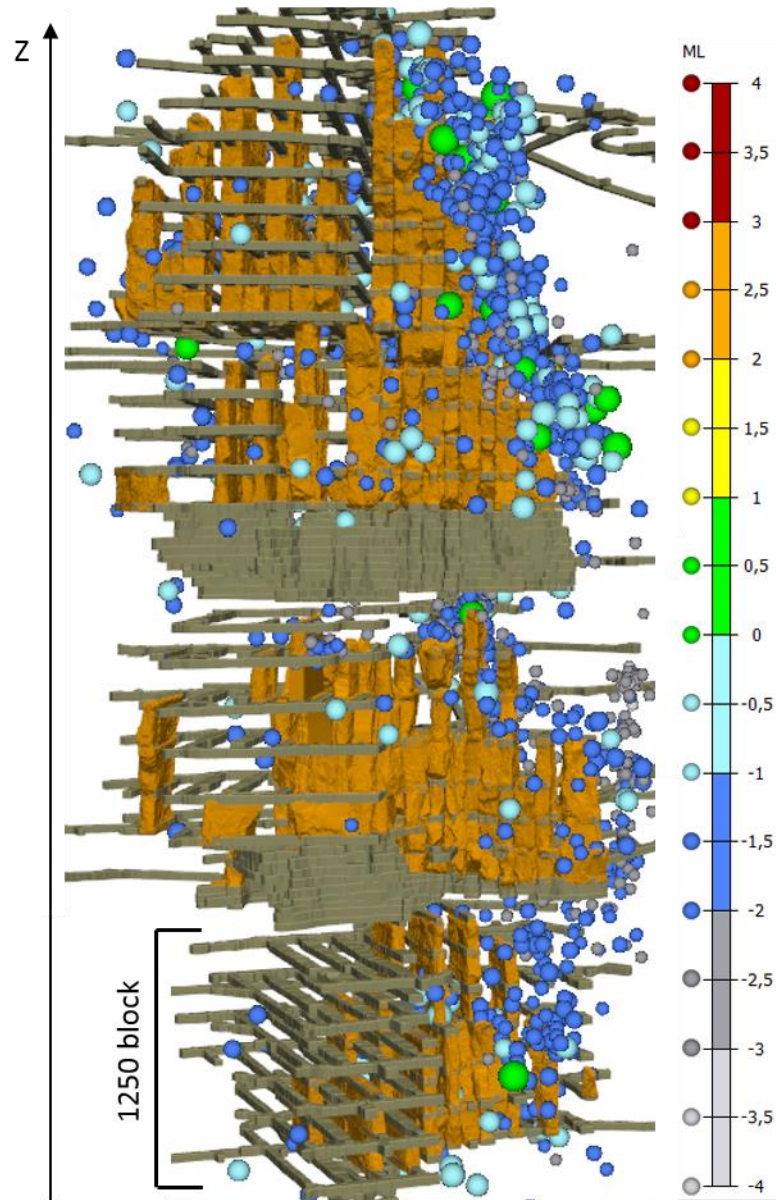






Fig. A.4 - Microseismic activity recorded by IMS network between 2015 and 2016 in the whole Lappberget orebody.

Tab. A.4 - Values of Hoek-Brown constant  $m_i$  for different rock types.

Rock Type		Rock Name and $m_i$ Values			
Igneous	Intrusive	Granite 32±3 Granodiorite 29±3	Diorite 25±5 Dolerite (16±5)	Gabbro 27±3 Norite 22±5	Peridotite (25±5)
	Extrusive	Rhyolite (16±5)	Andesite 25±5	Basalt (16±5) Diabase (16±5)	Porphyries (20±5)
	Volcanic		Agglomerate (19±3)	Tuff (13±5)	
Sedimentary	Clastic	Conglomerate (4±18) Breccia (4±16)	Sandstone 17±4	Siltstone 7±2 Marls (7±2)	Mudstone 4±2 Shale (6±2)
	Carbonate	Crystalline limestone (12±3)	Sparitic limestone (10±2)	Micritic limestone (9±2)	Dolomite (9±3)
	Chemical		Gypsum 8±2	Anhydrite 12±2	
	Organic			Coal (8±12)	Chalk 7±2
Metamorphic	Foliated	Gneiss 28±5	Schist 12±3	Phyllites (7±3)	Slate 7±4
	Slightly Foliated	Migmatite (29±3)	Amphibolite 26±6		
	Non Foliated	Quartzite 20±3	Meta-sandstone (19±3)	Hornfels (19±4)	Marble 9±3

Tab. A.5 - Geological Strength Index (GSI) as a function of rock mass structure and discontinuities.

GEOLOGICAL STRENGTH INDEX (GSI)		JOINT SURFACE CONDITION								
According to rock mass structure and discontinuity surface conditions observed on the rock mass at site, select the appropriate box in this chart. Estimate the average value of the GSI from the contours.		<p>VERY GOOD – very rough, fresh, unweathered joint surfaces</p> <p>GOOD – rough, slightly weathered, stained joint surfaces</p> <p>FAIR – Smooth, moderately weathered, and altered surfaces</p> <p>POOR – Slickensided, highly weathered surfaces with compact coating or fillings or angular fragments.</p> <p>VERY POOR – Slickensided, highly weathered, surfaces with soft clay coating or filling</p>								
ROCK MASS STRUCTURE		⇒ Decreasing of Surface Quality ⇒								
	BLOCKY – very well interlocked undisturbed rock mass consisting of cubical blocks formed by three orthogonal joint sets	Decreasing Interlocking of Rock Blocks ⇐	80	70	60	50	40	30	20	10
	VERY BLOCKY – interlocked, partially disturbed rock mass with multi-faced angular blocks formed by four or more joint sets.		60	50	40	30	20	10		
	BLOCKY/FOLDED – folded and faulted with many intersecting discontinuities forming angular blocks.		40	30	20	10				
	CRUSHED – poorly interlocked, heavily broken rock mass with a mixture of angular and rounded blocks.		20	10						



Tab. A.6 - Simulated mining sequence in the numerical modelling. Date of production is reported in year-month-day. Code for stope names is as follow: Stope name\_lower extraction level #blast round number. Volumes only refer to stopes volumes, without considering the additional amount rock extracted by galleries excavations.

Model step	Date of production	Stope	Excavated volume [m <sup>3</sup> ]	Model step	Date of production	Stope	Excavated volume [m <sup>3</sup> ]
0.1	14-03-24	13_1132 #1	45836	21	15-10-24	13_1207 #3	6702
0.2	14-04-05	13_1257 #1		22	15-11-09	15_1257 #5	4563
0.3	14-04-15	13_1132 #2		23	16-01-29	9_1232 #1	3611
0.4	14-05-03	13_1257 #2		24	16-02-06	9_1232 #2	2281
0.5	14-05-18	13_1257 #3		25	16-02-09	19_1232 #1	2562
0.6	14-08-20	13_1132 #3		26	16-02-12	17_1257 #3	3554
0.7	14-09-13	13_1132 #4		27	16-02-23	11_1207 #1	2266
0.8	14-09-21	13_1232 #1		28	16-02-24	19_1232 #2	5700
0.9	14-10-07	13_1232 #2		29	16-02-25	13_1182 #1	2758
0.10	14-10-23	13_1232 #3		30	16-03-06	11_1207 #2	5503
0.11	14-11-27	15_1257 #1		31	16-03-22	17_1257 #4	4510
0.12	15-01-15	13_1257 #2		32	16-04-09	17_1207 #1	2527
0.13	15-02-07	13_1257 #3		33	16-05-12	21_1257 #1	2341
1	15-03-15	11_1257 #1	3196	34	16-05-13	17_1207 #2	6497
2	15-03-22	17_1257 #1	2053	35	16-06-02	21_1257 #2	5700
3	15-03-31	11_1257 #2	4681	36	16-06-03	15_1207 #1	4345
4	15-04-10	13_1157 #1	2239	37	16-06-04	13_1182 #2	3978
5	15-04-15	17_1257 #2	5455	38	16-06-16	7_1257 #1	3707
6	15-05-13	15_1232 #1	3970	39	16-06-21	15_1207 #2	7078
7	15-05-15	19_1257 #1	2866	40	16-07-28	12_1257 #1	1118
8	15-06-03	15_1232 #2	7579	41	16-08-03	13_1182 #3	4346
9	15-06-10	19_1257 #2	5142	42	16-09-07	12_1257 #2	4954
10	15-07-08	13_1157 #2	2910	43	16-09-17	12_1257 #3	1044
11	15-07-28	13_1157 #3	5330	44	16-10-13	12_1257 #4	10024
12	15-08-11	13_1207 #1	3275	45	16-10-15	9_1207 #1	5168
13	15-08-19	11_1232 #1	2807	46	16-10-19	11_1182 #1	2590
14	15-08-29	11_1232 #2	3534	47	16-10-29	15_1232 #1	2437
15	15-08-31	17_1232 #1	2142	48	16-11-05	11_1182 #2	4532
16	15-09-23	17_1232 #2	2648	49	16-11-12	15_1232 #2	3672
17	15-10-04	9_1257 #1	4363	50	16-11-29	7_1232 #1	3915
18	15-10-06	13_1207 #2	2784	51	16-12-10	17_1182 #1	2729
19	15-10-07	17_1232 #3	4037	52	16-12-28	17_1182 #2	4191
20	15-10-23	15_1257 #4	2416				

# Annex B

## Galleries and stopes geometry reconstruction

Maps of the galleries at each level of block 1250 were provided by the mining company. After the smoothing of these profiles, boundary lines have been converted in 2D surfaces and then extruded for 6 m in the vertical direction, which corresponds to real galleries height, obtaining 3D surfaces of cross drifts and footwall drifts at each level of the block (Fig. B.1). Stopes between consecutive levels were reconstructed building rectangular surfaces from the lower cross drift toward the upper one, for a vertical extension of 16.2 m (Fig. B.2a). Rectangular surfaces were then connected with upper drifts by surfaces inclined of 45°. The overall stopes height is 25 m from the roof of the upper drift to the floor of the lower one (Fig. B.2a). However, real stopes do not have necessary such regular shape. For this reason, their design was further modified based on 3D laser scanner results of excavated stopes (provided by mining company), as illustrated in Fig. B.2b and c. This avoids overestimations (Fig. B.2b) or underestimations of stopes volumes (Fig. B.2c).

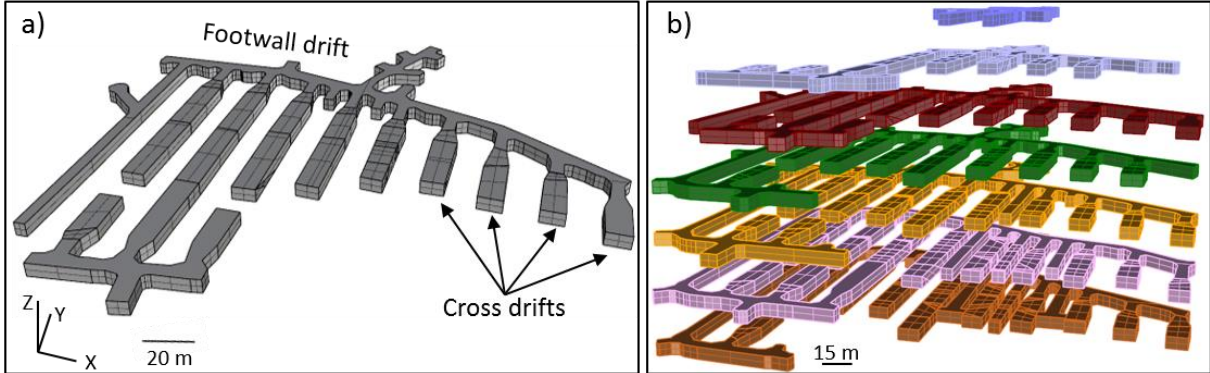


Fig. B.1 - 3D reconstruction of mine levels. (a) Zoomed view on level 1157. (b) All levels of block 1250.

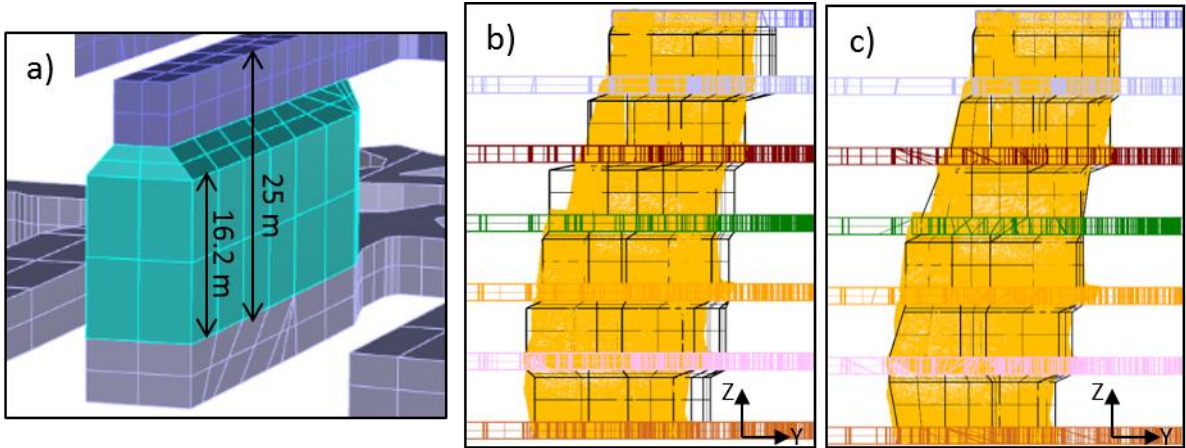


Fig. B.2 - Details of stopes reconstruction. (a) Zoom on one stope between two consecutive levels. Example of Stopes 13 profile (in black) before (b) and after (c) reshaping, based on 3D laser scanner results (in yellow).

To excavate stopes along the entire length of mine drifts, more than one blast is performed (Fig. B.3a). Thus, reconstructed stopes between consecutive levels need to be divided in separated blocks, which correspond to the volume of extracted rock mass for each step of the excavation (i.e. mine sequencing). However, the extension of these blocks along the Y direction of the mine is not

provided by mining company. To overcome this problem, blocks lengths were determined from drill holes coordinates (Fig. B.3b) and vertical or inclined surfaces have been placed at the retrieved Y coordinates, for separating stopes in subsequent blocks (Fig. B.3c). In this way, the model mesh will be homogeneous between blocks, ensuring a better resolution and avoiding numerical issues during the computation.

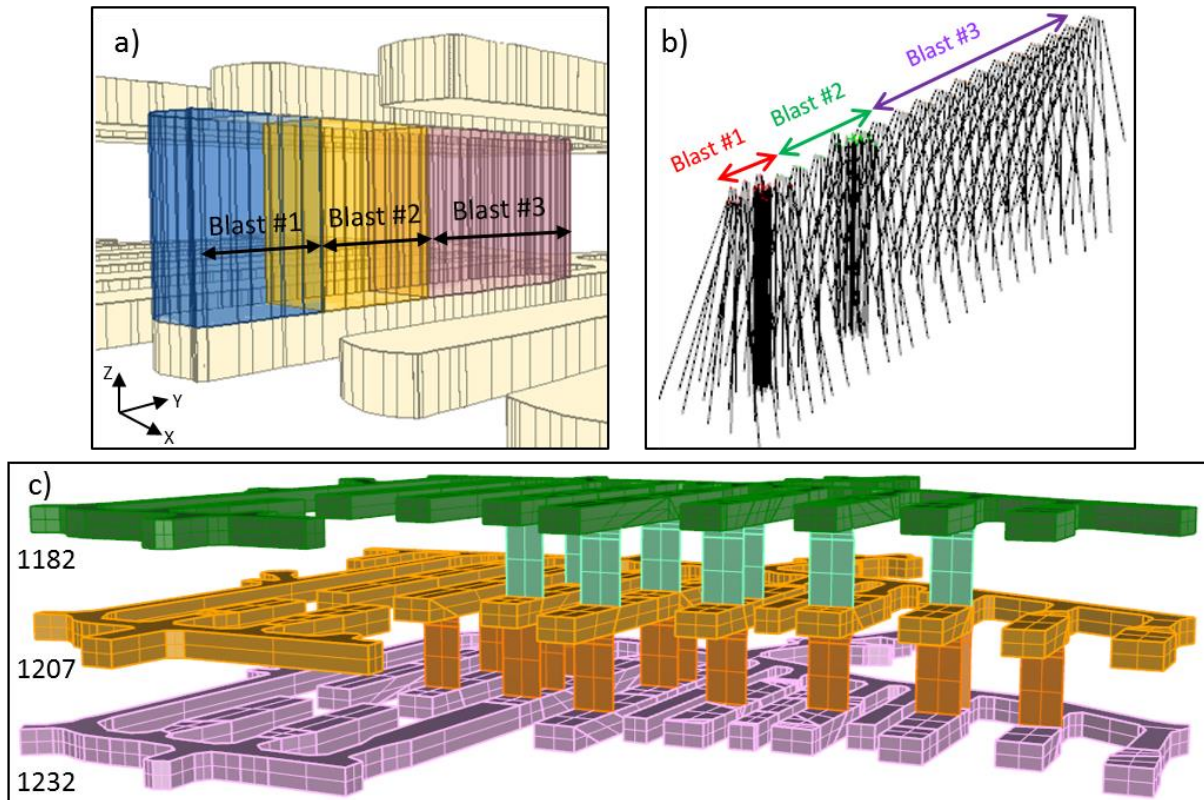


Fig. B.3 - Reconstruction of mine sequencing per each stope. (a) Example of stope excavation between two consecutive levels. (b) Example of drill holes design used for charging and then blasting each stope block. (c) Surfaces used for separating stopes in different blocks for numerical modelling. Note that only levels between -1182 m and -1232 m are shown.

Final result of galleries and stopes reconstruction is presented in Fig. B.4. As previously discussed, model meshing has been performed by choosing an automatic approach. However, before running the automatic mesh, galleries and stopes surfaces need some polishing. Nodes of each surface must be in continuity with the nodes of the adjacent elements, otherwise the subsequent volumetric meshing cannot be done. For this reason, numerous surfaces of the whole geometry have been manually redrawn to ensure continuity of nodes, as it is shown in the close-up of Fig. B.4.

Another issue which needs to be carefully considered during geometry reconstruction is to avoid free edges. Indeed, when dealing with complex geometries, where nodes are very close to each other, it can occur that separated surfaces, which must be in contact, are drawn leaving a small empty space, i.e. a free edge, in between, which is most of the time undetectable from a visual inspection. This generates errors in the mesh or even software crashing, which have been avoided by detecting and then correcting all free edges accidentally left in the geometry.

Finally, the whole galleries and stopes geometry needs to be converted in a non-manifold polysurface, where the term “polysurface” is used to indicate many surfaces joined together. A non-

manifold polysurface is basically a polysurface where some edges have more than two faces joined to a single edge. This is typically observed for the stopes that have been subsequently divided into separated block by adding vertical planes inside. When trying to mesh such geometries, it can occur that the intersecting surface is double-meshed on its sides, as the subsequent block are considered like separated volumes. To avoid this issue, the entire galleries and stopes geometries have been joined into a non-manifold polysurface which is then treated as a single polysurface, where each surface is counted and meshed only once.

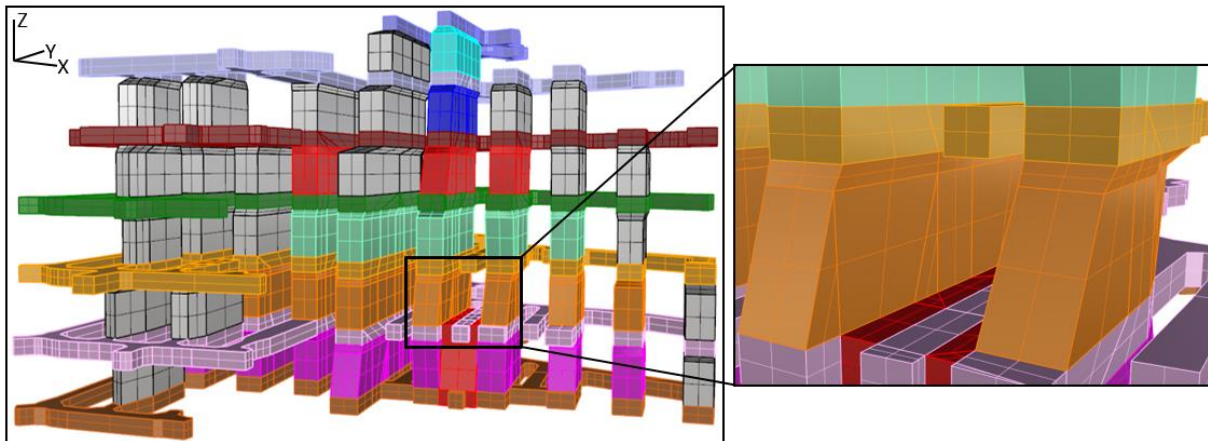


Fig. B.4 - Final result of galleries and stopes reconstruction in block 1250. The close-up shows the continuity of nodes between each surface needed for ensuring the validity of the mesh. See text for more details.

# Annex C

## Weakness zones geometry reconstruction

As discussed in Chapter 2, weakness zones geometry, as defined by mine geologists, is only provided in form of maps for each mine level. No information is given about weakness zones extension or continuity between consecutive levels. However, when doing a 3D numerical model, it is essential to reconstruct the shape of these elements in 3D. Moreover, the geometry of each weak lens can be sometimes extremely complex, characterized by thin wedges and very small dimensions. For this reason, based on the geometry provided by mine geologists and updated on May 2017, weak lenses at each level of the mine were firstly reshaped in order to simplify their geometry, reducing thin wedges and discarding lenses whose width is lower than 2 m, which would have a poor influence on model results having chosen a mesh resolution of 1 m. Then, where possible, simplified weak lenses have been connected between mine levels, treating weak and very weak layers separately.

Most of the weak layers deployed on the eastern side of the mine were easier to reconnect, due to their abundant presence at each level of the mine. This allowed reconstructing a large continuous block which covers the entire height of the study area and which extends from about 3680 m to 3850 m along X axis and from 380 m to 465 m in the Y direction (in green in Fig. C.1). Similarly, the very weak zone has been reconstructed in this area of the mine (in red in Fig. C.1). This latter is intersecting the previously described weak block along the entire height of the study area, even if it is thinner in the Y direction and less abundant for  $X < 3750$  m.

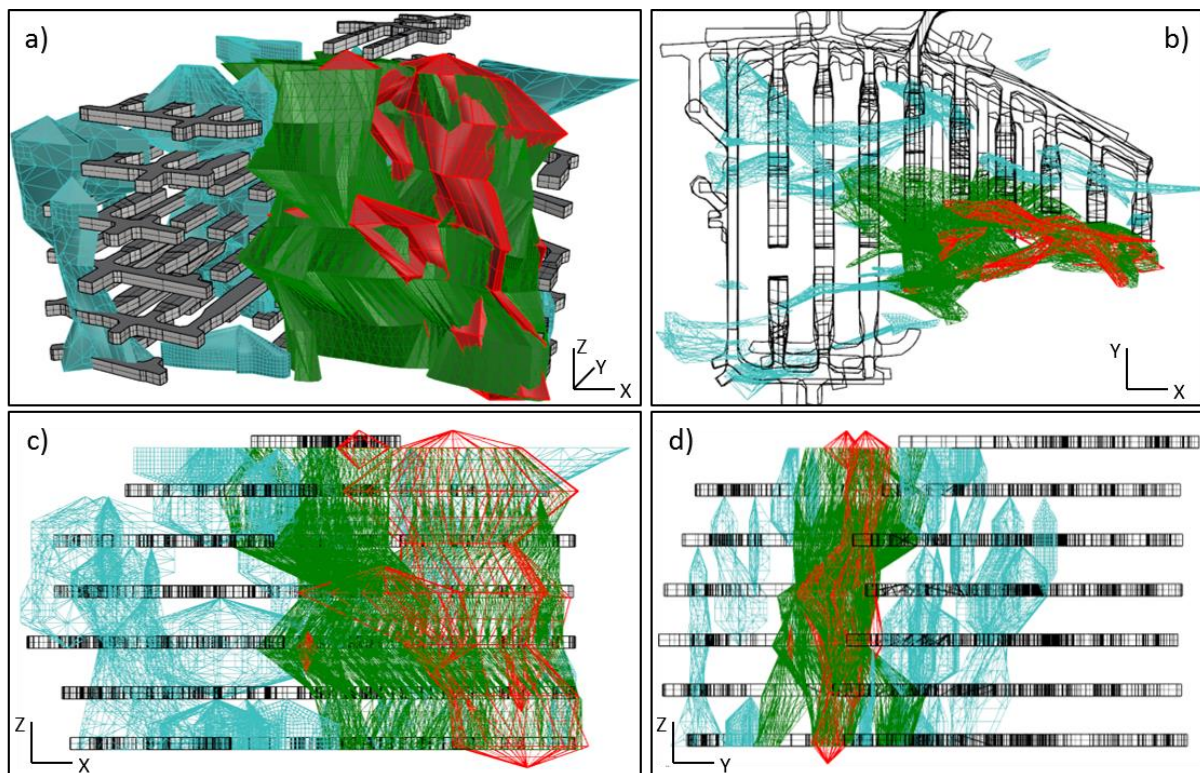


Fig. C.1 - Final reconstruction of weak (blue and green) and very weak (red) zones within block 1250. Blue weak zones represent the isolated type lenses.

All the other weak zones appeared isolated, which means that no other weak lenses were reported on the levels immediately above and/or below. These zones were thus extended in the vertical direction of 12.5 m up and down, which corresponds to a half of a level height, and then connected to the next level by making an extrusion toward a point (in blue in Fig. C.1). In this manner, the volume of reconstructed weak areas is maximized, and, at the same time, we ensure a correct reproduction of real geological observations made at each level of the mine.

## Annex D

### Model meshing

*Griddle* meshing is performed in three subsequent steps. First, a mesh intersector tool (i) creates a node-to-node triangular mesh which ensures continuity between nodes of intersecting surfaces. Then, (ii) re-meshing of the previous intersected mesh is performed, creating a surface meshing of all the elements of the model. During this step, type (triangular and/or quadrilateral) and size of the surface mesh can be chosen. Finally, the volume meshing (iii) creates a volumetric mesh using elements surfaces as boundaries. This latter mesh is then directly imported in FLAC3D, where meshes are automatically reproduced.

Using the described procedure, model meshing was firstly applied to separated elements of the model. The non-manifold polysurface of galleries and stopes within block 1250 (Fig. B.4) has been meshed with a maximum zone size of 1 m, while a 5 m mesh has been chosen for the upper levels of the mine. Finally, the cube which represents the model boundaries has been meshed with a 20 m size. These was done with the *Griddle* surface meshing tool, choosing a quad-dominant meshing type where triangles and quadrilaterals are mixed together, applying by preference quadrilateral meshes where possible. Orebody, weak and very weak zones were not remeshed with *Griddle*. Indeed, these elements (STL files) are directly imported in FLAC3D for defining ranges of zones to which different mechanical properties are affected. Excavation limits within these zones are already fixed by the non-manifold polysurface and by upper levels meshes.



Fig. D.1 - Envelope (in black) built around galleries and stopes (in gray) for controlling mesh size within this area. Note that, for an easier visualization, the upper surface of the envelope has been intentionally removed from the image.

Finally, the volume meshing tool has been applied to the whole model geometry for filling the interior of the model domain with volume elements whose faces are conforming to input surface mesh faces. However, volume meshing tends to minimize the number of elements that connect different surfaces. This means that mesh size cannot be controlled and zones larger than 1 m can be created within the area of interest of the model. To overcome this problem, an envelope with a 1 m surface mesh was built at about 6 m distance from galleries and stopes within block 1250 (Fig. D.1), to ensure that the mesh inside this envelope will keep a minimum size of 1 m. Outside the envelope zones can be larger, following the surface meshing of the boundaries box. The orebody, as well as weak and very weak profiles which fall inside the envelope are meshed with 1 m size. Automatic meshing procedure has taken around 4 hours of computation.



## **Comportement mécanique des massifs rocheux dans les mines profondes : surveillance in situ et modélisation numérique pour l'amélioration de l'évaluation de l'aléa sismique**

Afin de mieux comprendre les interactions entre les modifications des contraintes induites par l'exploitation minière et la génération d'activité sismique, une zone profonde de la mine de Garpenberg (Suède) a été instrumentée par l'Ineris avec de sondes microsismiques et de cellules géotechniques. L'analyse spatio-temporelle des événements microsismiques enregistrés entre 2015 et 2016, ainsi que leurs paramètres à la source, ont mis en évidence deux types de réponses sismiques : une locale et courte dans le temps directement induite par les tirs de production, l'autre plus persistante et distante des excavations étant principalement contrôlée par des hétérogénéités géologiques. L'analyse des données géotechniques a montrée l'occurrence de déformations aismiques, ainsi que de phénomènes de fluage induits par l'exploitation. De plus l'activité sismique décroît proportionnellement au taux de diminution des déformations mesurées. Cette dernière observation implique que le fluage peut être un autre mécanisme menant à la sismicité, s'ajoutant au changement de contrainte immédiat induit par les tirs de production. Dans la dernière partie de cette thèse, un modèle géomécanique élasto-plastique 3D a été réalisé et ses résultats ont été comparés aux données géophysiques. Cette comparaison a montré que les modèles numériques à l'échelle de la mine peuvent être des outils puissants pour étudier la sismicité induite à grande échelle. Cependant, il y a certains aspects de la sismicité induite que le modèle ne peut expliquer entièrement. Cela est le cas pour la sismicité déclenchée à distance des excavations, alors que de meilleures corrélations sont trouvées lorsque l'on considère la sismicité à proximité des zones de production. Les résultats de cette thèse ont démontré qu'une approche combinée associant les données sismiques et géotechniques à la modélisation numérique peut améliorer considérablement notre compréhension de la réponse des massifs rocheux à l'exploitation minière. La combinaison de ces méthodologies dans une approche intégrée peut réduire considérablement leurs limites explicites qui sont évidents lorsque ces instruments sont considérés séparément.

**Mots clefs** : sismicité induite, contraintes induites, surveillance in situ, modélisation numérique.

## **Rock mass mechanical behavior in deep mines: in situ monitoring and numerical modelling for improving seismic hazard assessment**

With the aim of better understanding interactions between stress modifications induced by mining and the generation of seismic activity, a deep area of Garpenberg mine (Sweden) was instrumented by Ineris with microseismic probes and geotechnical cells. Spatiotemporal analysis of recorded seismicity between 2015 and 2016, as well as seismic source parameters, have highlighted two types of seismic rock mass responses: one local and temporally short directly induced by production blasts, the other long-lasting over time and remote from excavations being mainly controlled by geological heterogeneities. Geotechnical data analysis showed the occurrence of aseismic deformations, as well as creep phenomena induced by mining exploitation. In addition, seismic activity decays proportional to the decaying rate of measured strains. This latter observation implies that creep may be another mechanism driving seismicity, in addition to the immediate stress change induced by blasting. In the last part of this thesis, a 3D elasto-plastic geomechanical model has been realized and its results have been compared with geophysical data. This comparison showed that mine-wide numerical models can be suitable for the analysis of mining induced seismicity at large-scale. However, there are some aspects of the induced seismicity that the model cannot fully explain. This is particularly true for remote seismicity occurring at a distance from excavations, while better correlations are found when considering seismicity close to production areas. Results of this thesis demonstrated that a combined approach which associates seismic and geotechnical data with numerical modelling can significantly improve our understanding of the rock mass response to mining. The combination of these methodologies in an integrated approach can significantly reduce their straightforward limitations, which appears evident when these instruments are considered separately.

**Key words**: induced seismicity, induced stresses, in situ monitoring, numerical modelling.